Joint use of dual-frequency electrowetting and interferometry in a digital microsystem : application to evaporation and surface ageing at drop scale

Johannes Theisen

UNIVERSITÉ DE GRENOBLE

THÈSE

Pour obtenir le grade de

DOCTEUR DE L'UNIVERSITÉ DE GRENOBLE

Spécialité : **Mécanique des fluides, procédés, énergétique**

Arrêté ministériel : 7 août 2006

Présentée par

Johannes Theisen

Thèse dirigée par **Laurent Davoust**

préparée au sein du **Laboratoire des Ecoulements Géophysiques et Industriels (LEGI)** et du **Laboratoire de Sciences et Ingénierie des Matériaux et Procédés (SIMaP)** dans **l'École Doctorale Ingénierie – Matériaux Mécanique Energétique Environnement Procédés Production (I-MEP²)**

Joint use of dual-frequency electrowetting and interferometry in a digital microsystem: Application to evaporation and surface ageing at drop scale.

Thèse soutenue publiquement le **05 février 2013**,
devant le jury composé de :

M. Charles Baroud
Professeur, Ecole Polytechnique Palaiseau, Rapporteur
M. Franz Bruckert
Professeur, Grenoble INP, Président
M. Laurent Davoust
Professeur, Grenoble INP, Directeur de thèse
M. Nicolas Faure
Chercheur, BioMérieux, Examinateur
M. Yves Fouillet
Chercheur, CEA Grenoble, Examinateur
Mme. Agnès Girard-Egrot
Professeur, Université Claude Bernard Lyon, Examinatrice
M. Vincent Senez
Directeur de recherche, CNRS-IEMN, Rapporteur

Für meine Eltern.

" There are many things in life that a man can possess,
But only what he interiorized cannot be taken from him.
No, he can even pass it on. "

Yap Voon Kheong

Remerciements

Merci en premier lieu à tous les membres du jury de thèse, avec lesquels la soutenance a vu de belles discussions pleines d'ouvertures pour le futur. J'espère de tout cœur que ce beau projet continuera à vivre encore quelques années.

Ladies first, merci à Mme **Agnès Girard-Egrot** pour l'opinion de l'"extra-terrestre" (avec un clin d'œil bien sûr), la lecture de ce manuscrit a dû être un exercice plutôt inhabituel. Merci aussi pour vos commentaires, l'anectode du dimanche et les compliments pour le pot de thèse qui m'ont presque plus ému que vos félicitations pour mon doctorat.

Merci à M. **Charles Baroud**, pour ses remarques pertinentes sur mon travail qui m'aident à bien évoluer toujours aujourd'hui. Merci d'avoir accepté la tâche de rapporteur de ce travail.

Merci à M. **Vincent Senez**, sa vision du projet a permis de planter plein de graines dans la matière grise de certaines personnes. Vivement que ces graines poussent et qu'elles arriveront à donner naissance à une idée bien développée ou encore à un partenariat. Ceci ne sera malheureusement plus entre mes mains. Egalement merci à toi d'avoir rapporté et d'avoir partagé ta vision sur ce travail.

Merci à M. **Yves Fouillet** sans qui cette thèse aurait eu du mal à voir le jour. Les discussions fructueuses et les prêts généreux de matériel ne seront pas oubliés. Merci également d'avoir assisté au jury de thèse ce qui a été un honneur pour moi, et un grand enrichissement scientifique.

Merci à M. **Nicolas Faure** pour ses remarques pertinentes en vue de l'application. Il aurait été très apprécié de te voir le jour de la soutenance, très enrichissant également. Tu avais la meilleure des excuses, et tes conseils et remarques que tu nous as transmis seront gardés entre de bonnes mains.

Last but certainly not least, un très grand merci à M. **Franz Bruckert**, j'ai un grand estime pour lui en tant que professeur et scientifique, qui voit toujours plus loin que le bord de son assiette. Elément immuable durant mon parcours académique depuis des années, tu as toujours su donner les bons conseils au bon moment. Merci pour ton immense disponibilité malgré ton emploi du temps extrêmement chargé. Ton altruisme et le caractère fort constructif de tes remarques et conseils font de toi un professeur et un scientifique que je suis très heureux de connaître.

Je tiens à remercier cordialement mon directeur de thèse, **Laurent**, pour son immense disponibilité et son écoute tout le long de cette thèse. Son exigeance

quant à mon travail a fait aboutir ce projet dont je suis très fier de la meilleure des façons. Merci pour ton humeur pour lisser les vagues des journées souvent stressantes et chargées. J'ai adoré passer ces dernières années sous ta direction, humainement et scientifiquement. A part le badminton, j'ai appris que tu jouais très bien au ping-pong, discipline scientifique qui va sûrement manquer dans les années à venir !

Un grand merci aussi aux membres de l'équipe MIP, ce travail contient aussi une part de vous ;) Merci à vous, **Benjamin**, **Cyril**, **Constant**, **Corinne**, **Janina** et **Jules** !

Qu'est un travail sans collègues ? Merci à tous les compatissants pour votre bonne humeur et les moments passées à papoter quand les journées étaient trop longues. Je pense particulièrement à **Sylvain** pour les sorties dans les canyons grenoblois magnifiques, **Lauriane**, **Ye** et **Johny** pour la compétition des gâteaux et de volley. Merci aussi aux personnes avec qui j'ai passé de bons moments au labo ou en dehors de la recherche, **Antoine**, **Bart**, **Clelia**, **David**, **Davide**, les deux **Guillaumes**, **Jean**, **Jon**, **Laurent**, **Manolo**, **Mariana**, **Martin**, **Matias**, **Max**, **Michael**, **Olivier**, **Sébastien**, **Thibaud**, **Tobit**, **Ulrich** et **Virginie**.

A ne pas oublier ! Les magiciens du pool technique, toujours présents pour une petite blague et pour donner un coup de main des plus précieux, je dirais mêmes les piliers du LEGI sans lesquels il serait impossible de mener un travail expérimental correctement ! Herzlichen Dank, grazie, merci à **Joseph**, **Laure**, **Mile**, **Muriel**, **Pierre**, **Pierre-Alain**, **Stéphane** et **Vincent** !

Merci également à **Patricia** et ses charmantes collègues du 2eme, **Julie**, **Nicole**, **Séverine**, **Sylvie** ainsi qu'à **Augustine** de l'école doctorale pour avoir subi avec moi les aléas de la vie administrative.

Un énorme merci à **Gaby** et **Olivier** du service informatique, qui m'ont souvent aidé à me sortir d'une impasse informatique ! Pas comme si c'était arrivé souvent. . . :)

Holá chicas y chicos de las Naciones Unidas de la Nutrición! Gracias á vosotros para las cenas increíbles que hemos compartido juntos! Merci **Benoît**, **Brunito**, chica **Christelle**, **Daniela**, **Fanny**, **Gabriele**, le sacré **Hernán**, **Izabel**, **José**, **Mayra**, **Pablo**, **Pedro**, **Sandrine**, **Yeshica** et **Yu Tian**!

Merci aussi à tous les franco-allemands de l'**ADKG** avec qui j'ai vécu des moments extraordinaires. J'espére pouvoir profiter encore longtemps de nos week-ends et certains d'entre vous sont devenus de vrais amis. Merci à vous tous et surtout à **Andy**, **Estelle**, **Fiston**, **Jochen**, **Martin**, **Nico** et notre **Wiebke** belge !

La plupart des journées libres, je les passais par beau temps sur les sommets des montagnes, suspendu à une corde ou encore en dévalant de belles pentes le genou dans la neige, respirant à pleins poumons les plaisirs simples de la

nature. **Jérémie**, pour moi tu es un frère de la montagne, ensemble nous avons appris à y trouver notre place, avons vécu les hauts et les bas, dans le sens figuré et propre.

Matthieu, ton amour pour la nature et tes proches, et ta passion à transmettre tes savoirs font de toi une personne extraordinaire. Je garde en très bon souvenir nos sorties, et je pense que les futurs projets ne vont pas manquer. . .

Merci également à tous les autres montagnards du dimanche, particulièrement **Daniel**, **JB** et **Perrine** ! Que le ciel bleu soit toujours avec nous ;)

La bande des physiciens (pour la majorité), vous m'épatez à chaque fois qu'on se voit, merci à vous tous ! **Adri**, **Alex**, **Aurel**, **Charlène**, **Emma**, **Fabien**, **Fabrice**, **Hélène**, **Isa**, **Justine**, **Michael**, **Olivier** et **Yannick**.

Calou, frère auvergnat, au plaisir de voir ta terre natale et de connaître encore plus d'excellentes personnes comme tu l'es ! *"Tout est possible dans ce monde, il suffit de faire preuve de persévérance."* Tu l'as bien montré !

Claire, merci pour tous les road-trips en quatre et en deux roues et surtout pour tout ce que tu m'as apporté ! *"May the Beat and the Pulse be with you!"*

Eugénie, la joyeuse, et **Nico**, l'homme au grand cœur, merci à vous deux pour tous les partages ! *"La vraie vie ne se mesure pas aux choses matérielles, mais aux moments passés avec ceux que nous aimons."*

Ina, bonne chance pour ton chemin de tout cœur, et merci pour tous ces merveilleux moments que nous avons passés ensemble ! La danse va rester une passion grâce à toi ! *"Les chemins de la vie peuvent mener ici ou là, la direction est toujours la bonne."*

Pierrot, le sage fou, merci pour toutes les découvertes ! *"Vivre, c'est rêver, et rêver, c'est vivre. L'un n'existe que rarement sans l'autre."*

Ein herzliches Dankeschön geht auch an den Teil meines Herzens, der in Deutschland geblieben ist, und immer bleiben wird. Meine Heimat bedeutet für mich Familie und Freunde. **Alex**, **Christina**, **Christine**, **Julia**, **Kristina**, **Nadine**, **Simon** und **Yvonne**, Freunde, die ich noch viel zu selten sehe.

Mein letzter Gedanke geht an **meine Familie**. Ich danke Euch für die Liebe, die Ihr mir entgegenbringt, und all die Unterstützung und Ratschläge, die mir jederzeit immer sehr weitergeholfen haben meinen Weg zu finden. Vielen Dank dafür, und dass ich diese Zeilen schreiben kann.

Enfin, merci à vous tous d'avoir enrichi ma vie durant ces trois années.

Johannes

Contents

Nomenclature

Abbreviations

AC	Alternate current
ALE	Arbitrary Lagrangian Eulerian method
APD	Avalanche photo diode
BSA	Bovine serum albumin
DC	Direct current
EWOD	Electrowetting on dielectric
FEM	Finite element method
FFT	Fast Fourier transform
FWHM	Full width at half maximum
GPIB	General purpose interface bus
GUI	Graphical user interface
LOC	Laboratory on a chip
LM	Langmuir
µTAS	Micro total analysis system
ODE	Ordinary differential equation
PBS	Phosphate buffered saline
PCB	Printed circuit board
PCR	Polymerase chain reaction
PCU	Processor control unit
PDE	Partial differential equation
POM	Polyoxymethylene
PTA	Cleanroom facilities at CEA Grenoble
rms	Root mean square
TCL	Triple contact line
USB	Universal serial bus

Roman symbols

a_n	Shape mode amplitude	[m]
c	Surface capacitance	[F m^{-2}]
C	Volume concentration	[m^{-3}]
d	Radial distance to drop center	[m]
D	Diffusivity	[m^2 s^{-1}]

e	Thickness of dielectric layer	[m]
$\boldsymbol{E}$,E	Electrical field and field strength	[V m^{-1}]
f	Excitation frequency	[Hz]
f_{osc}	Oscillation frequency	[Hz]
F	Force	[N]
$F, \hat{F}$	Sessile drop form factor, volume and V/S ratio	[1]
$\mathcal{F}$	Weak contribution	
H	Drop height	[m]
i_U	Electric current	[A]
I	Light intensity	[W m^{-2}]
j	Chemical flux	[m^{-2} s^{-1}]
J	Functional, implicit function	
K	Multielectrode EW correction factor	[1]
L	Length scale	[m]
n	Drop shape oscillation mode number	[1]
$\boldsymbol{n}$	Normal vector	[1]
$\tilde{n}$	Refractive index	[1]
N	Total amount of molecules	[1]
P	Perimeter	[m]
P_n	Legendre polynomial of degree n	[1]
p	Hydrodynamic pressure	[Pa]
R	Drop radius	[m]
R_{B}	Drop base radius	[m]
s	Laplace space variable	[s^{-1}]
S	Surface area	[m^2]
t	Time	[s]
$\boldsymbol{t}$	Tangent vector	[1]
T	Temperature	[K]
T_{EW}	Electrowetting tension	[N m^{-1}]
$\boldsymbol{u}$	Velocity	[m s^{-1}]
u_{osc}, U_{osc}	Streaming boundary condition, amplitude	[m s^{-1}]
U_{s}	Streaming velocity	[m s^{-1}]
U	(Electrowetting) Voltage	[V]
U_1	High-frequency voltage	[V]
U_2	Low-frequency voltage	[V]
$\tilde{U}$	Envelope voltage	[V]
V	Drop volume	[m^3]
w	Test function	
Z	Electric impedance	[Ω]

Greek symbols

δ_s	Stokes layer thickness	[m]
δ_{Stu}	Stuart length	[m]
d γ	Surface tension	[N m^{-1}]
Γ	Surface concentration	[m^{-2}]
Γ_∞	Maximum packing concentration	[m^{-2}]
ϵ	Dielectric constant of a dielectric layer	[1]
ζ	Droplet oscillation amplitude	[m]
θ	Contact angle	[°]
κ	Confinement	[m]
λ	Wavelength	[m]
λ_n	Sessile drop oscillation eigenvalue	[m]
Λ	Friction coefficient	[N s m^{-2}]
μ	Viscosity	[N m^{-1}]
ν	Electrowetting frequency	[Hz]
Π	Surface pressure	[N m^{-1}]
ρ	Density	[kg m^{-3}]
σ	Variance	
τ	Time scale	[s]
υ	Drop shape parameter	[1]
φ	Azimuthal angle	[rad]
$\boldsymbol{\Phi}$, Φ	Velocity potential	[m^2 s^{-1}]
ϑ	Polar angle	[rad]
ψ	Phase shift	[rad]
$\boldsymbol{\Omega}$	Vorticity	[m s^{-1}]
ω	Angular frequency	[rad s^{-1}]

Super-/subscripts

0	Initial value, maximal value
acq	Data acquisition/sampling
c	Critical value
d	Driving electrode
e	Equilibrium
g	Electrode gap
G	Ambient gas phase
hy	Hydrophobic layer
i	Instantaneous

ins	Insulating/dielectric layer
L	Liquid phase
μ	Micro
m	Maximum
met	Metal layer
osc	Drop oscillation
r	Reference electrode
s	Surface value
S	Solid substrate
stream	Streaming
vol	Volume

Dimensionless numbers

Bo	Bond number	$= \rho g R_0^2/\gamma$
Re	Reynolds number	$= \rho U_\infty L/\mu$
S	Strouhal number	$= \omega L/U_\infty$
R_s	Streaming Reynolds number	$= \rho U_\infty^2/\omega\mu$
ξ	Schlichting parameter	$= U_\infty/\omega L$
ε_0	Finiteness	$= \chi_d R_0/\chi_a$
η_{ea}	Dimensionless number	$= \tau_{evap}/\tau_{ads}$
η_{ed}	Dimensionless number	$= \tau_{evap}/\tau_{diff}$
η_{ad}	Dimensionless number	$= \tau_{ads}/\tau_{diff}$
Th	Thiele number	$= (\tau_{evap}/\tau_{ads})^{1/2}$
Pe	Volume Peclet number	$= \tau_{diff}/\tau_{stream}$
Da	Damköhler number	$= \tau_{stream}/\tau_{ads}$
Pe_s	Surface Peclet number	$= \tau_{diff,s}/\tau_{stream}$

Constants

c	Light speed in vacuum	$\approx 2.998 \times 10^8\,\mathrm{m\,s^{-1}}$
e	Euler's number	≈ 2.718
i	Imaginary unit	$= \sqrt{-1}$
g	Gravitational acceleration at earth surface	$\approx 9.807\,\mathrm{m\,s^{-2}}$
ϵ_0	Vacuum permittivity	$\approx 8.85 \times 10^{-12}\,\mathrm{F\,m^{-1}}$
π	Pi	≈ 3.142

Part I.

Introduction

Laboratories on a chip are a major innovation for the medical, biotechnology, food processing and environmental analysis industries of the late 20th century. The first microsystems named "micro total analysis systems" (μTAS) were developed in the 90s for chemical analyses. The international annual conference "microTAS" was first held in 1994, witnessing to a great expansion in microsystem research. The development of μTAS for biotechnological and medical applications was driven in the same period and accompanied by the creation of the international scientific journal "Lab on a chip", which is still a landmark today for publication of related research.

Closely associated to the development of lab-on-a-chips, is the development of a hydrodynamics discipline called microfluidics. Microfluidics is the science of fluidic systems, in which at least one dimension exhibits a micrometric length scale. Due to the often high aspect ratio, new phenomena may be found to play a key role, combining microfluidics with electrodynamics, magnetics, acoustics or other disciplines.

The developments in microfluidics lead to the fact that lab-on-a-chips can be divided into two major groups, concerning the handling of the liquid inside the system. The early developed group of lab-on-a-chips (LOC) is based on flow of reagents and samples in microchannels. These channels of several tens or hundreds of micrometers are fabricated in a substrate, often made of PDMS, glass or silicon, covered by a lid (cf. Fig. 1.1). Entries exist for supply of reagents and liquid samples, moved in the channels by external pumping systems. In some cases, microchannels serve to transport liquid entities, created by a shear flow of two immiscible liquids in T- or X-junctions. This technology is used to create drops containing single cells, e.g. for sorting and analysis, eventually surrounded by polymer capsules or membranes.

In contrast to microchannel microfluidics, electrowetting on dielectrics, used in this work, is a mechanism particularly adapted to the individual manipulation of a set of drops in a digital lab-on-a-chip, a discipline also called "digital microfluidics". Here, an electrode array is patterned on a substrate and covered by a thin dielectric layer. By means of electric actuation of the electrodes, basic operations on drops like displacement, coalescence / break-up, mixing and drop on demand are implemented. In order to commercialize digital lab-on-a-chips, a certain number of additional functionalities need to be developed, going further than the up to now well mastered sample preparation and manipulation. Thereunder count polymerase chain reaction (PCR, nucleic acid amplification), purification, detection/hybridization tests, among others. This work is an original contribution to adsorption and mixing enhancement by electrowetting-induced steady streaming, which might be a major contribution to the good functioning and enhanced rapidity of these biological assays in microsystems.

Bioassays are based on the interaction (chemical affinity) between biochemical receptor and ligand molecules, eventually present in a biological sample (blood plasma or serum, saliva, urine, etc.). In order to qualitatively, or even

quantitatively, indicate the presence of a ligand, different transduction mechanisms may serve to transform the receptor/ligand interactions into a physically measurable signal. In comparison with classic biochemical analytical methods, laboratories on a chip imply a significant time, space and reagent consumption gain, providing the possibility of a cost-effective and quick, even mobile biochemical analysis. In contrast to microchannel technology, digital lab-on-a-chips offer a reduced liquid/solid surface, limiting cross-contamination to a minimum.

This work is divided into six parts. The introduction recapitulates the state-of-the-art of lab-on-a-chip devices and how microfluidics is used to manipulate reagents and solutions for use in lab-on-a-chips. The characteristics of and differences between channel and discrete microfluidics are pointed out. The field of molecular recognition is presented: transducer principles and label-bound/label-free detection techniques are introduced briefly. Finally, the local context of the actual work is presented, with a quick focus on prior work and the actual objectives.

In the second part, the theory of electrowetting is introduced. Basic principles like surface tension and contact angle are explained, the difference between high- and low-frequency electrowetting regimes is elucidated. By combining these two regimes, dual-frequency electrowetting is introduced as a relevant methodology in this thesis. Finally, the theory of streaming current at drop scale is presented.

Technical developments and instrumentation are presented in the third part. Electrowetting technology and the experimental setup are detailed, including interferometry developments. Insight is given into experiment automation and signal processing.

Evaporation of a sessile drop will be examined in part four. The diffusive model of drop evaporation is presented. The interferometry technique is jointly used with electrowetting-induced capillary resonance of a sessile drop as a measurement method of drop evaporation. The shift of capillary resonance with time serves as a transduction mechanism for evaporation-driven mass transfer. Subsequent diminution of the drop radius induces a resonance shift. Furthermore, measurements of evaporation in a multi-drop environment are performed, providing information on the influence on evaporation time of confinement, inter-drop distance, drop number and drop position within the device. Using dual-frequency electrowetting, introduced in part two, the contact angle is kept at a constant value throughout the experiments.

In order to gain insight into physicochemical mechanisms, the subsequent part five covers a brief introduction on surface active molecules. Furthermore, a model is developed for a spherical micro-sized system, affected by diffusion, adsorption and a time-dependent geometry (free liquid microdrop). Several non-dimensional numbers are extracted. Based on this model and a set of

analytical benchmarks, a simulation is developed, and the non-dimensional numbers are discussed. The model is extended to the case of a sessile drop with arbitrary contact angle in an adsorption-limited regime. Moreover, for a sessile drop of contact angle $\pi/2$, the effects of a streaming current inside the liquid phase are examined and the enhancement of molecule adsorption at the drop surface and the liquid/solid interface are discussed.

The results of part five are used in the last (experimental) part of this work, which is dedicated to surface ageing enhancement induced by steady streaming. The considered experimental system is a sessile water drop contaminated with albumin molecules. The albumin protein is presented, the dynamic surface tension is measured and conclusions on electrowetting-induced enhancement of biochemical surface ageing are drawn while taking into account the simulation results.

1. Microfluidics and lab-on-a-chips – Of channels and drops

The idea of development of microsystems, micromechanical actuators and sensors, commonly called microelectromechanical systems or MEMS, became popular in the 80s, as a natural extension of the developments related to microelectronic circuits and personal computers. The first integrated circuits and other MEMS related technology were developed in the 60s, making the way free for first miniaturized valves, pressure and airbag sensors (early 70s, Honeywell, RCA, Motorola). Up to date, nearly every electrically powered system includes MEMS technology.

The MEMS technology quickly found its way into other disciplines, namely chemistry, biochemistry and biology. In the late 20^{th} century, the first so-called micro total analysis systems (μTAS) for chemical sensing were given birth, a gas chromatograph in 1979 [1] and the first high-pressure liquid chromatography (HPLC) in 1990 [2]. Laboratories on chip and so μTAS found their way into chemical, biochemical and biotechnological applications, where they are commonly called lab-on-a-chips with reference to the laboratory work place and work steps they replace. Laboratories on a chip (lab-on-a-chips, LOC) can be defined as analysis systems, integrated within a microsystem for automated processing of biological or biochemical protocols. The first applications for biotechnological lab-on-a-chips were found in genomics for DNA assays, and for military uses like neurotoxin detection, for instance.

Today, two decades later, the European Commission claims, that micro-nano-biotechnologies will constitute an increasingly significant part of the global economy in decades to come, with major impacts in sectors including healthcare, agriculture, environmental surveying and industrial processes [3]. Biosensing in LOC will especially impact each of these sectors and healthcare particularly. From an economical point of view, the global market for biotechnologies used in medical applications is about $110.5 billion dollars in 2010 with an annual growth rate of 12.6 % expected over the next 5 years [4].

Closely associated to the development of lab-on-a-chips, is the development of an emerging discipline called microfluidics. Microfluidics is often considered as the science of fluidic systems, in which at least one dimension exhibits a micrometric length scale. Due to the often high surface to volume ratio, new phenomena arise, combining fluidics with electrodynamics, magnetics, acoustics or other disciplines. This work is based on a coupling called "electrohydrodynamics", using electrostatic phenomena for handling dipolar, ionic or otherwise electrically active liquids, in liquid bulk or on a liquid surface. As microfluidic phenomena involves small length scales, surface effects may find great applications; they are not necessarily important at macroscopic scale, but gain their relevance at high surface to volume ratios, S/V. A drawback of a high surface

to volume ratio is the process of unspecific adsorption to non-functional parts of the system, which is also called biofouling.

1.1. Microchannel microfluidics and lab-on-a-chips

Concerning the handling of the liquid inside the system, lab-on-a-chips can be divided into two major groups. The early developed group of lab-on-a-chips (LOC) is based on continuous flow of reagents and samples in microchannels [5]. The channels are fabricated by etching or molding. The two most common materials are glass or poly(dimethylsiloxane) (PDMS, $(C_2H_6OSi)_n$), which are both biocompatible. Liquid inlets exist for supply of reagents and liquid samples. The chip is then closed with a glass lid using a plasma treatment. The channels exhibit a size of several tens or hundreds of micrometers, cf. Fig. 1.1. The liquids are translated within the channels using an external pump system.

The second group is based on "discrete microfluidics", microchannels serve to transport liquid entities, created by a shearing between two immiscible liquids flowing in T- or X-junctions. This technology is used to create drops containing single cells, e.g. for sorting and analysis, eventually surrounded by polymer capsules or membranes.

Microchannel microfluidics exhibits special characteristics in contrast to macroscopic hydrodynamics. The Reynolds number,

$$\mathrm{Re} = \rho v L/\mu,$$

with ρ, the density of the liquid, v, the flow velocity, L, the principal length scale and μ, the viscosity, describes the flow regime of a flow in a channel. In microfluidics, it is small with respect to macroscopic systems, $\mathrm{Re} \approx 1$, while $\mathrm{Re} = 2300$ marks commonly the onset between a laminar and a turbulent flow regime, for low and high Re, respectively. This means that flow in microchannels is most often laminar and creeping, which is a hurdle for efficient mixing. In fact, the diffusive time scale is often shorter than the stirring time scale, signifying that two flows of different, but miscible liquids, may remain separated for quite a while, only mixed by a slow diffusion process. Diffusion acts on a time scale, $\tau_{\mathrm{diff}} = L^2/D$, where $D \approx 10^{-7}\,\mathrm{cm}^2/\mathrm{s}$ is a standard value of the diffusivity of particles. For a 100 µm wide channel, $\tau_{\mathrm{diff}} \approx 10^3\,s$, which is slow compared to the typical time scale of the liquid flow, $\tau_{\mathrm{flow}} \approx 1\,\mathrm{s}$. Research devoted to mixing enhancement is still going on [6, 7]. A promising technology is e.g. acoustofluidics [8].

Another issue is the fluidic resistance of microchannels (pressure drop), which is rather high compared to macroscopic systems. The flow rate $Q = \Delta p/\bar{R}$ is given by the channel resistance, $\bar{R}$, and the pressure drop, Δp. The pressure drop, to supply a significant flow rate, scales as vL/R^2, where L is the microchannel length and R the radius of the supposed cylindrical channel. Since R is usually pretty small, the necessary input pressure to deliver at the liquid inlet may rise quickly.

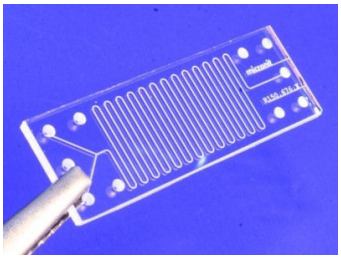

(a) Glass Microreactor. Source: Micronit, Enschede, Netherlands.

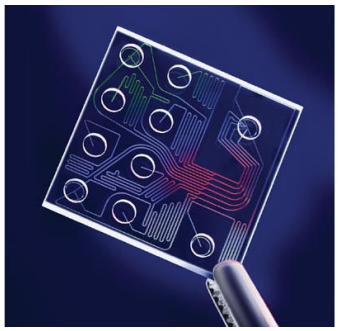

(b) The core of an industrial lab-on-a-chip cartridge. Source: Agilent Technologies, Santa Clara (CA), United States.

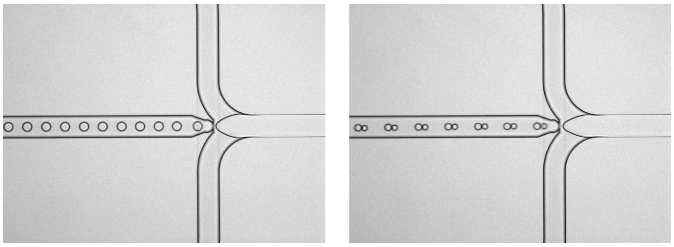

(c) Hexadecane drop generation at a microchannel junction in water at different pumping velocities. Source: Micronit, Enschede, Netherlands.

Fig. 1.1.: Different examples of microchannel lab-on-a-chip elements.

Microfluidic technology requires different devices in order to operate correctly: Microvalves are used with different actuation mechanisms, electromagnetic or air-driven pressure valves. Others even use the energy from the fluid in the channel, eliminating the need for an external power source. Stimuli-responsive hydrogel materials were demonstrated. Some authors were inspired by valves in the human body, impeding backflow in veins. Mixing technologies also play an important role. The mechanisms are often based on folding fluid streams within a microchannel (static mixers), increasing the efficiency of diffusion by downsizing the length scale. Vortex mixers (active mixers) can be based on acoustic, electric, magnetic or piezo-based technologies. Pumps are an essential part of a microchannel lab-on-a-chip, different actuation mechanisms exist: shape memory alloy pumps, piezoelectric actuation, pumps using magnetohydrodynamics, ferrofluidic movement (similar to a rotary vane pump), and others like osmotic or bubble pumps, which are not realizable on a macroscopic scale.

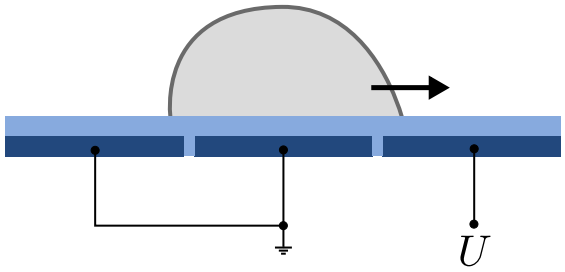

Fig. 1.2.: Drop movement using electrowetting-on-dielectrics: The electrode beneath the drop is activated with the voltage U, while the other electrodes stay grounded. The electrowetting tension creates a driving force and makes the contact line move over to the activated electrode, which is accompanied by a change of contact angle. Light blue: dielectric substrate, dark blue: electrode.

1.2. Digital microfluidics – digital lab-on-a-chips

In contrast to microchannel microfluidics, electrowetting on dielectrics, used in this work, is a mechanism particularly adapted for the individual manipulation of a set of drops in a digital lab-on-a-chip, a discipline also called "digital microfluidics". These microsystems are designed with a substrate consisting of a dielectric-covered electrode array. By applying an electric potential difference between drop and substrate, the contact angle may be tuned by increasing and diminishing the voltage. When applying the voltage, the drop experiences an electric stress, acting on its contact line with the substrate. This stress will act radially outwards, expanding the contact line and thus lowering the contact angle. As a consequence, the application of a voltage actuation allows a drop to switch from a non wetting to a wetting situation. By applying a non-uniform constraint at the contact line, a wetting gradient is created and the drop is brought into movement (cf. Fig. 1.2). By electrically-driven motion, this actuation method allows the implementation of drop displacements (up to 25 cm/s), coalescence / break-up of drops and hence aliquoting, mixing and drop dispense at precise volumes. Implementing these methods in a digital lab-on-a-chip means that these basic operations can be performed:

- quickly,
- in parallel, at high throughput,
- with less reagent than in classic biological assays,
- with less sample material,
- in a sterile environment and
- without human intervention (automated, no risk of contamination).

Using different reservoirs, several reagents and samples may be used during the analysis. The same sample may even be divided into several liquid entities for different biochemical assays. In order to commercialize digital lab-on-a-chips, a certain number of additional functionalities still need to be developed, going further than the up to now well mastered sample preparation and manipulation. Thereunder count polymerase chain reaction (PCR, nucleic acid amplification), purification and detection/hybridization tests, among others. An example of

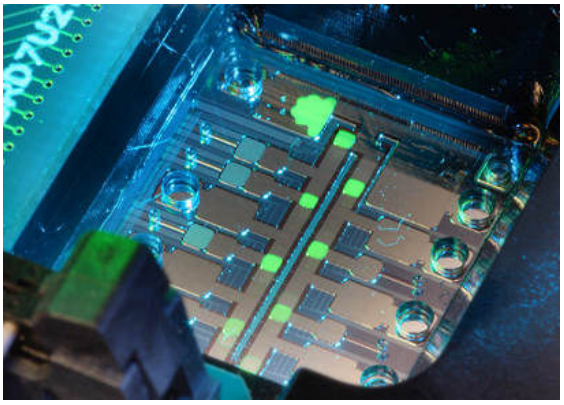

Fig. 1.3.: Picture drawn from the smartdrop project, an example for a drop-based lab-on-a-chip. Green fluorescent drops are dispensed from a reservoir and moved to different sites for manipulation. Source: CEA Grenoble.

the actual state of the art is shown in Fig. 1.3, which is taken from the smartrop project at CEA Grenoble.

1.3. Stirring enhancement

By electrically-driven motion, two different but miscible drops may be moved side by side and coalesced, e.g. sample and reagent drop. In order to enhance stirring or mixing process, different techniques are already implemented. Besides the volume-based approach for mixing, a different methodology consists in gaining benefit from the high suface to volume ratio, by developing a surface driver: Different physical mechanisms are used to generate a surface flow, which is further propagated into the volume under viscosity, inducing thus stirring whose efficiency rises with diminishing S/V. This is one example to demonstrate the major advantage of small-scale digital lab-on-a-chips.

Regarding drop-based lab-on-a-chips (LOC), several methods are proposed in scientific literature to realize stirring enhanced adsorption and hybridization. Not all are meant for digital LOC, but may easily be adapted. Gast et al. [9] use a chain of paramagnetic beads subject to a rotating magnetic field. The chains start a swirling motion and thereby mixes the liquid surrounding the chains. Fair et al. [10] propose a hydrodynamical approach: using electrowetting, a droplet is moved back and forth over three or four electrodes in a digital LOC, which stirs the volume with a recirculating flow due to friction and viscosity. Bau et al. [11] use magneto-hydrodynamics (MHD) to induce chaotic advection in a liquid volume. Finally, Ginot et al. [12] use a temperature gradient in a pendent drop, inducing a Marangoni flow at its surface. The flow propagates via viscosity into the so stirred volume. They also consider hybridization of analyte molecules on a support with ligands solubilized in the volume, whose kinetics is measured. It is found that the kinetics with Marangoni flow is sped up by a factor of 2.3 compared to the classical assay without Marangoni flow. Several research groups develop another promising technique, consisting in generating steady streaming along a liquid surface layer [13–15]. This flow is

induced by shape oscillations of a drop, generated by oscillating electrowetting. This streaming flow behaves as a surface driver with a momentum propagating again under viscosity from the drop surface to the volume [13].

1.4. Aliquoting

Once a sufficient stirring is achieved, drop break-up may serve for aliquoting the preparation. This mechanism is similar to drop displacement: Instead of activating the electrode beneath the drop for moving, the two adjacent electrodes are activated, while keeping the underneath electrode grounded. This will separate the droplet in two equal parts. Reiterating this operation using electrodes adapted to the drop size, the aliquots may be split further.

A similar technique is used for drop dispensing, or drop-on-demand (DOD): From a large sample droplet or reagent reservoir, a liquid neck is formed by activating a line of electrodes. When grounding one or more of the in-between electrodes, the neck will break up and a drop of a volume corresponding to the area of activated/grounded electrodes is left behind in the LOC [16]. Using capacitance measurements, for example, the liquid volume may be controlled precisely [17].

2. Molecular recognition: the needle in a haystack

The scientific domain at the interface of biochemistry and nanotechnology experienced strong developments during the last decades. The great advances in the knowledge of biomolecular processes in living systems were accompanied and even only made possible by nanotechnological and physical developments for characterization and analysis, like huge advances in fluorescence, molecular and atomic imaging and microscopy, as well as material analysis in mass spectrometers, HPLC and radiation facilities. The role of chemistry engineering for analysis and synthesis of new biomolecules also played a very important role. Hence, decisive proteins and molecular structures were identified and connected to biological processes, making possible the understanding of many pathologies. The origins of these pathologies can be linked to biomolecules, like proteins, viruses or to the modification or partial damage of genetic material in cells. In order to detect certain pathologies, practitioners and hospitals can now rely on a whole panoply of biochemical tests, or bioassays.

Bioassays are based on the interaction between a biochemical ligand and a receptor molecule. The ligand molecule is representative for the pathology. For example, a DNA sequence, which is significant for a certain pathology, may be extracted from a patient sample and amplified by a polymerase chain reaction. Or an antigen or antibody found in the blood of patients attained by a pathology may serve as a ligand molecule. Also, saliva samples or smears are used to identify certain diseases. The receptor molecule is often a synthesized molecule, serving to test a patient sample to an eventual pathology. The receptor molecule exhibits a chemical affinity to the ligand molecule, hence the two molecules bind to each other when getting in contact. This state is called hybridization.

Apart from detecting pathologies, the advances in biotechnology serve pharmacologists to identify new active components for pharmaceuticals. In pathologies, the components intervene in complex biological processes of different biochemical interactions in cells. The discovery of active components requires testing the effectiveness of a huge number of molecules concerning their effects on particular molecules interacting during a pathology. This search for active components is realized on substrates, called biochips or microarrays, testing a great number of different components for a fast and reliable screening process.

These two in vitro approaches, pathology analysis in medicine and active component search in pharmacology, use the same biochemical principles and the methodology may be recapitulated in five steps:

- Finding the specific receptor molecule for a certain ligand
- Receptor molecule binding on a solid support
- Chosing an effective transduction mechanism, label-free/label-bound (e.g. fluorescent, radionuclear, electric transduction, . . .)
- Miniaturization and multiplexing of several receptor molecules
- Detection of several ligand molecules

In order to qualitatively, or even quantitatively, indicate the presence of a ligand, different transduction mechanisms may serve as a means to transform the receptor/ligand interactions into a physically measurable signal.

2.1. Receptor/substrate binding.

In order to conceive a biochip or microarray, the chosen receptor molecule for a specific ligand needs to be fixed to the substrate. This is done using standard approaches in surface chemistry, often by a linker molecule, linking receptor and substrates (e.g. thiol linker on gold, silane linker on silicon dioxide). Some common techniques include:

- electrostatic interaction (electrically charged receptor, e.g. DNA/amine)
- covalent interaction (silan or thiol to amine functional group, which is possible for amino acids and proteins)
- hydrophobic interaction (hydrophobic receptor linked to octadecyltrichlorosilane (OTS) with its terminal group CH_3, e.g. antibodies)
- streptavidin/biotin (biotinylated receptors binding to a surface with grafted streptavidin)

2.2. Detection

Different detection mechanisms were developed in the past, and which mechanism to chose depends on the receptor and ligand molecules in use. The mechanisms are separated into two groups, a group using labels for detection, and a second group not using labels.

2.2.1. Label-bound detection

Fluorescence. This is the most common detection mechanism, which was industrialized several decades ago. A fluorescent labeling consists in attaching a fluorescent molecule (fluorophore, e.g. Alexa, GFP, fluorescein) to the ligand. Once the hybridization step is over, the substrate is rinsed and the fluorescent probe is excited by light of a molecule-specific wavelength. The fluorescent light emission (in the case of ligand-receptor interaction) is evaluated concerning its intensity. When it is not possible to graft a fluorescent probe on the ligand, it is possible to use different fluorescent techniques for the receptor molecule. In the case of DNA, several intercalating dyes exist, which only interact with hybridized DNA without grafting them (e.g. ethidium bromide, SYBR green). Some fluorophores (e.g. green fluorescent protein (GFP)) are polypeptides, which makes it possible to synthesize them in cells using plasmids, and even incorporate them readily in proteins and enzymes using gene modifications.

Radioactive labeling. This mechanism is rarely used for two reasons: due to the high contamination risks for end-users, and because radioactive elements can not be as easily integrated into protein or nucleotide structures as fluorescent molecules. The principle is equivalent to fluorescent labeling, instead that there is no need for excitation with a light source.

Nano-particles. Due to their size, metal or metalloid nanoparticles exhibit outstanding optical properties (diameter $\lesssim 100\,\text{nm}$ which is smaller than the wavelength of the employed light). Gold is a widely used material for synthesizing nanoparticles. By modifying the nanoparticles' properties, by adsorption or hybridization, the absorbance is modified [18], which is used to detect these processes. Also simple visual detection like fluorescence imaging is used.

2.2.2. Label-free detection

Surface plasmon resonance. A monochromatic and transverse magnetic polarized light beam is diffracted on a thin metal film at the angle of total reflection. The non-reflected part of the beam is propagated into the metal film by excitation of electron oscillations (surface plasmons). The angle of total reflection of the light beam depends on the refractive index of the material surrounding the metal film and is therefore dependent on the hybridization of ligands to receptor molecules, the latter of which are immobilized on the metal film. Upon interaction, the refractive index and therefore the reflected light intensity changes, which is measured using a photo diode.

Acoustic sensors. The resonance frequency of a **quartz micro-balance** (QCM) is linearly dependent on the square root of the mass adsorbed to its surface. Upon hybridization of ligand molecules on grafted receptor molecules, the resonance frequency shifts and indicates interaction. A similar technology is the **surface acoustic wave sensor**, based on the resonance frequency shift of surface acoustic waves on a substrate. The difference between the two approaches is that the QCM is based on bulk acoustic waves (BAW), and the latter on surface acoustic waves (SAW).

Cantilevers. A microcantilever, similar to an atomic force microscope cantilever, is surface modified with receptor molecules. Two transduction mechanisms exist: the mass rise upon hybridization deflects the cantilever from its initial position, which is detected by means of a deviated laser beam at the tip. Also, its resonance frequency changes, which gives insight into receptor/ligand interaction.

Interferometry techniques. These methodologies rely upon a similar principle to the surface plasmon technique. The tip of an optical fiber is functionalized with receptor molecules. Two reflections of light in the fiber emerge, the first reflection at the fiber/biomolecular layer interface, the second at the biomolecular

layer/buffer interface. Upon ligand/receptor interaction, the refractive index of a medium and thickness of the biomolecular layer changes, creating a difference of optical path traveled by the polarized light beam. The optical path difference between the two reflections is measured.

2.2.3. Label-free biosensing in a drop for digital lab-on-a-chips

Here follows a short summary of current techniques, deliberately developed for electrowetting-based lab-on-a-chips. This list is not exhaustive, and many methodologies, primarily not meant for electrowetting-based devices, may nevertheless be adapted. Here are three examples of recent literature, published during the preparation of this work, between 2009 and 2012:

Biochip functionalization using EWOD digital microfluidics for SPR imaging. Malic et al. present an electrowetting-based lab-on-a-chip for detection of DNA hybridization [19]. The device is equipped with four surface plasmon imaging (SPRi) detection sites (cf. Fig. 2.1(a)) for sub-microliter volume drops. The detection sites are included in holes in the Teflon coating on the top gold electrode for SPR measurements. By application of a DC voltage bias, the hybridization kinetics are enhanced as DNA is charged negatively when correctly adjusting the pH value. DNA receptor strands have a thiol surface chemistry for attaching them to the SPR gold electrode.

Molecular recognition by contact angle. Bergese et al. [20] developed a molecular recognition methodology, which is based on the change in contact angle on adsorption of biomolecules to the substrate surface (cf. Fig. 2.1(b)): The substrate is functionalized by single-stranded DNA receptor molecules. A change of up to 25 % of contact angle upon hybridization of complementary DNA is detected. A 50 % complementary DNA exhibits a less significant signal, non-complementary DNA does not affect the contact angle. It is possible to measure the hybridization kinetics, the time to completion for a 30 µL drop is about 600 s.

Integration of field effect transistor-based biosensors with a digital microfluidic device. Choi et al. present a technique [21] using the drain current dependence on hybridization of an avian influenza antibody to the functionalized surface of the drain electrode of a field effect transistor (FET). The sensing region of the drain (cf. Fig. 2.1(c)) is functionalized by an avian influenza antigen. The field effect transistor is embedded into the substrate between the driving electrodes. Above the FET, the dielectric passivation layer and the hydrophobic CYTOP coating are not applied, leaving access to the transistor. Upon drop deposition (volume 2.5 µL) above the sensing electrode pair, antibody molecules can diffuse to the sensing surface. The response time is less than one minute, which is extremely rapid.

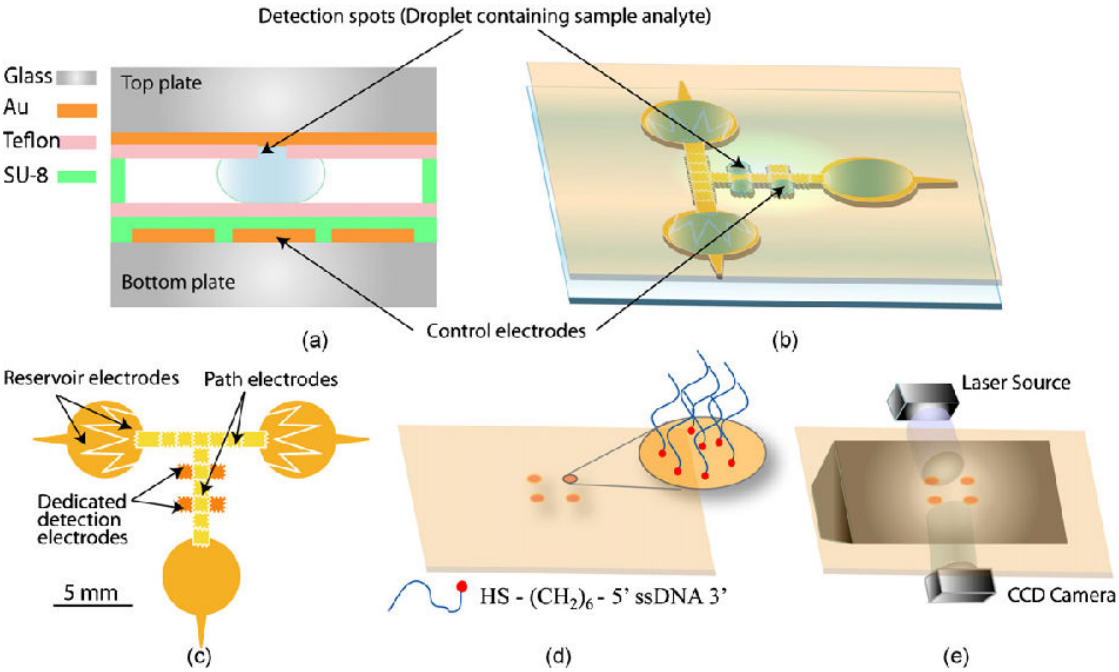

(a) Electrowetting architecture for a lab-on-a-chip using a surface plasmon resonance sensor (lab-on-a-chip "sandwich" design with top plate). Detection sites are included in holes in the Teflon coating for SPR measurements. The top reference electrode is also used for surface plasmon excitation. Source: Malic et al. [19].

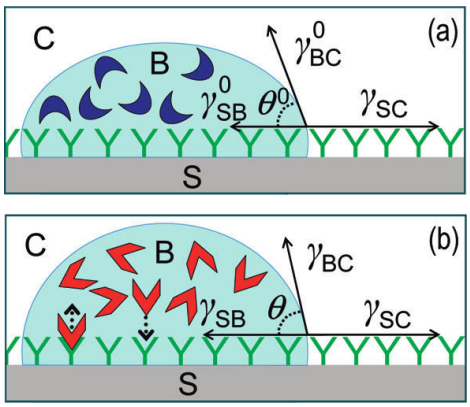

(b) Molecular recognition by contact angle: Complementary ligand molecules adsorb to the receptor-functionalized surface and change the solid-liquid surface tension. Source: Bergese et al. [20].

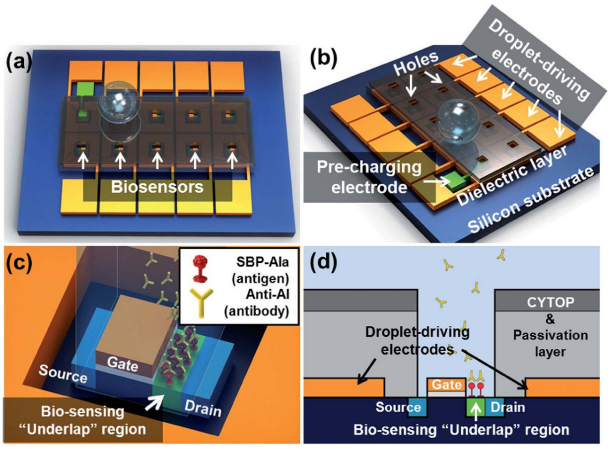

(c) Adsorption of avian influenza antibodies to the avian influenza antigen functionalized sensing area modifies the drain current of a field effect transistor. Source: Choi et al. [21].

Fig. 2.1.: Examples of different biosensing mechanisms for integration in electrowetting-based lab-on-a-chips.

3. Final remarks

3.1. Reconsidering surface functionalization

The methodologies presented in the foregoing chapter are diverse, and offer a broad panoply of support, surface chemistry and detection mechanisms, even if the list is probably not complete. With the different choices, it is possible to adapt the conception of a bioassay to almost every receptor/ligand system. Though using very different mechanisms, the detection technologies are all based on solid substrates requiring surface functionalization of the substrate surface by linker and receptor molecules. Nevertheless for digital microfluidics, it is possible to disengage from the solid support and transfer the biomolecular detection to the liquid/liquid or liquid/gas interface, making use of a lipid functionalization of the latter. This methodology bears the advantage of multiple chip usage by facile cleaning, which is not possible for most of the surface chemistry on solids, especially covalent binding. Furthermore, using a functionalization at a fluid interface, receptor molecules stay mobile, and flow focusing methods may be applied. These may consist in concentration of molecules at specific sites by hydrodynamic, electrostatic, acoustic or other methodologies. By these means, molecules may be directed to the drop apex for augmented detection sensitivity, or for substrate protection against biofouling, to cite just two application examples. The lipids used for establishment of the functional monolayer at the drop surface may be functionalized by linker molecules, such as biotin, amine groups or others, in order to fix receptor molecules. In the case of DNA, it may be sufficient to use lipids with an amine group, which exhibits affinity for single- and double-stranded DNA due to the positive charge of amine.

3.2. Context of the work

This work aims at contributing to the development of laboratories on a chip (LOC) for micro- and nano-biotechnologies, i.e. to the maturation of a droplet-based (or digital) LOC. This emergent technology is potentially much more versatile than the more mature, channel-based microfluidic technology. Innovation steps, though, are still necessary to facilitate an industrial release of the droplet-based technology. During the past decade, scientific developments were mainly devoted to drop motion, typically driven by electrowetting on dielectric (EWOD) or surface acoustic waves. At the time being, basic processes based on drop displacement, namely moving, merging or aliquoting, can be performed. However, the ultimate goal of a real industrial drop-based microsystem, will only be achieved if decisive operations, such as label-free detection, are implemented easily and at low cost. In this framework, this work focuses on an innovative label-free detection means of biomolecules, which takes benefits of

the specific features of EWOD actuated drop-based lab-on-chips:

- The large proportion of liquid/liquid or liquid/air interfaces compared to liquid/solid interfaces bears the advantage of less interaction in contrast to microchannels.
- The presence of EWOD electrodes that can be used for further operations than solely displacement of droplets and its derivatives (merging and aliquoting).
- The enhancement of molecule adsorption by electrowetting-induced streaming currents.

The proposed label-free detection methodology at microdrop scale is based on an opto-rheological detection of biomolecules captured to a liquid/gas interface. The feasibility of this detection means was already demonstrated for a macroscopic liquid/gas surface [22]. The present work is a main step of the implementation of this label-free detection means of bio-molecules to the liquid/gas surface of a microdrop [23].

All the biomolecular microsensors developed until now, without exception, are based on the immobilization of biomolecules on solid substrates. In this context, the capture of biomolecules to a liquid interface that is a long term objective of this work, by means of amphiphilic probe molecules, spread and self-assembled on the liquid surface, could reveal itself as a complete innovation. On the one hand the capture to a liquid interface is particularly well suited for an integration in droplet-based LOC. On the other hand, beyond the straightforward biomimetism of such a capture preserving both the conformation and the integrity of the bio-molecules, new prospects are offered through the possibility of:

- deforming the liquid interface,
- moving bio-molecules within the liquid surface.

Thanks to the deformability of the liquid surface, the binding of target molecules to the probe molecules in the liquid surface can be optically revealed by its impact upon the surface-rheology-dependent geometry of electrowetting-induced capillary waves. To improve even more the detection threshold, bio-molecules might be further concentrated focusing them to the apex of the liquid drop surface by an innovative mechanism based on streaming, induced by capillary waves [13]. Compared to solid substrate sensors, on which biomolecules are definitely bonded on the detection area of the substrate, the liquid surface approach allows the user to easily move the microdrop covered by the biomolecules to another point of the LOC after the detection stage for any desired operation.

3.3. From a meniscus...

In a recent PhD thesis, defended by Dr. Cyril Picard in 2007 [22], a feasibility study on a fluid biochip was conducted. The idea was to prove the micromechanical detection of DNA strand hybridization at a liquid interface. The chosen

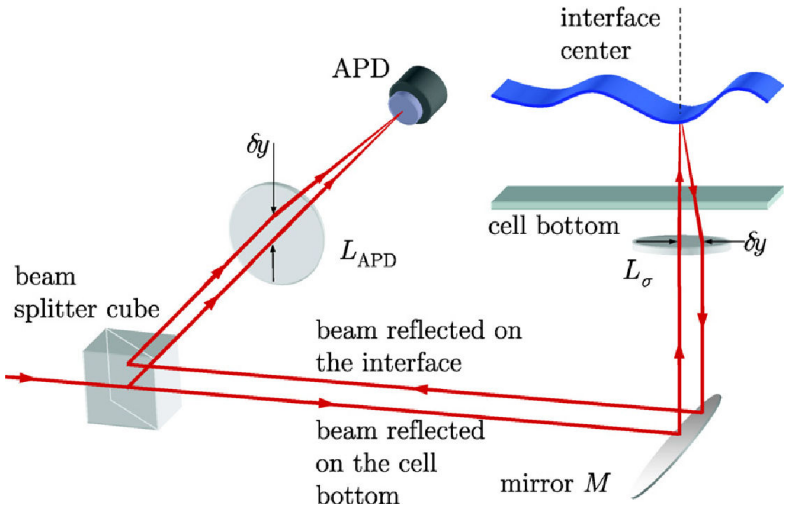

Fig. 3.1.: Optical scheme for the interferometry technique with the typical paths followed by the reflected laser beams. Source: Picard & Davoust, 2009 [24].

methodology consists in the usage of a stationary capillary wave network on a meniscus (diameter 5 cm), which is created by electromechanical agitation of a cylindrical cell. The wave amplitude is of the order of several micrometers, in a frequency range of 20 to 150 Hz. Two optical techniques are realized, refractometry for measurement of the meniscus geometry, and interferometry for evaluation of the wave amplitude at the meniscus center (cf. Fig. 3.1). Contamination of the meniscus surface by surface active molecules leads to drastic diminution of the wave amplitude, and to a shift of the resonance frequencies to lower values.

To implement a DNA assay, the liquid/air surface is functionalized by a monolayer of lipid molecules (DOGS, commercial name: Transfectam). These lipids have a positively charged polyamine headgroup and therefore exhibit an affinity to both single-stranded and double-stranded DNA. By injecting a solution of two types of DNA strands into the aqueous subphase, the frequency shift response is different according to whether the two types of strands are complementary or not.

3.4. . . . to a drop.

The objective of the present PhD research is to miniaturize the macroscopic approach explained earlier at the scale of a microliter-sized drop. Instead of the electromechanical actuation, a technique based on electrowetting on dielectrics, is developed in this thesis. This technique permits an easy control of actuation parameters like excitation frequency, oscillation amplitude and contact angle, and bears the further advantage of being little power consuming. The transduction mechanism is essentially the same, as a capillary wave network along the drop surface will be created. However, the underlying physics is different. This capillary network exhibits several resonance frequencies in the oscillation frequency range of 10 to 1000 Hz, depending essentially on drop volume and

surface tension. The oscillation amplitudes will be kept in the range of several micrometers, at most. Due to the new spherical geometry under consideration, the double approach of refractometry and interferometry for amplitude measurement can no longer be pursued, solely interferometry is developed at drop scale.

Concerning the application part, it is not pursued to integrate the whole process of DNA detection, which is a too ambitious goal for the available duration of a thesis. Instead, the drop characterization is prepared supplying all instrumentation and technical developments, and testing the developed system for the case of evaporation. In parallel, analytical and numerical calculations are conducted in order to accompany physicochemical measurements, which are effected for a simple system of an albumin molecule, without a specific detection mechanism. Special attention is paid to electrowetting-induced steady streaming, which enhances adsorption of molecules to the surface.

Part II.

Theory on Electrowetting-induced Droplet Oscillations

This part gives an introduction on the physical background of electrowetting on dielectrics. The notions of surface tension and contact angle are addressed. Then, electrowetting is discussed as a means of interacting with surface tensions on an electrostatic basis, and thereby modifying the contact angle of a fluid/fluid interface. This theory was first explained by Lippmann in 1875. In the 20th century, electrowetting was rediscovered for modifying the contact angle of a sessile drop. The classic electrowetting "plunging wire" geometry is discussed, and a recent approach for multi-electrode coplanar electrowetting is presented. In this first chapter, electrowetting is introduced using a DC (direct current) approach for the electrowetting actuation voltage. This approach is shown to be equivalent to the high-frequency electrowetting theory, provided that the high-frequency electrowetting voltage exhibits a root mean square value equivalent to the DC amplitude, and that the voltage frequency is sufficiently high with respect to the low-frequency electrowetting regime.

The low-frequency electrowetting regime is introduced in the second chapter of this part, and constitutes the basis for electrowetting-induced drop shape oscillations. The origin of the oscillations lies in the time-dependent actuation of the contact line, from which capillary waves of spherical symmetry are excited and generate a wave network along the drop surface. These oscillations are characterized by resonance frequencies, depending on drop volume, surface tension and contact angle of the drop, among other factors. In order to circumvent the dependency on contact angle, a technique referred to as "dual-frequency electrowetting" was developed during this thesis. The principle is simple and relies on the joint use of two actuation voltages: The amplitude of a high-frequency voltage is adjusted in order to regulate the contact angle to a certain value. Then, this potential is perturbed by a low-frequency voltage generating droplet shape oscillations along the drop surface. This low-frequency component may be adjusted in frequency to detect, for instance, a specific resonance peak or to stimulate a certain resonance mode. It may also be adjusted in order to control the oscillation amplitude.

The use of drop shape oscillations implies an unexpected fluid mechanical phenomenon at such microscale, known under the name of "streaming current" in the literature of ocean waves in the literature of ocean waves. This hydrodynamic flow is generated by a non-linear contribution of the Navier-Stokes equation of fluid mechanics, which states that an oscillating liquid/liquid or liquid/gas interface is a source of a net flow rate (in contrast to the intuitive purely linear theory of waves). This phenomenon is primarily known for ocean waves, but it is demonstrated to be still valid for drop shape oscillations, under specific conditions. The generated flow pattern is dependent on the frequency of drop oscillations and not restricted to electrowetting-induced shape oscillations.

4. Electrowetting on dielectrics & contact angle control

4.1. Surface tension & contact angle

Consider a water drop resting on a plane substrate in an ambient gas phase. Due to intermolecular interactions, which give rise to different surface tensions, as will be explained in the next paragraph, the drop adopts a certain physicochemical contact angle, referred to as Young angle, θ_0. The contact angle is defined as the angle between the plane of the solid substrate and the tangent of the liquid/gas interface, evaluated at the solid substrate on the side of the liquid phase (cf. Fig. 4.1(b)). Depending on the value of the contact angle, the configuration is called hydrophilic ($\theta_0 < \pi/2$) or hydrophobic ($\theta_0 > \pi/2$). The value of the contact angle depends on the interplay of the different surface tensions at the contact line, where the three phases, solid (S), liquid (L) and gas (G), are in contact. When referring to oily liquids, the technical terms are not referred to as hydrophilic and hydrophobic, but as lipophilic and lipophobic. More general terms are liophilic and liophobic for liquids in contact with a low energy or a high energy medium, respectively.

Surface tension, or more generally surface energy, originates from intermolecular interactions. A molecule in a liquid will attract surrounding molecules and therefore be attracted by them. These interactions are mainly dipole-dipole interactions (especially water), electrical multi-poles (all liquids) or ionic attraction/repulsion (mainly ionic liquids or salt solutions). A molecule at the liquid/gas interface (i.e. water/vapor) will have less partners for interaction, which results in a superposition of intermolecular forces that is non-zero (cf. Fig. 4.1(a)). In the case of liquid/liquid or liquid/solid interfaces, the surface tension will be due to the interactions between the molecules on either side of the interface. For example, a water/glass interface has weak interactions, and often gives rise to a liophilic configuration. The molecular interactions are not as repellent as on e.g. a Teflon surface, which contains fluorine molecules. A Teflon surface is a liophobic substrate for most liquids.

To exactly know the configuration of a three-component system, in the case of a sessile droplet resting on a solid substrate, the interplay of the three surface tensions needs to be considered. One surface tension for each interface: solid/liquid (SL), liquid/gas (LG) and solid/gas (SG). The balance between the three surface tensions leads to the value of contact angle, which is calculated from the horizontal component of the balance between surface tensions γ_{SL}, γ_{SG} and $\gamma_{LG} = \gamma$:

$$\gamma_{SG} = \gamma_{SL} + \gamma \cos\theta_0 \tag{4.1}$$

This so-called Young equation means that, at the triple contact line (TCL), the solid/gas surface tension is balanced by the solid/liquid surface tension and the liquid/gas surface tension projected with respect to the wetting plane (cf. Fig. 4.1(b)). By modifying the surface tension, e.g. γ_{SL}, the contact angle can thus be modified. With this idea in mind, the phenomenon of electrowetting can be discussed in the next section.

4.2. Lippmann-Young law of electrowetting

A first insight into electrowetting was given by Lippmann [25], who understood that the surface energy, γ_{SL}, between a solid metal electrode and an electrolyte depends on the voltage U_{SL} applied across the solid/liquid interface:

$$\frac{\mathrm{d}\gamma_{SL}}{\mathrm{d}U_{SL}} = -\sigma. \tag{4.2}$$

The interfacial charge, σ, that appears due to electrostatic effects (as in any capacitor), is the reason for a decrease in surface energy. According to this, Lippmann designed an electro-meter based on the capillary rise in a tube: the higher the rise, the greater the surface charge. Then, the idea of electrowetting has been nearly "forgotten" for about a century. Pierre-Gilles de Gennes (at the Collège de France, Paris) [26], Bruno Berge (at the Laboratoire de Spectrométrie Physique, Grenoble) [27] [28] and collaborators rediscovered it for new applications in biotechnology, optics and other fields in the 80s and 90s, using droplets instead of a water column.

When referring to droplets, the Young equation (4.1) may be substituted into the Lippmann equation (4.2), in combination with the expression for the surface charge in a capacitor, $\sigma = cU_{SL}$, where c [F/m^2] is the surface capacitance of the solid substrate. Equation (4.2) may thus be rewritten:

$$\frac{\mathrm{d}}{\mathrm{d}U_{SL}}[\gamma_{SG} - \gamma_{LG}\cos\theta(U_{SL})] = -cU_{SL}.$$

The hypothesis is made that γ_{SG} and γ_{LG} do not depend on the applied voltage. Then, the equation may be simplified to:

$$\mathrm{d}\cos\theta(U_{SL}) = \frac{c}{\gamma}\, U_{SL}\, \mathrm{d}U_{SL}.$$

By integrating with $\theta(U_{SL} = 0) = \theta_0$, the Lippmann-Young equation for a sessile droplet on a substrate is found:

$$\cos\theta - \cos\theta_0 = \frac{c}{2\gamma}\, U_{SL}^2. \tag{4.3}$$

Note that according to this equation, $\cos\theta$ is linear in function of U_{SL}^2, so whether applying $+U_{SL}$ or $-U_{SL}$ has the same effect on the contact angle. This can be easily understood by considering at the basic Lippmann equation (4.2): when

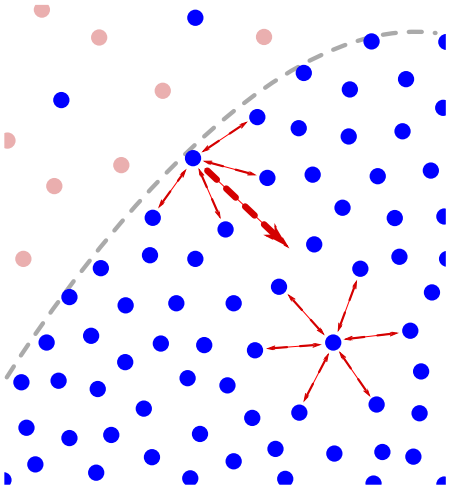

(a) Illustration explaining the origin of surface tension. Intermolecular attractions (little red arrows) tend to keep the molecules in the liquid subphase (right). At the liquid/gas interface, a resulting force acts on the molecules. Light red: gas molecules, blue: liquid molecules, gray dashed line: liquid-gas interface.

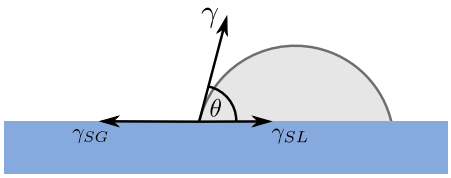

(b) Illustration explaining the relation between the different surface tensions and the contact angle θ: The solid/gas surface tension is balanced by the solid/liquid surface tension and the liquid/gas surface tension projected with respect to the wetting plane.

Fig. 4.1.: Surface tension and contact angle.

changing the sign of U_{SL}, it may be reasoned that the surface charge σ at either side of the interface also changes its sign. Therefore, the change of surface tension $d\gamma_{SL}$ will be the same, whichever the sign of U_{SL}.

The electrowetting tension, $T_{EW} = cU_{SL}^2/2$, in the Lippmann-Young equation (4.3) is of dimension N/m, like a surface tension. It may be related to the energy in the system, which is composed of the surface energies, γ_{IJ}, $I, J \in \{S, L, G\}$, and the respective dependent surface areas S_{IJ}. The total surface energy, W_s, in the system can be written as follows:

$$W_s = -T_{EW}S_{SL} + \gamma_{IJ}S_{IJ} = (\gamma_{SL} - T_{EW})S_{SL} + \gamma_{LG}S_{LG} + \gamma_{SG}S_{SG}. \tag{4.4}$$

For an illustration of electrowetting actuation, please refer to Fig. 4.2 (a) and (b): In (a), a droplet is sketched with the corresponding surface tensions on a hydrophobic substrate. The influence of the electrowetting tension, $T_{EW} = cU_{SL}^2/2$ (Fig. 4.2(b)), is responsible for an effective surface energy, γ_{SL}, lower than without actuation (red arrow).

It is important to note that, whether applying a DC voltage of amplitude U or an AC voltage of root mean square value $U_{rms} = U$, does not have an influence on the electrowetting equations. The only condition being that the frequency of the AC voltage is higher than the critical frequency separating low- and high-frequency electrowetting regimes, $f_c \approx 1\,\text{kHz}$. AC voltages with $f < f_c$ will generate additional phenomena, which will be discussed in the next chapter devoted to oscillating EWOD, which is a major mechanism discussed

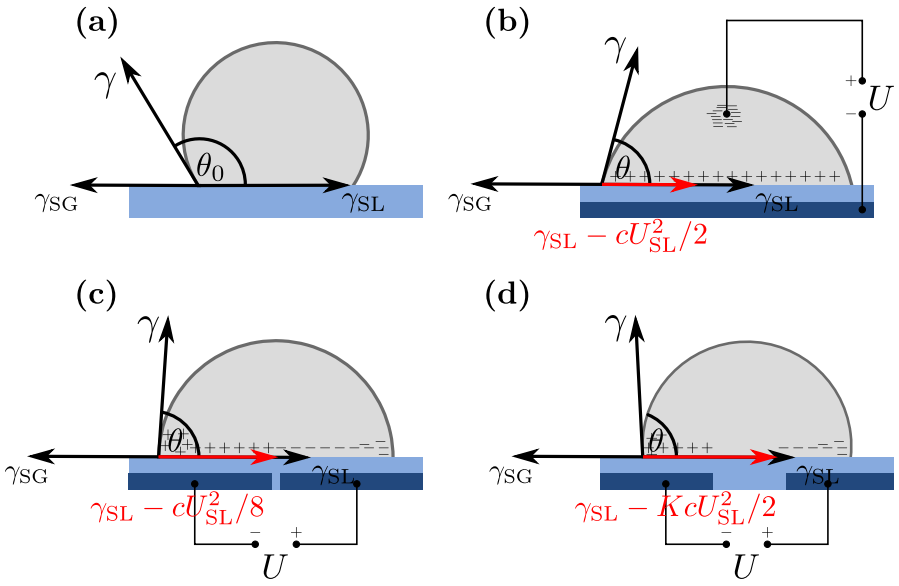

Fig. 4.2.: The voltage-induced surface charge modifies the surface tension and thus the contact angle. Blue: electrode, light blue: dielectric, +/-: positive/negative charge. (a) Configuration without electrowetting, unmodified contact angle θ_0 on a hydrophobic substrate, (b) wire-in-drop configuration, θ is modified, (c) coplanar configuration, the electrowetting tension T_{EW} changes with respect to (b) by a factor $K = 1/4$, (d) a correction factor $K < 1/4$ for a large gap is taken into account.

throughout this thesis. From a practical point of view, applying a DC voltage to the electrodes is not recommended, since the thickness of the substrates rarely exceeds 1 µm. An electric break-down would be otherwise most probable. For this reason, applying an AC voltage of several kHz with an equal root mean square value is highly recommended when modifying the macroscopic wetting angle.

4.3. Correction factor for multi-electrode coplanar electrowetting

Electrode design for EWOD differs strongly from author to author, since it depends on the application: The historical and widespread electrowetting configuration consists of a conducting substrate, which is usually covered by a hydrophobic and dielectric coating. The counter electrode is a (platinum) wire, which is plunged into the droplet [16, 29] (cf. Fig. 4.3(a)). In this configuration, the electrowetting voltage, U_{SL}, is strictly equal to the applied tension between the electrodes, U. It is commonly used for contact angle measurements and drop shape oscillations. In a related configuration, the reference electrode is a catenary [30], with a multi-electrode substrate. This configuration is mainly used in digital LOCs for drop displacement (cf. Fig. 4.3(b)). This is also the case for the sandwich design [16]: Drops of interest are inserted between two plates, a top plate, which serves as reference electrode and a multi-electrode bottom plate, which is used for drop displacement (cf. Fig. 4.3(c)). This design is primarily used in biotechnological applications for lab-on-chips, often in com-

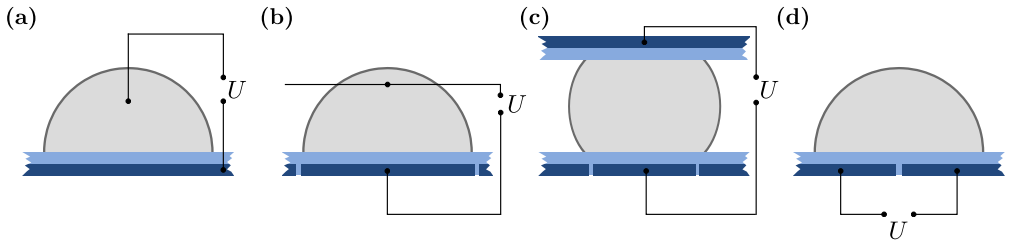

Fig. 4.3.: Sketch of different electrowetting configurations: (a) classical drop-in-wire configuration (plunged wire), (b) drop-in-wire configuration (catenary), (c) sandwich configuration and (d) coplanar configuration. Configurations (b) and (c) are essentially used for moving drops on a substrate (e.g. lab-on-chips), (a) and (d) are convenient configurations for contact angle measurements and shape oscillations. Blue: electrode, light blue: dielectric.

bination with e.g. silicone oil as a filler medium. The most recent and elegant configuration, a droplet on two coplanar electrodes [31,32], is used in this work (cf. Fig. 4.3(d)). The reference electrode is integrated into the underlying substrate, either by separating the substrate electrode in two electrodes, separated by a gap, or it is integrated into the substrate electrode, similar to the plunging wire. The substrates used as insulators are often PTFE, Teflon AF or Parylene C, which exhibit excellent surface properties for electrowetting.

When working with a wire-in-drop or a sandwich electrode design, the potential difference U_{SL} for calculation of the contact angle, equation (4.3), is equal to the applied potential difference U between the two electrodes. In contrast to this, with a coplanar electrode design, the potential difference U_{SL} needs to be adapted, as the drop will adopt a different potential with respect to the electrodes. In addition to this, the different electrodes need to be separated by a gap for electric insulation, which also needs to be taken into account, as the surface for electrowetting actuation will diminish. This implies that the energy is not transmitted equally, according to equation (4.4).

In order to calculate the impact of the multi-electrode configuration on electrowetting, the surface area S_{SL} needs to be divided into the different electrode areas, corresponding to the applied electric voltages: The electrode areas are named S_d for the surface of all driving electrodes, and S_r for the surface of all reference electrodes. The gap area is designated by S_g. The total surface is referred to as $S_t = S_d + S_r + S_g$. The electric potentials are named U_d, U_r and U_g, respectively. As a hypothesis, it is imposed that $U_g = 0$. This is a hypothesis which was questioned at the beginning of this thesis, due to experimental observations [33]. It was finally found that the hypothesis is justifiable, and that the difference between theory and experiment was due to an oil film applied to the electrodes. For further details, please refer to appendix A. To understand the reasoning of Kim et al., the energy balance and the electric equivalent circuit of the electrode system need to be considered:

The drop is considered as a perfect conductor at a frequency ν of several kHz. The electronic equivalent circuit (cf. Fig. 4.4) can thus be represented by a capacity $C_d = cS_d$, representing the equivalent capacity of all driving electrodes,

in series with a capacity $C_r = cS_r$, representing the equivalent capacity of all reference electrodes. The circuit is alimented by the electrowetting voltage U.

The energy balance (4.4) needs to be rewritten, with and without applied tension, including the contributions of the different electrodes, U_d, U_r and U_g, for driving and reference electrodes, and the gap area, respectively. These two equations translating the two energy states of the system need to be subtracted, which gives rise to a modified Lippmann equation:

$$\gamma_{SL}(U) - \gamma_{SL}(0) = -\frac{c}{2}\left(\frac{S_d}{S_t}U_d^2 + \frac{S_r}{S_t}U_r^2 + \frac{S_g}{S_t}U_g^2\right). \tag{4.5}$$

The different voltages need to be calculated as a function of the applied voltage U, which is possible using the electric equivalent circuit of the configuration: The two capacities, C_d and C_r, are serially connected in an electronic circuit with impedance $Z_{tot} = (S_d + S_r)/i2\pi fcS_dS_r$, where i is the imaginary unit $i = \sqrt{-1}$. The total voltage U can be related to the current in the circuit, $i_U = U/Z_{tot}$, and thus the voltages $U_d = Z_d i_U$ and $U_r = Z_r i_U$ can be calculated:

$$U_{d/r} = \frac{S_{r/d}}{S_d + S_r}U.$$

This expression can be substituted in equation (4.5), combined with the foregoing Lippmann-Young equation (4.3) and the hypothesis $U_g = 0$, the expression for the contact angle is found to be:

$$\cos\theta(U) - \cos\theta_0 = \frac{c}{2\gamma_{LG}}\left(\frac{S_d}{S_t}\left(\frac{S_r}{S_d + S_r}\right)^2 + \frac{S_r}{S_t}\left(\frac{S_d}{S_d + S_r}\right)^2\right)U^2. \tag{4.6}$$

This equation describes coplanar multi-electrode electrowetting with the hypothesis that the gap potential is constant throughout the gap. As shown in appendix A, the fair assumption can be made, that the gap area, $S_g = 0$, is equal to zero, and that the driving and reference electrode areas, $S_d = S_r$, are of the same size. In this case, equation (4.6) reduces to:

$$\cos\theta(U) - \cos\theta_0 = \frac{cK}{2\gamma_{LG}}U^2, \text{ with } K = 1/4, \tag{4.7}$$

introducing the correction factor K with respect to the classic Lippmann-Young equation (4.3). This equation is usually employed for coplanar electrowetting. However, for a finite gap area $S_g \neq 0$, the correction factor is $K = S_d/2S_t$ needs to be calculated, assuming that the drop is equally positioned on both electrodes (electrostatic equilibrium), hence $S_d = S_r$. Assuming that the contact line is perfectly circular, the areas S_d and S_g can be written as:

$$S_d = \frac{1}{2}\left(\pi R_B^2 - S_g\right),$$

$$S_g = R_B g\sqrt{1 - (g/2R_b)^2} + 2R_b^2 \arcsin\left(g/2R_B\right) = 2R_B g + O(g/2R_B), \tag{4.8}$$

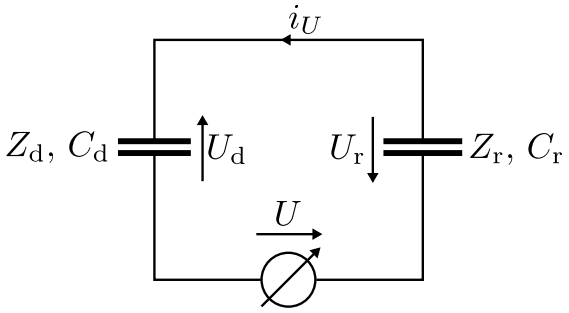

Fig. 4.4.: The equivalent circuit of an electrowetting setup: The substrate (capacity density c) constitutes with the drop and the driving and reference electrodes the capacities C_d and C_r, respectively. The applied potential between driving and reference electrodes, U, leads to a capacitive current, i_U and thus to the capacitive impedances Z_d and Z_r. The gap potential in this circuit is approximated equivalent to zero, $U_\mathrm{g} = 0$.

where R_B is the base diameter of the drop. If the gap is considered to be much smaller than the base diameter, $g \ll R_\mathrm{B}$, which is a rather fair assumption, the previous expression (4.8) can be simplified as:

$$S_\mathrm{g} = 2R_\mathrm{B}g, \tag{4.9}$$

where the gap area is assumed rectangular, such that $K = 1/4 - g/2\pi R_\mathrm{B}$.

The different configurations described above are illustrated in Fig. 4.2. Panel (b) shows the classic plunging wire configuration, for which no correction is necessary. Panel (c) represents the case for small gaps with respect to the wetted area, $K = 1/4$, the contact angle will not be as low as for the previous configuration, electrowetting is not as efficient for the same applied voltage U. The last panel (d) illustrates the case of a large gap area with respect to the wetted surface. The electrowetting performance is even less efficient, the contact angle will flatten less significantly.

5. Low-frequency electrowetting: drop shape oscillations

In this chapter, a model for drop shape oscillations induced by oscillating electrowetting is presented. Emphasis is put on the spectrum of these oscillations, which are excited by application of an alternate frequency voltage bias in a coplanar electrowetting setup. The driving force is concentrated on the contact line [34], from which the oscillations will be excited. The methodology of dual-frequency electrowetting is explained. Furthermore, transient oscillations of sessile drops are presented as a transduction mechanism to measure natural frequency and decay time of drop oscillations. Finally, streaming current induced by drop shape oscillations is introduced.

5.1. Forced oscillations of free drops: spectrum & shape

Having understood the phenomenon of electrowetting in the high-frequency regime, the way to bring a sessile droplet to oscillate is now no longer complicated. For excitation frequencies, $\omega = 2\pi f$, lower than $\approx 1\,\mathrm{kHz}$ (transition frequency between the electrowetting low and high frequency regimes), the wetting dynamics come into play. This means that the position of the triple contact line and thus also the value of the contact angle are time-dependent. A sophisticated analysis, theoretical as experimental, is given by Kang et al. [29]. A theoretical model for the shape oscillations of a sessile drop in AC electrowetting, is compared to experimental data.

5.1.1. Calculation of the eigen-frequencies for a free oscillating drop

The first scientific works on oscillating free drops in vacuum were carried out by Lord Rayleigh [35] and Lord Kelvin et al. [36] in the 19$^{\text{th}}$ century. In 1932, Lamb calculated the resonance frequencies of a free liquid sphere in an ambient medium [37] under the assumption of a small oscillation amplitude.

In this chapter, the drop is modeled as the upper half of a free liquid sphere of radius R and density ρ. Without loss of generality, the shape of the oscillating sphere may be described by a linear combination of Legendre polynomials $P_n(\cos\varphi)$, where n is the degree of the Legendre polynomial and $\varphi \in [0, \pi]$ is the azimuthal angle with respect to the vertical axis of the sphere, which is the axis of rotational symmetry (cf. Fig. 5.1(a)). The distance from the sphere center, d, can be described by:

$$d(\varphi, t) = R + v \sum_{n=2}^{\infty} a_n(t) P_n(\cos\varphi), \tag{5.1}$$

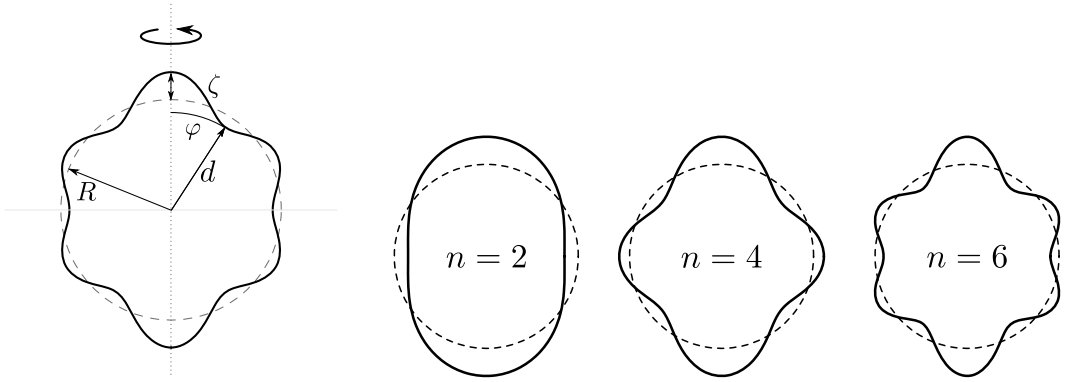

(a) Definition of the coordinates d and φ with respect to the symmetry axis. The central amplitude ζ is defined as the difference between d and the spherical radius R.

(b) Different shape modes for $d = 1 + 0.3P_n(\cos\varphi)$. The dashed line shows the state of rest.

Fig. 5.1.: Drop oscillations: shape and the three first principal modes, $n = 2$, 4 and 6.

where v is an arbitrary small parameter, scaling the drop deformation to a certain magnitude, and $a_n(t)$ are a set of coefficients associated to the Legendre polynomials. The central amplitude of the drop apex oscillation is referred to as $\zeta(t) := d(0,t) - R = v\sum_{n=2}^{\infty} a_n(t)P_n(0)$. For examples of Legendre polynomials, P_n, please refer to appendix B.

Following the assumptions of Lamb [37], and supposing the flow irrotational, the velocity $\boldsymbol{u}$ may be expressed by a velocity potential, Φ:

$$\boldsymbol{u} = -\nabla\Phi.$$

Hence, the assumption of incompressible flow is made:

$$\nabla\cdot\boldsymbol{u} = 0,$$

and the potential is found to be a harmonic function:

$$\Delta\Phi = 0. \tag{5.2}$$

In the case of a spherical geometry, the solution to the Laplace equation for the velocity potential may be decomposed in a linear combination of Legendre polynomials. In the case of resonance, the shape coefficients $a_n(t) = a_n^0 \sin(\omega_n t + \psi_n)$ may be decomposed in a constant amplitude, a_n^0, and a sinusoidal contribution of oscillation frequency ω_n with an arbitrary phase, ψ_n. The drop shape (5.1) may then be expressed as:

$$d = R + v\sum_{n=2}^{\infty} a_n^0 \sin(\omega_n t + \psi_n)P_n(\cos\varphi). \tag{5.3}$$

The normal velocity at the interface on the inner (i) and the outer (e) side of the

sphere is written:

$$\frac{\partial d}{\partial t} = -\frac{\partial \Phi^{\mathrm{i}}}{\partial r}\Big|_{d=R} = -\frac{\partial \Phi^{\mathrm{e}}}{\partial r}\Big|_{d=R}, \tag{5.4}$$

and the velocity potentials using equations (5.2), (5.3) and (5.4):

$$\Phi^{\mathrm{i}} = -\sum_{n=0}^{\infty} \frac{v a_n^0 \omega_n R}{n} \frac{d^k}{R^k} P_n(\cos\varphi) \cos(\omega_n t + \psi_n),$$

$$\Phi^{\mathrm{e}} = \sum_{n=0}^{\infty} \frac{v a_n^0 \omega_n R}{n+1} \frac{R^{k+1}}{d^{k+1}} P_n(\cos\varphi) \cos(\omega_n t + \psi_n),$$

Via the linearized Bernoulli relation and supposing small deformations, velocity potential and pressure are related according to [38]:

$$\frac{\partial \Phi}{\partial t}\Big|_{d=R} = \frac{p}{\rho}.$$

Hence, the pressure jump across the interface is given, using the two latter relations:

$$p^{\mathrm{e}} - p^{\mathrm{i}} = -v a_n^0 \, \omega_n^2 \, R \, P_n(\cos\varphi) \sin(\omega_n t + \psi_n) \left(\frac{\rho^{\mathrm{e}}}{n+1} + \frac{\rho^{\mathrm{i}}}{n} \right).$$

The Young-Laplace law relates the pressure jump to the surface curvature of the interface:

$$p^{\mathrm{e}} - p^{\mathrm{i}} = \gamma \, (\nabla \cdot \boldsymbol{n}).$$

Here, $\boldsymbol{n}$ is the normal vector all along the deformed interface, oriented to the outside of the drop. This expression may be calculated using equation (5.3):

$$\nabla \cdot \boldsymbol{n} = \frac{2}{R} + \sum_{n=2}^{\infty} (n+2)(n-1) \, \frac{v a_n^0}{R^2} \, \sin(\omega_n t + \psi_n) \, P_n(\cos\varphi). \tag{5.5}$$

The last three equations may be used to express the resonance frequencies ω_n of a spherical isolated drop in an ambient phase of density ρ^{e}:

$$\omega_n^2 = \frac{n(n-1)(n+1)(n+2)}{\rho^{\mathrm{e}} n + \rho^{\mathrm{i}}(n+1)} \frac{\gamma}{R^3}.$$

In the case of a low density ambient phase, with $\rho^{\mathrm{e}} \ll \rho^{\mathrm{i}}$, e.g. a drop in air, the last expression simplifies to:

$$\omega_n^2 = n(n-1)(n+2) \, \frac{\gamma}{\rho \, R^3}. \tag{5.6}$$

These are the resonance frequencies of an isolated drop in air. The mode number n corresponds to the nth resonance mode, which is proportional to the surface tension γ, as well as to the inverse of the drop volume. This resonance spectrum

may be used as a transduction mechanism for measuring surface functionalization and evaporation, respectively.

5.1.2. Calculation of the shape modes of drop oscillations

In section 5.1.1, it is explained how to calculate the resonance frequencies of an isolated drop in an ambient phase. In order to find the shape mode equations, $a_n(t)$, and to calculate the drop shape, a convenient differential equation needs to be found. This may be done by considering the normal stress balance on (normal component of the jump momentum balance) at the interface, expressed by the stress tensor, $\boldsymbol{T}$:

$$\left[\!\left[\boldsymbol{n}\cdot(\boldsymbol{n}\cdot\boldsymbol{T})\right]\!\right]=\left[\!\left[\boldsymbol{n}\cdot(\boldsymbol{n}\cdot\boldsymbol{T}_\mathrm{h})\right]\!\right]+\left[\!\left[\boldsymbol{n}\cdot(\boldsymbol{n}\cdot\boldsymbol{T}_\mathrm{e})\right]\!\right]=\gamma\,(\nabla\cdot\boldsymbol{n}). \tag{5.7}$$

Here, $[\![\ f\ ]\!]$ is a jump term, signifying the difference $[\![\ f\ ]\!] := (f_\mathrm{i}-f_\mathrm{e})$, of a variable f, evaluated at either side (i/e) of an interface. The tensors $\boldsymbol{T}_\mathrm{h}$ and $\boldsymbol{T}_\mathrm{e}$ are the hydrodynamic and Maxwell stress tensors, respectively. The capillary pressure given by the Young-Laplace equation, $\Delta p = \gamma\,(\nabla\cdot\boldsymbol{n})$, expresses the pressure difference between two phases, separated by an interface of curvature $\kappa = \nabla\cdot\boldsymbol{n}$, under surface tension γ.

Concerning the Maxwell stress, it may be expressed by considering the Gauss law and Coulomb force. The electrical force on the triple contact line, F_TCL, exhibits only a radial component and is considered equal to the electric force F_el, neglecting the capillary force and the contact line friction due to rugosities. The force is concentrated on a narrow region of the triple contact line [34]. For this reason, the normal electric stress is modeled as a δ-function on the TCL, at $\varphi = \pi/2$:

$$\left[\!\left[\boldsymbol{n}\cdot(\boldsymbol{n}\cdot\boldsymbol{T}_\mathrm{e})\right]\!\right]=T_\mathrm{e}\delta(\cos\varphi)=\frac{cU^2}{2}\frac{2}{R}\delta(\cos\varphi).$$

In order to integrate the δ-function correctly into the differential equations, its representation in the basis of Legendre polynomials needs to be found. It can be expressed as $\delta(\cos\varphi)=\sum_{n=0}^{\infty} d_n P_n(\cos\varphi)$, and the coefficients are represented by [39]:

$$d_n=\frac{2n+1}{n}\int_{-1}^{1}\delta(\cos\varphi)P_n(\cos\varphi)\,\mathrm{d}\cos\varphi=\frac{2n+1}{2}\,P_n(0).$$

The normal stress can thus be reformulated as the following series:

$$\left[\!\left[\boldsymbol{n}\cdot(\boldsymbol{n}\cdot\boldsymbol{T}_\mathrm{e})\right]\!\right]=\frac{cU^2}{2}\frac{2}{R}\sum_{n=0}^{\infty}\frac{2n+1}{2}P_n(0)P_n(\cos\varphi).$$

The capillary pressure may be expressed using equation (5.5),

$$\nabla\cdot\boldsymbol{n}=\sum_{n=2}^{\infty}(n+2)(n-1)\,\frac{va_n(t)}{R^2}\,P_n(\cos\varphi).$$

The hydrodynamic stress tensor is given by Plesset and Prosperetti [40,41], and

for a low-density and low-viscosity ambient phase, it writes:

$$\left[\!\left[\boldsymbol{n}\cdot(\boldsymbol{n}\cdot\boldsymbol{T}_{\mathrm{h}})\right]\!\right]=\sum_{n=2}^{\infty}\left(\frac{\rho R}{n}\ddot{a}_n+2\mu\frac{(n-1)(2n+1)}{nR}\dot{a}_n\right)P_n(\cos\varphi),$$

where μ is the viscosity of the drop liquid. Making use of the three last equations and equation (5.7), the balance of normal stress on the interface may be written for a mode number n:

$$\ddot{a}_n+2(n-1)(2n+1)\,\frac{\mu}{\rho R^2}\,\dot{a}_n+n(n-1)(n+2)\,\frac{\gamma}{\rho R^3}\,a_n=n(2n+1)\frac{cP_n(0)}{2v\rho R^2}\,U^2. \quad (5.8)$$

This equation is an ordinary differential equation for the shape mode coefficients $a_n(t)$, describing the linear evolution of the drop shape during oscillations. The structure of the equation is the structure for a forced damped oscillator: The left hand side is composed of the inertial term, the dissipation term and the restoring force term, respectively. The dissipation term originates from momentum diffusion due to bulk viscosity, neglecting contact line friction and capillary forces related to the solid substrate. The restoring force term is due to surface tension, which inhibits surface stretching (neglecting e.g. gravity). The right hand side of (5.8) is the forcing term with a square dependence on the actuation voltage, U. The factor $P_n(0)$ is in agreement with the up to now supposed fact that odd oscillation modes do not occur, since $P_n(0) = 0$ for n odd.

When solving equation (5.8) for a Heaviside forcing term, it is found that a transient time for installing harmonic stationary drop oscillations is expected [29]. This transient time depends on the mode number n and can last up to about 100 periods. In reality, the transient time will be reduced a lot, as the contact line friction needs to be included, please refer to the later section 5.3. After this transient time ("stabilizing time"), steady harmonic motions prevail. The amplitude of oscillation depends on the input frequency, f, and on the dominant shape mode, $\hat{n}$. One speaks of dominant shape mode, since for a resonance, all other even modes, $n = 2k$, $k \in \mathbb{N}_{\setminus\{\hat{n}/2\}}$, are expected to contribute to shape oscillations (cf. Fig. 5.1(b)), but only with a minor contribution.

5.1.3. Corrected resonance frequencies for sessile drops

Using a similar approach with potential flow theory, Strani and Sabetta [42] refine the preceding model for isolated drops to the case of sessile drops on a substrate. Using spherical harmonics, they establish an integral equation defining the surface deformation of the drop. This integral equation is solved using the method of Green's function. As a function of the contact angle, θ, correction factors $\lambda_n(\theta)$ are found, scaling the resonance frequencies for the different oscillation modes n:

$$\omega_n^2=n(n-1)(n+2)\,\lambda_n(\theta)\,\frac{\gamma}{\rho R^3}. \quad (5.9)$$

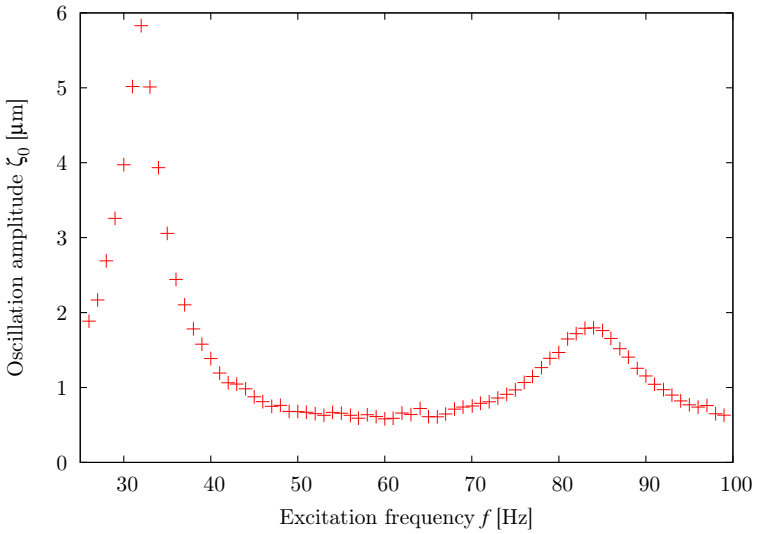

Fig. 5.2.: Spectrum of a 10 µL water drop between 25 to 100 Hz, measured by drop interferometry. Two resonance peaks $f_2 = 32$ Hz and $f_4 = 84$ Hz are visible.

The calculation of $\lambda_n(\theta)$ is outlined in appendix C. The solution suggests that an additional mode, $n = 1$, is introduced due to the presence of the substrate, in addition to the even oscillation modes. This mode is associated with a net oscillatory displacement of the drop, and therefore referred to as "rocking mode". The presented model is based on a sessile drop with a pinned contact line, which is not necessarily true for the drop oscillations induced by electrowetting in this work. This may generate a discrepancy between theory and experiment, as will be seen in part IV. The experimental work done by Stransi ans Sabetta [42] also suggests a disagreement between theory and experiment; it is found that theory slightly overestimates the coefficients λ_n.

To check the correctness of the theoretical resonance spectrum (5.9), water drops of different volume are tested with respect to their resonance response by interferometry (description of the technique in part III). For a drop volume of 10 µL, a typical spectrum can be observed from the dependence of apex displacement on actuation frequency. In Fig. 5.2, the values of the two resonance frequencies, f_2 and f_4, depend on the drop radius and therefore on evaporation kinetics, a fact which will be exploited in part IV. The resonance frequencies for different volumes are presented in Fig. 5.3(a), taking into account the frequency correction proposed by Strani and Sabetta. Three successive oscillation modes, $n = \{2, 4, 6\}$, are considered for comparison with theory. The four experimental points below the $n = 2$ curve (cf. Fig. 5.3(a)) belong to the additional rocking mode, $n = 1$, for sessile drops, originating from the underlying substrate [42]. In Fig. 5.3(b), a different representation of the same data is chosen, once again considering the resonance frequency, this time in function of $R^{-3/2}$. This relationship is linear in theory. A linear fit via a proportionality parameter, $f_{\text{res}} \propto R^{-3/2}$, is done for resonant modes $n = 2$ and $n = 4$. Finally, Fig. 5.4 presents long-time exposure photos of drop shape oscillations at different excitation frequencies, corresponding to the shape modes $n = 2$ to 12. The node number scales with

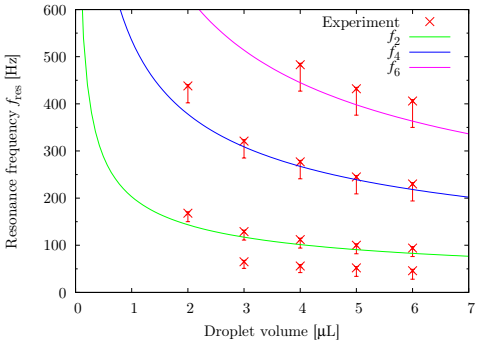

(a) Dependence of resonance frequency on droplet volume. The downward error bars account for the evaporation kinetics during the duration of the measurement.

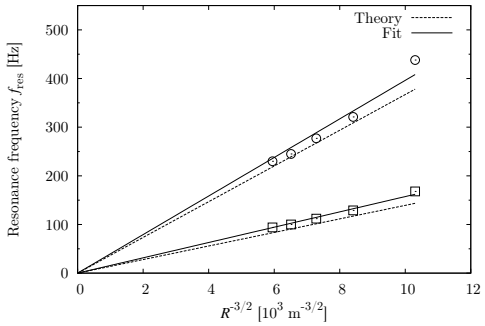

(b) This relationship $f_{res}(R^{-3/2})$ is linear in theory. A linear fit via a proportionality parameter, $f_{res} \propto R^{-3/2}$, is done for resonant modes $n = 2$ (□) and $n = 4$ (○).

Fig. 5.3.: Spectral properties of sessile drops: Comparison between between experiment and theory. The data are post-processed, including the theory of sessile drop oscillations by Strani and Sabetta [42]. Surface tension is evaluated using a tensiometer (refer to appendix E.2 for experimental details). Contact angle $\theta = 100°$.

the mode number, n, and the amplitude is diminishing with frequency (the excitation voltage amplitude is kept constant to $U = 63\,V_{rms}$ for all frequencies).

5.2. Dual-frequency electrowetting

An innovative methodology developed during this work is the technique of "dual-frequency electrowetting" (DF-EW). This technique exploits both electrowetting regimes, high- and low-frequency electrowetting, for actuation of drop shape oscillations. A high frequency is used as a carrier signal. This first electrowetting voltage is modulated by a voltage of low frequency and smaller amplitude. For experimental details, please refer to section 8.3 on electrowetting voltage generation.

The purpose of working with a dual-frequency actuation is that, when a high frequency $\nu > 1\,kHz$ is used, its amplitude tunes the contact angle (for instance $\theta = \pi/2$) in a range, which depends on composition of the underlying substrate and contact angle saturation. Due to minimization of electrostatic energy, the high-frequency voltage contribution makes the droplet straddle the underlying electrode pair [32], making droplet position far more stable than in standard geometries. Therein lies a second feature of prior importance, since interferometry measurements on a curved surface require a high degree of local accuracy to be feasible. Furthermore, high-frequency electrowetting helps reducing contact angle hysteresis by about 5°, depending on the substrate condition, which is important for high quality drop shape oscillations.

The low-frequency voltage modulation is characterized by a frequency in the range $f \sim 10 - 1000\,Hz$. This voltage is used to oscillate radially the contact line of the drop, otherwise stabilized in position, and therefore to induce drop shape oscillations of frequency $f_{osc} = 2f$, thereby controlling a capillary wave

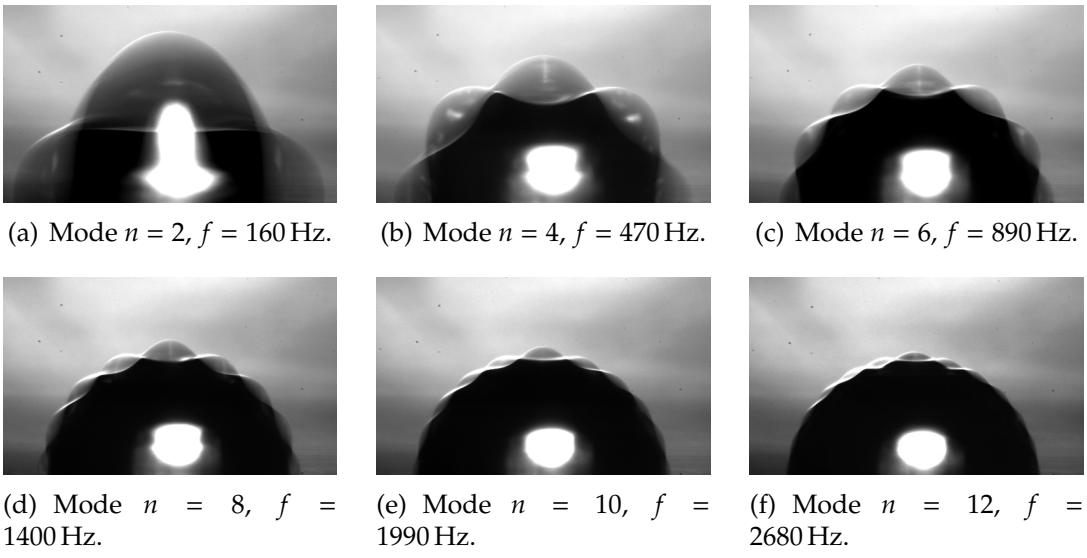

(a) Mode $n = 2$, $f = 160\,\mathrm{Hz}$. (b) Mode $n = 4$, $f = 470\,\mathrm{Hz}$. (c) Mode $n = 6$, $f = 890\,\mathrm{Hz}$.

(d) Mode $n = 8$, $f = 1400\,\mathrm{Hz}$. (e) Mode $n = 10$, $f = 1990\,\mathrm{Hz}$. (f) Mode $n = 12$, $f = 2680\,\mathrm{Hz}$.

Fig. 5.4.: Long-time exposure photos of drop shape oscillations at different mode numbers, $n = 2$ to 12, of a 1.5 µL water drop. The number of oscillations nodes scales with the mode number. Amplitude of excitation voltage is $U = 63\,\mathrm{V_{rms}}$ at variable frequency, f (cf. part III for the corresponding experimental details).

network standing along the drop surface. Hence, as demonstrated below, by changing the frequency f_{osc}, it is easy to select capillary resonance with a given set of spherical standing wave modes along the drop surface.

5.3. Transient oscillations of sessile drops: natural frequency and decay time

Studies on the decay regime of capillary waves on droplets were recently published by Kang [43] and Garimella [44] for over-damped systems. In contrast to section 5.1.2, contact line friction needs to be included in order to correctly describe the motion of sessile drops, stick-slip motion of the contact line is neglected, since the substrate is lubricated, according to the experimental methodology developed during the course of this thesis. In their model for transient drop oscillations, Kang includes the contact line friction via a friction factor, λ [43]:

$$F_{\mathrm{f}} = -\Lambda u,$$

where u is the contact line velocity. The differential equation (5.8) for the shape mode coefficients is rewritten with the contact line friction:

$$\ddot{a}_n + 2(n-1)(2n+1)\frac{\mu}{\rho R^2}\dot{a}_n + \frac{2n\Lambda}{\rho R^2}A_{nn}\dot{a}_n + n(n-1)(n-2)\frac{\gamma}{\rho R^3}a_n = -\frac{2n\Lambda}{\rho R^2}\sum_{k=2,\,k\neq n}^{\infty} A_{nk}\dot{a}_k. \tag{5.10}$$

The third term is a linear friction term with a friction coefficient, Λ. The right hand side term takes into account the non-linear coupling of the oscillation modes $k \neq n$ due to contact line friction. In Kang's work [43], this non-linear coupling is of utmost importance, since a step potential is used for electrowetting actuation, exciting all of the oscillation modes during the over-damped transition. In this work, dealing with under-damped oscillations, the self-sustained coupling may be neglected, since the oscillation rapidly adopts the natural frequency of the system, f_2 [45]. As a consequence, the oscillation mode $n = 2$ is the preponderant oscillation mode after cutting the actuation. In this case, equation (5.10) may be reformulated:

$$\ddot{a}_2 + 2\left(5\frac{\mu}{\rho R^2} + \frac{2\Lambda}{\rho R^2}\right)\dot{a}_2 + 8\frac{\gamma}{\rho R^3}a_2 = 0. \tag{5.11}$$

Using basic harmonic oscillator theory, the damping time scale τ may be derived from (5.11):

$$\tau^{-1} = (5\mu + 2\Lambda)/\rho R^2.$$

From this expression, it is possible to calculate the contact line friction coefficient, Λ:

$$\Lambda = \frac{1}{2}\left(\frac{\rho R^2}{\tau} - 5\mu\right). \tag{5.12}$$

A direct application of this theory-guided method is demonstrated in appendix D, where use is made of (5.12) to characterize contact line friction. Also, transient drop oscillations may be used to serve as a transduction mechanism for the natural frequency of a sessile drop. This may be exploited as a complementary means of characterizing the spectrum of drop oscillations, or even replace the spectrum measurement in steady conditions. The advantages of this method are explained in chapter 11. The technique is not commonly used all throughout this work, since it was not a primary objective. As of its simplicity and rapidity concerning measurement and analysis, it may nonetheless be very interesting to develop it for future work.

As a last point, the dependence of natural frequency on excitation frequency is tested and characterized using the interferometry method developed in part III, in which experimental details are described. Use is made of dual-frequency electrowetting using a first high-frequency voltage adjusting the contact angle of the drop to $\theta = \pi/2$, and a second voltage of low frequency f to induce shape oscillations in mode $n = 2$. The oscillation frequency is measured before and after cutting the low-frequency excitation signal. It is found that the decay frequency (natural frequency of drop oscillations) does not depend on the applied excitation frequency, f, after cutting the perturbation voltage (cf. Fig. 5.5). The natural frequency is only modified by a slow time-dependence of the drop radius due to evaporation. Excitation frequencies lower and higher than the resonance frequency, f_2, are tested.

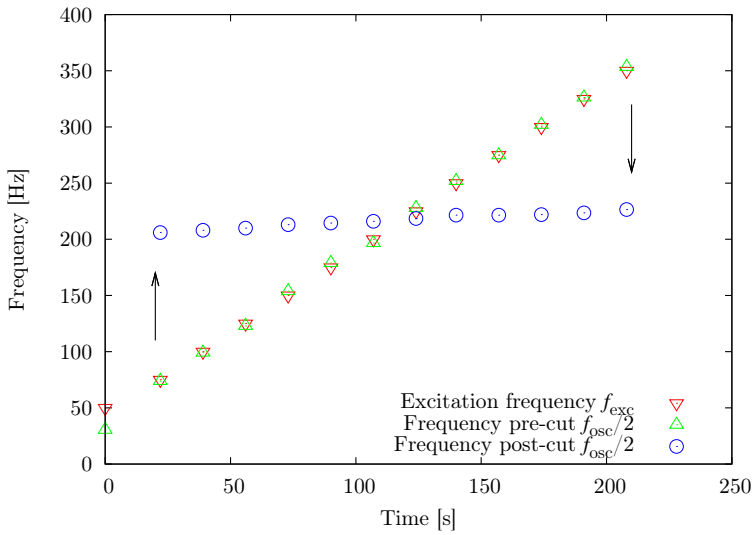

Fig. 5.5.: Relation between excitation and measured natural frequency. The evaluated natural frequency does not depend on the excitation frequency, it is only modified by evaporation acting on the drop radius. Low and high excitation frequencies are tested.

6. Steady streaming

This chapter introduces the theory of streaming flow, which is a hydrodynamic phenomenon, explaining the net flow of liquid matter induced by an oscillatory interface motion, e.g. a wavy liquid surface. As taught in basic physics and fluid mechanic courses, a wave is not linked to mass transport of the affected medium. The phenomenon of steady streaming is though possible due to a non-linear term in the Navier-Stokes equation of hydrodynamics. Steady streaming is involved in many domains: In hydraulics and oceanology, it is implicated in sediment transport by waves [46]. In physiology, steady streaming is involved in the transformation of a sonar signal into a neuronal signal via the cochlea liquid [47,48], or in blood recirculation mechanisms [49].

In microfluidic applications, steady streaming is one of the rare phenomena based on inertial effects. It is often generated by means of acoustic waves, then named acoustic streaming [50]. It may be used to pump a liquid [51], capture chemical species in a solution [52], or to favor stirring or mixing in microchambers [8,53]. Concerning drop physics, steady streaming was already investigated experimentally in microdrops [13–15], and once numerically in the opposite configuration (microbubble in aqueous bath, semi-infinite geometry) [54].

The first experiments on steady streaming were realized by Faraday studying the flow induced by a vibrating plate [55]. The first theoretical advances were done by Lord Rayleigh [56], concerning the flow induced by acoustic waves between two plates. More advanced theories were developed by Stuart [57,58] and Riley [59].

6.1. Basic streaming theory

Consider an incompressible fluid domain of dimension L concerned by an oscillatory boundary condition of frequency ω:

$$u_{\text{osc}}(x,t) = U_{\text{osc}} \sin(\omega t + \psi),$$

with ψ, an arbitrary phase, and U_{osc}, the magnitude of the velocity. The Navier-Stokes equation for the liquid bulk writes:

$$\rho \frac{\partial \boldsymbol{u}}{\partial t} + \rho(\boldsymbol{u} \cdot \nabla)\,\boldsymbol{u} = -\nabla p + \mu \Delta\, \boldsymbol{u},$$

with $\boldsymbol{u}$ is the volume velocity, p is the pressure and μ is the newtonian viscosity of the liquid. The equation may be rewritten in its non-dimensional form, using

L, ω^{-1} and U_{osc} as characteristic scales for length, time and velocity, respectively:

$$\mathrm{S}\frac{\partial \hat{\boldsymbol{u}}}{\partial \hat{t}} + (\hat{\boldsymbol{u}} \cdot \hat{\nabla})\,\hat{\boldsymbol{u}} = -\hat{\nabla}\hat{p} + \frac{1}{\mathrm{Re_d}}\hat{\Delta}\,\hat{\boldsymbol{u}}.$$

Here, $\hat{t} = t/\omega$, $\hat{\boldsymbol{u}} = \boldsymbol{u}/U_{\mathrm{osc}}$ and $\hat{p} = p/\rho U_{\mathrm{osc}}^2$ are the non-dimensionalized variables for time, velocity and pressure, respectively; $\hat{\nabla} = L\nabla$ and $\hat{\Delta} = L^2\Delta$ are the non-dimensionalized differential operators. The non-dimensional Strouhal and Reynolds numbers are:

$$\mathrm{S} := \frac{\omega L}{U_{\mathrm{osc}}}, \quad \mathrm{Re} := \frac{\rho U_{\mathrm{osc}} L}{\mu}.$$

For convenience, the hat symbol, $\hat{}$, designating dimensionless variables is dropped, and the variables t, $\boldsymbol{u}$ and p, as well as the operators ∇ and Δ are referred to as dimensionless variables and operators, respectively. For a two-dimensional incompressible flow, it is worthy to introduce the flow potential, $\boldsymbol{\Phi} = \Phi\,\boldsymbol{n}$, such that:

$$\boldsymbol{u} = \nabla \times \boldsymbol{\Phi}.$$

Making use of the vorticity, $\boldsymbol{\Omega} = \nabla \times \boldsymbol{\Phi} = -\Delta\boldsymbol{\Phi}$, the vorticity equation is expressed as the curl of the Navier-Stokes equation:

$$\frac{\partial}{\partial t}(\Delta\Phi) - \xi\left(\frac{\partial \Phi}{\partial x}\frac{\partial \Delta\Phi}{\partial y} - \frac{\partial \Phi}{\partial y}\frac{\partial \Delta\Phi}{\partial x}\right) = \frac{\xi^2}{\mathrm{R_s}}\Delta^2\Phi, \tag{6.1}$$

with the dimensionless numbers:

$$\xi := \frac{U_{\mathrm{osc}}}{\omega L} = \mathrm{S}^{-1}, \quad \mathrm{R_s} := \frac{\rho U_{\mathrm{osc}}^2}{\omega\mu} = \mathrm{Re}\,\mathrm{S}^{-1}.$$

For the case $\xi = 0$, equation (6.1) is linear and the solution is proportional to $\cos(\omega t)$. On the contrary, for the case $\xi \neq 0$, the equation becomes non-linear and the solution contains terms proportional to $\cos^2(\omega t) = (1 + \cos(2\omega t))/2$. The streaming flow represents the stationary part of equation (6.1), appearing when the non-linear part is no more negligible. The non-linearity is a significant difficulty for finding any solution of the vorticity equation (6.1). Nevertheless, when $\xi \ll 1$, it is possible to find an approximation using a perturbation method, as described by Schlichting [60]:

$$\Phi = \Phi_0(t) + \xi\Phi_1(t) + \mathcal{O}(\xi^2). \tag{6.2}$$

Here, Φ_0 is the solution of the linear equation for $\xi = 0$. The term Φ_1 is subsequently decomposed into a time-dependent part $\Phi_1^{\mathrm{u}}(t)$ and a stationary part Φ_1^{s}, representing the streaming flow:

$$\Phi_1 = \Phi_1^{\mathrm{s}} + \Phi_1^{\mathrm{u}}(t). \tag{6.3}$$

Injecting equations (6.2) and (6.3) into the partial differential equation (6.1), a system of equations is obtained, which was resolved by Riley [61]. The solution exhibits one unsteady term confined to a Stokes boundary layer of thickness $\delta_s = \sqrt{\mu/\rho\omega}$, in which the mean vorticity over one period is zero. Beyond this so-called Stokes layer, a stationary streaming flow, characterized by the velocity u_s, arises:

$$u_s = -\frac{3}{8\omega}\left(\frac{\mathrm{d}U_{osc}^2}{\mathrm{d}x} + 2U_{osc}^2\frac{\mathrm{d}\Phi}{\mathrm{d}x}\right).$$

The first term on the right hand side corresponds to a standing wave, the second term to a traveling wave. For a liquid surface populated by standing waves, the steady streaming velocity is thus:

$$u_s = -\frac{3}{8\omega}\frac{\mathrm{d}U_{osc}^2}{\mathrm{d}x} = -\frac{3U_{osc}}{4\omega}\frac{\mathrm{d}U_{osc}}{\mathrm{d}x}. \tag{6.4}$$

This streaming flow causes a net and stationary flow persisting beyond the Stokes layer, in the liquid bulk. The flow regime depends on the streaming Reynolds number, R_s: For $R_s \ll 1$, a Stokes flow is induced in the volume. For $R_s \gg 1$, Stuart showed that the flow persists beyond the Stokes layer, on a depth $\delta_{Stu} = O(\sqrt{\mu/\rho\omega}/\xi)$.[1] By these theoretical results, it is demonstrated how capillary waves sustained along the surface of a drop can generate a steady bulk flow, provided Rs is small enough. This phenomenon will therefore be developed in the following section of steady streaming in drops.

6.2. Steady streaming induced by drop shape oscillations

The shape of a drop oscillating with a frequency ω_n is given by equation (5.1). In the resonance state, the shape is mainly dictated by the predominant shape mode, n:

$$d_n(\varphi, t) = R + va_n^0\cos(\omega_n t + \psi_n)P_n(\cos\varphi).$$

The oscillation velocity is associated to the oscillatory motion of the drop, calculated using the flow potential expressed at the inside of the drop:

$$\Phi = -\frac{a_n^0\omega_n R}{n}\frac{d_n(\varphi,t)^n}{R^n}P_n(\cos\varphi)\cos(\omega_n t + \psi_n).$$

The surface velocity writes:

$$u_{osc,n} = -\frac{1}{R}\frac{\partial\Phi}{\partial\varphi}\Big|_{r=R} = \frac{a_n^0\omega_n}{n}\frac{\partial P_n(\cos\varphi)}{\partial\varphi}\cos(\omega_n t + \psi_n).$$

[1] It is interesting to note that the streaming-induced flow type in the volume is not directly related to the Reynolds number Re.

This is a standing wave with a velocity amplitude of:

$$U_{\mathrm{osc},n} = \frac{a_n^0 \omega_n}{n} \frac{\partial P_n(\cos\varphi)}{\partial \varphi}.$$

Hence, using equation (6.4), the steady streaming flow at the surface of the Stokes layer writes:

$$u_{\mathrm{s},n} = -\frac{3U_{\mathrm{osc},n}}{4R\omega_n} \frac{\mathrm{d}U_{\mathrm{osc},n}}{\mathrm{d}\varphi} = -\frac{3(a_n^0)^2\omega_n}{8Rn^2} \frac{\mathrm{d}}{\mathrm{d}\varphi}\left[\left(\frac{\mathrm{d}P_n(\cos\varphi)}{\mathrm{d}\varphi}\right)^2\right] \tag{6.5}$$

For a drop oscillating with a mode $n = 2$ at $\omega_2 = 1500\,\mathrm{rad/s}$, and at an amplitude to radius ratio of $va_2/R = 0.1$ ($R = 1\,\mathrm{mm}$, $va_2 = 100\,\mu\mathrm{m}$, the Stokes layer is about $\delta_\mathrm{s} = 30\,\mu\mathrm{m}$ thick, and the dimensionless numbers exhibit values of $\xi \approx 0.05$ and $\mathrm{R_s} \approx 3.75$. The fact of using the standing wave approximation for the streaming velocity, equation (6.4), is justified by the standing wave character of drop oscillations. Furthermore, the small value of ξ justifies the approximation of Schlichting (6.2). The value of $\mathrm{R_s}$ is found slightly superior to 1, which raises a reasonable doubt on the nature of the flow regime. It may help to consider the depth $\delta_\mathrm{Stu} \approx 500\,\mu\mathrm{m}$, which is six-fold the Stokes layer, and equals nearly the drop radius. Hence, it is most probable that the volume effects of steady streaming are not negligible. Please refer to Fig. 6.1 for a comparison between experimental imaging of tracer particles and numerical simulations based on the present model, without neglecting the non-linear convective term of the Navier-Stokes equation [62, 63]. The first three shape modes $n = \{2, 4, 6\}$ are displayed. The flow pattern is a horizontal multi-toroidal structure. The number of tori depends on the shape mode of oscillation.

6.3. Steady streaming and high-frequency electrowetting actuation

In the course of the work, the question may come up if high-frequency electrowetting actuation can create a steady streaming flow or not. As seen in the two foregoing sections, the creation of streaming current is coupled to an oscillatory motion of an interface. Furthermore, the Schlichting condition, $\xi \ll 1$, and the Stuart condition, $\mathrm{R_s} \gg 1$, need to be verified in order for streaming to be created and act on a sufficiently large extension, called the Stuart length, δ_Stu.

As far as shape oscillations are concerned, there is a further parameter which needs to be taken into account. The transmission of oscillatory motion from the contact line to the apex of the drop, and vice versa, is driven by a balance between surface tension and damping effect of the liquid viscosity, μ: the less viscous the liquid, the easier it is to transmit oscillations of high frequency, creating the capillary wave network all along the drop surface. Hence, a critical frequency scale, $f_\mathrm{visc} := \mu/\rho a_0^2$, exists, characterizing a low-pass filter for oscillatory motions of amplitude $a_0 = 0.1\,R_0$. For a sessile 1 µL water drop, this frequency limit takes the value $f_\mathrm{visc} = 164\,\mathrm{Hz}$. This means two consequences for drop oscillations and

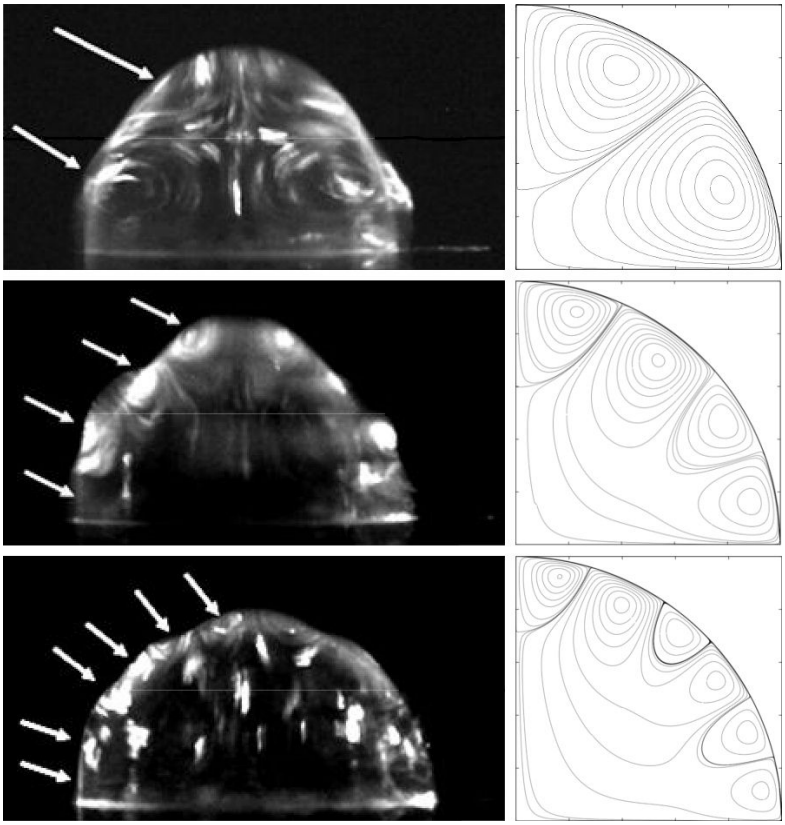

Fig. 6.1.: Streamlines for three electrowetting-induced oscillation modes, from top to bottom: $n = \{2, 4, 6\}$. Comparison of experimental imaging of tracer particles (left) and simulation results (right). The arrows indicate the vortex structures also made evident in the simulation. Experimental data are a courtesy by Rachid Malk [62].

streaming with excitation frequencies beyond the limit $f_{\text{visc}}/2$:

- The wave network changes from a standing wave network to two superimposed travelling waves of different mechanical energy. This implies that the wave amplitude along the drop surface is maximal at the triple contact line, the point source of excitation, and at the apex, the point of capillary resonance. In between, the upward and downward travelling waves are damped under viscosity and the oscillation amplitude will be less significant. This phenomenon may be seen on Figs. 5.4(e) and 5.4(f) on page 53.
- A second important point to mention is that subsequent momentum of the steady streaming current, such as induced by low-amplitude waves and diffused under viscosity, is no longer significant into the drop bulk. The streaming pattern seen in Fig. 6.1 is then altered since at high frequencies, it is restricted to the vicinity of the surface and it does no longer develop in the bulk.

7. Conclusion

In this part, a review on electrowetting and electrowetting-induced drop shape oscillations is presented. Static wetting is explained, and different correction factors are introduced to correctly describe multi-electrode coplanar electrowetting and shape oscillations of sessile drops. It is seen that drop oscillations are characterized by a mode number n, giving rise to different resonance frequencies. Each resonance frequency drives a dominant shape mode, described by Legendre polynomials. This shape, in the case of resonance, gives rise to specific flow patterns in the drop volume, since induced by streaming current. A flow velocity of several mm/s is reached for millimeter-sized drops. Standing capillary waves along the drop surface behave as a bulk flow generator with an efficiency that rises with a diminishing surface to volume ratio.

The next part is devoted to the implementation of instrumentation, signal acquisition and data processing, which is necessary to properly characterize drop shape oscillations.

Part III.

Instrumentation and Technical Developments

This part presents the experimental developments for the accurate characterization of drop shape oscillations. All elements are presented, beginning with electrowetting actuation of a water drop in a coplanar configuration. The chip technology, the experimental setup and dual-frequency electrowetting voltage generation are described. A second chapter presents the experimental setup and the theory of the implemented Michelson interferometer. It is explained, in which way the frequency-modulated interferometry signal can translate the oscillation amplitude. Two different approaches – transient and free decaying drop oscillations – are used. The two approaches need distinct automation and signal processing algorithms, which are explained in the following chapters. Finally, the influence of the silicone oil film on interferometry measurements is explained, as well as the possible solutions to avoid parasitic interferometric fringes.

8. Electrowetting setup

8.1. Chip technology

Electrowetting chips are fabricated on 8 inch silicon wafers in a cleanroom environment (Plateforme technologique amont (PTA), CEA Grenoble). A thermal treatment at 1100 °C is applied to form a SiO_2 oxide layer (Fig. 8.1(a)) on the wafer. Via a succession of plasma-enhanced chemical vapor deposition (PECVD), photolithography and dry-etching steps, conductor lines and EW electrodes, made of $e_{\mathrm{met}} = 200\,\mathrm{nm}$ thick AlSi, are created, and the dielectric coating made of $e_{\mathrm{ins}} = 600\,\mathrm{nm}$ thick Si_3N_4, is deposited (Fig. 8.1(b)-(e)). The last step consists of coating and etching the surface with a hydrophobic layer of SiOC, $e_{\mathrm{hy}} = 1000\,\mathrm{nm}$ thick (Fig. 8.1(f)). After cutting the wafer in 21.7 mm square chips, they may be used for the experiments.

There exist several geometry designs on the wafers, of which two are used throughout this work. Both geometries consist of two half-moons facing each other (refer to Fig. 8.1(g)). One geometry measures 4 mm in diameter with a gap of 100 µm, the second geometry measures 2 mm in diameter with a gap of 3 µm. In Fig. 8.1(g), a different geometry of dimensions $2\,\mathrm{mm} \times 2\,\mathrm{mm}$ is presented. Connection between the electrodes and the EW voltage supply is made via an array of 41 contacts located on one side of the chip. This array of electrical contacts is placed under a connector, as described in the next section.

8.2. Chip support

For the experiments, chips are inserted into a chip support, which may be covered by a lid to limit evaporation. The chip support receives a connector for delivery of the electrowetting voltage via a 40 wire cable connected to a printed circuit board (PCB) (confer Fig. 8.2).

The chip support is made of Plexiglas and mounted on two translation stages (M-UMR5-16 and PT1/M, Newport, Irvine (CA), USA and Thorlabs, Newton (NJ), USA) for horizontal alignment of the electrode geometry in use with a focused laser beam. It contains a milled flat cavity for insertion of the electrowetting chip. A U-shaped channel is milled beneath the outer borders, which may be filled with water, in order to limit evaporation during experiments. Two locking pins are inserted next to the EW chip to fit the connector into place above the chip. A lift is milled all around the chip support, which serves to keep the Plexiglas lid in place. The lid is transparent such that imaging of the drop in brightfield with a standard camera is possible. The lid may receive disks of different thickness to create a variable confinement of the evaporating drop. This will be used in part IV on drop array evaporation.

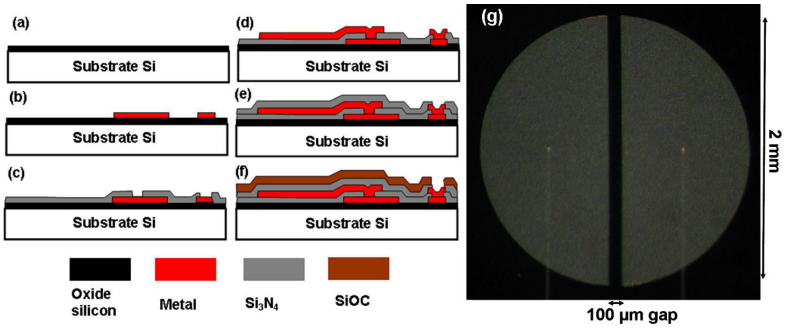

Fig. 8.1.: Illustration of cleanroom chip fabrication done at PTA/CEA Grenoble. (a) SiO_2 layer, (b) and (c) conductor line and dielectric deposition, (d) and (e) EW electrode and dielectric deposition, (f) hydrophobic layer deposition, (g) example geometry of two half-moons measuring 2 mm in diameter with a 100 µm gap. The thin lines visible in the photograph are the conductor lines to the connector plots. Source: CEA Grenoble.

The connector is assembled of two polyoxymethylene (POM) plates, mounted underneath a printed circuit board. The POM plates are fabricated by PMP (Eybens, France), the PCB is assembled by Cari-Electronic (Châteauneuf-sur-Isère, France). The POM plates have drilled openings for the positioning of test pins, type B1316-K11 fabricated by Rika Denshi America (Attleboro (MA), USA, cf. Fig. 8.3). The test pins establish contact between the chip contacts (plunger B, 1-40 out of 41 contacts are used) and the contact of the printed circuit board (plunger A, cf. Fig. 8.4). The printed circuit board is then connected via a female connector (FFSD-20-01-N, Samtec, New Albany (IN), USA) and a 40 wire cable to the EW tension supply.

Visualization is realized perpendicularly to the gap axis by illuminating the droplet in bright-field with a light-emitting diode HighLED blue, emission wavelength 470 nm, manufactured by Qioptiq (Göttingen, Germany) and a convenient condenser. The used camera is a AF622f (Basler, Ahrensburg, Germany) with an optical zoom for more suitable imaging. Recording is done by LabVIEW IMAQdx (National Instruments, Austin (TX), USA). Contact angle measurements have been realized with the ImageJ-plugin *LB-ADSA*, created by the Biomedical Imaging Group at EPFL Lausanne [64].

8.3. Electrowetting voltage generation

Two AC voltages, U_1 (frequency ν) and U_2 (frequency f), are provided by two separate frequency generators TG2000 (TTi, Fort Worth (TX), USA). The two devices are piloted via National Instruments LabVIEW and connected through a universal serial bus (USB), in order to have a constant and automated control over U_1 and U_2. These two signals are treated by an electronic circuit (Fig. 8.5, using an analog multiplier AD734, fabricated by Analog Devices (Norwood (MA), USA), and an operational amplifier OPA2227, fabricated by Texas Instruments (Dallas (TX), USA). Voltage U_1 corresponds to the *Carrier* signal, while

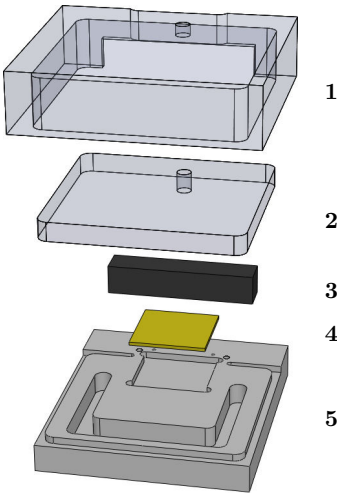

(a) 1, Plexiglas lid; 2, Plexiglas disk for variable confinement; 3, connection part for voltage supply; 4, EWOD chip; 5, chip support with U-shaped water channel.

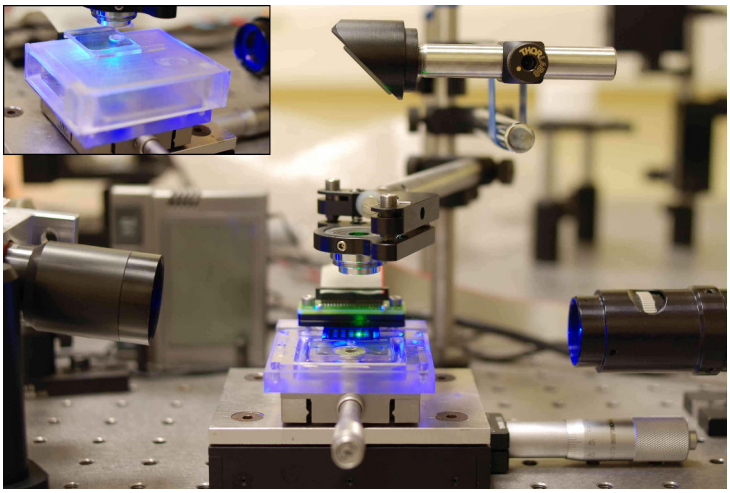

(b) Photo of the experimental setup with optical parts (cf. chapter 9) and lid (insert): light-emitting diode (left), camera (right) and x-y translation stages (bottom).

Fig. 8.2.: Illustration of the chip support assembly and surrounding elements.

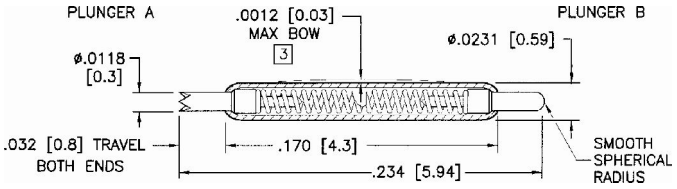

Fig. 8.3.: Sketch of a B1316-K11 test pin fabricated by Rika Denshi America (Attleboro (MA), USA). Measures are given in inch [mm]. Source: Rika Denshi America.

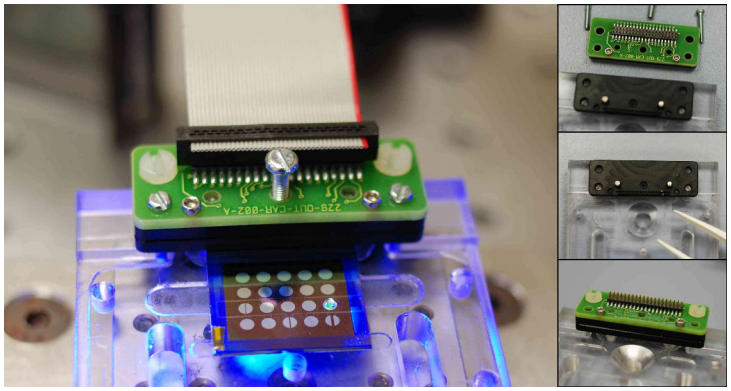

Fig. 8.4.: The assembly steps of the connector are displayed in the inserts: The lower and upper parts are disassembled (top) to place the pogo pins in the position corresponding to the chip electrodes (middle). The connector is reassembled (bottom) and the chip and connecting cable put into place (left). The middle screw serves to unplug the connector from the support.

voltage U_2 constitutes the *Modulation* signal. The left part of the circuit, constituted by the diode, the 10 kΩ resistance and the 35 µF polarized capacitor, supplies the envelope of the carrier signal, $\tilde{U}_1$. The envelope is equal to a constant voltage, which will be used to decorrelate the modulation and the carrier signal in the multiplication/division provided by the AD734. The envelope of the carrier signal is supplied to the positive entry of the OPA2227 operational amplifier. The *Output* signal of the AD734 corresponds to tension U_3. The final voltage furnished by this integrated circuit is:

$$U_3 = \left(1 + \frac{U_2}{\tilde{U}_1}\right) U_1.$$

By the division of $\tilde{U}_1$, the modulation signal, U_2, is decorrelated of the amplitude of U_1. Hence, whatever value exhibits the amplitude of U_1, the modulation U_2 always keeps the same amplitude. In practice this means, that whichever the value of the high-frequency electrowetting voltage (translating the drop surface curvature), the oscillation-generating signal keeps the same amplitude. Thus, the oscillation amplitude does not depend directly on the high-frequency voltage, although the amplitude may depend on the contact angle and thus the curvature of the drop surface.

The AD734 and OPA7222 are provided a stabilized feed-in of ±11 V by a Hameg power supply HM7042-3 (Hameg, Mainhausen, Germany). The voltage U_3 is amplified by a high-voltage amplifier 601c fabricated by TREK (Medina (NY), USA), and delivers the high voltage, $U = G\,U_3$, with G, the amplifier gain. The electrode pair in use has one electrode connected to the ground, and the other electrode connected to the voltage signal U. The frequency dependence of the amplifier gain, G, is displayed in Fig. 8.6.

The benefit of using two voltages is, when imposing a high frequency $\nu >$ 1 kHz to U_1, its amplitude may be used to control the contact angle and thus the curvature of the droplet within the range of the low Bond number regime,

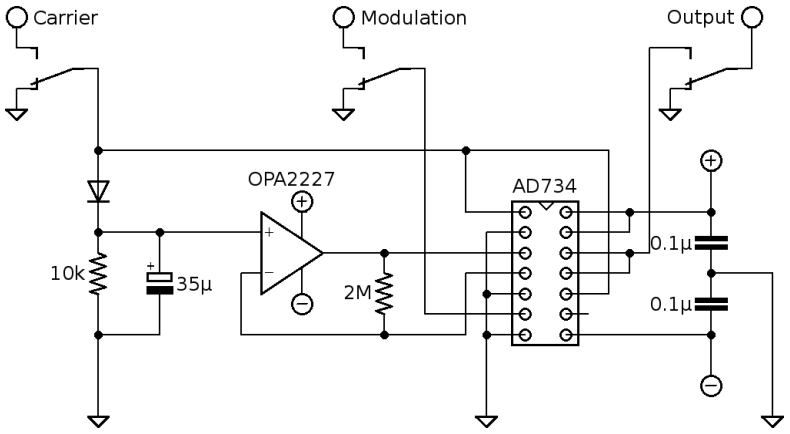

Fig. 8.5.: Equivalent circuit of the electronic tension generation. *Carrier* corresponds to the high-frequency carrier signal, U_1, *Modulation* to the low-frequency electrowetting voltage, U_2, and *Output* to the resulting tension, $U_3 = \left(1 + U_2/\tilde{U}_1\right) U_1$.

which means that the spherical shape of the surface has always to be respected as described in section 4.1. The second voltage, U_2, is of low frequency with respect to electrowetting in the range of $f \sim 10 - 1000\,\mathrm{Hz}$, depending on drop volume and oscillation mode. This modulation voltage is used to force the triple contact line into an oscillatory motion and to control its oscillation frequency, thereby controlling the capillary wave network along the surface of the drop. For more details on dual-frequency electrowetting, please refer to section 5.2.

The electrowetting curves for both electrode geometries with 3 µm and 100 µm gap width, described in section 8.1, are displayed in Fig. 8.7. For the 3 µm curve, the influence of a silicone oil film lubricating the substrate, is taken into account. By fitting the theoretical curve to the experimental data, an oil film thickness of 260 nm is found. More information on the oil film and lubrication is given in the materials and methods sections of the corresponding experimental analyses. Importantly, throughout this thesis, the electrowetting voltage, U, never goes beyond $100\,\mathrm{V_{rms}}$ so that contact angle saturation never arises.

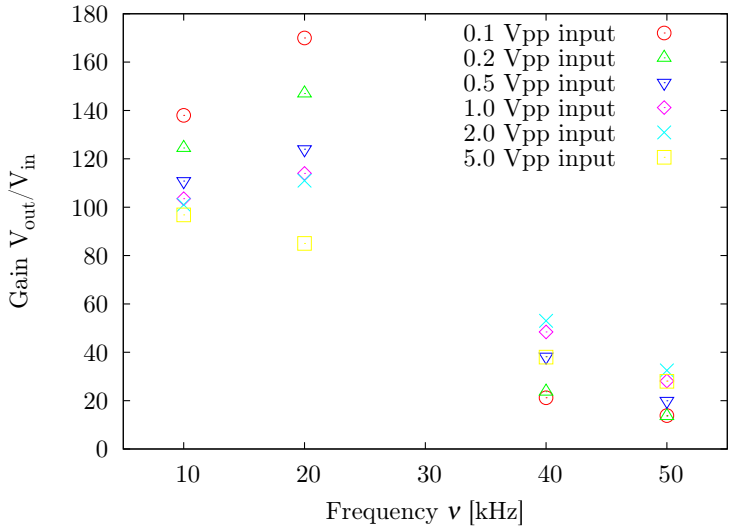

Fig. 8.6.: The gain of the TREK high voltage amplifier. There is a strong dependence on input frequency. The linear regime is restrained to 0-8 kHz (data not shown, refer to TREK data sheet).

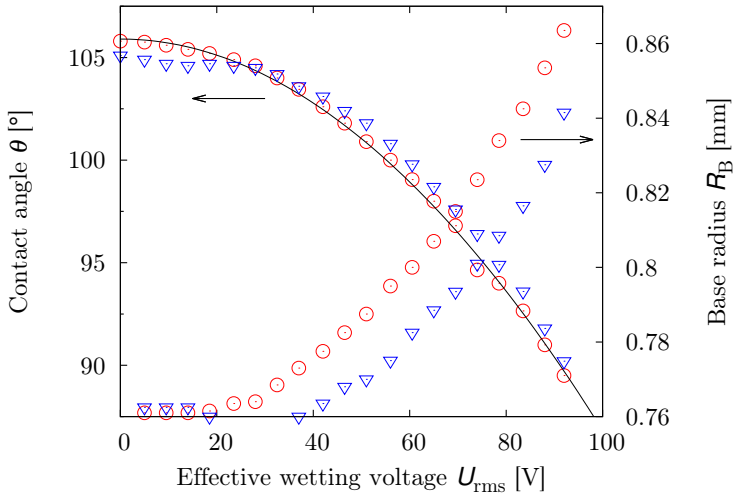

Fig. 8.7.: Wetting characteristics of a 1.3 µL drop in the coplanar electrode configuration on a substrate lubricated by a thin silicone oil film. The wetting curves and wetting radii correspond to a 3 µm gap (∘) and the 100 µm gap (△). The black line corresponds to a fit of the Lippmann-Young equation (4.3) with d_{oil} = 260 nm as a free parameter.

9. Michelson interferometry

The drop apex is chosen as the location where drop shape oscillations are measured by local interferometry. This choice can be justified as follows: First, the amplitude of the droplet during oscillation is maximal at its apex. So the best sensitivity is obtained at this point. Second, the close vicinity of the apex theoretically remains parallel to the bottom electrode whilst translating vertically to it, provided that drop shape deformation is purely axisymetric. Hence, the apex of the drop (slope zero in the reference system of the electrode support) may be used as a semi-reflecting mirror, and the electrode underneath as a mirror. Both interfaces provide two reflections of the input laser beam. This has the advantage of directly working in the electrodes' reference system, and to have an elegant way of realizing the interferometry measurement without an external reference mirror. With a precise optical alignment, which means a laser beam impacting normally with respect to the electrode and the drop surface, it might thus be possible to obtain a precise interferometry signal from an optical path difference whose time-dependence originates from the moving drop apex.

9.1. Optical setup

The laser source is a CDPS532M model fabricated by JDS Uniphase (Milpitas (CA), USA) with wavelength $\lambda = 532\,\mathrm{nm}$ and power 50 mW. It is placed on an optical table, where its horizontally aligned beam crosses a planar polarizer, to limit light intensity, and a beam splitter. A mirror reflects the beam vertically onto the drop apex and the electrode underneath a microscope objective. The microscope objective is used for precise focusing of the laser beam at the drop apex all along the distance of motion, and for subsequent collection of the reflected light. Please refer to Fig. 9.1 for a sketch of the optical setup. At the drop, two reflections arise: a first reflection of the laser beam at the liquid/gas interface of the drop apex and a second reflection at the solid substrate, on which the drop rests. These two reflections take the same path back to the beam splitter, where they are finally routed through a second microscope objective to collect the maximum light intensity on the active surface of an avalanche photo diode (APD), located at the focal point. The avalanche photo diode (C5460-SPL-S5821-02-1, Hamamatsu, Shizuoka, Japan), characterized by a very high cut-off frequency > 6 MHz, delivers an analog signal proportional to the received light intensity, I. Further, higher order reflections of the laser beam at drop scale are not observed to interfere with the primary reflections because they are deviated away from the microscope objective by the curved drop surface.

The convex lens inserted at its focal length L_a (microscope objective 1) above the droplet has two advantages. First, the laser beam (beam diameter, $1/e^2$-point: 0.6 mm) is well focused on the apex in order to suppress contributions of

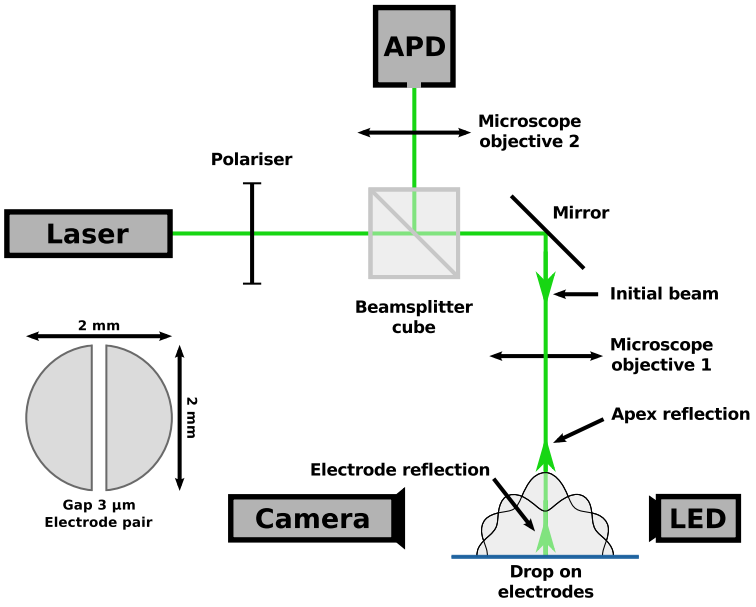

Fig. 9.1.: Setup of the interferometry system. The laser beam crosses the optical system to form two first-order reflections on the drop apex and the solid substrate, which are detected by the APD. (Inset) Electrode pair in use for electrowetting actuation.

the wider apex region. Second, the drop interface at the apex is not necessarily perfectly horizontal when oscillating, or the droplet may not be precisely aligned with the laser beam. With this lens, even stray light deflected due to these two reasons may be collected. A second convex lens (microscope objective 2), inserted at its focal length L_{APD} in front of the diode, provides a good focusing of the laser beam onto the sensitive region of the photodiode device.

9.2. Interferometry signal

The avalanche photo diode receives a linearly polarized laser beam, composed of two waves corresponding to two optical reflections issued from the apex (wave 1) and the electrode (wave 2):

- Wave 1: Electrical field $E_{\mathrm{e}} = A_{\mathrm{e}} e^{i(2\pi(x_{\mathrm{e}}-ct)/\lambda-\psi)}$, with $x_{\mathrm{e}} = 2\tilde{n}\zeta_0(R/\zeta_0 + \sin(\omega_{\mathrm{osc}}t))$
- Wave 2: Electrical field $E_{\mathrm{a}} = A_{\mathrm{a}} e^{i2\pi(x_{\mathrm{a}}-ct)/\lambda}$, with $x_{\mathrm{a}} = 2\zeta_0(1 - \sin(\omega_{\mathrm{osc}}t))$

with A_{a}, $A_{\mathrm{e}} \in \mathbb{R}$, the amplitudes of the two waves coming from the drop apex and the electrode, respectively. The waves exhibit a wavelength, λ, and a propagation velocity, c, in vacuum. They may be shifted by an arbitrary phase difference, ψ. Anticipating on the experimental findings, the oscillation of the droplet with frequency $\omega_{\mathrm{osc}} = 2\pi f_{\mathrm{osc}}$ and maximum amplitude of the vertical apex motion ζ_0 is supposed harmonic:

$$\zeta(t) = \zeta_0 \sin \omega_{\mathrm{osc}} t.$$

The light intensity, I, received by the APD is calculated as:

$$I\frac{2}{c\tilde{n}\epsilon_0} = |E_\mathrm{e} + E_\mathrm{a}|^2 = A_\mathrm{e}^2 + A_\mathrm{a}^2 + 2A_\mathrm{e}A_\mathrm{a}\cos\left(\frac{2\pi}{\lambda}(x_\mathrm{e} - x_\mathrm{a}) - \psi\right)$$
$$= A_\mathrm{e}^2 + A_\mathrm{a}^2 + 2A_\mathrm{e}A_\mathrm{a}\cos\left(\frac{4\pi}{\lambda}\left[(\tilde{n}-1)\zeta(t) + (\tilde{n}R - \zeta_0)\right] - \psi\right),$$

where ϵ_0 is the vacuum permittivity. Fig. 9.2 shows a typical experimental APD signal for a drop oscillation at frequency $f_\mathrm{osc} = 60\,\mathrm{Hz}$. The instantaneous frequency, f_i, of this signal, which translates the instantaneous velocity $\zeta(t)$ of the interface, writes as:

$$f_\mathrm{i} = \frac{1}{2\pi}\frac{\partial}{\partial t}\arg(I(t)) = \frac{\partial}{\partial t}\left(\frac{2\zeta_0}{\lambda}\left[(\tilde{n}+1)\sin(\omega_\mathrm{osc}t) + (\tilde{n}R/\zeta_0 - 1)\right]\right).$$

The maximum frequency, $f_\mathrm{m} := \max(f_\mathrm{i})$, which is evaluated via a fast Fourier transform of the APD signal, gives thus the maximum amplitude of the oscillation, for a given oscillation frequency:

$$f_\mathrm{m} = \frac{2(\tilde{n}+1)\omega_\mathrm{osc}}{\lambda}\zeta_0,$$

where $\zeta_0\omega_\mathrm{osc}$ is the maximum velocity of the interface. By evaluating f_m via a fast Fourier transform (FFT) of the APD signal, one may thus calculate the maximum amplitude, ζ_0, of the oscillation,

$$\zeta_0 = \frac{\lambda}{4\pi(\tilde{n}+1)}\frac{f_\mathrm{m}}{f_\mathrm{osc}}.$$

The raw APD signal is subsequently delivered to an analog filter (Krohn-Hite model 3362, band-pass 1 kHz/200 kHz, type Butterworth) before being recorded at a sampling frequency of 250 kHz.

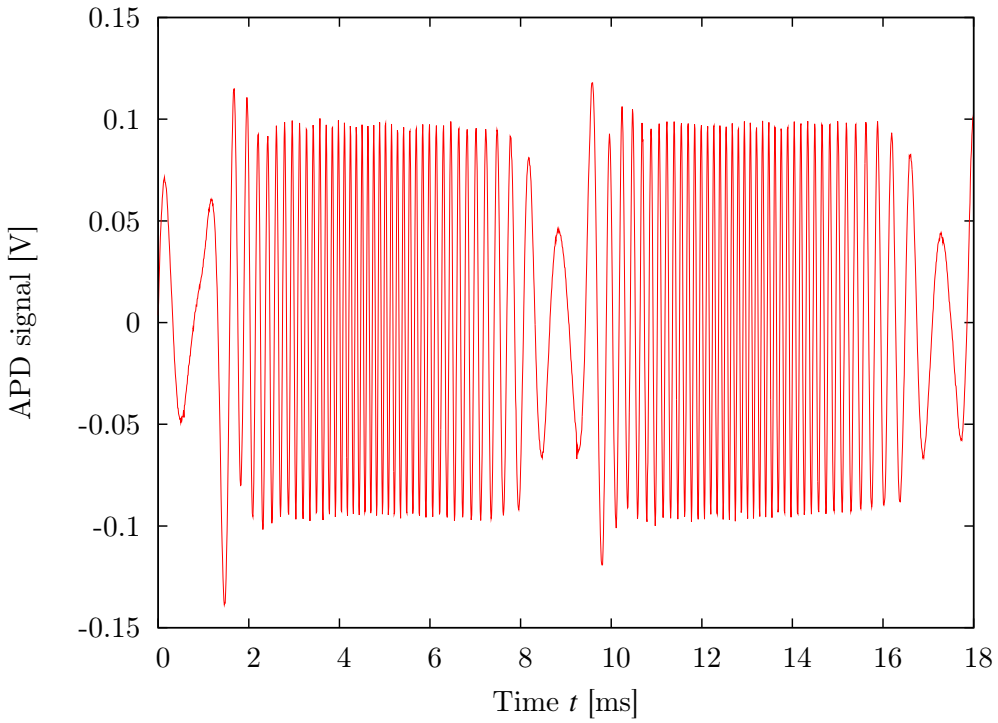

Fig. 9.2.: Typical signal of a drop oscillation obtained by interferometry. The distance $\Delta t \approx 17\,\text{ms}$ between the outer interferometry signal minima signifies one period of a droplet oscillation, which corresponds to a frequency $f_{\text{osc}} = 58.8\,\text{Hz} \approx 2f$, two times the excitation frequency.

10. Experiment automation & data acquisition

The experiment, except drop dispensing and drop position control, is completely automated via the software LabVIEW, developed by National Instruments, and a personal computer. The frequency generators TTi TG2000 for control of $U_1(\nu)$ and $U_2(f)$ are piloted via universal serial bus (USB). Data acquisition is done via a National Instruments BNC 2110 connector block on a National Instruments data acquisition card PCI-6014. Photos are taken via a LabVIEW driver and transferred to the computer using an IEEE 1394 (FireWire) connection.

10.1. Automation (stationary): *ExAcqT*

A LabVIEW program named *ExAcqT* is developed for the automation and data recording of the experiments. It facilitates the data recording and permits nearly complete automation of the experimental system. Several parameters are configured via its graphical user interface.

Concerning data acquisition, the sampling frequency may be chosen (default value 250 kHz), the time-out before each frequency measurement (default value 0.2 s) and the maximal amplitude for the APD signal (pre-defined to ±0.5 V). The sampling frequency is chosen according to the maximal amplitude at a given excitation frequency. The time-out serves to wait for the stabilization of drop shape oscillations, before measuring the amplitude by interferometry: as seen in appendix D on transient oscillations, a time of 0.2 s should be sufficient to reach the steady oscillatory regime. Note that the stabilization time scale of several seconds, depending on the oscillation mode number n, found by Kang [29], is theoretically demonstrated for a free spherical drop. This means that contact line friction and internal viscous dissipation of streaming flows are neglected. The maximal amplitude value for the avalanche photo diode is crucial for the precision after sampling the delivered voltage signal: the smaller this value is chosen, the higher the sampling precision will be. Care needs to be taken not to cut the APD output signal, which might exceed the given range by saturation. The choice of the range ±0.5 V is sufficient for a good balance between precision and signal amplitude. The usual, filtered APD signal does not exceed 200 mV. These parameters are not meant to be changed by the user, and are fixed for the entire measurement upon hitting *Start*. Additionally, measurement information may be included with each measurement. It may consist of supplementary information of practical interest such as the chip and electrodes in use, ambient temperature and humidity, measured liquid and any other information worthwhile to be noted, which is stored in a separate info file along with a second set of parameters.

A second set of parameters is defined for EWOD actuation, and may be modified by the user at each measurement and even on the fly, namely:

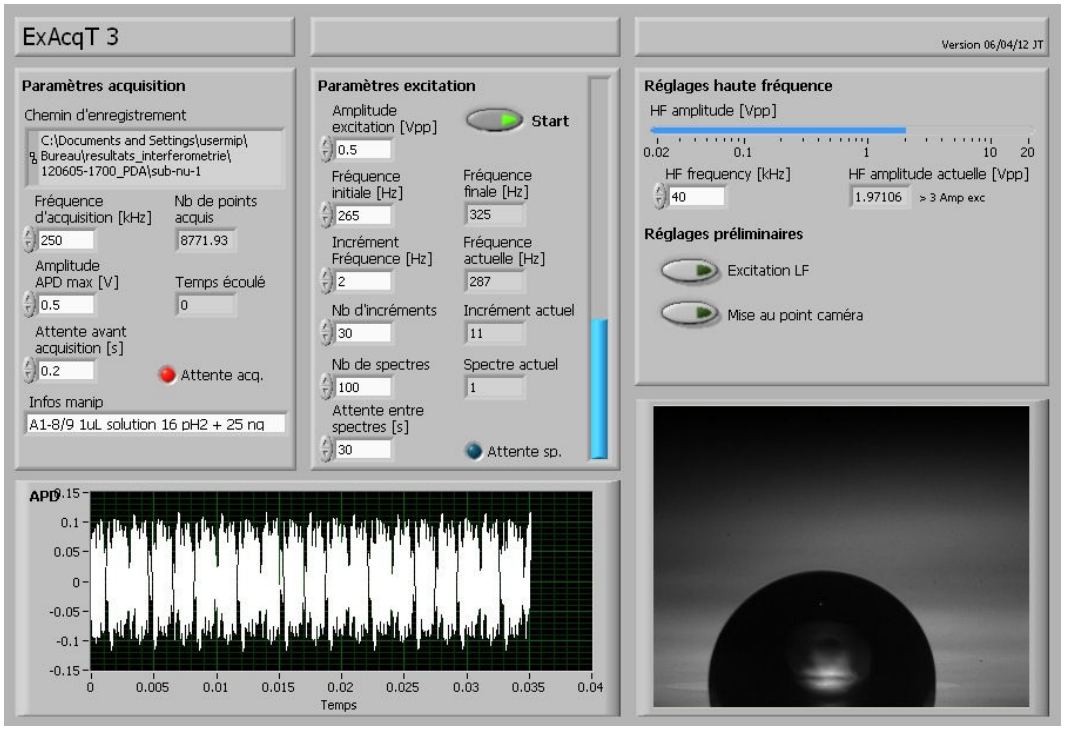

Fig. 10.1.: Graphical user interface of the LabVIEW program *ExAcqT*, developed for this thesis.

- Frequency ν,
- Amplitude of U_1 – drop surface curvature,
- Amplitude of U_2 – oscillation excitation & resonance control,
- Initial frequency, frequency increment, number of increments – spectrum parameters,
- Number of recorded spectra, pause between two spectrum recordings.

The excitation amplitude controls the amplitude of U_2 via the frequency generator. The initial frequency, its increment and the number of increments define the frequency range and interval, at which the amplitude of the drop oscillation is measured. This set of amplitudes constitutes one spectrum. The number of spectra is also determined by this set of parameters, as well as the lapse of time between two successive spectra, which may be used to adjust experimental parameters and the horizontal position of the drop with respect to the laser beam if required. This second set of parameters may be modified at each spectrum on the fly, which facilitates the readjustment of the measurement.

The option *Focusing* provides the user a fifteen seconds window to visually adjust the focusing of the camera prior to the measurement. The option *Camera calibration* measures the tilt angle of the camera. The blue vertical bar serves as visual count-up counter for the spectrum sweep and as count-down for the pause between two spectra.

A usual experiment starts by choosing the parameters for the measurement. The frequency range for the spectrum is determined via the frequency variables, as well as the time-outs and voltages. The experiment parameters may be entered into the *Measurement info* field. Using a micro-pipette, a drop is

positioned on the electrodes, which are under actuation, since U_1 is activated automatically by executing *ExAcqT*. The droplet will then spread on the electrodes with a contact angle, which may be modified by adjusting the amplitude of U_1. Upon hitting *Start*, the measurement begins by taking a picture of the droplet. Afterwards, the tension U_2 is activated to stimulate droplet oscillations with the initial frequency entered into the corresponding field on the second panel. The transition to harmonic oscillations is waited for, before starting the actual measurement by sampling the tension of the avalanche photo diode on the National Instruments acquisition card. The excitation frequency is then incremented until reaching the maximal frequency of the spectrum. For each interval, the transition time is respected. After the last measurement of the spectrum, the tension U_2 is cut and the contact angle may be readjusted. Before the measurement of a new spectrum, a picture of the drop is taken. After the last spectrum has been measured, or after the *Start* button has been released by a second click, a final image is taken, and the measurement infos are written into the info-file.

The info-file consists of all the parameters used for the measurement, and the time, frequency range and frequency intervals for each spectrum. Also the tensions U_1 and U_2 are noted for each spectrum. This file is used later on for the evaluation of the different oscillation signals by MATLAB, serving as correspondence between the APD voltage data and physical parameters.

10.2. Automation (transient): *ExAcqTrans*

A second LabVIEW program, *ExActTrans*, based on *ExAcqT* is developed, serving as experimental support for measurements of the transient regimes of drop shape oscillations. Only the second set of parameters (middle panel) is modified in order to correctly pilot the frequency generators:

- Frequency ν,
- Drop surface curvature amplitude of U_1,
- Oscillation excitation amplitude of U_2,
- Excitation frequency f,
- Pause between two recordings.

There are two main operation modes for choosing the excitation frequency f. Either f is entered by the user and may be modified between two measurements, or f is calculated by MATLAB in order to be close to half of the natural frequency (which is the resonance condition). In this case, the parameter for the excitation frequency serves as initial frequency and will be modified automatically during the measurement. This on-the-fly data evaluation and interaction between LabVIEW and MATLAB permits to adjust the experiment parameters for each single measurement. This is a very appreciated tool to follow the natural frequency without the constant manual adjustment of the parameters. This is particularly useful when trying to follow a quick shift of natural frequency.

In practice, a data file is created by LabVIEW for each measurement. Once the data file is written, the MATLAB routine is programmed to start the data

evaluation, which will measure the natural frequency of the signal. Afterwards, the next excitation frequency is written into a file in the actual LabVIEW working directory, which will be used for actuation of the next oscillation. Once all the LabVIEW recordings are finished, an end condition is written to MATLAB, which then creates a summary of the up to then evaluated results. More details on signal processing are given in the next chapter 11.

11. Signal processing: MATLAB

The signal processing is implemented in a MATLAB environment. Stationary and transient drop oscillation signals are evaluated regarding the oscillation frequency and amplitude. In the first case, a pre-defined part of the oscillation spectrum is measured via interferometry. For each frequency, a signal is recorded, serving to analyze the oscillation amplitude for the specific frequency. Information on the resonance behavior may be obtained by this technique. Transient oscillation analysis uses the decay of an oscillation with the natural frequency of the system, to analyze the resonance frequency.

Concerning the oscillation frequency, the same algorithm based on a Fourier transform is used for both types of measurement. The evaluation of the oscillation amplitude differs in the two cases: For stationary oscillations, the interferometry signal is frequency modulated by the drop surface velocity, which is used to calculate the oscillation amplitude. Hence, the oscillation amplitude is correlated to the maximum interferometry signal frequency. In the case of transient oscillations, the phase shift between the two reflections of the laser beam on the drop apex and on the substrate is evaluated. The phase shift can be related to the optical path between the two reflections, and hence to the droplet oscillation amplitude.

As far as the advantages and drawbacks of the two different approaches are concerned, the algorithm for stationary oscillations permits to measure the whole spectrum of droplet oscillations. Depending on the excitation frequency, each corresponding amplitude is evaluated. Thus, for each oscillation mode number, n, the corresponding resonance frequencies and full width at half maximum (FWHM) of each mode may be calculated. The algorithm for transient oscillations is used to calculate the natural frequency, corresponding to f_2, and the decay time, which may also be related to the FWHM. From a scientific point of view, the major difference between the two algorithms is the information on mode number > 2, which is not accessible via the transient analysis. From a practical point of view, the transient analysis needs much less computational resources, and is a much faster algorithm. The duration for a single evaluation is approximately 1 s, which permits rapid measurements while evaluating the results on the fly. This may be used to adjust the excitation frequency right away in the range of the natural frequency and to characterize rapid physicochemical processes.

11.1. MATLAB routine for stationary signal processing

Before each measurement, a time of 0.3 seconds is respected for acheiving the stedy state of drop oscillations. The interferometry signal is then recorded for the

duration of 10 periods of AC actuation, which corresponds to 20 drop oscillation periods. The data is subsequently prepared for post-processing in MATLAB to calculate the oscillation amplitude as described in section 9.2.

To each frequency in the range of the spectrum, a processing algorithm is applied, which can be divided roughly in three parts: preparation of the signal, determination of the oscillation frequency and phase shift in comparison to the electrowetting voltage U_2.

In the first part of the routine, standard parameters are defined and the sampling frequency is calculated. The high-frequency noise of the signal is suppressed by eliminating low-amplitude frequencies in the high-frequency part of the spectrum via FFT. The high-frequency part of the spectrum is defined via the power spectral density, as the frequency range above the last significant frequency. In the second part, the interferometry signal is derived with respect to time. Its absolute value will be zero when the drop surface is at rest (no frequency modulation) and it will be positive, when the surface is moving. After performing a Gaussian smoothing of the derivative, the excitation frequency is estimated via FFT. With this approximation, a second FFT may be performed giving a more accurate result for the excitation frequency. Furthermore, the phase shift between excitation and oscillation signal is calculated, in order to separate the interferometry data in 20 half-periods. In the third part of the routing, the amplitude is calculated via FFT for each oscillation half-period: For each data, an FFT is applied to determine the maximum frequency of the interferometry signal, translating the velocity of the drop surface. The maximum frequency is then used to calculate the oscillation amplitude for the actual half-period. By averageing the twenty calculated oscillation amplitudes the final oscillation amplitude for a given frequency is obtained. This algorithm is applied to the whole data set of the spectrum. On this basis, the resonance frequency is determined.

11.2. MATLAB routine for transient signal processing

This routine, devoted to signal processing of transient drop oscillation signals, may be divided into three parts. The first two parts are the same as for stationary analysis, only the third part changes. Attention needs to be drawn to the point, that what was described in the previous section 11.1 as the excitation frequency, is the natural frequency of free decaying drop oscillations for the transient analysis. After determination of the natural frequency and the phase shift in the first and second part of analysis, the signal is divided into half-periods. For each of these half-periods, the local extrema due to sweepings of the optical path are counted and weighted by the absolute value of the voltage amplitude, $|U_{\mathrm{APD}}|$, delivered by the APD:

$$\zeta_0^j \propto \sum_{i=1}^{N} |U_{\mathrm{APD}}|\, \delta_{t,t^i},$$

where N is the total number of local extrema contained in one half-period of oscillation, which corresponds to one burst, ζ_0^j is the oscillation amplitude

calculated from one given burst j, the index i designates the ith extremum during this burst, and δ is the Kronecker symbol, t is the time and t^i is the time corresponding to the ith extremum. The time-dependent amplitude is then fitted to an exponential curve, whose decay rate is used for the friction coefficient analysis. The data used for the fit are the data beginning at the first data point with amplitude ζ_0^1, and ending at the first data point with an amplitude smaller than $\zeta_0^{j^*} = 0.1\,\zeta_0^1$. This threshold is chosen to diminish the influence of the noise at low oscillation amplitudes on the fitting. Please refer to appendix D for an application of this methodology and an example of a transient interferometry signal.

12. Impact of the silicone oil film on interferometry measurements

Oil films or oil baths are a popular means in electrowetting applications for lubricating droplet motion, inhibiting evaporation, or surrounding droplets by a liquid phase [10, 16, 65–70]. A first insight into electrowetting-induced destabilization of a silicone oil film was found by Staicu and Mugele [71]. They discovered that a water drop in a silicone oil bath, actuated by electrowetting, will entrap a thin oil film between the underlying solid substrate and the aqueous phase. In order to investigate the impact of the electrowetting voltage on the draining of the oil film, they use a wire-in-drop geometry. The voltage is increased with different ramp speeds, $\mathrm{d}U/\mathrm{d}t$, and the thickness of the oil film is measured by evaluating the Newton rings, created by the variable oil film thickness and the interference of the observed light. The draining of the oil film increases the slower the electrowetting tension is applied, which means that slow voltage ramp speeds will favor a thin oil film thickness. Subsequently, the oil film will destabilize in the form of microscopic droplets due to van der Waals interaction between substrate and water. The size distribution of the instability depends on the thickness of the entrapped oil film and the applied electrowetting voltage.

12.1. Description & origin of the phenomenon

In this chapter, a different phenomenon in relation with electrowetting is examined briefly. A silicone oil film is deposited on the EWOD substrate: A several micro-litre sized oil droplet (silicone oil Fluka AS4, viscosity 6 mPa s) is brought into contact with the SiOC-surface and dispersed all over it. After draining, the formed film is about several hundred nanometers to one micrometer thick [62]. This oil film is influenced by a difference of electrical potential between the two electrodes: an electrowetting phenomenon similar to water is generated and causes the film to oscillate vertically with an amplitude of less than some hundred nano-meters, depending on the actuation voltage and frequency. The oscillation may be detected, but not quantified, by means of interferometry with the actual laser ($\lambda = 532\,\mathrm{nm}$). As experiments suggest, the oscillations are closely localized at the electrode gap. The purpose of this chapter is purely practical, to find a quick and purposeful solution to a measurement problem. It is not meant to be an elucidating work on electrowetting of entrapped oil films.

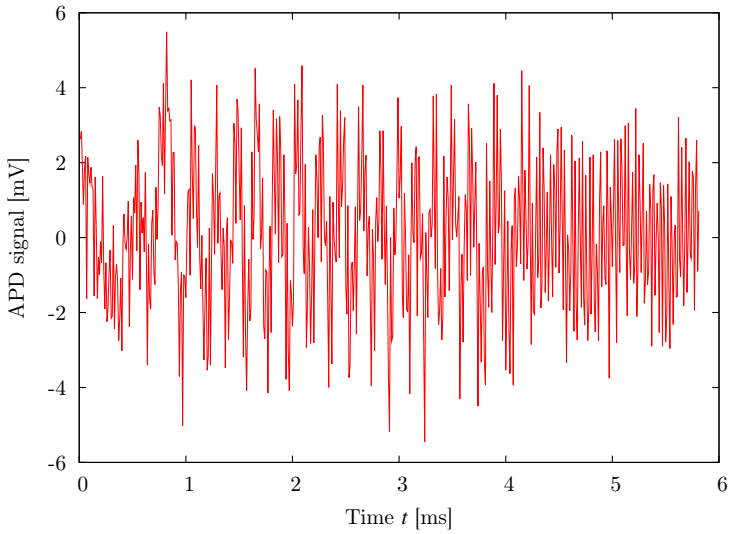

Fig. 12.1.: Interferometry signal of a 2 µL-droplet oscillation on a silicone oil film with a voltage actuation of 71 V_{rms} at 15 kHz and with a 100 Hz modulation. The droplet oscillation signal is perturbed by a 15 kHz signal. This signal is investigated without droplet in Fig. 12.2.

12.2. Impact of oil film oscillations on interferometry measurements

Interferometry measurements are effectuated on the drop apex for several reasons (cf. chapter 9 for further details). To realize the interferometry measurement, the laser beam needs to be precisely aligned with the apex region perpendicular to the substrate, in order to capture beam reflections along the optical axis. This makes that usually, the laser beam is also precisely focused on the electrode gap where the oil film oscillations take place, as the droplet straddles the two electrodes due to electrostatic energy reasons. Due to the precision of the interferometry method in combination with the exact alignment of the laser beam with the symmetry axis of the droplet, three reflections of the laser beam are captured in the avalanche photo diode: the reflection on the air-water interface (drop surface), the reflection on the water-oil interface and the reflection on the oil-substrate interface (wetting plane). The technique bears no way of distinguishing between an interface movement on the first or the second reflection. Since both interfaces are in movement, the measured interferometry signal will be a modulation of the two signals: exploiting the interferometry measurement seems to be impossible (cf. Fig. 12.1). As an example, Fig. 12.2 represents an oil-film-oscillation conditioned signal without drop. The actuation frequency of $\nu = 15\,\text{kHz}$ as well as the low frequency modulation of $f = 100\,\text{Hz}$ are present in the interferometry signal.

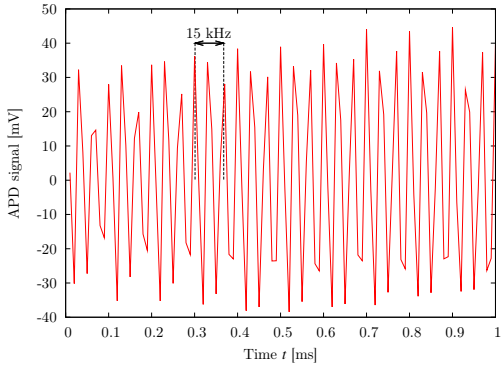

(a) High frequencies are perfectly in par with the 15 kHz HF voltage. Slight deviations might be due to the 100 kHz sampling, which is a little low for a 15 kHz signal.

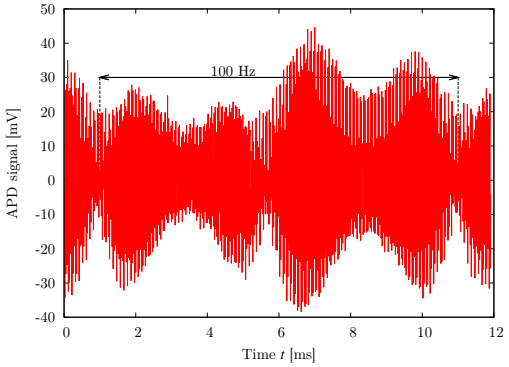

(b) The low frequency modulation of 100 Hz is also found in the interferometry signal. The quadruplication of the periodicity is due to the electrowetting mechanism: An interface moves four times during one period of electrical excitation.

Fig. 12.2.: Interferometry signal of an oil film without drop with a voltage actuation of 71 V_{rms} at $\nu = 15$ kHz and a $f = 100$ Hz modulation.

12.3. Signal quality dependence on frequency ν and on gap width

In order to diminish the impact of the oil film actuation on interferometry measurements, several solutions are conceivable. Here, the dependence on the frequency ν and the local measurement are considered.

It is found that the amplitude of the oil film interferometry signal diminishes with higher frequencies (between 1 and 20 kHz, data not shown). This signifies a smaller amplitude of the oil film oscillations, and might be useful for suppressing the signal in comparison with the signal for drop oscillations. Above 20 kHz, the gain of the high-voltage amplifier diminishes drastically, which is in conflict with a proper electrowetting actuation.

Furthermore, the oscillations are found to be very precisely located in the vicinity of the electrode gap. The gap width is varied to find lower and upper limits concerning spatial extension of the phenomenon:

- 3 µm – 100 µm: The oscillations are measurable by interferometry on a narrow spatial extent coinciding with the electrode gap. The smaller the electrode gap, the more restricted is the phenomenon locally.
- 200 µm – 400 µm: The oscillations are still measurable, but this time on a narrow spatial extent along the electrode borders. In the middle of the electrode gap, no interferometry signal is present.

One may deduce that the oil film oscillations are present at a distance of about $\gtrsim 50$ µm off the electrode borders. This value is a roughly estimated order of magnitude for a silicone oil of a viscosity of 6 mPa s.

As demonstrated here, it is preferential to work with small gap sizes for interferometry measurements. The laser beam may be directed right besides the gap,

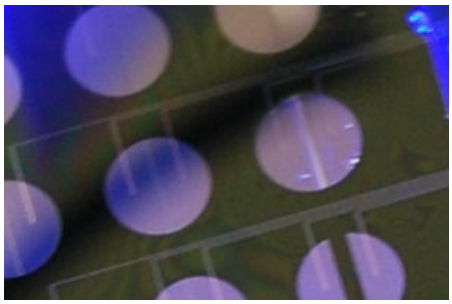

Fig. 12.3.: Modification of the oil film on the electrodes. Left electrode pair: 5 µm-gap electrodes without applied tension. Right electrode pair: 3 µm-gap electrodes at 71 V_{rms} at ν = 15 kHz. The oil film is modified at the electrode gap. The reflection of lighting is disturbed by electrowetting-induced actuation of the oil-air interface.

so that the laser beam and thus the reflection will not be in the direct vicinity of the oil film oscillations. When directing the laser beam away from the electrode gap, the influence of the interferometry signal due to oil film oscillations diminishes. This is the more efficient as the gap between the electrodes is small (cf. Fig. 12.4). In such a way, one may avoid to measure the oil film oscillations in addition to the droplet oscillations: The interferometry signal will be solely due to droplet oscillations. See Fig. 12.4 for the dependence of the signal quality on gap width. The reason why one may not use large-gap electrode pairs ($\approx$ 100 µm), is that the laser beam is too much dislocated when misaligning it strongly from the symmetry axis to have a good signal: the reflections will not be accessible to the avalanche photo diode as they will be strongly deviated by the droplet's interface and thus not captured by the microscope objective above the drop apex.

One might think about using electrodes with an even larger gap (200 or 400 µm), since the oil film oscillations do not reach the interior gap space. However, droplets on large gaps tend to lose their symmetrical form when subject to a radial Maxwell stress [31, 62], which is contradictory to the hypothesis of axial symmetric droplet oscillations made in order to apply Kang's theory [29]. Furthermore, the electrowetting voltage is less efficient for large gap sizes [31].

An interesting finding is that the oil film oscillations may even be experienced by the nude eye. By application of a tension (71 V_{rms} at 15 kHz) to the 3 µm electrodes, it can be observed that, at the gap, the oil film is modified. Figure 12.3 shows oil film covered electrodes, on the left a 5 µm-gap electrode without tension, on the right a 3 µm-gap electrode with applied tension. At the location of the gap, a surface modification is visible, since the reflection of the lighting is modified.

12.4. Possible remedies

There exist several possible solutions to the oil film oscillation problem:

- Interferometry measurements may be carried out besides the gap, but electrodes with a small gap width need to be used, more difficult and precise fabrication is needed. Furthermore, the laser beam needs to be misaligned, which are not optimal measurement conditions.
- Concentric circular electrodes may be used. The phenomenon will not be present on the spot for laser interferometry, since the electrode gap is circular and not located on the measurement area. The inconvenience is that the droplet is less confined horizontally due to a different electrowetting setup. It will be able to move more freely on the substrate, and measurements need particular surveillance for readjusting the drop position relative to the laser beam.
- Signal filtering may be effectuated at the actuation frequency ν, which must be chosen far below or far above the frequencies corresponding to measured drop resonance velocities. Though, the interferometry signal due to droplet oscillations might be deteriorated as well.
- A silicone oil of higher viscosity may be used to favor viscous dissipation of the oil film ripples.

The most rapid and highly efficient solution was to chose a 50 mPa s silicone oil (VWR Labopro), which is less influenced by the EWOD actuation due to viscous dissipation, in combination with a frequency of $\nu = 40\,\text{kHz}$ for U_1, instead of 3 kHz as previously intended. This reduces the oil film oscillation amplitude, the oil film oscillation signal is almost not present anymore in the interferometry signal. Due to the lowered gain of the high voltage amplifier at 15 kHz to 20 kHz, the amplitude of the input voltage U_1 needs to be adjusted.

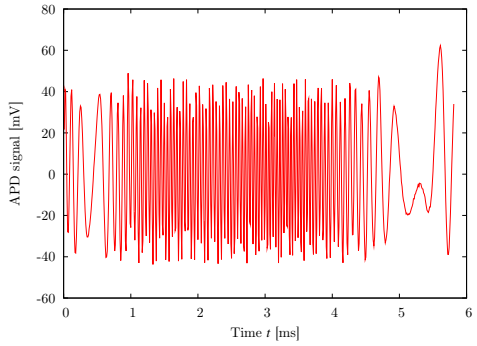

(a) Gap 100 µm, measurement on gap.

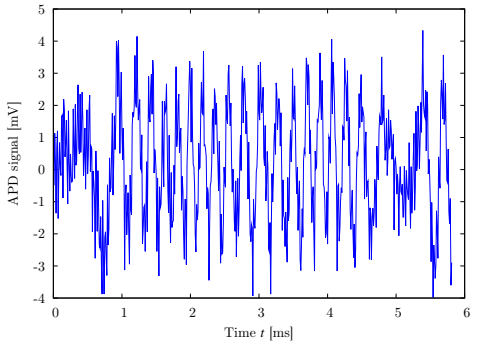

(b) Gap 100 µm, measurement besides gap.

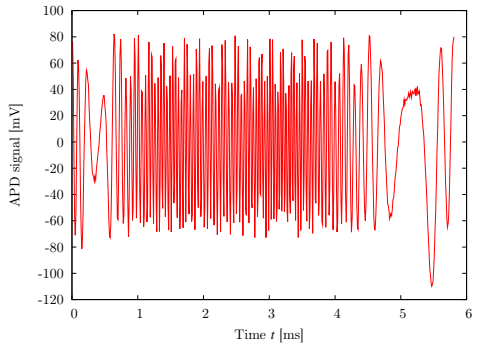

(c) Gap 10 µm, measurement on gap.

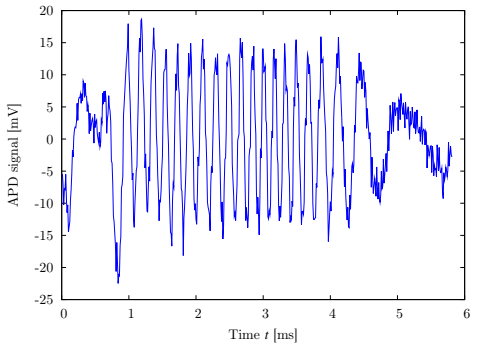

(d) Gap 10 µm, measurement besides gap.

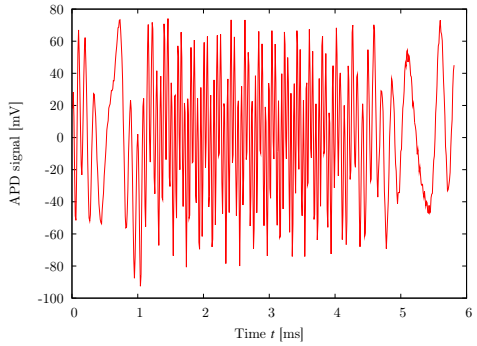

(e) Gap 5 µm, measurement on gap.

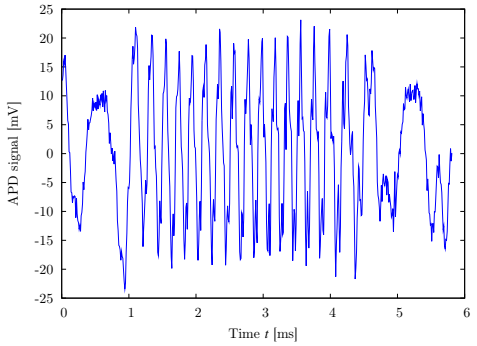

(f) Gap 5 µm, measurement besides gap.

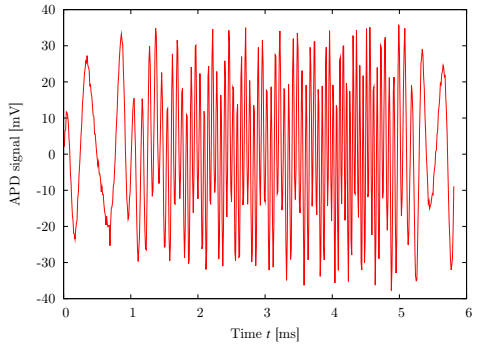

(g) Gap 3 µm, measurement on gap.

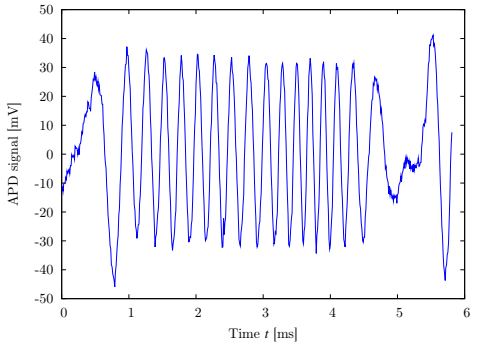

(h) Gap 3 µm, measurement besides gap.

Fig. 12.4.: Interferometry signal of a 2 µL droplet oscillation for a voltage actuation of 71 V_{rms} at 15 kHz and a 100 Hz modulation. Dependence on gap width.

13. Conclusion

During this thesis, a set of technical developments have been implemented, in order to realize a precise measurement for micrometric displacements of liquid-air interfaces, actuated by coplanar electrowetting on dielectrics. Three ingredients need to work together in order to realize this technique:

First of all, an electrowetting technique needs to be implemented to generate the interface movement. Thanks to our colleagues at LETI (CEA Grenoble), electrowetting chips of high quality could be used. An adapted chip support was developed, including a sophisticated voltage connector and imaging. Dual-frequency electrowetting was developed, allowing a precise control over contact angle and drop oscillations characteristics at the same time.

Second, a drop-adapted Michelson interferometer was conceived, allowing a locally precise measurement with micrometric resolution. Several instrumentation and measurement problems (e.g. the impact of the silicone oil film on interferometry measurements) needed to be addressed. With good calibration of the optical system and an adapted measurement device like the avalanche photo diode, it is possible to have very stable signals and reproducible results to characterize droplet shape oscillations. By this means, EWOD droplet oscillations could be analyzed and evaluated.

Last but not least, an adapted automation and signal processing setup needed to be implemented, allowing preparation, acquisition and evaluation of stationary and free decaying (transient) drop oscillation signals. LabVIEW and MATLAB served here as user-friendly and professional working environments able to manage all encountered situations.

For future work, small improvements might be worthwhile thinking about. Up to now, the droplet is able to move on the substrate along the interelectrode space (especially due to the lubricating oil film), only stuck by the energy minima over the electrodes in one direction. These movements are small, but hinder a proper interferometry measurement without realigning the drop symmetry axis and the laser beam every couple of minutes. A particular help would be to fix the droplet in one position in order to minimize the up to now necessary adjustments of the drop position via the translation stages, even if they are minuscule. One means of doing this is to divide the electrodes in four equal quadrants in contrast to the up to now used two halfmoons. This would restrain the transversal drop motions in two directions, thus fixing the drop at a precise position on the solid substrate. The interferometry measurement would not need any more attention despite at the beginning of an experiment. However, this means producing new electrowetting chips, which is a rather big financial effort. At the same time, one might think about leaving the central point of the motif without electrode to create a measurement site, which would resolve the problem of the oil film signal, which would not affect electrowetting performance. By adapting the

reflectivity of the substrate at this point (by deposition of a particular material with a certain reflectivity), the sensitivity of interferometry may certainly be ameliorated.

Part IV.

Evaporation Measurements

The theory and technical developments, presented in the previous parts II and III, are put to the test in this part of the work. An academical example of evaporation measurement on a sessile drop is chosen to validate the dependence of resonance spectrum of drop shape oscillations on the radius R of a sessile drop. As evaporation proceeds, the radius will diminish and thus the spectrum of oscillations will be affected. Doing this, the experimental setup, automation, data acquisition and signal processing will be used for real experimentation. In order to comply with evaporation theory, dual-frequency electrowetting is used and the contact angle of the sessile drop is controlled.

This approach does not only serve as a validation for the above cited aspects. It is also devoted to developers of microsystems using electrowetting on dielectrics, which are concerned by evaporation of drops inside their systems. Often it is not easy to characterize evaporation in such systems, as they usually use multi-drop environments, which most of the time are conceived as a closed geometry. Interferometry measurements in combination with electrowetting-induced shape oscillations as a transduction mechanism, represent a means of non-intrusive, non-imaging measurement of evaporation in open and partially or fully closed systems. To demonstrate the feasibility of this approach, the following chapters will discuss the theory of evaporation, and its application to evaporation of a single drop in a microsystem (chapter 16) and in a multi-drop environment (chapter 17). In chapter 17 on multi-drop environments, emphasis is put on the aspects of vertical confinement, drop position within the drop array and inter-drop distance.

14. Electrowetting as transduction mechanism

Microfluidic applications using the electrowetting technique [28, 65] for displacement of droplets [23, 32] are subject to a number of difficulties: contact line friction during displacement [43, 44, 72], surface contamination by biological species (bio-fouling) [73, 74] and evaporation [75], which is obviously not shared with micro-channel microfluidics [16]. This last issue is one striking reason why, typically, in digital microsystems for bio-assays, drop evaporation needs to be controlled by means of imaging techniques: the time-dependent profile of the drop is recorded, wetting radius and angle of the drop are extracted, and the data are compared to the available theory.

The aim of this part is to furnish a fully integrated methodology for drop evaporation gauging within an automated digital microsystem. Among important objectives, there is the essential need to avoid drop imaging and to address open and covered microsystems. Among typical non-imaging techniques for monitoring the evaporation of sessile drops, there is, for instance, the well-known quartz crystal microbalance (QCM), which is able to measure the mass variation of millimeter sized drops [76, 77]. A different technique to monitor the evaporation rate of minuscule droplets in the 1 μm range was presented by Arcamone et al. [78]: a microresonator is used to transduce the mass change into a frequency variation in a MEMS system. This method also bypasses imaging analysis. Another method uses a cantilever sensor developed by Liu and Bonaccurso [79], which is a non-imaging technique able to measure mass, radius and contact angle simultaneously. This method is adapted to one micro-meter sized sessile droplet (diameter between 20 and 80 μm of pure liquids and mixtures). A further non-imaging technique is developed by Gong and Kim [80], making advantage of the capacitance measurement of a droplet in a capped lab-on-a-chip between top and bottom plates. By deducing the foot print area of the drop, its volume may be estimated. Concerning digital lab-on-a-chips, the QCM and the capacity measurement can be easily integrated in state-of-the-art systems. These two techniques are at the same time adapted to common droplet volumes for lab-on-a-chips. For a summary of the above methodologies, please refer to table 14.1.

In this chapter, a new methodology is presented, based both on electrowetting on dielectrics (EWOD) as a transduction mechanism, and interferometry, to measure evaporation of a sessile drop, with a volume ranging between 0.5 and 10 μL, typically. Here, our methodology is compatible with configurations of variable confinement (open, partially or fully closed systems) provided that the sessile drop remains free to oscillate.

A dedicated electrowetting chip with coplanar electrodes [32] is developed. Hydrophobic and dielectric layers on the electrodes acting in combination with

electrowetting enable monitoring of an effective wetting angle for an aqueous drop at a constant value of $\theta = \pi/2$ during the entire evaporation process. The drop is then made oscillate by perturbation of the actuation voltage between the buried electrodes. The resonance spectrum of this capillary oscillation depends on the radius, which may be calculated progressively in the course of evaporation.

This technique offers the advantages of the QCM with respect to volume range, and is fully compatible with integration requirements for digital lab-on-a-chips, as well as offering the advantage of permanently adjusting the contact angle (at $\theta = \pi/2$ for instance, in this work) using electrowetting on dielectrics (EWOD) at a high frequency in AC mode (15 kHz). Therefore, the two classical evaporation regimes [81] can be applied: constant contact angle mode or constant contact radius mode. A more practical advantage compared with the imaging method is the possible measurement of evaporation in a confined environment with a drop distribution, which might hinder proper imaging. This situation is usually encountered in lab-on-a-chips, as parallelization of tasks is one of the main goals of these systems.

This work is focused on coplanar electrowetting of a sessile drop in contrast to a setup with needle [29] or catenary [30] counter-electrodes, for both of which an interferometry measurement would be impossible. The coplanar electrode configuration is also a reference configuration for development of EWOD-based lab-on-a-chips. In this case, the imaging method is nevertheless developed for purpose of validation of our methodology. Drop shape oscillations, and the subsequent capillary resonance induced in low-frequency EWOD regime, are observed to form a convenient transduction mechanism for gauging evaporative mass transfer. As regards bioassay applications for instance, the need should be pointed out for controlling drop solvent quantities when performing chemical reactions. This is particularly relevant when chemical and evaporation kinetics are of the same order.

The contact angle is tuned by the high frequency voltage U_1. The purpose of working with a dual-frequency actuation is that its amplitude may be used to tune the contact angle (for instance $\theta = \pi/2$) in a range, which depends on composition of the underlying substrate. Due to the minimization of electrostatic energy, voltage contribution U_1 means that the droplet straddles the underlying electrodes [32], making droplet position far more stable than in standard geometries. Therein lies a second feature of prior importance, since interferometry measurements on a curved surface require a high degree of local accuracy to be feasible. Voltage modulation U_2 is characterized by a low frequency in the range of $f \sim 10 - 1000$ Hz. This voltage is used to oscillate the contact line of the drop radially, otherwise stabilized in position, and therefore to induce drop shape oscillations of a frequency $f_{\text{osc}} = 2f$, thereby controlling a capillary wave network along the drop surface. As demonstrated later on, from a change in the frequency f, it is easy to select capillary resonance with a given set of spherical standing wave modes along the drop surface.

Technique, ref.	Transduction	Measurement	Drop vol.
QCM [76,77]	Quartz resonance frequency	Electrical	some μL
Microresonator [78]	Resonator frequency change	Electrical	aL
Cantilever [79]	Solid vibrations	Optical	fL
Capacitance [80]	Ring oscillator circuit	Electrical	some μL
This work:			
Dual-frequency EW	Capillary oscillations	Optical	some μL

Table 14.1.: Summary of different available mass/volume sensing techniques.

15. Evaporation theory

In this chapter, evaporation of sessile drops is presented from a theoretical point of view. It needs to be distinguished between different evaporation regimes, convective evaporation and diffusive evaporation. Convective evaporation takes into account phenomena like thermal convection in the ambient gas phase, or gas movement (wind). Here, emphasis is put on diffusive convection, which is based on the concentration gradient and subsequent diffusive transport of water vapor in the ambient gas phase. There are two important works concerning diffusive evaporation of sessile drops, the first was written by Picknett and Bexon [81], with a theoretical and experimental analysis, the second by McHale et al. [82], with a sophisticated experimental analysis for a non-wetting drop. In both works, emphasis is put on the distinction between two evaporation modes: a constant contact radius mode for which the contact radius does not evolve, and contact angle diminishes; and a constant contact angle mode for which the contact angle stays the same, and the contact radius decreases. McHale also comments on a mixed evaporation mode, which can be commonly found at the end of drop evaporation processes.

15.1. Diffusive evaporation of a single sessile drop at constant contact angle

Consider one single sessile spherical water drop with base radius $R_B(t)$ and curvature radius $R(t)$, whose initial value is R_0. Base radius and curvature radius are linked by the contact angle θ, $R_B = R \sin\theta$. Evaporation acts to downsize the droplet radially inwards with a constant contact angle. The volume may be characterized by the radius of curvature and a form factor F, depending on the contact angle, $V = \pi/3 \cdot FR^3$, where

$$F(\theta) := 2 - 3\cos\theta + \cos^3\theta. \tag{15.1}$$

The form factor expresses the volume for a sessile drop, such that $F(\pi) = 4$ for a totally hydrophoic or spherical drop, and $F(\pi/2) = 2$ for a half-spherical drop.

Water vapor diffusion is governed by Fick's law of diffusion transport, introducing the water vapor diffusivity, D_{vap}, and the water vapor concentration, c. The concentration gradient is denoted ∇c, and the mass flux of water vapor is characterized by $\boldsymbol{j}_w = -D_{vap}\nabla c$, directed radially outwards. The evaporative-driven mass transfer can be described by diffusion through the liquid-vapor interface,

$$\rho \frac{\mathrm{d}V}{\mathrm{d}t} = -D_{vap} \oint_s \nabla c \cdot \mathrm{d}\boldsymbol{S},$$

where $\boldsymbol{S}$ is the normal vector to the drop surface. The normal component of

the concentration gradient in the vicinity of the drop surface is approximated as $\nabla c = (c_0 - c_\infty)/R \cdot \boldsymbol{S}/\|\boldsymbol{S}\|$, which means that it is homogeneous all over the surface. The concentrations c_0 and c_∞ are the vapor concentration at the interface and far from it, respectively. The hypothesis that the concentration gradient may be approximated by the ratio of vapor concentration difference to the radius, is empirically justified, as demonstrated by numerical simulations and comparison with experiments of one single evaporating drop [75]. The integral reduces to:

$$\rho \frac{\mathrm{d}V}{\mathrm{d}t} = -D_{\mathrm{vap}} \oint_s (c_0 - c_\infty)/R \cdot \mathrm{d}\boldsymbol{S}.$$

By substituting $V = \pi/3 \cdot FR^3$ for the volume:

$$R \, \mathrm{d}R = -\frac{4D_{\mathrm{vap}}(c_0 - c_\infty)}{\rho F(\theta)} \, \mathrm{d}t,$$

the evaporation law for the constant contact angle mode can be found by integrating both sides of the equation:

$$R^2(t) = R_0^2 \left(1 - \frac{t}{\tau_{\mathrm{evap}}}\right). \tag{15.2}$$

The evaporation time scale is identified as $\tau_{\mathrm{evap}} = R_0^2 \rho F(\theta)/8D_{\mathrm{vap}}(c_0 - c_\infty)$. In the case of a half-sphere with contact angle $\theta = \pi/2$, the form factor reduces to $F(\pi/2) = 2$. The evaporation time scale for this special case is $\tau_{\mathrm{evap}} = R_0^2 \rho / 4D_{\mathrm{vap}}(c_0 - c_\infty)$. Typically, the characteristic evaporation time scale for a sessile drop of $\theta = \pi/2$ is found to be:

$$\tau_{\mathrm{evap}} \approx 1 \times 10^3 \, \mathrm{s},$$

for the following values: $R_0 = 1 \times 10^{-3} \, \mathrm{m}$, $D_{\mathrm{vap}} = 1 \times 10^{-5} \, \mathrm{m^2 \, s^{-1}}$, $c_0 - c_\infty = 0.01 \, \mathrm{kg \, m^{-3}}$ and $\rho = \rho_{\mathrm{H_2O}} = 1 \times 10^3 \, \mathrm{kg \, m^{-3}}$.

15.2. Negligible increase of the drop surface under oscillations

To estimate surface stretching due to EWOD-induced drop shape oscillations and its potential impact on mass transfer, a calculation is presented in this section for the deformation mode $n = 2$. Surface stretching induced by oscillating EWOD is found negligibly small, $\Delta S/S \approx 1 \times 10^{-6}$, where ΔS is the stretched surface area, and S is the surface area without oscillations.

Under the effect of surface oscillations, the liquid-air interface is stretched, and thus could offer more surface for mass transfer. Hence, evaporation kinetics may be enhanced from drop oscillations. To estimate the impact of drop shape oscillations, the analytic expression for the shape of a sessile droplet as given by Kang [29] could be considered, stating that the droplet shape $d(t)$ at a given

resonance frequency f_n is given by the coefficients v and a_n, and the Legendre polynomials P_n:

$$d(t) = R_0\left(1 + v\sum_{n=2}^{\infty} a_n P_n(\cos\varphi)\right).$$

When regarding the capillary spectrum and the importance of the resonance frequency, f_2, at mode $n = 2$, the amplitudes a_n for modes $n > 2$ are much smaller than a_2, making it possible to disregard those contributions and reduce the previous sum to its first element $n = 2$. To estimate surface increase due to shape oscillations, one may consider the maximum droplet amplitude measured by interferometry for this resonance mode, $va_2 = 3\,\mu\text{m}$. The area of the drop surface, S, may be calculated via the surface integral over the droplet hemisphere:

$$S = 2\pi\int_0^{\pi/2} d(\varphi)^2 \sin\varphi\,\mathrm{d}\varphi = 2\pi R_0^2\int_0^{\pi/2}\left(1 + \frac{va_2}{R_0}P_2(\cos\varphi)\right)^2 \sin\varphi\,\mathrm{d}\varphi,$$

which scales as:

$$S = 2\pi R_0^2\left(1 - 2.53\times10^{-6}\right).$$

This permits to calculate the relative surface stretching:

$$\frac{|\Delta S|}{2\pi R_0^2} = 2.53\times10^{-6}.$$

Hence, surface enhancement is found negligible for evaporation provided that oscillation amplitudes remain much smaller than the drop radius ($a_2^0/R_0 \ll 1$): this last criterion is by far compatible with classical abilities of interferometry.

16. Evaporation measurements on a single drop

This chapter addresses a method to estimate the size of a single sessile drop and to measure its evaporation kinetics by making use of both Michelson interferometry and of coplanar dual-frequency electrowetting. Beyond the aim to stabilize the position of the sessile drop, by using the high-frequency electrowetting voltage, the contact angle of the sessile droplet can be adjusted to permanently obtain a liquid hemisphere. This way, the experiments comply perfectly with the drop evaporation theory based on a constant contact angle [81]. Low-frequency modulation of the electrowetting actuation is applied to cause droplet shape oscillations and capillary resonance. Interferometry allows us to measure a time-dependent capillary spectrum, and in particular the shift of natural frequencies induced by drop evaporation. Consequently, diffusive kinetics of drop evaporation can be properly estimated, as demonstrated. Owing to the coplanar electrode configuration, our methodology can be integrated in open and covered microsystems such as digital lab-on-a-chip devices.

16.1. Materials & Methods

The drops with an initial volume of 4 µL are derived from ultra-pure water (resistivity 18.2 MΩ) and pure glycerol (99 %+, Alfa Aeser). One first solution (a) is pure water only, a second aqueous solution (b) contains 1/6 of glycerol by weight, and a third and last aqueous solution (c) contains 1/4 of glycerol by weight. The surface tensions are measured to be 57, 47 and 39 mN/m for solutions (a), (b) and (c), respectively. Surface tension measurements have been performed with the Wilhelmy technique using a NIMA tensiometer. Due to traces of contamination, surface tensions are found to be lower than those expected by theory. It is important to know the actual surface tension of the used liquids, in order to correctly calculate the drop radius from the resonance frequencies, equation (5.6).

The coplanar electrowetting electrode geometry consists of two half-moons with a 4 mm base width, separated by a 100 µm gap. This geometry is used for all the experiments of this chapter. The drops are deposited on the electrodes, which are covered by a very thin film of silicone oil (VWR Prolabo, viscosity 50 mPa s) to avoid stick-slip motion as well as an excessive value of contact angle hysteresis. The oil film after drainage is estimated to have a thickness of 260 nm (data not shown, refer to [33]). A droplet of oil is deposited on the chip, sponged up by a piece of paper (Whatman 3MM filter paper) and spread by striking gently with a finger protected by a latex glove for homogenization of the thickness (visible by Newton rings in reflected room light). The chip is then covered to protect it from dust.

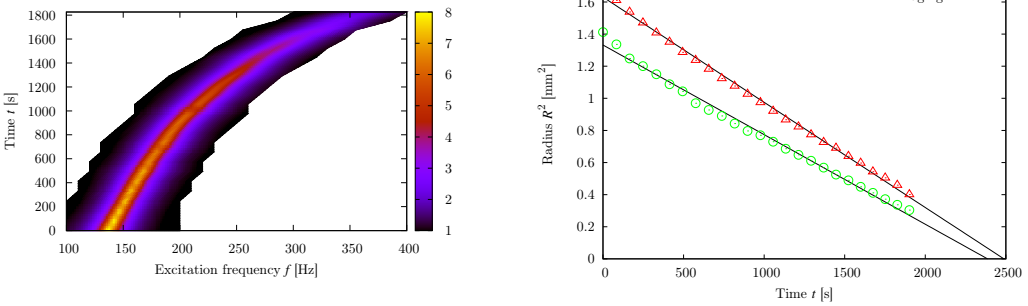

(a) The color coding represents the oscillation amplitude in µm at resonance frequency f_2, as measured by interferometry. The shift of frequency f_2 is due to the diminishing drop radius, as induced by evaporation.

(b) Comparison between imaging results (○, τ_{evap} = 2488 s) and interferometry measurements (△, τ_{evap} = 2386 s).

Fig. 16.1.: Evaporation of a 4 µL droplet for 47 minutes. Ambient temperature is 22.3 °C and relative humidity is 44.5 %.

16.2. Comparison between interferometry and imaging measurements

In Fig. 16.1(a), the evolution of the resonance spectrum is shown for a mode number $n = 2$. In the course of time, the drop radius diminishes under evaporation, and as a result, the resonance frequency, f_2, is found to increase. As detailed hereafter, the resonance frequency may then be converted into the droplet radius, as illustrated in Fig. 16.1(b), showing the evaporation-driven downsizing of a 4 µL droplet for 47 minutes at ambient temperature 22.3 °C and relative humidity 44.5 %. The red triangles in Fig. 16.1(b) show the experimental time-dependence of R^2, derived from the resonance frequency values f_2, as expected from the resonance spectrum (5.6), taking into account the modified eigenvalues for sessile drop resonance frequencies by Strani and Sabetta (cf. [42] and appendix C). This quantity is compared to image post-processing (green circles). A discrepancy between the two curves can be seen in Fig. 16.1(b). This discrepancy could be due to the correction factors introduced by Strani and Sabetta, and the existence of a mismatch between theory and experiment pointed out by the same authors [42].

A linear fit is applied to the experimental data on the square of the radius, which gives a typical value of the evaporation time scale, τ_{evap}. The evaporation time scales are found to be (2488 ± 31) s and (2386 ± 47) s from the interferometry and the imaging data, respectively, which represents a relative error of 4 % between the two methods. The given error is calculated from the expression $((\delta_{R_0^2}\tau_{evap})^2 + (R_0^2\tau_{evap}^2\delta_{\tau_{evap}})^2)^{1/2}$, where $\delta_{R_0^2}$ and $\delta_{\tau_{evap}}$ are the errors on R_0^2 and τ_{evap} for a linear fit of the data, respectively. The discrepancy between the imaging and interferometry measurements probably results from an error in the relationship $R(f)$, e.g. due to the theory of Strani and Sabetta for sessile drops, which may be

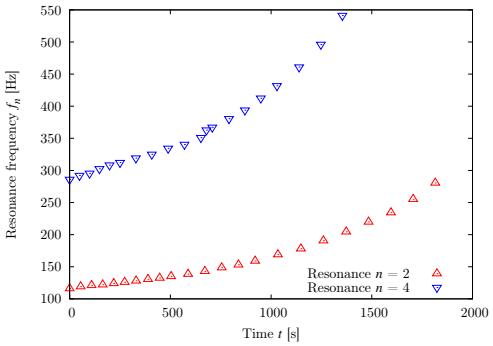

(a) Time dependence of the drop resonance frequencies f_2 and f_4 for the first two resonant modes, obtained using interferometry.

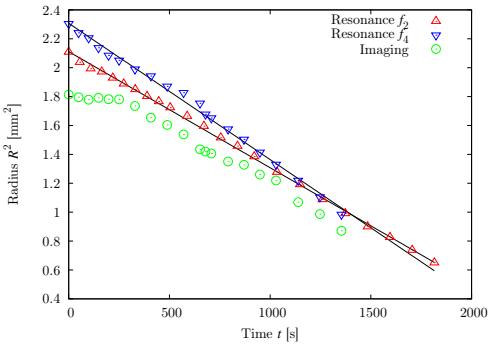

(b) The radius data is calculated for mode 2 (△) and mode 4 (▽), compared to imaging (○). The measured evaporation times are $\tau_{\text{evap},2} = 2627\,\text{s}$ and $\tau_{\text{evap},4} = 2445\,\text{s}$ for mode 2 and 4, respectively.

Fig. 16.2.: Evaporation of a 5 µL water drop for 30 minutes, measured on half-circular electrodes with a 4 mm diameter and a 100 µm electrode gap. The ambient temperature is 26.8 °C, and relative humidity is at 40 %.

calculated by equation (5.6). This error is quantifiable by:

$$\delta_{R^2} = \frac{4}{3} R^2 \frac{\delta_f}{f} \propto \sqrt{R}\,\delta_f.$$

This means that the error on R^2 scales with the square root of R, thus decreases as evaporation advances, which is the case as seen in Fig. 16.1(b): With diminishing value of R^2, the two curves (imaging and interferometry) converge to approximately the same value on the axis of ordinates.

A second measurement of the same type is demonstrated in Fig. 16.2, this time including two resonant modes, $n = 2$ and $n = 4$: Panel (a) shows the resonance shift in time of both resonant modes. The shift of f_4 is steeper than the shift of f_2, which is in par with theory, please refer to Fig. 5.3 on page 52. The calculated radius in panel (b) is compared to the imaging method. The results for the two modes are in good agreement compared to each other and compared to imaging. This graph is crucial for working in a higher resonant mode, which is more sensitive to variations of the drop radius, R. However, the quality factor, reciprocal of the width at half maximum of the resonant peak, is not as good as for the $n = 2$ mode, leading to a less precise measurement.

16.3. Water/glycerol mixtures

The evaporation curves for the three different solutions (a), (b) and (c) are measured for mode $n = 2$ and are displayed in Fig. 16.3. They are all non-dimensionalized according to R/R_0^{fit} and t/τ_{evap}, where R_0^{fit} is the initial radius of the fitted curve. Due to the non-dimensionalization, the three curves should match, a fact that is fairly checked. The evaporation time scales measured by

linear fitting are (a) $\tau_{evap} = (2488 \pm 31)$ s for pure water, (b) $\tau_{evap} = (3100 \pm 39)$ s for the 5:1 water-glycerol mixture, and (c) $\tau_{evap} = (3739 \pm 77)$ s for the 3:1 water-glycerol mixture. Ambient temperature and relative humidity values for the three different solutions are measured, respectively, 22.3 °C / 44.5 % for pure water, 23.2 °C / 43.5 % for the 5:1 mixture and 22.8 °C / 39.5 % for the 3:1 mixture.

16.4. Final remarks

In this section, oscillating coplanar electrowetting is proven to be a convenient transduction mechanism to measure evaporation kinetics of sessile drops. Drop shape oscillation frequencies are shown to convert a time-dependent radius into a resonance frequency shift, as illustrated in this case from the evaporation regime at constant contact angle. Furthermore, addition of a high frequency voltage, a regime that is referred to as dual-frequency electrowetting, allows independent monitoring of either the contact angle or the base radius.

As a means of drop shape oscillation detection, interferometry performed at the drop apex offers several advantages. In addition to accurate measurement of apex motion of the order of one laser wavelength, this technique is adapted to situations in which imaging could not be conveniently performed. For instance, the proposed methodology can be performed in confined geometries such as those in digital lab-on-a-chips. Moreover, it is possible to estimate the size of a drop (and therefore its volume) provided that the dependence of the contact angle on the EWOD voltage has been calibrated. More generally, this methodology can be used to measure the local impact of evaporation on a population of drops involved throughout the different processes developed in a digital microsystem based on electrowetting (cooling [83] or bio-sensing [84]). This approach will be further elucidated in the next chapter on evaporation-driven mass transfer in drop array environments.

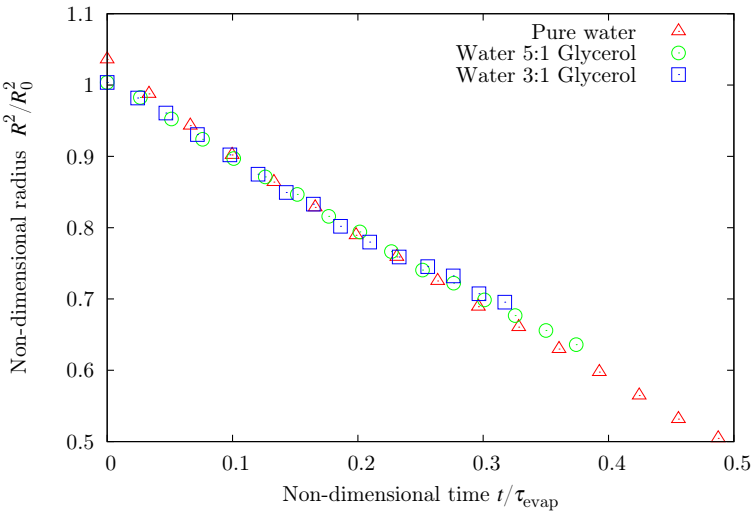

Fig. 16.3.: Evaporation of three different drops of initial volume 4 µL consisting of water and glycerol, as measured by interferometry (mode $n = 2$): (a) pure water (△): $\tau_{evap} = (2488 \pm 31)$ s, (b) water 5:1 glycerol (○): $\tau_{evap} = (3100 \pm 39)$ s, and (c) water 3:1 glycerol (□): $\tau_{evap} = (3739 \pm 77)$ s. Radius and time are non-dimensionalized by R_0 and τ_{evap}, respectively (Ambient temperature / relative humidity: 22.3 °C / 44.5 % for pure water, 23.2 °C / 43.5 % for the 5:1 mixture, 22.8 °C / 39.5 % for the 3:1 mixture).

17. Evaporation of a drop in a multi-drop environment

In the past years, more and more applications of digital microfluidics using electrowetting on dielectrics [28, 65] have emerged. Besides drop-based lenses [68] and displays [85], end-users of EWOD are lab-on-a-chips [84] or biological environmental monitoring [86]. More recently, new applications of electrowetting for PCR [87, 88] have been developed. A more recent application consists of a cooling methodology for active heat transfer management on processor units [83]. EWOD is also commonly used in digital lab-on-a-chips [16, 69]: Although a large part of bio-technological applications in lab-on-a-chips may be performed with silicone oil as a filler medium, some applications such as lyophilization or chemical noses still require an ambient gas phase [84]. For all these applications, evaporation is either not wanted, since there is the need to avoid mass loss, or deliberate since there is the need to gain benefit from phase change. In both applications, it is therefore important to control evaporative mass transfer.

Digital microsystems involve normally not only one single drop, as their strong point is the possible parallelization of multiple drops in a drop array, which makes it difficult to properly evaluate evaporation via methods based on imaging or microscopy [89, 90]. The impossibility of developing imaging is particularly important given that confinement is often deliberately intense for obvious reasons of miniaturization and portability. Brightfield imaging is the only practical way to obtain suitabe imaging of a time-dependent drop. This imaging technique is only practicable in completely transparent devices and for individual drop on which a non-obstructed view is possible, strictly limiting the choice of materials (e.g. ITO electrodes in combination with PDMS or glass walls) and thus LOC technology implementation. Furthermore the contact angle can not be monitored. An alternative methodology for non-imaging control of evaporation is capacitive gauging of drop volume in a closed, or sandwich, electrowetting setup [80, 91]. In the present work, the widely used sandwich configuration is not suitable, and a coplanar configuration is more adapted to different methodologies. Using coplanar electrowetting, it is shown how EWOD-induced drop shape oscillations can be provided and may easily be integrated in a closed or open microsystem [31].

In this chapter, the evaporative mass transfer of a drop in a microfluidics drop-array is investigated, as typically encountered in digital microsystems. Different patterns are proposed to compare the mass transfer of a droplet in the center or at the edge of a drop pattern. Furthermore, different confinements are studied to examine the effects of a reduced drop array volume. Last but not least, the inter-drop distance is varied, providing information on proximity effects on evaporation.

The methodology presented in this part is again based both on dual-frequency

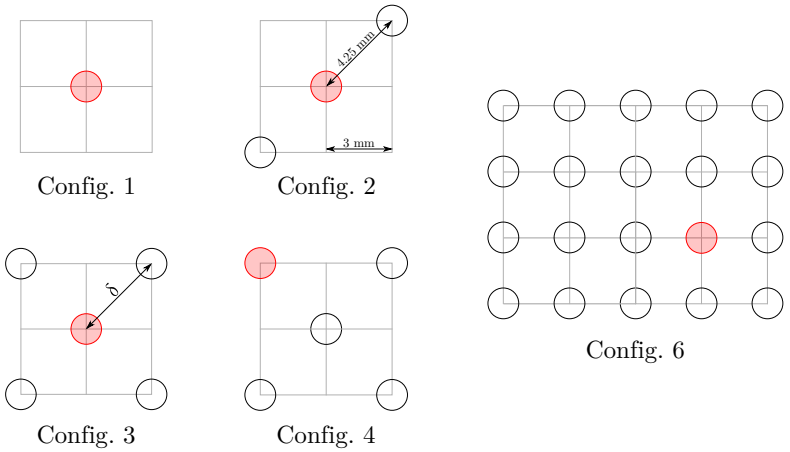

Fig. 17.1.: Sketch of the different configurations: a black blank circle corresponds to a sacrificial droplet, a red shady circle corresponds to the droplet being measured.

electrowetting and interferometry, similar to the last chapter, to measure evaporation of a sessile drop, with a volume ranging between 0.5 and 10 µL. A dedicated electrowetting chip with coplanar electrodes [32] is used, which can be easily inserted in microsystems devoted to drop PCR with thermal cycling [92, 93] or to PCB / PCU cooling.

17.1. Liquid and geometries

The drops with an initial volume of 1.5 µL consist of ultra-pure water (MilliQ-filtered water, resistivity: 18.2 MΩ cm). The corresponding radius of a sessile drop is $R_0 = 0.895$ mm for a contact angle of $\theta = \pi/2$. The surface tension is measured to be 57 mN/m. Surface tension measurements have been performed with the Wilhelmy technique using a NIMA tensiometer. Due to traces of contamination, the surface tension is found to be lower than the expected theoretical value.

In this chapter, the coplanar electrowetting electrode geometry consists of two half-moons with a 2 mm base width facing each other, separated by a 3 µm gap. The chip with the electrodes is positioned on a Plexiglas support, which can be covered by a Plexiglas lid (53×56 mm^2 bottom area, cf. sketch in Fig. 8.2(a) on page 67). The lid has an opening of 12 mm^2 above the measured droplet to allow the laser beam to pass. Into the lid can be inserted several slides of different thickness to adjust the vertical confinement.

Four confinements are tested: (a) no confinement (no lid), (b) a vertical confinement of 12 mm (lid only), (c) a vertical confinement of 6.5 mm and (d) a vertical confinement of 3 mm.

The drop arrays investigated are shown in Fig. 17.1: A single droplet, a line of three droplets and a die-like five droplets arrangement are chosen. Drop patterns under consideration are namely: (1) a single drop, (2) a line of three drops, (3) an array of five drops with measurement at the center, (4) an array of five drops with measurement at the corner and (5) a single drop surrounded by a U-shaped channel filled with water (cf. Fig. 8.2(a)5 on page 67). In addition,

Confinement			Inter-drop distance		
#	In mm	In units of R_0	#	In mm	In units of R_0
d	3	3.4	8	2	2.2
c	6.5	7.3	1-6	4.25	4.7
b	12	13.4	7	8.5	9.5

Table 17.1.: Confinement and inter-drop distances in units of R_0.

a drop pattern (6) is proposed: for the drop pattern (3), use is made of the U-shaped channel filled with water and moreover, sacrificial drops are added on the EWOD chip according to a 4×5 square grid with 3 mm side length to have an array of twenty drops on the chip (cf. Figs. 17.1 and 8.2(a)).

In order to estimate the impact of the inter-drop distance, δ, on evaporation, drop pattern (3) is modified by doubling and reducing to the half, the distance between the drops ($\delta = 8.5$ mm and $\delta = 2$ mm for drop patterns (7) and (8), respectively, instead of $\delta = 4.25$ mm for drop pattern (3)). The inter-drop distance and confinement values are converted into units of R_0 in the following table 17.1.

The drops are deposited with a micro-pipette on the substrate[1] and the lid is closed immediately. The ambient relative humidity and temperature (outside the lid) throughout the experiments are between 56 % to 60 %, and 25.3 °C to 26.8 °C, respectively.

17.2. Results & discussion

The different drop patterns, (1) to (8), are tested with different confinements, a to d, and the results are presented in Fig. 17.2 as well as in table 17.2 in terms of the evaporation time scale, τ_{evap}^{i-j}, with the superscripts $i = \text{a, b, c, d}$ and $j = 1, 2, ...8$ for designating the confinement and drop patterns, respectively. The curves are non-dimensionalized by the initial radius whose value is extrapolated by a linear fit of $R(t)^2$. A distinct decline of mass loss due to evaporation is demonstrated when diminishing the vertical confinement from no confinement to 5 mm (a to c). Beyond the confinement c, the slower evaporation rate is only significant for a small number of sacrificial drops.

Drop patterns and confinements: The comparison between drop pattern (3) with four sacrificial drops, and one single drop surrounded by a water bath (configuration 5), is only significant for low confinements (confinement a ($\kappa \to \infty$) and confinement b ($\kappa = 12$ mm)). In both cases, the water bath efficiency is not clearly demonstrated. For stronger confinements, water bath and sacrificial droplets nearly exhibit the same efficiency in preventing evaporative mass loss ($\tau_{\text{evap}}^{\text{d-3}}/\tau_{\text{evap}}^{\text{d-5}} = 1.3$).

The 20 drops-based pattern with water bath (d-6), which exhibits the slowest evaporation kinetics, has a six-fold slower evaporation kinetics than a single drop without confinement, $\tau_{\text{evap}}^{\text{d-6}}/\tau_{\text{evap}}^{\text{a-1}} = 6.3$. To consider the influence of the

[1] In this part of the work, no oil film is used for lubrication of the solid substrate.

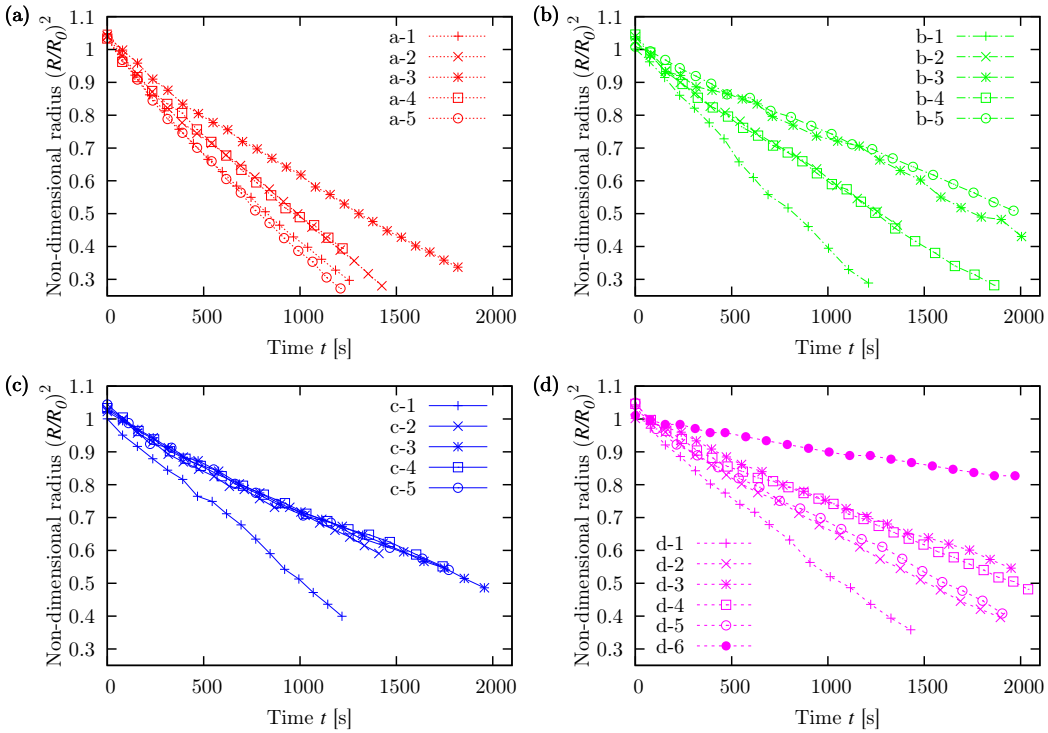

Fig. 17.2.: All evaporation dynamics at a glance: the confinement is distinguished by the letters a - d, the configuration by the numbers 1 - 6. For easy comparison, the axis scales are the same on all graphs.

relative position on evaporation kinetics, one may compare drop pattern (3) to drop pattern (4). For weak confinements (a and b), there is a great difference in evaporation kinetics, whereas for strong confinements (c and d), the relative position of the drop does not strongly influence mass loss.

Evaporation kinetics: Concerning evaporation kinetics of the different drop patterns and confinements, one recognizes two different kinetics during the measurement. The evaporation time scale τ_{evap} is inversely proportional to the slope of the R^2-curve, assuming that the evaporation law (15.2) is valid. The first data points in Fig. 17.2 exhibit a slope slightly steeper than the one for the last (majority of) data points. When placing the lid onto the support, the drops follow first a non-confined evaporation regime at ambient temperature and humidity, as long as the humidity under the lid does not change significantly. When the thermodynamical equilibrium is reached, the evaporation regime changes: the water vapor exchange at the liquid surfaces (drop(s) + water bath as far as configurations 5 and 6 are concerned) is equal to the water vapor exchange between the inside and the outside of the lid, through the 12 mm^2 hole. From our results, one can say that the initial evaporation regime is essentially characterized by drop pattern a-1. As the confinement and total initial water-air interface area is raised, the different evaporation kinetics will more and more tend to the kinetics of drop pattern d-6, which for the geometry of the confinement discussed in this paper, represents the slowest possible evaporation dynamics.

Patt. / Confinem.	a ($\kappa \to \infty$)	b ($\kappa = 12\,$mm)	c ($\kappa = 6.5\,$mm)	d ($\kappa = 3\,$mm)
1	1703	1653	2050	2161
2	1966	2530	3410	3034
3	2651	3610	3753	4192
4	1959	2519	3761	3897
5	1614	3998	3686	3215
6	–	–	–	10767
7	–	–	2494	–
8	–	–	4518	–

Table 17.2.: Evaporation time scale τ_{evap} [s] for all confinements, a to d, and drop patterns, 1 to 8, considered in this work.

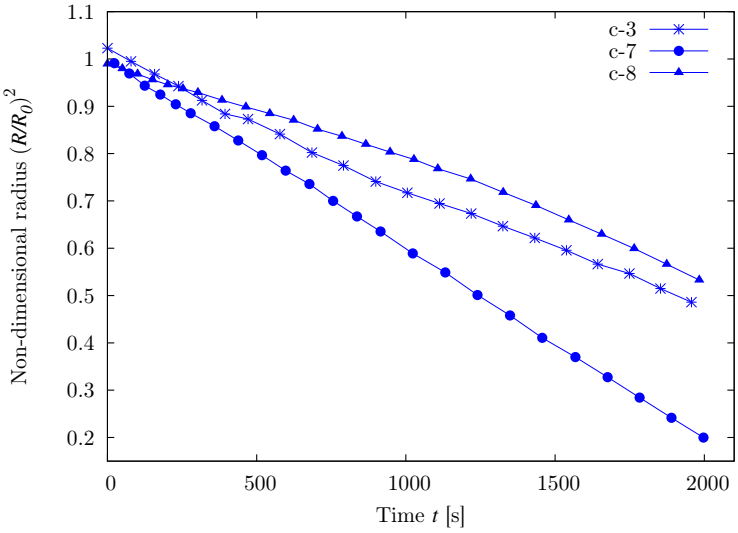

Fig. 17.3.: Evaporation dynamics for configurations 7, 3 and 8 for a confinement of 6.5 mm: The inter-drop distance is adjusted to 2 mm, 4.25 mm and 8.5 mm, respectively.

Role of the inter-drop distance, δ: Concerning the study on the impact of the inter-drop distance, one may refer to the drop patterns c-3, c-7 and c-8, represented in Fig. 17.3. In comparison to the initial drop pattern c-3, drop pattern c-7 exhibits a time-ratio of $\tau_{evap}^{c\text{-}7}/\tau_{evap}^{c\text{-}3} = 0.7$ (shorter evaporation time). Drop pattern c-8 exhibits a time-ratio of $\tau_{evap}^{c\text{-}8}/\tau_{evap}^{c\text{-}3} = 1.2$ (longer evaporation time). The inter-droplet distance, δ, thus impacts significantly on the evaporation time scale. This is though only true for a strong enough vertical confinement. In these cases, evaporation might be considered as being constrained to a horizontal 2D plane [94], which is a significant parameter for evaluating the effects of a modified inter-drop distance[2].

[2]Regarding applications of EWOD microsytems, the minimum inter-drop distance is delivered by the geometrical characteristics of the electrode matrix (electrode size and electrode gaps) or by the actual distance between droplets moving along the electrode paths. Hence, these distances are decisive parameters for evaluating the effect of evaporation kinetics of a drop array in a microsystem.

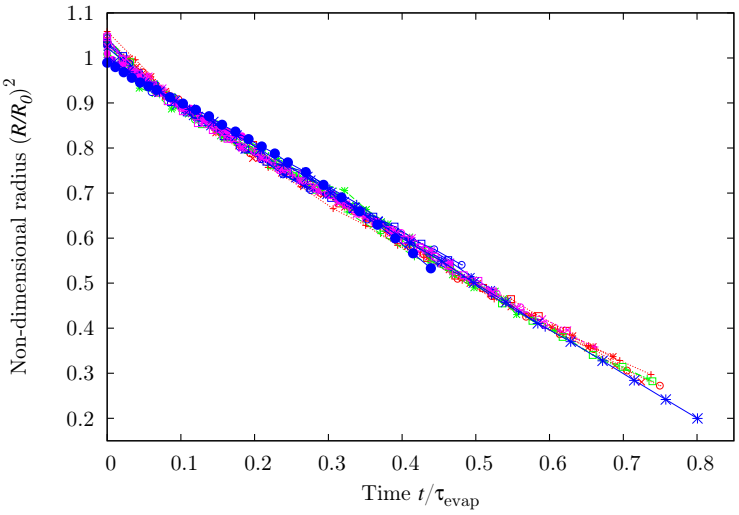

Fig. 17.4.: Presentation of all experimental curves in non-dimensionalized form.

Physical interpretation: Fig. 17.4 shows the totality of the evaporation curves, non-dimensionalized by τ_{evap} and the fitted initial radius. This graph shows that equation (15.2) is valid for describing the evaporation of a population of drops in our confined system. The law (15.2) for evaporation is based on diffusion kinetics of the water vapor in the ambient gas phase. This leads to the evaporation time scale,

$$\tau_{evap} = R_0^2 \rho / [4 D_{vap} (c_0 - c_\infty)]. \tag{17.1}$$

When the inter-drop distance is altered, the governing factor for changing the evaporation time scale is the ambient vapor concentration c_∞. This vapor mass concentration "far" from the drop surface is expected to increase when approaching the drops. It is necessarily calculated at mid-distance between two drops, as soon as the confinement is no longer the limiting parameter. As a result, $(c_0 - c_\infty)$ decreases and therefore τ_{evap} increases, according to equation (17.1). Conversely, c_∞ is expected to lower when increasing the distance between neighboring drops. Other factors like D_{vap} and c_0 should not be influenced so significantly.

17.3. Final remarks

Evaporation of drops in a microsystem can never be avoided since the volume can not be completely sealed with non permeable walls, for instance. This phenomenon is a key-issue for biological applications such as drop-based PCR with thermal cycling, for which the concentration of solubilized molecules and its dependence on evaporation must be anticipated.

Interferometry of drop shape oscillations sustained by dual-frequency electrowetting (DF-EW) has been shown to be a convenient measurement technique to capture the evaporation kinetics of a drop in a closed microsystem. In this

paper, the time-dependence of a half-spherical drop within a matrix of drops has been examined with respect to both the number of neighboring (sacrificial) drops and their proximity (inter-drop distance). The efficiency of limiting evaporation by making use of a water bath or sacrificial drops has been demonstrated to be dependent on the vertical confinement, κ. The even stronger influence of distance between drops, δ, has been evaluated for three different values. The impact of δ upon evaporation kinetics is significant, especially when the strong enough confinement gives rise to a quasi -two-dimensional evaporation process.

For slight confinements, the evaporation of a drop located at the edge of a five drop pattern is consistently found faster than the evaporation kinetics of a drop located at the center of the pattern. Conversely, for a strong enough confinement, the relative position of a target droplet (edge versus center) is no longer significant: all drops evaporate according to the same kinetics.

Finally, if the objective is to damp the evaporation process of one target drop, our experimental data suggest that the near presence of sacrificial drops must be preferred to the use of a liquid bath at a greater distance. As typical guidelines for end-users of digital microsystems, it is worthy to note that for biological applications with millimeter-sized drops, the confinement needs to be smaller than 6 mm, and any opening in the system leads inevitably to evaporation-driven mass loss, even for multiple drop patterns. For cooling applications involving phase change of millimeter-sized drops, the confinement should be at least 12 mm in order not to influence the evaporation kinetics and to have an efficient cooling effect.

The validity of the diffusive model developed originally by Picknett and Bexon for one single and isolated drop with constant contact angle, is extended here to the case of one target drop, again with a constant angle, selected among a population of drops and whatever the confinement is (cf. Fig. 17.4). This reveals to be an important finding for designers or end-users of digital microsystems. It is known that surface wettability is a determining parameter for the evaporation of a sessile drop [95]. In this chapter, only one contact angle, $\theta = \pi/2$, was studied, but it is easy to set another value of the contact angle by changing the high frequency voltage component of DF-EW. This ability of DF-EW delivers interesting outlooks for any other evaporation processes. Typically, the two classical evaporation regimes [81] can be applied: constant contact angle mode or constant contact radius mode.

As far as integration purposes are concerned, a practical advantage of jointly using interferometry and DF-EW is the possible measurement of evaporation in a confined environment with a drop distribution which might hinder proper imaging. This situation is usually encountered in lab-on-a-chips, as parallelization of tasks is one of the main goals.

18. Conclusion

The interferometry measurement of electrowetting-induced drop shape oscillations is applied to reflect the evaporation of a drop. Due to imperfections in the theory by Strani and Sabetta and subsequent biased errors, the measurement of the absolute drop radius is not perfect. On the contrary, a good accuracy is proven for the estimation of the evaporation time, that is, relative radius measurements.

The presented methodology is used all along this chapter to characterize evaporation in a drop array environment. Different aspects like inter-drop distance, confinement, drop number and drop position are investigated. In this regard, the developed methodology gives useful results and sufficient information is retrieved to characterize a digital system correctly. Guide lines for end users may be formulated.

In part VI, the same methodology will be extended to the measurement of surface ageing, characterized by a change of surface tension, caused by time-dependent adsorption of biomolecules [24, 96]. Therefore, the contribution of evaporation kinetics in equation (II.5.6) must be properly measured and subtracted. Also, the results will need to be interpreted carefully, as it is shown that the methodology is more appropriate for measuring relative changes of dynamic surface tension, than estimating absolute values. In order to prepare the measurements of surface tension, it is appropriate to have a look into theory on diffusion and adsorption, which will be done in the next part of this work.

Part V.

Chemical Transport and Surface Ageing at Drop Scale

This part represents the theoretical basis for the following experimental work on surface fonctionalization and biological assays. In order to have an idea, how biomolecules are distributed locally inside a droplet, diffusion as well as adsorption need to be considered, since biomolecules often exhibit surfactant properties. Here, the geometry is considered finite, in contrast to semi-infinite systems, which exhibit physical assumptions that no longer hold at microscale. Emphasis is also put on a time-dependent geometry, since evaporation can effect the experiments. The equations for diffusion and adsorption are discussed and solved for a spherical finite geometry to start with. The evaporation law (15.2) is taken into account via the boundary conditions. Because of the spherical symmetry, the mathematical problem can be reduced to a one-dimensional case. Three fundamental regimes are discussed, adsorption-limited, diffusion-limited and evaporation-limited regimes. The influence of different non-dimensional numbers, representing mixed regimes, is then investigated using a finite-element method. A major result of this work is the identification of the equilibrium surface concentration of a physicochemical system of finite size, which stands as an important parameter for design of a digital microsystem. It is found that by reducing the drop volume in a microsystem or emulsion, the total amount of solute particles is drastically decreased, in order to reach the same surface coverage as for a macroscopic system. This may be particularly important for applications using expensive solutes or solutes of time-consuming synthesis like e.g. poly-peptides. This equilibrium surface concentration is characterized by a non-dimensional number, ϵ_0, reflecting the ratio between solute molecules in the volume and adsorbed molecules at the drop surface. This non-dimensional number is defined and discussed throughout this part and constitutes a major mathematical help for analysis and distinction between macro- and microsystems. Finally, for the special case of adsorption-limited regimes, the model is extended to arbitrary contact angles, and thus to a symmetry, which is no longer spherical. This constitutes a clear-cut increased difficulty regarding the involved mathematics. In an adsorption-limited regime, in which molecular diffusion can be assumed instantaneous, this difficulty is avoided, and it is shown how an analytical solution can be found.

Besides constituting the theoretical basis for part VI on surface functionalization and biological assays, this investigation introduces new insights into physico-chemical microsystems concerned by diffusion and adsorption of surface active agents. After explaining some mathematical insights into symmetry and adsorption in spherical and hemispherical systems, a general solution for adsorption and diffusion is calculated for a finite-sized drop of time-dependent size. Usually, the time-dependence of geometry in physicochemical processes is neglected in research articles and scientific textbooks. Nevertheless it is very important for microsystems for two reasons: First, the involved volumes are small, normally smaller than $1\,\mu$L*, hence even surface ageing may have an effect on volume concentration. Second, the aspect ratio of microsystems (surface to volume ratio) is pretty high, which means that a change in volume has a strong influence on this parameter. Concerned systems are lab-on-chips for biotech-*

nology, affected (or not) by evaporation. In lab-on-chips for biotechnological applications, water drops in the femtoliter to microliter range are used.[1]

Chapter 22 on steady streaming current will enhance the foregoing theory to this physical mechanism. Streaming affects diffusion and adsorption in the volume and at the surface by convection of molecules. This phenomenon is not isotropic and hence needs a new implementation of the theory for numerical calculus. For diffusion-limited systems, steady streaming may represent an interesting mechanism for enhancing adsorption kinetics, a fact which will be discussed in this part of the work.

[1] Another domain concerned by these processes are emulsions, used e.g. in food processing and biotechnology. Ostwald ripening is a process which induces volume changes in emulsions: A mass loss of small particles of the dispersed phase is found in favor of bigger particles. Thus a change in volume and aspect ratio takes place, induced by either mass loss and mass gain, respectively.

19. Generalities

19.1. What does “finite system” mean?

In macroscopic physics problems, boundary conditions are often presented in an approximative fashion. For example in heat theory and heat transfers, when examining the heat dynamics of a cool chamber in a hot environment, the environment is supposed to be infinite, or of big enough size not to change its temperature when exchanging an amount of heat with the cool chamber. This facilitates the calculations in the way that the temperature at the walls of the cool chamber is supposed to be constant.

A different example is the active sensor surface of a biosensor, which may react with a solute in its reaction chamber filled with a reagent. The reaction of solute molecules with the active surface is supposed not to influence the bulk concentration of solute in the aqueous phase, far enough from the reactive surface. The bulk regarded as an infinite source thus supplies the diffusion flux in solute molecules without changing its concentration. This is obviously not correct from a physical point of view, but it reveals to be a surprisingly good approximation for macroscopic geometries.

In the last couple of decades, the miniaturization of experimental devices is more and more radical concerning many areas of applications. Nowadays, microelectronic devices become nanoelectronic devices, bioassays are no longer performed with instruments like micropipettes or microwells, but transferred into lab-on-chips of micro size. Along with this quick revolution of miniaturization come the corresponding characterization techniques, e.g. atomic force microscopy, optical profilometry, locale spectroscopy techniques and many others.

The evolution of theory and mathematical models for these domains needs to be incorporated as well. This means it is important to abandon certain well-known assumptions like nearly infinite heat or particle content, or concentrations that are not affected by heat exchange or reactions on surfaces.

The present work tries to promote the actual state of the art given in literature by enhancing the diffusion-adsorption model incorporating evaporation-driven mass transfer in a sphere. The “finiteness” of the problem is given by the ratio of bulk molecules over adsorbed molecules $CV/S\Gamma$, where C is the bulk and Γ the surface concentration for a volume V and a surface S. If this ratio is larger than unity, the situation is considered as macroscopic, the drop may mathematically be considered as a nearly infinite reservoir of surfactant molecules (classic case). Though it is considered microscopic for $CV/S\Gamma$ being smaller than unity. In this case, the adsorption of molecules at the air-water surface engenders a significant impact upon chemical diffusion within the drop: the surface concentration rises

and the bulk concentration in the center of the drop falls in order to sustain the adsorption flux at the interface. A dimensionless number, ε_0, permits to introduce the finite-size impact on drop ageing.

19.2. Surface active agents

Surface active agents, commonly called with their acronym "surfactants", are molecules acting on the surface tension of liquids, which explains their designation. Common examples of surfactants are fatty acids and lipids, which are amphiphilic molecules. This means that they contain both hydrophobic and hydrophilic chemical entities. They are composed in general of a hydrophilic head group and one or more hydrophobic tail groups, which makes them adsorb to a water/gas or a water/oil interface with the head in the aqueous phase, and the tail in the gas or oil phase. "Classic" surfactants like fatty acids and lipids are classified either by the tail composition, or by the head composition. The tail composition can consist of hydrocarbons, alkyl ethers, fluorocarbons or siloxanes. The more common classification is though according to the head group. It is then distinguished between ionic and nonionic surfactants. Nonionic surfactants, like Triton X-100, polysorbates (Tween), polyethylene glycol (PEG) and poloxamers (Pluronics), have a charge-free head group. Ionic surfactants are further classified by the nature of the head charge:

- Cationic surfactants: positively charged head group (e.g. cetyl trimethylammonium bromide (CTAB))
- Anionic surfactants: negatively charged head group (e.g. sodium dodecyl sulfate (SDS))
- Zwitterionic surfactants: zero net charge (e.g. amino acids)

The charge of a surfactant usually depends on the ionic content of the aqueous solution, notably the pH value. Via the ionic content of the solution, the amphiphilic capacity of a surfactant may be influenced, which determines its capacity to adsorb to interfaces. This makes it act more or less on surface tension. Among other biological molecules, proteins also have surfactant properties, but the different hydrophilic and hydrophobic groups are not as easily classifiable as with "classic" surfactants. The difference of pH does not only act on the charge of proteins, but also on their conformation.

Due to their amphiphilic character, surfactants have a rather strong influence on surface tension. In general, a surfactant contaminated water interface experiences a reduced surface tension. This behavior is described by the so-called adsorption isotherms which represent the dependence of the surface pressure, $\Pi := \gamma_0 - \gamma$, on the molecular area at the interface, A [m^2/molecule]. The surface tension, γ_0 [N/m], is the surface tension for a clean surface ($A \to \infty$). As the surface concentration of surfactants, Γ, at the air/liquid interface rises, the molecular area shrinks and γ will fall, the surface pressure, Π, will rise.

The surface tension is linked to the surface concentration of surfactants via the Gibbs Law, valid for isothermal processes:

$$\Gamma = -\frac{C}{RT}\frac{\partial\gamma}{\partial C}\Big|_T,$$

where R is the gas constant and T is the temperature. With a second equation, a constitutive law for the ad- and desorption process, $f(C,\Gamma)$, the surface tension at equilibrium may be evaluated. The equation emerging out of the combination of the Gibbs law and the constitutive law for ad- and desorption is called Gibbs isotherm (called isotherm, since it is an isothermal process). It relates the volume concentration, C, and the surface tension, γ.

In contrast to the Gibbs isotherm, which describes equilibrium values of surface tension, the constitutive law may also be used to evaluate dynamic surface tension values due to surface ageing. The role of the constitutive law will be explained in the section on adsorption and desorption.

A modified surface concentration of surfactants, Γ, is also linked to the contact angle, θ, of a sessile drop. As surfactants lower the surface tension γ of the liquid interface, the contact angle will evolve according to the Young law:

$$\gamma_{\mathrm{LG}}\cos\theta = \gamma_{\mathrm{SG}} - \gamma_{\mathrm{SL}}.$$

Here, the surface tensions $\gamma_{\mathrm{LG}} = \gamma$ and γ_{SL} may be influenced by Γ, depending on the affinity of the solute surfactant species.

In this work, the influence of surfactants on surface tension is used to characterize dynamic surface tension via the resonance shift in the droplet oscillation spectrum. This is an indicator for the successful surface functionalization. Usual methods, such as pendant drop tensiometry or the Wilhelmy plate technique can not be recommended at the scale of microsystems. Please refer to appendix E for a review of these two techniques.

20. Case of a free spherical droplet

Surface ageing of drops is of prior importance for a variety of applications involving liquid aerosols, emulsions or lab-on-chips based on digital microfluidics, which is the main concern in this work. Surfactant molecules are used for stabilization of emulsions or as a supporting tool in immunoassays [70, 97, 98]. Considerations presented in this work are concerned with transient non-equilibrium adsorption especially induced by the time-dependence of the drop size. A general ageing model is developed in this chapter, which may also be found relevant to modeling Ostwald ripening (stability of water/oil or oil/water emulsions) [99, 100], liquid aerosols [101] as well as evaporation-driven mass transfer of biochemically-functionalized droplets, such as those involved at microscale [73, 74]. Typically, the considered system of a free spherical drop is similar to a sessile drop on a superhydrophobic substrate with $\theta \approx \pi$, or to a sessile drop in microfluidic applications, provided that the contact angle is close to a value $\theta \approx \pi/2$, which is the case for a significant number of applications (EWOD-based lab-on-a-chips for instance). For the case of a (quasi-)instantaneous diffusive regime within a sessile drop, the present model is extended to the case of an arbitrary contact angle.

In this chapter, special attention is paid to the evaporation of a free liquid drop under surface ageing. The general case of a time-dependent liquid drop whose non-material spherical surface, $R(t)$, is moving radially inwards, is considered. Beyond the liquid surface, $r > R(t)$, r being the space coordinate for an isotropic spherical system, surfactants are considered as insoluble. The system at the initial time is characterized by a liquid surface free of surfactant, $\Gamma(0) = 0$, a bulk concentration which is homogeneous throughout the domain, $C(r, 0) = C_0$, and an initial radius $R(0) = R_0$.

Since the early work conducted by Ward & Tordai on diffusion-limited regimes, theoretical advances have constantly focused on improving modeling of surface ageing with special emphasis on chemical coupling, adsorption constitutive laws, initial transient non-equilibrium and, more recently, with successful attempts to take into account the influence of surface curvature upon diffusional kinetics [102–104]. All of these works are based on the assumption of a half-space ($r > 0$) adjacent to an interface ($r = R$), outside which surfactant are solubilized. To our knowledge, the only work for which the far field condition on the concentration is not invoked, is developed by Filippov & Filippova [105], who make use of a symmetry condition at the center of a drop ($\partial C/\partial r|_{r=0} = 0$) in order to address diffusion-limited ageing at its surface.

In current literature, at least two fundamental points are still worth investigating, because they may be viewed as prerequisites for digital microfluidics: the first is the impact of a finite size upon volume concentration, while the second

is the ageing of a moving (non-material) surface. Both of them are addressed in the present chapter.

20.1. Preliminary theory on adsorption and diffusion processes

Consider a spherical water droplet with radius $R(t)$, volume $V(t)$ and surface $S(t)$. The initial values are R_0, V_0 and S_0 for radius, volume and surface respectively. The origin of the coordinate system is placed at the center of the droplet. As we consider the system spherically symmetric in all cases, it is described by a single radial space variable, r, with $\boldsymbol{n}$, its unit normal vector. Time dependence of the geometry is described by the variable t. All physical properties are considered isotropic in the bulk phase. The density of the liquid is ρ. In the droplet, an isotropic concentration of surfactants $C(r,t)$ is present, the surface concentration is $\Gamma(t)$, with initial values $C(r,0) = C_0$ and $\Gamma(0) = 0$, respectively.

20.1.1. Considerations on symmetry

This section constitutes a summary on the different simplifications using symmetry in the evoked system, which will be used to simplify the models of evaporation, diffusion and adsorption. A spherical system with isotropic diffusion and adsorption constants is considered, hence all variables depend solely on the space coordinate r with normal vector $\boldsymbol{n} = \boldsymbol{e}_\mathrm{r}$, where $\boldsymbol{e}_\mathrm{r}$ is the unit base vector for the radial coordinate. Therefore, azimuth and latitude dependencies are disregarded.

The water drop is assumed to be in a quiescent atmosphere, which means that for a spherical system, evaporation-driven mass transfer takes places isotropically and the evaporation flux is constant throughout the surface. On that account, no bulk flow in the volume is allowed. For a sessile drop on a substrate, to whom this theory may be compared, things are different. Three cases exist, depending on the value of the contact angle θ [75, 106]:

- $\theta < \frac{\pi}{2}$: The evaporation flux is high at the contact line, since the solid angle for water vapor diffusion is greater near the substrate.
- $\theta > \frac{\pi}{2}$: The evaporation flux is high at the apex, as the flux at the contact line is delayed by the substrate.
- $\theta = \frac{\pi}{2}$: As for the case of an aerosol droplet in a quiescent atmosphere, the evaporation flux is constant throughout the whole surface, and corresponds to the perfectly symmetric case of a sphere.

Depending on the contact angle, evaporation in a droplet may thus be concerned by an inner flow due to a net flow to the TCL ($\theta < \pi/2$) or to the apex ($\theta > \pi/2$). In this work, the hypothesis is made, that there is no hydrodynamic flow in the droplet. The latter hypothesis is only true concerning the flow due to evaporative mass transfer. In addition, for a sessile droplet, there is the heat exchange with the substrate and cooling of the liquid due to evaporation. Hence, thermal

convection can occur in the bulk [107,108] and a thermal Marangoni effect may install at the surface [109–111]. Such that even in the case $\theta = \pi/2$, where there is no flow due to evaporation, the cooling of the droplet and the subsequent heat exchange of the drop with the substrate may induce a net flow.

20.1.2. Diffusion & sorption phenomena

In this section, a mathematical model for diffusion and adsorption phenomena is proposed for a water droplet subject to evaporation. The theory developed throughout this section constitutes the basis for the calculations done later in this part of the work. The considered system is a finite system meaning that it is not semi-infinite. This implies, that the droplet is of finite size, and that the molecular content is considered as a finite molar quantity. In addition to this, the droplet is affected by a mass transfer of water vapor into the adjacent phase, which means that the model studied in this work is representative for a broad range of cases, concerning evaporation, Ostwald ripening or other mass transfer mechanisms.

Diffusion within a spherical droplet

Diffusion of solute molecules in a liquid phase is due to Brownian motion of the molecules in solution, characterized by the diffusivity of surfactant molecules, D, and due to the concentration gradient, ∇C. Based on these two mechanisms, a diffusive transport with flux j_{diff}, may be written as follows, according to Fick's law:

$$j_{\text{diff}}\,\boldsymbol{n} = -D\nabla C = -D\frac{\partial C}{\partial r}\,\boldsymbol{n}, \tag{20.1}$$

where ∇ is the vector differential operator for the space coordinate r. With the continuity equation for the conservation of mass, $\frac{\partial C}{\partial t} + \nabla \cdot \boldsymbol{j}_{\text{diff}} = 0$, the transport equation describing bulk diffusion of surfactants (Fick's second law) may be written:

$$\frac{\partial C}{\partial t} = D\Delta C, \tag{20.2}$$

where $\partial/\partial t$ is the partial derivative with respect to time, and $\Delta = \frac{1}{r^2}\frac{\partial}{\partial r}(r^2\frac{\partial}{\partial r})$ is the Laplace operator as written in a spherical geometry.

Sorption phenomena at a liquid/gas interface – The surface boundary condition revisited

Mass conservation is an underlying support of Fick's second law. Nevertheless, it is worthwhile revisiting it as a mass balance for an interesting finding. The mass balance for a total number of surfactant molecules, $N = C_0V_0$, reads:

$$C_0V_0 = 4\pi\int_0^{R(t)} r^2C(r,t)\,\mathrm{d}r + 4\pi R^2\Gamma(t).$$

Due to mass conservation, this quantity never changes:

$$\frac{1}{4\pi}\frac{\mathrm{d}}{\mathrm{d}t}(C_0 V_0) = \frac{\mathrm{d}}{\mathrm{d}t}\int_0^{R(t)} r^2 C \,\mathrm{d}r + 2R\frac{\mathrm{d}R}{\mathrm{d}t}\Gamma + R^2\frac{\mathrm{d}\Gamma}{\mathrm{d}t} = 0,$$

where $\mathrm{d}/\mathrm{d}t$ represents the total derivative with respect to time. When using the Leibniz integral rule[1] for differentiation under the integral sign with variable limits, the equation reads:

$$\int_0^R r^2\frac{\partial C}{\partial t}\,\mathrm{d}r + R^2 C(R,t)\frac{\mathrm{d}R}{\mathrm{d}t} + 2R\frac{\mathrm{d}R}{\mathrm{d}t}\Gamma + R^2\frac{\mathrm{d}\Gamma}{\mathrm{d}t} = 0,$$

where $\equiv \mathrm{d}R/\mathrm{d}t$ is the normal velocity of the moving drop surface. Using Fick's second law of diffusion (20.2), one may substitute $\partial C/\partial t$ by $D\Delta C$:

$$D\int_0^R r^2\left[\frac{1}{r^2}\frac{\partial}{\partial r}r^2\frac{\partial C}{\partial r}\right]\mathrm{d}r + R^2 C(R,t)\frac{\mathrm{d}R}{\mathrm{d}t} + 2R\frac{\mathrm{d}R}{\mathrm{d}t}\Gamma + R^2\frac{\mathrm{d}\Gamma}{\mathrm{d}t} = 0.$$

After applying Gauss's integral theorem[2] to the first term and dividing by R^2, the equation reads:

$$\frac{\mathrm{d}\Gamma}{\mathrm{d}t} = -D\frac{\partial C}{\partial r}\Big|_R - \frac{\mathrm{d}R}{\mathrm{d}t}\left(C(R,t) + \frac{2\Gamma}{R}\right). \tag{20.3}$$

This expression redefines the rate of change of surfactant concentration, $\mathrm{d}\Gamma/\mathrm{d}t$, as it must be used from now on for time-independent geometries [112]. This transport equation along a two-dimensional surface is referred to as interfacial surfactant balance. Note that in literature only the first term on the right hand side is taken into account (cf. Filippov & Filippova [105], equation [4b] for model A, and equations (3) and (4) in Ward & Tordai [113]). By applying Fick's law to mass conservation, the missing terms are elegantly calculated for a time-dependent geometry. The last two terms illustrate the surface concentration increase due to non-material interface motion: The first term $(\mathrm{d}R/\mathrm{d}t)C$ indicates that the inflating interface collects the residual surfactant molecules in the evaporating outer spherical shell of the drop, which will be adsorbed at the interface. The second term $(\mathrm{d}R/\mathrm{d}t)(2\Gamma/R)$ represents the surface concentration increase due to surface area shrinkage, $(\mathrm{d}R/\mathrm{d}t)/R$, and thus compression of the surfactant monolayer. These two terms are referred to as the evaporation flux,

$$j_{\mathrm{evap}} := -\frac{\mathrm{d}R}{\mathrm{d}t}\left(C(R,t) + \frac{2\Gamma}{R}\right). \tag{20.4}$$

On the basis of this general formulation, asymptotic solutions for different cases may be recovered, i.e. adsorption and diffusion limited regimes, no evaporation, evaporation-limited regime, etc., all these particular regimes will be discussed

[1] $\frac{\partial}{\partial t}\int_{a(t)}^{b(t)} f(x,t)\,\mathrm{d}x = \int_{a(t)}^{b(t)}\frac{\partial f}{\partial t}\,\mathrm{d}x + f(b(t),t)\frac{\partial b}{\partial t} - f(a(t),t)\frac{\partial a}{\partial t}$

[2] $\int_V \nabla\cdot\boldsymbol{F}\,\mathrm{d}^{(n)}V = \oint_S \boldsymbol{F}\cdot\boldsymbol{n}\,\mathrm{d}^{(n-1)}S$

Law	$\chi_a(\Gamma)$	$\chi_d(\Gamma)$
Henry	k_a	k_d
Langmuir	$k_a\left(1-\frac{\Gamma}{\Gamma_\infty}\right)$	$\frac{k_d}{\Gamma_\infty}$
Volmer	k_a	$\frac{k_d}{\Gamma_\infty-\Gamma}\,e^{\frac{\Gamma}{\Gamma_\infty-\Gamma}}$
Frumkin	$k_a\left(1-\frac{\Gamma}{\Gamma_\infty}\right)$	$\frac{k_d}{\Gamma_\infty}\,e^{-\frac{2\alpha\Gamma}{k_B T}}$
Van-der-Waals	k_a	$\frac{k_d}{\Gamma_\infty-\Gamma}\,e^{\frac{\Gamma}{\Gamma_\infty-\Gamma}-\frac{2\alpha\Gamma}{k_B T}}$

Table 20.1.: Summary of constitutive laws describing ad- and desorption processes by the equation $j_{ads} = \chi_a C|_R - \chi_d \Gamma$. The symbol Γ_∞ is the maximum package concentration at the interface, k_a and k_d are ad- and desorption constants respectively. The constant α represents the energy per molecular surface area, k_B is the Boltzmann constant and T the temperature at which the process takes place.

in the following sections.

In order to express the continuity of the diffusive chemical flux at the surface, $j_{diff} = -D(\partial C/\partial r)|_R$, use is made of a constitutive law, describing the ad- and desorption processes, j_{ads}:

$$-D\frac{\partial C}{\partial r}\Big|_R = j_{ads} = \chi_a(\Gamma)C|_R - \chi_d(\Gamma)\Gamma, \tag{20.5}$$

where χ_a and χ_d are adsorption and desorption rate parameters, respectively. Equation (20.5) describes the continuity of chemical species flux at the surface: The diffusion flux, $j_{diff} = -D(\partial C/\partial r)|_R$, is equal to the adsorption flux, $j_{ads} = \chi_a C|_R - \chi_d \Gamma$. The respective expressions of χ_d and χ_a depend on the constitutive law used to describe surface ageing. Table 20.1 recapitulates some of the commonly used laws, for instance the well-known laws established by Henry or Langmuir. The symbol Γ_∞ is the maximum package concentration at the interface, k_a and k_d are ad- and desorption constants respectively. The constant α represents the energy per molecular surface area, k_B is the Boltzmann constant and T the temperature at which the process takes place. The Henry law is sufficient for surface concentrations, Γ, much smaller than the maximum package concentration at the interface, Γ_∞, whereas the Langmuir law may be used to describe systems with a high level of surface coverage.

20.2. Mathematical model & general solution

As discussed in chapter 20.1.2 on diffusion and adsorption phenomena, the diffusion-adsorption model includes Fick's second law of diffusion and the constitutive law for adsorption as the two main differential equations. Fick's law of diffusion (20.2) permits to calculate the bulk diffusion, whereas the rate of change of surface concentration (20.3) holds at the interface. Thus, two phenomena, evaporative-driven mass transfer and sorption via the flux j_{evap} and j_{ads} (equations (20.4) and (20.5), are taken into account. The model under

consideration in this chapter writes as:

$$\frac{\partial C}{\partial t} = D\Delta C = \frac{D}{r^2}\frac{\partial}{\partial r}\left(r^2\frac{\partial C}{\partial r}\right), \tag{20.6a}$$

$$\frac{\mathrm{d}\Gamma}{\mathrm{d}t} = j_{\mathrm{ads}} + j_{\mathrm{evap}}, \tag{20.6b}$$

along with the boundary conditions at $r = 0$ and $r = R(t)$ are:

$$C(0,t) \neq \infty, \tag{20.6c}$$

$$-D\frac{\partial C}{\partial r}\Big|_{r=R(t)} = j_{\mathrm{ads}}. \tag{20.6d}$$

The first boundary condition at $r = 0$ represents the physical assumption that the bulk concentration, C, can not be infinite. Note that the value of C is not fixed as in a diffusion-adsorption model of Ward & Tordai type [113], for which $C(0,t) = C_0$. The boundary condition at $r = R(t)$ represents the flux corresponding to Fick's first law of diffusion (20.1), which is equal to the net molecular flux from and to the interface. The initial conditions for C and Γ read:

$$C(r,0) = C_0, \tag{20.6e}$$

$$\Gamma(0) = 0. \tag{20.6f}$$

The adsorption and evaporation fluxes are defined as follows:

$$j_{\mathrm{ads}} = \chi_{\mathrm{a}} C|_{R(t)} - \chi_{\mathrm{d}}\Gamma, \tag{20.6g}$$

$$j_{\mathrm{evap}} = -\frac{\mathrm{d}R}{\mathrm{d}t}\left(C(R,t) + \frac{2\Gamma}{R(t)}\right). \tag{20.6h}$$

The kinematic condition for evaporation-driven motion of drop surface is derived from Picknett and Bexon's law of drop evaporation [81]:

$$\frac{\mathrm{d}R}{\mathrm{d}t} = -\frac{1}{2\tau_{\mathrm{evap}}R(t)}. \tag{20.6i}$$

The equations (20.6a) to (20.6i) represent the complete model for surface ageing and diffusion in a liquid sphere with isotropic properties. Figure 20.1 illustrates chain of involved serial phenomena, diffusion, ad- & desorption and evaporation, whose respective kinetics are competing.

20.2.1. Non-dimensionalization

In order to analyze different time scales (kinetics) and diffusion- or adsorption-limited regimes (which will be explained later), it is relevant to non-dimensionalize the model and to extract different dimensionless numbers for a similitude analysis. We will rewrite the variables, coordinates and derivatives with weight-

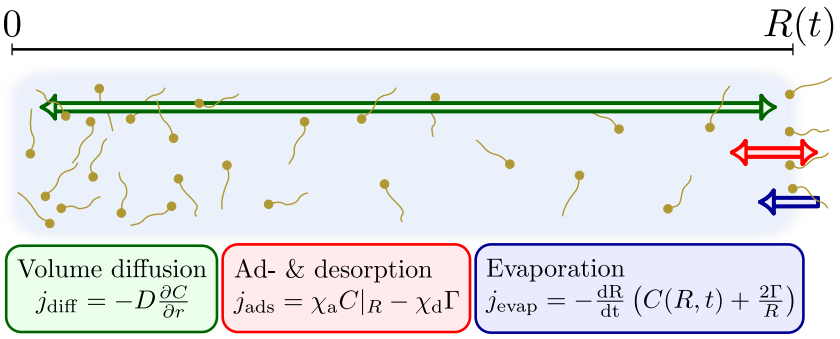

Fig. 20.1.: Illustration of the phenomena involved in the system under consideration: volume diffusion (top arrow), ad- & desorption (middle arrow) and evaporation (bottom arrow). The geometry is represented on the top axis: 0 represents the center of the drop, $R(t)$ the outer boundary, evolving with evaporation.

ing constants representing their natural order of magnitude:

$$\begin{aligned} t &\to T\, t^* \\ r &\to R_0\, r^* \\ C(r,t) &\to C_0\, C^*(r^*, t^*) \\ \Gamma(t) &\to \Gamma_{\mathrm{e}}\, \Gamma^*(t^*) \\ R(t) &\to R_0\, R^*(t^*) \end{aligned} \tag{20.7}$$

The reference time scale for time-dependent variables is chosen as T which is a generic variable for the time being. For different regimes, a dedicated time scale needs to be considered. For instance, the diffusion time scale, τ_{diff}, is chosen for a diffusion-limited process. The principal length scale in the system is the initial radius, R_0, which will be used to non-dimensionalize the time-dependent radius, $R(t)$, as well as the radial coordinate, r. The scale for bulk concentration, C, is the initial value C_0. The scale for surface concentration, Γ, is Γ_{e}, which is calculated from the assumption of thermodynamical equilibrium with the bulk concentration, C_0: the ad-/desorption equilibrium delivers a relation between the bulk concentration at the surface, $C|_R$, and the surface concentration, Γ_{e}. The value of Γ_{e} is given by the constitutive law for ad- and desorption (20.6d), evaluated for $\mathrm{d}\Gamma/\mathrm{d}t = 0$ and $\mathrm{d}R/\mathrm{d}t = 0$, implying that the molecule exchange $\partial C/\partial r|_R$ at the interface vanishes:

$$\frac{\Gamma_{\mathrm{e}}}{T}\frac{\mathrm{d}\Gamma^*}{\mathrm{d}t^*} = \chi_{\mathrm{a}} C_0 C^*|_{r^*=1} - \chi_{\mathrm{d}}\Gamma_{\mathrm{e}}\Gamma^* = 0.$$

The above equation may be rearranged to:

$$T\frac{\chi_{\mathrm{a}} C_0}{\Gamma_{\mathrm{e}}} C^*|_{r^*=1} - T\chi_{\mathrm{d}}\Gamma^* = 0.$$

This yields two helpful relations. The first is the value of Γ_{e} expressed by the volume concentration scale C_0 and the ad- and desorption parameters χ_{a} and χ_{d}

(cf. table 20.1):

$$\Gamma_e := \frac{\chi_a}{\chi_d} C_0. \tag{20.8}$$

The second relation allows the adsorption time scale to be extracted:

$$\tau_{ads} := \frac{\Gamma_e}{\chi_a C_0} = \frac{1}{\chi_d}. \tag{20.9}$$

A third important time scale is the time scale for diffusion, the time a particle with diffusivity D needs to cover a distance R_0 in a medium. Non-dimensionalization of Fick's second law (20.6a) yields:

$$\frac{C_0}{T}\frac{\partial C^*}{\partial t^*} = -\frac{DC_0}{R_0^2}\Delta C^*,$$

from which the diffusive time scale can be deduced[3]:

$$\tau_{diff} := \frac{R_0^2}{D}. \tag{20.10}$$

From now on, the superscripts, *, designating dimensionless variables are dropped for convenience. The variables t, r, C, Γ and R are referred to as dimensionless variables from which the model (20.6a)-(20.6i) may be re-written in its dimensionless formulation,

$$\frac{\partial C}{\partial t} = \frac{DT}{R_0^2}\frac{1}{r^2}\frac{\partial}{\partial r}\left(r^2\frac{\partial C}{\partial r}\right),$$
$$\frac{\mathrm{d}\Gamma}{\mathrm{d}t} = -\frac{DT}{R_0^2}\frac{R_0 C_0}{\Gamma_e}\left(\frac{\partial C}{\partial r}\Big|_{r=R} + \frac{\mathrm{d}R}{\mathrm{d}t}\left(\frac{R_0 C_0}{\Gamma_e}C(R,t) + \frac{2\Gamma}{R}\right)\right),$$

along with the boundary conditions at $r = 0$ and $r = R$:

$$C(0,t) \neq \infty \quad \left(\text{or } \frac{\partial C}{\partial r}\Big|_{r=0} = 0\right),$$
$$\frac{\partial C}{\partial r}\Big|_R = -\frac{R_0^2}{D}\frac{\Gamma_e}{C_0 R_0}\left(\frac{\chi_a C_0}{\Gamma_e}C|_{r=R} - \chi_d\Gamma\right).$$

The initial conditions for $\Gamma(t)$ and $C(r,t)$ write:

$$C(r,0) = 1,$$
$$\Gamma(0) = 0.$$

The dimensionless numbers associated with the kinetics in the system are:

$$\eta_{ed} := \tau_{evap}/\tau_{diff} = D\rho/2D_{vap}(c_0 - c_\infty), \text{ and}$$

[3] As proposed by Alvarez et al. [104], a time scale based both on the radius and on the depletion length may be introduced for τ_{diff}.

$\tau_{\mathrm{evap}} = \frac{R_0^2\,\rho}{2D_{\mathrm{vap}}(c_0 - c_\infty)}$	$\eta_{\mathrm{Te}} := \frac{T}{\tau_{\mathrm{evap}}}$	$\eta_{\mathrm{ea}} = \frac{\tau_{\mathrm{evap}}}{\tau_{\mathrm{ads}}}$
$\tau_{\mathrm{diff}} = \frac{R_0^2}{D}$	$\eta_{\mathrm{Ta}} := \frac{T}{\tau_{\mathrm{ads}}}$	$\eta_{\mathrm{ed}} = \frac{\tau_{\mathrm{evap}}}{\tau_{\mathrm{diff}}}$
$\tau_{\mathrm{ads}} = \frac{\Gamma_{\mathrm{e}}}{\chi_{\mathrm{a}} C_0} = \frac{1}{\chi_{\mathrm{d}}}$	$\eta_{\mathrm{Td}} := \frac{T}{\tau_{\mathrm{diff}}}$	$\eta_{\mathrm{ad}} = \frac{\tau_{\mathrm{ads}}}{\tau_{\mathrm{diff}}}$

Table 20.2.: Recapitulation of the different time scales and associated non-dimensional numbers.

$$\eta_{\mathrm{ea}} := \tau_{\mathrm{evap}}/\tau_{\mathrm{ads}} = \chi_{\mathrm{a}} C_0 R_0^2 \rho / 2D_{\mathrm{vap}}(c_0 - c_\infty)\Gamma_{\mathrm{e}} = \chi_{\mathrm{d}} R_0^2 \rho / 2D_{\mathrm{vap}}(c_0 - c_\infty).$$

The subscripts are chosen according to the ratio of a first time scale to a second time scale so as to facilitate writing of the equations. Another useful dimensionless number is the ratio which expresses the balance between the molar mass of material contained in the interface and the mass contained in the drop volume:

$$\varepsilon_0 := \frac{C_0 R_0}{\Gamma_{\mathrm{e}}} \overset{(20.8)}{=} \frac{\chi_{\mathrm{d}} R_0}{\chi_{\mathrm{a}}}. \tag{20.11}$$

An interesting finding emerges when having a look at the ratio of the diffusion length scale to adsorption length scale. The diffusion length scale is about the size of the droplet $\lambda_{\mathrm{d}} = R_0$. The thickness of the depletion zone due to adsorption λ_{a} is the product of the adsorption rate throughout the diffusion layer χ_{a} multiplied with the adsorption time scale τ_{ads}, hence $\lambda_{\mathrm{a}} := \chi_{\mathrm{a}}\tau_{\mathrm{ads}} = \chi_{\mathrm{a}}\Gamma_{\mathrm{e}}/\chi_{\mathrm{a}}C_0$. The ratio of both lengths is $\lambda_{\mathrm{d}}/\lambda_{\mathrm{a}} = R_0 C_0/\Gamma_{\mathrm{e}} = \varepsilon_0$, which yields the same value as ε_0. This result shows that the length scales of diffusion and adsorption processes in finite sized systems are inherently coupled to the repartition of molecules in the system. In a macroscopic system, the number of molecules adsorbed to the surface is considered much smaller than the number of molecules in the bulk phase, $\varepsilon_0 = C_0 R_0/\Gamma_{\mathrm{e}} \gg 1$, since $C_0 CV \gg \Gamma_{\mathrm{e}} S$. Also the length scales of diffusion and adsorption layers will be disproportionate $\lambda_{\mathrm{d}} \gg \lambda_{\mathrm{a}}$, which yields the same result, not only on a mathematical plan. This is directly connected to the notion of finiteness as seen in section 19.1. As soon as the two length scales have the same order of magnitude, the bulk concentration far from the interface can no longer be regarded as a constant source of surfactants with concentration C_0. Table 20.2 shows a recapitulation of the different time scales and dimensionless numbers. The dimensionless number η_{ad} is the equivalent of the often used Thiele number, a measure for the preponderant regime, diffusion-limited ($\eta_{\mathrm{ad}} < 1$) or adsorption-limited ($\eta_{\mathrm{ad}} > 1$).

The new-introduced dimensionless numbers ε_0, η_{Te}, η_{Ta} and η_{Td} are used to express the existing model, equations (20.6a) to (20.6i), in a more comprehensive form:

$$\frac{\partial C}{\partial t} = \frac{\eta_{\mathrm{Td}}}{r^2}\frac{\partial}{\partial r}\left(r^2 \frac{\partial C}{\partial r}\right), \tag{20.12a}$$

$$\frac{\mathrm{d}\Gamma}{\mathrm{d}t} = -\left(\varepsilon_0 \eta_{\mathrm{Td}} \frac{\partial C}{\partial r}\Big|_{r=R} + \frac{\mathrm{d}R}{\mathrm{d}t}\left(\varepsilon_0 C|_{r=R} + \frac{2\Gamma}{R}\right)\right), \tag{20.12b}$$

along with the boundary conditions at $r = 0$ and $r = R$:

$$C(0,t) \neq \infty \quad \left(\text{or } \frac{\partial C}{\partial r}\Big|_{r=0} = 0\right), \tag{20.12c}$$

$$\frac{\partial C}{\partial r}\Big|_{r=R} = -\frac{1}{\varepsilon_0 \eta_{\text{ad}}}(C|_{r=R} - \Gamma). \tag{20.12d}$$

The initial conditions for $\Gamma(t)$ and $C(r,t)$ write:

$$C(r,0) = 1, \tag{20.12e}$$

$$\Gamma(0) = 0. \tag{20.12f}$$

And the radius evolution becomes:

$$\frac{\mathrm{d}R}{\mathrm{d}t} = -\frac{1}{2\eta_{\text{Te}} R(t)}. \tag{20.12g}$$

20.2.2. Converting the model into the Laplace space

In this section, the general solution of the system (20.12a) to (20.12g) is demonstrated. This solution permits to gain analytical expressions for the time-dependence of the surface concentration, Γ, for different asymptotic regimes. These are used further as analytical benchmark for numerical calculations.

As the Laplace transform is applied, care needs to be taken: a multiplication or composition of two time-dependent functions does not have a trivial equivalent in the Laplace domain. This is the case for products of $\mathrm{d}R/\mathrm{d}t$ and Γ, and for the composite function $C|_{R(t)}$. As a consequence, the analysis primarily focuses on cases with a time-independent radius, meaning that $R(t) = 1$ for all t. This also fixes the choice of the constitutive law for ad- and desorption, cf. table 20.1 on page 123. In order not to have any function products or composite functions depending on time involved in the calculation, the linear Henry law is involved:

$$\chi_{\text{a}}(\Gamma) = k_{\text{a}},$$

$$\chi_{\text{d}}(\Gamma) = k_{\text{d}}.$$

The choice of the Henry law for a finite system is not as naive as it might seem. In a real finite system, the non-dimensional number ε_0 is smaller than unity, $\varepsilon_0 < 1$, meaning that the number of surfactants in the volume is comparable or smaller as the total allowed number of surfactants adsorbed to the surface. This is consistent with the fact that the steric limit at the surface is not reached, making the use of a Langmuir constitutive law not a necessity.

Brief generalities

As mentioned above, a way to solve the initial value problem under consideration here, is to make use of the Laplace transform with respect to time:

$$\mathcal{L}(f(q,t))(s) = \int_0^\infty e^{-st} f(q,t)\,\mathrm{d}t = \tilde{f}(q,s).$$

Here, the function $f(q,t)$ depending on a variable q and on time t, is a function to be transformed into the Laplace (or frequency) domain. The subsequently transformed function $\tilde{f}(q,s)$ depends on q and on the complex variable, s, valid for the Laplace domain. Note that both t and s are dimensionless variables from now on. When evaluating the Laplace transform for a first-order time-derivative, one obtains:

$$\mathcal{L}\left(\frac{\partial f(q,t)}{\partial t}\right)(s) = s\tilde{f}(q,s) - f(q,0) \tag{20.13}$$

This is especially helpful for the differential equations in question. Thus, transforming a partial differential equation (PDE) into the Laplace domain might facilitate the solution of the original PDE in transcribing it into an ordinary differential equation (ODE). The solution of the ODE in the Laplace domain yields a solution depending on the non-transformed coordinates, like spatial coordinates, and on s. The problem of finding a solution to the original differential equation in the time domain has now been shifted to retransforming the solution in the Laplace domain back to the time domain. Finding the inverse Laplace transform $\mathcal{L}^{-1}(\tilde{f}(q,s))(t)$ may often be not trivial at all:

$$\mathcal{L}^{-1}\left(\tilde{f}(q,s)\right)(t) = \frac{1}{2\pi i}\lim_{y\to\infty}\int_{\alpha-iy}^{\alpha+iy} \tilde{f}(q,s)e^{st}\,\mathrm{d}s = f(q,t)$$

where $i = \sqrt{-1}$. For many functions $\tilde{f}(q,s)$, transform tables exist. If not, several methods of finding the inverse transform exist, like the residue theorem for the evaluation of integrals in the complex plane or the Heaviside expansion theorem which is based on the latter. The inverse transform may also be found by making use of numerical methods.

Transforming the model

Fick's second law, the boundary and initial conditions, as well as the constitutive law for adsorption, need to be written in the Laplace domain in order to facilitate the solution of the problem. We consider the transformed variables C and Γ in the Laplace domain:

$$\mathcal{L}(C(r,t)) = \tilde{C}(r,s),$$
$$\mathcal{L}(\Gamma(t)) = \tilde{\Gamma}(s).$$

This is a very elegant way of transcribing the differential equations, as the initial conditions, (20.12e) and (20.12f), are naturally incorporated into the differential

equation according to (20.13). Fick's second law (20.12a) and the interfacial surfactant balance (20.12b) in connection with the respective initial conditions (20.12e) and (20.12f) in the Laplace domain write as follows:

$$s\tilde{C} - 1 = \frac{\eta_{\mathrm{Td}}}{r^2}\frac{\partial}{\partial r}\left(r^2\frac{\partial \tilde{C}}{\partial r}\right), \tag{20.14a}$$

$$s\tilde{\Gamma} = -\varepsilon_0\eta_{\mathrm{Td}}\left.\frac{\partial \tilde{C}}{\partial r}\right|_{r=1}, \tag{20.14b}$$

to be completed by the boundary conditions in the Laplace domain:

$$\tilde{C}(0,s) \neq \infty \quad \left(\text{or } \left.\frac{\partial \tilde{C}}{\partial r}\right|_{r=0} = 0\right), \tag{20.14c}$$

$$\left.\frac{\partial \tilde{C}}{\partial r}\right|_{r=1} = -\frac{1}{\varepsilon_0\eta_{\mathrm{ad}}}\left(\tilde{C}|_{r=1} - \tilde{\Gamma}\right). \tag{20.14d}$$

These four equations sum up the model for diffusion and adsorption to be solved in Laplace space.

20.2.3. Simplification of the problem and general solution for time-independent geometries

Although the time derivative has been removed from Fick's second law (20.14a), the differential equation still looks a little awkward to treat. To facilitate the analysis, one may consider the change of variable:

$$\tilde{C} = \frac{1}{r}\bar{C}$$

After substitution, Fick's second law in the Laplace domain becomes:

$$\frac{\partial^2 \bar{C}}{\partial r^2} - \frac{s}{\eta_{\mathrm{Td}}}\bar{C} = -\frac{r}{\eta_{\mathrm{Td}}}$$

which is a non-homogeneous ordinary differential equation of second order. A particular solution can be found:

$$\bar{C}^* = \frac{r}{s}.$$

Two solutions of the homogeneous ODE are:

$$\bar{C}_1^+ = \sinh\left(\sqrt{\frac{s}{\eta_{\mathrm{Td}}}}r\right) \quad \text{and} \quad \bar{C}_2^+ = \cosh\left(\sqrt{\frac{s}{\eta_{\mathrm{Td}}}}r\right).$$

Taking into account the variable change from $\bar{C}$ to $\tilde{C}$, the general solution of the differential equation (20.14a) reads then:

$$\tilde{C} = \frac{1}{s} + \frac{A}{r}\sinh\left(\sqrt{\frac{s}{\eta_{\mathrm{Td}}}}r\right) + \frac{B}{r}\cosh\left(\sqrt{\frac{s}{\eta_{\mathrm{Td}}}}r\right),$$

where $(A, B) \in \mathbb{R}^2$. The boundary condition (20.14c) at $r = 0$ signifies that $\tilde{C}$ has to remain finite at the origin. Since $\lim_{x\to 0}\cosh(x)/x \to \infty$, one finds that $B = 0$. According to Hôpital's rule[4] one finds $\lim_{x\to 0}\sinh(x)/x = \cosh(0)/1 = 1$, which does not signify any constraint for A, thus:

$$\tilde{C} = \frac{1}{s} + \frac{A}{r}\sinh\left(\sqrt{\frac{s}{\eta_{\mathrm{Td}}}}r\right).$$

Application of equation (20.14b) results in:

$$\frac{s\tilde{\Gamma}}{\varepsilon_0\eta_{\mathrm{Td}}} = -\frac{\partial\tilde{C}}{\partial r}\Big|_{r=1} = A\sinh\left(\sqrt{\frac{s}{\eta_{\mathrm{Td}}}}\right) - A\sqrt{\frac{s}{\eta_{\mathrm{Td}}}}\cosh\left(\sqrt{\frac{s}{\eta_{\mathrm{Td}}}}\right),$$

which permits to calculate A:

$$A = \frac{s\tilde{\Gamma}}{\varepsilon_0\eta_{\mathrm{Td}}}\frac{1}{\sinh\left(\sqrt{\frac{s}{\eta_{\mathrm{Td}}}}\right) - \sqrt{\frac{s}{\eta_{\mathrm{Td}}}}\cosh\left(\sqrt{\frac{s}{\eta_{\mathrm{Td}}}}\right)}.$$

Thus the general solution of equations (20.14a), (20.14c) and (20.14d) is found to be:

$$\tilde{C}(r,s) = \frac{1}{s} + \frac{s\tilde{\Gamma}}{r\varepsilon_0\eta_{\mathrm{Td}}}\frac{\sinh\sqrt{\frac{s}{\eta_{\mathrm{Td}}}}r}{\sinh\left(\sqrt{\frac{s}{\eta_{\mathrm{Td}}}}\right) - \sqrt{\frac{s}{\eta_{\mathrm{Td}}}}\cosh\left(\sqrt{\frac{s}{\eta_{\mathrm{Td}}}}\right)}.$$

One may evaluate the general solution of (20.14a), (20.14b) and (20.14c) at the interface $r = 1$ in the Laplace domain:

$$\tilde{C}(1,s) = \frac{1}{s} + \frac{\tilde{\Gamma}}{\varepsilon_0}\frac{1}{\frac{\eta_{\mathrm{Td}}}{s} - \sqrt{\frac{\eta_{\mathrm{Td}}}{s}}\coth\left(\sqrt{\frac{s}{\eta_{\mathrm{Td}}}}\right)}. \tag{20.15}$$

The last remaining equation, equation (20.14d), will be integrated separately into this general solution. These calculations are presented for the different asymptotic cases in the next section.

[4] Hôpital's rule may be applied if the limits of two functions $\lim_{x\to x^*} f(x) = \lim_{x\to x^*} g(x) = 0$ or $= \pm\infty$, and if $\lim_{x\to x^*}\frac{\mathrm{d}f/\mathrm{d}x}{\mathrm{d}g/\mathrm{d}x}$ exists; then $\lim_{x\to x^*}\frac{f(x)}{g(x)} = \lim_{x\to x^*}\frac{\mathrm{d}f/\mathrm{d}x}{\mathrm{d}g/\mathrm{d}x}$.

20.2.4. Asymptotic regimes and approximations

In different situations, one or two asymptotic cases concerning diffusivity and adsorption behavior may be applied. The two main simplifications which may be made are possible when considering diffusion-limited and adsorption-limited regimes. For each regime, a major simplification is found. When considering a diffusion-limited regime, the surface concentration Γ results from thermodynamical equilibrium, which corresponds to fast adsorption kinetics and $\mathrm{d}\Gamma/\mathrm{d}t = 0$. Hence, equation (20.14d) simplifies to:

$$\tilde{C}|_1 = \tilde{\Gamma}. \tag{20.16}$$

This simplifies the equation for $\tilde{\Gamma}(s)$ in order to find its transformation into the real domain $\Gamma(t)$.

When considering an adsorption-limited regime (which means a high diffusivity in the liquid domain), the concentration throughout the liquid volume is uniform and is approximated by the concentration in the vicinity of the drop surface:

$$C = C|_R. \tag{20.17}$$

Also, for an adsorption-limited regime, the general solution in the Laplace domain (20.15) may be approximated. A high diffusivity means that the time scale for equilibrating the diffusion gradient τ_{diff}, generated by evaporation or ad-/desorption of surfactants to/from the interface, is small compared to other time scales. In order to simplify the general solution (20.15), consider the Taylor expansion of $\coth(x)$:

$$\coth(x) \approx x^{-1} + \frac{x}{3} - \frac{x^2}{45} + \dots,$$

with $x = \sqrt{\frac{s}{\eta_{\mathrm{Td}}}}$, equation (20.15) may be developed:

$$\tilde{C}|_1 \approx \frac{1}{s} - \frac{3\tilde{\Gamma}}{\varepsilon_0}, \tag{20.18}$$

for a development of first order in x. This is an interesting finding, since the non-dimensionalized mass balance for a high diffusivity and constant radius in the Laplace domain yields the same result. The dimensionless mass balance reads:

$$C_0 = C_0 C + \frac{4\pi R_0^2}{\frac{4}{3}\pi R_0^3}\Gamma_{\mathrm{e}}\Gamma.$$

Transcribed into the Laplace domain, this becomes:

$$\frac{C_0}{s} = C_0\tilde{C}|_1 + \frac{3\Gamma_{\mathrm{e}}}{R_0}\tilde{\Gamma} \quad \text{or equivalently,} \quad \tilde{C}|_1 = \frac{1}{s} - \frac{3\tilde{\Gamma}}{\varepsilon_0}.$$

The agreement with expansion (20.18) suggests that the general solution (20.15) is correct.

Geometry	Diffusion	Adsorption	Time scale T	Case	Regime
$\frac{\mathrm{d}R}{\mathrm{d}t} = 0$	$D \to \infty$	$\frac{\mathrm{d}\Gamma}{\mathrm{d}t} = 0$	n.a.	1	Thermodyn. equil.
		$\frac{\mathrm{d}\Gamma}{\mathrm{d}t} \neq 0$	τ_a	2	Adsorption-limited
	$D \ll \infty$	$\frac{\mathrm{d}\Gamma}{\mathrm{d}t} = 0$	τ_d	3	Diffusion-limited
$\frac{\mathrm{d}R}{\mathrm{d}t} \neq 0$	$D \to \infty$	$\frac{\mathrm{d}\Gamma}{\mathrm{d}t} = 0$	τ_e	4	Evaporation-limited
		$\frac{\mathrm{d}\Gamma}{\mathrm{d}t} \neq 0$	τ_a	5	Adsorption-limited

Table 20.3.: Summary of the different regimes with a time-dependence associated to either evaporation, diffusion kinetics or adsorption kinetics.

20.3. Analytical solutions for different cases

Recall that the analytical solutions will be useful in serving as a benchmark for the simulation. One may consider different cases concerning the geometry, as R might depend on time, and concerning different time scales for diffusion and sorption processes. Table 20.3 outlines a large number of possible cases.

The assumption that adsorption acts after Henry's law of adsorption (cf. table 20.1) is still valid. This permits to use the solution in the Laplace domain and prevents non-linear differential equations for the analytical solution of cases with a variable radius. The value of $\varepsilon_0 = k_\mathrm{d} R_0 / k_\mathrm{a}$ is kept to 0.1 for all cases to ensure comparability and the fact that the considered system is of finite size.

20.3.1. Systems without volume variation

Case 1 – Thermodynamic equilibrium

The simplest case to be considered consists in assuming infinite diffusivity, thermodynamic equilibrium at the drop surface and a constant radius. For $D \to \infty$, the general solution at $r = 1$ reduces to equation (20.18):

$$\tilde{C}|_1 = \frac{1}{s} - \tilde{\Gamma}\frac{3}{\varepsilon_0}$$

The equilibrium condition $\mathrm{d}\Gamma/\mathrm{d}t = 0$ implies that $\tilde{C}|_1 = \tilde{\Gamma}$ (cf. equation (20.16)), hence:

$$\left(1 + \frac{3}{\varepsilon_0}\right)\tilde{\Gamma} = \frac{1}{s} \quad \to \quad \tilde{\Gamma} = \frac{1}{s(1 + \frac{3}{\varepsilon_0})}.$$

By transforming this result into the time domain, the solution reads:

$$\Gamma(t) = \frac{1}{1 + \frac{3}{\varepsilon_0}}, \tag{20.19}$$

for a development to the first order in $\sqrt{s/\eta_\mathrm{ed}}$ (quasi-instantaneous diffusion).

A different approach: For an adsorption-limited regime, it is useful to consider the fact that the bulk concentration is uniform (cf. equation (20.17)):

$$\tilde{C}(r,s) = \tilde{C}|_1.$$

Then the mass balance may be evaluated via the concentration in the vicinity of the surface, $\tilde{C}|_1$, in connection with the first-order development of the general solution (20.18):

$$N/s = \frac{4}{3}\pi R_0^3 C_0 \tilde{C}|_1 + 4\pi R_0^2 \Gamma_e \tilde{\Gamma},$$

equation which may be rearranged to, using (20.16):

$$\tilde{\Gamma} = \frac{1}{s\left(1 + \frac{3}{\varepsilon_0}\right)}.$$

By transformation into the time domain, $\Gamma(t)$ yields the same result:

$$\Gamma(t) = \frac{1}{1 + \frac{3}{\varepsilon_0}}.$$

As shown in Fig. 20.2, a strong variation of Γ is obvious for $\varepsilon_0 = R_0 k_d/k_a$ close to unity. As ε_0 rises over 10^2 or falls under 10^{-1}, the dependence becomes negligibly small. For a better understanding, consider a fixed value of k_a/k_d, then ε_0 is proportional to the radius R_0 of the droplet. Considering values of R_0 for which $R_0 < k_a/k_d$ (or $\varepsilon_0 < 1$), the ageing of the surface quickly empties all of the droplet's bulk of surfactants. For a value of $R_0 > k_a/k_d$ (or $\varepsilon_0 > 1$), enough molecules are present in the bulk, in order to maintain the adsorption rate at the surface. This is the situation of a weak coupling as for different scenarios described in section 19.1 on finite systems, where the variation of a quantity in the central part of the system does not have an influence on the bulk content of the same quantity, e.g. as surfactant adsorption or molecular reactions on bulk concentration, or even heat transfer on ambient temperature (the heat transfer equation is a diffusion equation).

When reconsidering the earlier non-dimensionalization of variables (cf. equation (20.7)), one recognizes that the surface concentration has been non-dimensionalized using Γ_e. In the graph of Fig. 20.2, this surface concentration is reached for high ε_0, which means that Γ_e signifies the equilibrium value only for macroscopic systems, in which a nearly infinite amount of surfactant molecules is supposed available in the liquid bulk. This is obvious, as the constitutive law for adsorption (here the Henry's law) does not take into account the finite character of the geometry. Hence, when dealing with microscopic systems ($\varepsilon_0 < 1$), Γ_e does not necessarily describe the actual equilibrium value of the surface concentration. The latter might though be described, for microscopic as well as for macroscopic systems, by:

$$\Gamma_e^{\mu} := \frac{\Gamma_e}{1 + \frac{3}{\varepsilon_0}}, \tag{20.20}$$

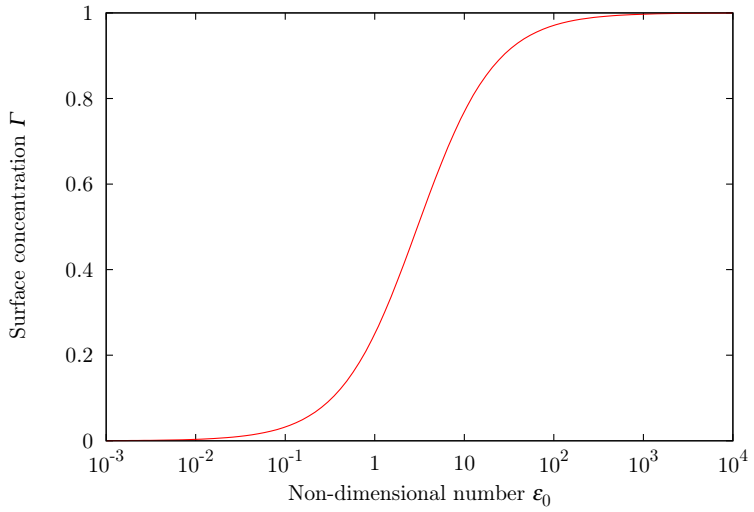

Fig. 20.2.: Case 1 – Thermodynamic equilibrium. The graph shows the variation of Γ with the non-dimensional number $\varepsilon_0 = k_d R_0 / k_a$.

which follows out of equation (20.19). Keeping this in mind, a modified quantity which is more convenient than Γ for microscopic systems may be defined:

$$\Gamma^{\mu} := \frac{\Gamma}{1 + \frac{3}{\varepsilon_0}}. \tag{20.21}$$

This result is a major achievement of this work: the parameter $\Gamma_e^{si\mu}$ reflects perfectly the finiteness of the geometry. In practice, it is useful to know how to conceive microsystems without oversizing the ingredient amounts. This might be especially helpful when considering surfactants like expensive or rare molecules, or molecules with a complex synthesis process (e.g. poly-peptides, molecular rafts).

Case 2 – Adsorption-limited regime

Case 1 may be considered with a slight modification: The evolution of surface concentration, $\Gamma(t)$, reveals the fact that thermodynamic equilibrium is broken, but an adsorption-limited process, described by Henry's law (equation (20.14b)), is supposed to take place. The appropriate time scale for this process is thus $T = \tau_{ads}$, which leads to $\eta_{Ta} = 1$, and thus:

$$C|_1 = (s+1)\tilde{\Gamma}. \tag{20.22}$$

The infinite diffusivity and the constant radius remain untouched. The general solution for $\tilde{C}$ for an infinite diffusivity and first-order development in $\sqrt{s/\varepsilon_0}$ (20.18) reads then:

$$\tilde{C}|_1 = \frac{1}{s} - \frac{3\tilde{\Gamma}}{\varepsilon_0} = (s+1)\tilde{\Gamma},$$

and an expression for $\tilde{\Gamma}(s)$ can be obtained:

$$\tilde{\Gamma} = \frac{1}{s\left(s + \left(1 + \frac{3}{\varepsilon_0}\right)\right)}.$$

From Doetsch [114] and the inverse transform, $\mathcal{L}^{-1}([s(s+a)]^{-1})(t) = \frac{1}{a}(1 - e^{-at})$, it can be written:

$$\Gamma(t) = \tau_2\left(1 - e^{-\frac{t}{\tau_2}}\right), \tag{20.23}$$

with $\tau_2 = 1/(1 + 3/\varepsilon_0)$, the characteristic (non-dimensional) time scale for case 2.

Calculation of Γ via the mass balance: The mass balance also holds in the Laplace domain:

$$N/s = \frac{4}{3}\pi R_0^3 C_0 \tilde{C} + 4\pi R_0^2 \Gamma_e \tilde{\Gamma}.$$

This equation may be simplified to an expression independent of $\tilde{C}$ using (20.22):

$$C_0 = C_0 s\left(s + 1 + \frac{3}{\varepsilon_0}\right)\tilde{\Gamma},$$

and which may be transformed to an expression for $\tilde{\Gamma}(s)$:

$$\tilde{\Gamma} = \frac{1}{s\left(s + \left(1 + \frac{3}{\varepsilon_0}\right)\right)}.$$

The transformation into the time domain yields the same result as (20.23).

$$\Gamma(t) = \tau_2\left(1 - e^{-t/\tau_2}\right).$$

The equations describing an adsorption-limited regime for a drop without volume variation are displayed in Fig. 20.3. The concentration at the surface (and therefore the bulk concentration throughout the whole domain) diminishes rapidly with the adsorption of molecules at the surface.

Case 3 – Diffusion-limited regime

A diffusion-limited regime signifies a regime in which adsorption is considered instantaneous compared to diffusion of surfactants. Hence, the appropriate time scale for this process is τ_{diff}. This kind of regime was examined by Filippov and Filippova [105] for a spherical geometry. They make use of the initial and final value theorems for Laplace transforms, which consist in writing that the limits $\lim_{t\to 0} f(t)$ and $\lim_{t\to\infty} f(t)$ of a function $f(t)$ can be found from its Laplace transform $\tilde{f}(s)$, when calculating $\lim_{s\to\infty} \tilde{f}(s)$ and $\lim_{s\to 0} \tilde{f}(s)$, respectively. Filippov and Filippova make use of these asymptotic formulations to calculate the behavior of $\Gamma(t)$ at short and long times.

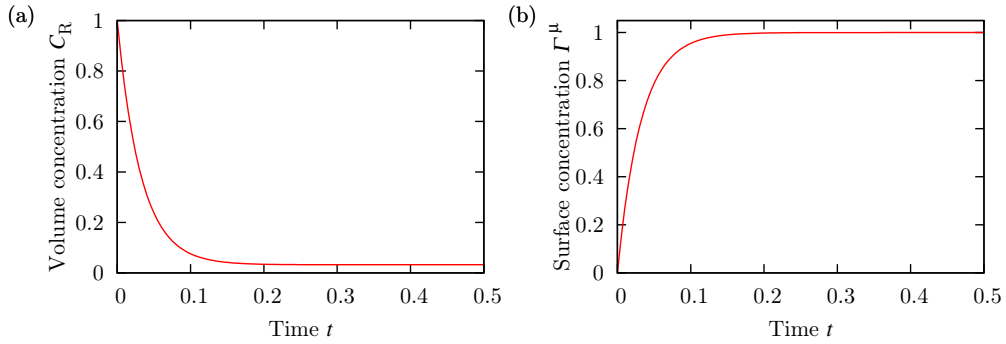

Fig. 20.3.: Case 2 – Adsorption limited system without volume variation. (a) volume concentration at the interface, $C|_R$, (b) surface concentration, $\Gamma^\mu(t)$. Time is measured in units of τ_{ads}.

Short-time limit: Consider the general solution of the diffusion-adsorption model for a spherical geometry not subjected to evaporation (cf. equation (20.15)). For the short-time limit, the Laplace variable tends to infinity, $s \to \infty$, and the general solution tends to:

$$\tilde{C}(1,t) \approx \frac{1}{s} - \frac{\tilde{\Gamma}}{\varepsilon_0}\sqrt{s}.$$

Rearranging the equation, this yields for $\tilde{\Gamma}$:

$$\tilde{\Gamma} = \frac{\varepsilon_0}{\sqrt{s}}\left(\frac{1}{s} - C|_R\right).$$

The second term in the parentheses is neglected by Filippov and Filippova, as $C|_R \ll 1$. This hypothesis is justified, since the system is diffusion-limited. Therefore, chemical flux, responsible for surface ageing, mainly originates from radial pumping into the chemical boundary layer in the direct vicinity of the drop surface. The transformation of $\tilde{\Gamma}(s)$ into the time domain is done by retransforming the previous equation using $\mathcal{L}^{-1}\left(s^{-3/2}\right) = \sqrt{4t/\pi}$ as described in [114]. The solution for short times is thus expressed by:

$$\Gamma(t) = \varepsilon_0\sqrt{\frac{4t}{\pi}}. \tag{20.24}$$

Long-time limit: The general solution (20.15) may now be considered for calculating the long-time limit. Then the Laplace variable tends to $s \to 0$, which allows to write the following series expansion:

$$\tilde{C}|_1 \approx \frac{1}{s} - \frac{3\tilde{\Gamma}}{\varepsilon_0}\left(1 + \frac{s}{15}\right),$$

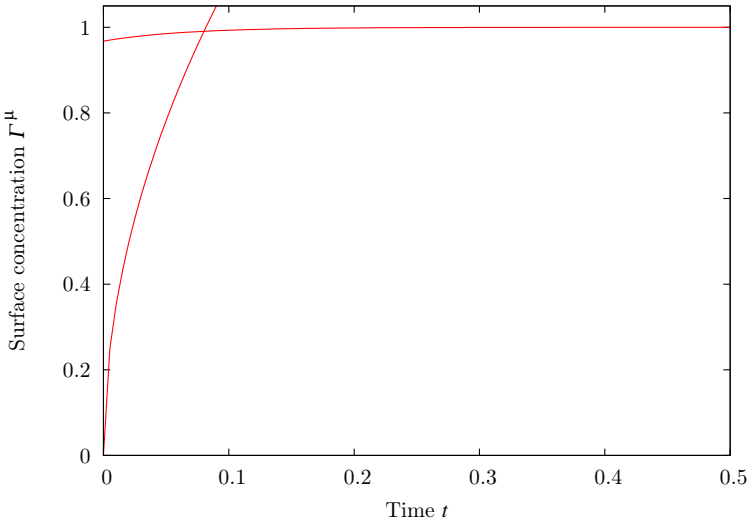

Fig. 20.4.: Case 3 – Diffusion-limited system without volume variation. Surface concentration $\Gamma^\mu(t)$ as calculated by Filippov and Filippova [105] for short and long times. Time is measured in units of τ_{diff}.

which writes also:

$$\frac{s\tilde{\Gamma}}{5\varepsilon_0} = \frac{1}{s} - \frac{3\tilde{\Gamma}}{\varepsilon_0} - C|_1.$$

In their article, Filippov and Filippova [105] impose $\tilde{\Gamma} = \Gamma_0/s$, with $\Gamma_0 := \Gamma(C = C_0)$, on the right hand side, which comes up to fixing the surface concentration equal to its equilibrium value after initial adsorption, without diffusion. With $C_\infty := 1 - 3\Gamma_0/\varepsilon_0$, they find:

$$\frac{s\tilde{\Gamma}}{5\varepsilon_0} = \frac{C_\infty}{s} - C|_1.$$

This leads to the solution for long times:

$$\Gamma^\mu(t) = 1 - \tilde{\epsilon}\, e^{-t/\tau_3}, \tag{20.25}$$

where $\tilde{\epsilon} = (1 + 3/\varepsilon_0)^{-1}$ and $\tau_3 = 5\varepsilon_0(1 + 3/\varepsilon_0)$. Fig. 20.4 shows the solutions for short and long times.

20.3.2. Ageing drop under evaporation

The elegant approach of the Laplace transform is now no longer possible, due to the law for ad- and desorption (20.12b) and to the second boundary condition (20.12d), both of which have variables depending on a time-dependent boundary $r = R(t)$ with $C|_{R(t)}$, a composite function. Therefore, the following calculations are performed in physical space, and no more in Laplace space.

Case 4 – Thermodynamic equilibrium

This case describes the simple model system assuming thermodynamic equilibrium all over the drop, in the bulk as well as at the drop surface, but a

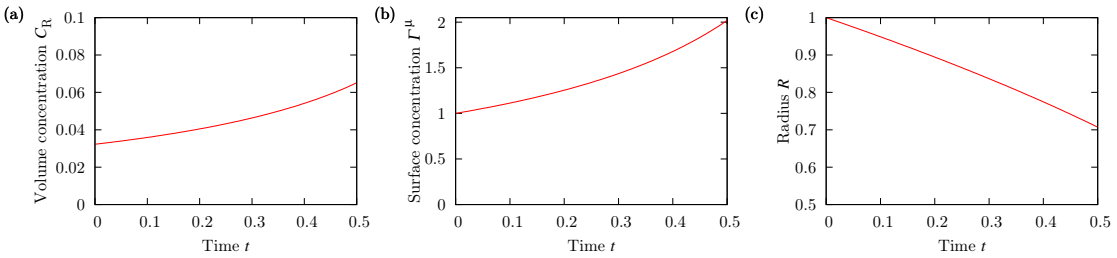

Fig. 20.5.: Case 4 – System in thermodynamic equilibrium with volume variation. (a) Volume concentration $C|_R$, (b) surface concentration $\Gamma^\mu(t)$, (c) radius $R(t)$. Time is measured in units of τ_{evap}.

time-dependent radius as dictated by equation (20.12g). In such conditions, the appropriate time scale for the process is $T = \tau_{\text{evap}}$ such that the non-dimensionalized radius of the drop may be expressed by $R(t) = \sqrt{1-t} \in [0,1]$. Thermodynamic equilibrium means that the bulk concentration is constant throughout the domain with:

$$\forall_t, \quad C(r,t) = C(R,t),$$

and that the surface concentration Γ follows $C(R,t)$, according to equation (20.16):

$$\forall_t, \quad \Gamma = C(R,t).$$

The mass balance always holds, even for a variable radius. In this case, it permits to calculate $\Gamma(t)$:

$$N = \frac{4}{3}\pi R_0^3 R(t)^3 C_0 C + 4\pi R_0^2 R(t)^2 \Gamma_e \Gamma,$$

with $C(R,t) = \Gamma$, $C_0 = N/\frac{4}{3}\pi R_0^3$ and $\varepsilon_0 = R_0 C_0/\Gamma_e$ one may write:

$$C_0 = C_0(R^3 + \frac{3}{\varepsilon_0}R^2)\Gamma$$

$$\Gamma(t) = \frac{1}{R^3 + \frac{3}{\varepsilon_0}R^2} = \frac{1}{(1-t)^{3/2} + \frac{3}{\varepsilon_0}(1-t)} \tag{20.26}$$

which is in fair agreement with case 1 ($\mathrm{d}R/\mathrm{d}t = 0$) when $\tau_{\text{evap}} \to \infty$, and for a constant radius, $R(t) \equiv 1$.

Fig. 20.5 represents the analytical solutions for different variables. At the beginning, Γ is already equal to its equilibrium value Γ_e^μ for a radius $R = 1$. As the radius diminishes, the bulk and surface concentrations consistently rise. Since the system is under thermodynamic equilibrium ($\eta_{\text{ea}} > 1$ and $\eta_{\text{ed}} > 1$), the values of C and Γ^μ rise equally: as the volume gets smaller, molecules are more packed in the bulk and along the surface.

Case 5 – Sorption-limited system

In case 5, an adsorption-limited regime with a time-dependent radius $R(t)$ is considered. This time, the appropriate time scale for the process is $T = \tau_{\text{evap}}$.

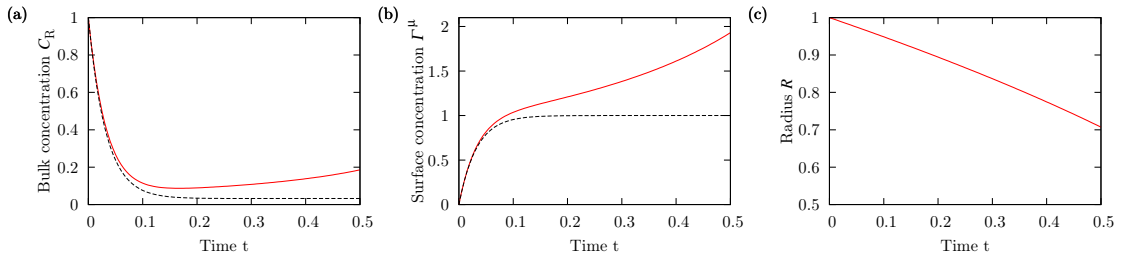

Fig. 20.6.: Case 5 – Adsorption limited system with volume variation. (a) Volume concentration $C|_R$, (b) surface concentration $\Gamma^{\mu}(t)$, (c) radius $R(t)$. (–) Graph corresponding to case 5, (- -) graph corresponding to case 2 without evaporation, (· · ·) graph corresponding to case 3 at thermodynamic equilibrium. Time is measured in units of τ_{evap}.

Starting from the mass balance, it is found that :

$$N = \frac{4}{3}\pi R_0^3 R(t)^3 C_0 C + 4\pi R_0^2 R(t)^2 \Gamma_e \Gamma,$$

$$1 = R^3 C + \frac{3}{\varepsilon_0} R^2 \Gamma.$$

With equation (20.12b) for expressing $C(r,t)$ by Γ for an adsorption-limited system, one finds the ordinary differential equation:

$$\frac{R(t)^3}{\eta_{\text{ea}}} \frac{\mathrm{d}\Gamma}{\mathrm{d}t} + (R(t)^3 + \frac{3}{\varepsilon_0} R(t)^2)\Gamma = 1$$

This differential equation has the following analytical solution:

$$\Gamma(t) = -e^{\eta_{\text{ea}}\left(\frac{6R(t)}{\varepsilon_0}\tau_{\text{evap}} - t\right)} \int_0^t \frac{\eta_{\text{ea}}}{R(t')^3} e^{-\eta_{\text{ea}}\tau_{\text{evap}}\left(\frac{6R(t')}{\varepsilon_0}\tau_{\text{evap}} - t'\right)} \,\mathrm{d}t'.$$

The integral may be evaluated numerically; the solution is shown in Fig. 20.6. As compared to case 2 (dashed line) without evaporation, the variable radius has a major influence on the adsorption behavior. For this case with $\eta_{\text{ea}} = 1$, evaporation and adsorption act about on the same time scale, which is why the interference between both processes is quite remarkable.

20.4. Finite element method

This section describes the numerical evaluation of different cases using the finite element method. The finite element method (FEM) consists in calculating the variation of a variable C defined throughout a spatial domain Ω with respect to a space variable r and time t. The variation is defined by a partial differential equation $F(C, \frac{\partial C}{\partial r}, \frac{\partial^2 C}{\partial r^2})$, initial conditions and boundary conditions on the boundary $\partial\Omega$ of the domain.

The finite element method is based on the variational principle, which relies on the fact that a functional J on a domain between two points $p_0(r_0, C(r_0))$ and

$p_1(r_1, C(r_1))$,

$$J = \int_{r_0}^{r_1} F\left(C, \frac{\partial C}{\partial r}, \frac{\partial^2 C}{\partial r^2}\right) \mathrm{d}r,$$

is characterized by a minimum value for an a priori unknown function $C(r)$. When $C(r)$ denotes the function for which J has a minimum, a variation $\bar{C}(r) := C(r) + \alpha\eta(r)$ with a constant α and an arbitrary function $\eta(r)$ makes J move away from its minimum around $C(r)$. It is demanded that $\eta(r_0)$ and $\eta(r_1)$ vanish on the borders. It may be written:

$$\left.\frac{\partial J}{\partial \alpha}\right|_{\alpha=0} = \int_{r_0}^{r_1} \left[\frac{\partial F}{\partial \bar{C}}\,\eta(r) + \frac{\partial F}{\partial\left(\frac{\partial \bar{C}}{\partial r}\right)}\frac{\partial \eta}{\partial r}\right]_{\alpha=0} \mathrm{d}r = 0.$$

From integration by parts of the second term in the integral, at $\alpha = 0$, with $\eta(r_0) = 0$ and $\eta(r_1) = 0$, it is found that:

$$\int_{r_0}^{r_1} \eta(r)\left[\frac{\partial F}{\partial C} - \frac{\mathrm{d}}{\mathrm{d}r}\frac{\partial F}{\partial(\frac{\partial C}{\partial r})}\right] \mathrm{d}r = 0,$$

which leads to the Euler-Lagrange-Equation in 1D supposing that the test function $\eta(r)$ is arbitrary:

$$\frac{\partial F}{\partial C} - \frac{\mathrm{d}}{\mathrm{d}r}\frac{\partial F}{\partial(\frac{\partial C}{\partial r})} = 0.$$

The differential equation and boundary conditions have to be transferred into their variational formulation (also "weak" formulation) which permits the solution of the problem by the finite element method. The spatial domain is divided into a mesh, consisting of different points along the domain. The domain within each mesh element is described by so-called test functions $w(r)$ which are a basis for the space coordinates. As the earlier seen test functions are of arbitrary form, $\eta(r) = w(r)$ may be chosen, without loss of generality. The temporal domain is divided into several time steps. In order to numerically calculate the solution at each time step, the variation of the variables is calculated in function of the weak formulation (calculated in the next section for the specific problem addressed in this work), consisting of the partial differential equation and the boundary conditions. The value of the variables at the actual time step are calculated in function of their values at the foregoing time step (respectively the initial condition for the first time step). In the present work, the FEM software COMSOL is used in which the weak formulation of the differential model to solve must be implemented.

20.4.1. Weak formulation

The strong formulation of the chemical problem presented in this work is basically Fick's second law of diffusion:

$$\frac{\partial C}{\partial t} - \eta_{\mathrm{Td}} \nabla \cdot \nabla C = 0.$$

After multiplication of the differential equation with a test function $w(r)$ and integration over the domain Ω, it is obtained:

$$\int_0^{R(t)} w(r) \left[\frac{\partial C}{\partial t} - \eta_{\mathrm{Td}} \nabla \cdot \nabla C \right] \mathrm{d}r = 0.$$

To find a valid weak formulation of the differential equation, any higher-order derivative needs to be transformed into a derivative of first order. One way to do this is to transcribe the differential operators in their spheric representation and to integrate by parts:

$$\int_0^{R} w(r) \left[\frac{\partial C}{\partial t} - \eta_{\mathrm{Td}} \frac{1}{r^2} \frac{\partial}{\partial r} \left(r^2 \frac{\partial}{\partial r} \right) \right] \mathrm{d}r = 0,$$

$$\int_0^{R} \left[w(r) \frac{\partial C}{\partial t} - \eta_{\mathrm{Td}} \left(\frac{2}{r} w - \frac{\partial w}{\partial r} \right) \frac{\partial C}{\partial r} \right] \mathrm{d}r - \eta_{\mathrm{Td}} w(R) \frac{\partial C}{\partial r}\Big|_R + \eta_{\mathrm{Td}} w(0) \frac{\partial C}{\partial r}\Big|_0 = 0,$$

$$\int_0^{R} \left[w(r) \frac{\partial C}{\partial t} - \eta_{\mathrm{Td}} \left(\frac{2}{r} w - \frac{\partial w}{\partial r} \right) \frac{\partial C}{\partial r} \right] \mathrm{d}r = 0. \tag{20.27}$$

In the last step it is used that the test function may be chosen such that $w(0) = w(R) = 0$ vanish at the boundaries of the domain.

Furthermore, the boundary conditions have to be transcribed into their weak formulations. Since the strong formulations are:

$$\frac{\partial C}{\partial r}\Big|_{r=0} = 0,$$

$$-\frac{\partial C}{\partial r}\Big|_{r=R} = \frac{1}{\varepsilon_0 \eta_{\mathrm{Td}}} \left(\frac{\mathrm{d}\Gamma}{\mathrm{d}t} + \frac{\mathrm{d}R}{\mathrm{d}t} \left(\varepsilon_0 C(R,t) + \frac{2\Gamma}{R} \right) \right),$$

the associated weak formulations for the boundary conditions read, respectively for $r = 0$ and $r = R$:

$$\int_0^{R} w \frac{\partial C}{\partial r}\Big|_{r=0} \mathrm{d}r = 0,$$

$$-\int_0^{R} w \frac{\partial C}{\partial r}\Big|_{r=R} \mathrm{d}r = \int_0^{R} \frac{1}{\varepsilon_0 \eta_{\mathrm{Td}}} w \left(\frac{\mathrm{d}\Gamma}{\mathrm{d}t} + \frac{\mathrm{d}R}{\mathrm{d}t} \left(\varepsilon_0 C(R,t) + \frac{2\Gamma}{R} \right) \right) \mathrm{d}r.$$

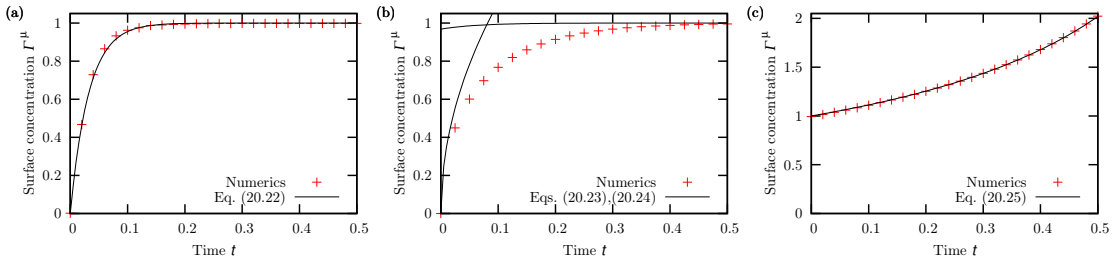

Fig. 20.7.: Comparison between numerical calculations and analytical solution ($\varepsilon = 0.1$. (a) Asdorption-limited regime without evaporation. (b) Diffusion-limited regime without evaporation. (c) Sorption equilibrium with evaporation. Time is non-dimensionalized by τ_{ads}, τ_{diff} and τ_{evap} for (a), (b) and (c), respectively.

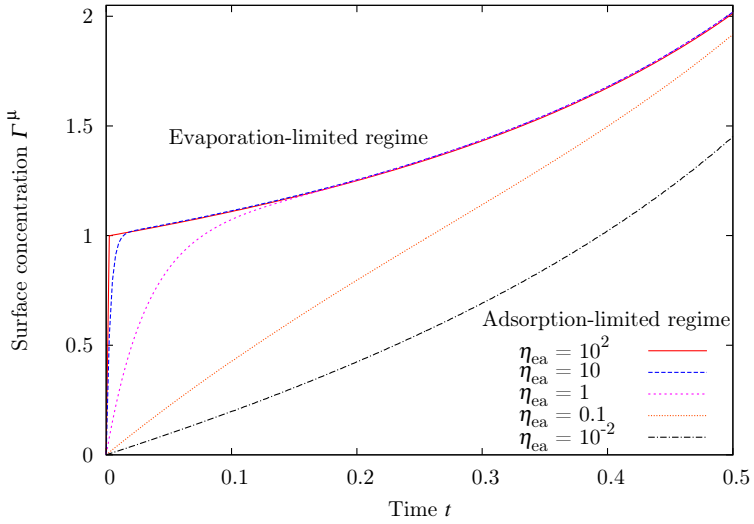

Fig. 20.8.: Dependence of surface ageing on the non-dimensional number η_{ea}: from bottom to top: 0.01, 0.1, 1, 10, 100. Time is measured in units of τ_{evap}, the other non-dimensional numbers are $\gg 1$, except $\varepsilon_0 = 0.1$.

20.4.2. Validation of the numerical simulation

To benchmark the simulation and the respective numerical parameters (cf. appendix F) under COMSOL software, a comparison is made to the analytical solutions derived in section 20.3. Figure 20.7 demonstrate the analytical predictions for cases 2, 3 and 4, which are compared to the results delivered by the simulation: Case 2 represents a benchmark for an adsorption-limited regime, case 3 follows a diffusion-limited regime and case 4 is calculated for thermodynamic equilibrium with a variable radius. Thus, each element of the simulation is compared to its analytical equivalent. The agreement between the numerical and analytical solutions is excellent.

Furthermore, the mass conservation is calculated using $\mathrm{abs}(N - N0)/N0$, comparing the total amount of molecules in the system, $N(t) = \oint_\Omega C(r,t)\mathrm{d}V + S\Gamma$, to the initial amount of molecules in the system, $N_0 = C_0 V_0$. The conservation of mass is obeyed to the order of about 1.5 ‰, which may be increased arbitrarily by refining the mesh structure and time stepping in the numerical calculation, to the detriment of the duration of the calculations.

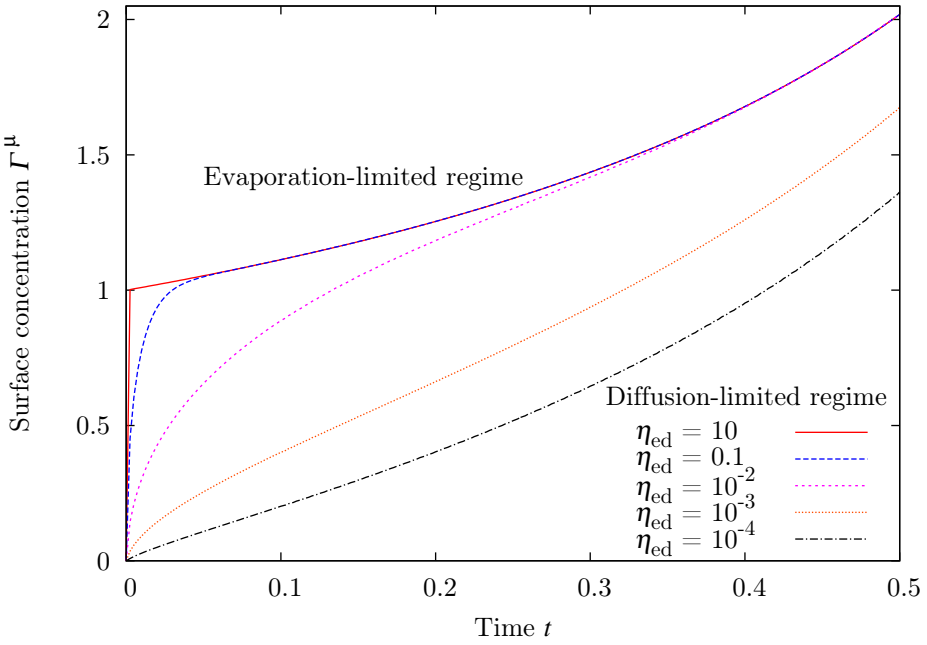

Fig. 20.9.: Adimensional number η_{ed}. Time is measured in units of τ_{evap}, the other non-dimensional numbers are $\gg 1$, except $\varepsilon_0 = 0.1$.

20.5. Non-dimensional analysis

In the case of diffusion-adsorption modeling, four dimensionless numbers have been made evident, η_{ea}, η_{ed}, η_{ad} and ε_0 (cf. equation (20.2)). By varying the factors constituting these non-dimensional numbers, generic predictions about different systems may be made. Throughout this section, the studied systems exhibit a finiteness of $\varepsilon = 0.1$, and all other dimensionless numbers are $\gg 1$, if not indicated otherwise. This ensures analyzing a finite system, and not being affected by a limiting regime except for the non-dimensional number studied.

20.5.1. Evaporation-limited versus adsorption-limited regime

The examined system is considered as adsorption-limited with a variable radius. Fig. 20.8 shows $\Gamma^{\mu}(t)$ curves for different $\eta_{ea} = 10^{-4} \ldots 100$. For $\eta_{ea} = 10^{-4}$, adsorption kinetics is slow and evaporation is fast (lowermost curve). For $\eta_{ea} = 100$, adsorption kinetics is fast and evaporation is slow (uppermost curve).

For $\eta_{ea} = 10^{-4}$, the small amount of initially adsorbed molecules and the molecules initially solubilized in the vicinity of the surface contribute to raise the surface concentration during deflation of the surface, induced by evaporation. The actual adsorption kinetics is too slow to be detected in the curve. As η_{ea} increases, the adsorption kintics is more and more evident, the system approaches the adsorption-limited regime as described in case 6. For $\eta_{ea} = 100$, adsorption is fast (or evaporation is slow), that thermodynamic equilibrium may be assumed, which corresponds to the regime described in case 2.

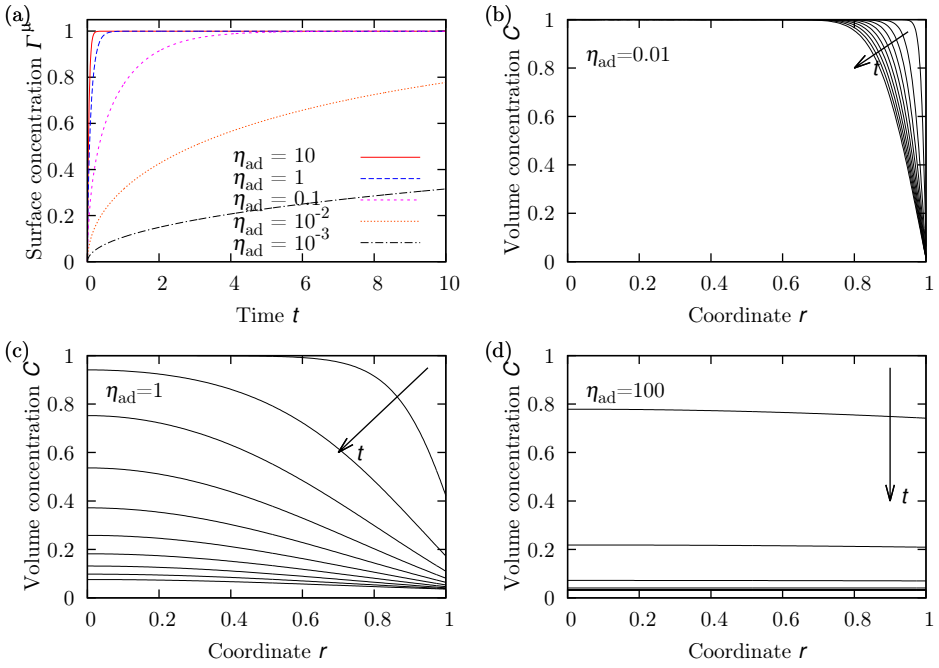

Fig. 20.10.: Impact of the non-dimensional number η_{ad} ($\varepsilon_0 = 0.1$) with (a) Γ^{μ}-t-curves for different values of $\eta_{ad} = 0.001 \ldots 10$ and radial distributions of the bulk concentration for (b) $\eta_{ad} = 0.01$, (c) $\eta_{ad} = 1$, (d) $\eta_{ad} = 100$, respectively, from the diffusion-limited to the adsorption-limited regimes. Time is measured in units of τ_{ads}, the time step between adjacent curves is $t = 0.005$. The other non-dimensional numbers are $\gg 1$, except $\varepsilon_0 = 0.1$.

20.5.2. Evaporation-limited versus diffusion-limited regime

Consider a diffusion-limited regime in presence of evaporation. The adsorption kinteics is considered as instantaneous such that thermodynamic equilibrium holds at any instant. Hence, the governing non-dimensional number is η_{ed}. The values of η_{ed} vary from 1×10^{-4} to 10 as described in Fig. 20.9. For small values (lowermost curve), diffusion kinteics is found much slower than evaporation. For high values (uppermost curve), diffusion acts much faster than evaporation.

The reasoning is similar to the adsorption-limited regime in the previous section. For $\eta_{ed} = 10^{-4}$, the main part of surface concentration increase is achieved by evaporation and subsequent deflation of the surface. For intermediate η_{ed}, the regime is mixed. For $\eta_{ed} = 10$, the system may be considered in thermodynamic equilibrium, since diffusion kinetics reveals to be instantaneous.

20.5.3. Adsorption-limited versus diffusion-limited regime

Consider now a finite-sized system without evaporation. The considered non-dimensional number is η_{ad}, which is a measure of the balance between adsorption and diffusion kinetics. A high η_{ad} will indicate an adsorption-limited regime, while a low η_{ad} will indicate a diffusion-limited regime. The difference is shown in Fig. 20.10 where several curves are presented for $\eta_{ad} = 0.001 \ldots 10$.

The bulk concentration behavior for $\eta_{ad} = 0.01$ is similar to a diffusion-limited regime: compared to adsorption, diffusion kinetics is so slow that it is not possible to recover a uniform distribution of the volume concentration. For $\eta_{ad} = 10$, diffusion is quick enough to re-establish a uniform volume concentration in the vicinity of the surface, despite adsorption of surfactant molecules (adsorption-limited regime). These two graphs, (b) and (d), show the main difference between a diffusion- and an adsorption-limited regime, a point which is not necessarily made evident from the adsorption-kinetics presented in Fig. 20.10(a).

20.5.4. Finite-sized systems versus half-space systems

To demonstrate the impact of finite size, the non-dimensional number ε_0 has been introduced. A liquid system with a sufficiently high value of ε_0 is approximated relatively well by the classical half-space approximation with, equivalently, an infinite source of surfactants far from the interface (far field condition for volume concentration). Conversely, a system with a small value of ε_0 is characterized by its finite size (a droplet typically) with a finite amount of surfactants. At this point, it is useful to recall the expression, $\varepsilon_0 = R_0 C_0/\Gamma_e$, which might be seen as a balance between two molar amounts: a first amount distributed throughout the liquid surface and a second amount solubilized within the liquid system. By recalling thermodynamic equilibrium far from steric conditions, $k_a/k_d = \Gamma_e/C_0$, and the radius, R_0, characterizing the initial geometry, the following is recovered: $\varepsilon_0 = k_d R_0/k_a$.

The foregoing analysis is illustrated in Fig. 20.11, which depicts the impact of ε_0 on chemical kinetics. For systems with a small value of ε_0, surface ageing kinetics is consistently sped up, since system size is diminished (diffusion is enhanced), but the outcome stays the same: all systems tend to $\Gamma^\mu = 1$ at long times, whichever the value of ε_0. Conversely, the bulk diffusion of such systems is greatly affected by ε_0: systems with a small value of ε_0, like those shown in Fig. 20.11(b) and (c), yield a strong variation of concentration throughout the entire domain. For a small ε_0, the system is practically emptied of molecules at long times, and the asymptotic limit for the volume concentration, $C(r, t \to \infty) \to 1/(1+3/\varepsilon_0)$, is represented as a dashed line in Fig. 20.11. For a large ε_0, the impact of adsorption on the bulk concentration is clearly reduced, and its value tends consistently to unity (the far field condition, $\lim_{x\to\infty} C(x,t) = 1$, tends to be recovered). For a liquid system where $\varepsilon_0 \gg 1$, the classical results based on the far field condition are consistently recovered with the present model: the far field condition, $\lim C(x,t) = 1$, is perfectly satisfied.

20.5.5. Triton X-100 as an example of surfactant among others.

As an example, Triton X-100 is considered as a well-known non-ionic surfactant [115], with a chemical diffusivity, $D = 7 \times 10^{-7}\,\mathrm{cm^2/s}$, and an initial concentration, $C_0 = 1.55 \times 10^{-10}\mathrm{mol/cm^3}$. The critical drop radius for an air/water interface is found to be $R_c^{\mathrm{TRX100,w/a}} = 17\,\mu\mathrm{m}$, using $\varepsilon_0 = 1$, $k_d = 100\,\mathrm{s^{-1}}$ and

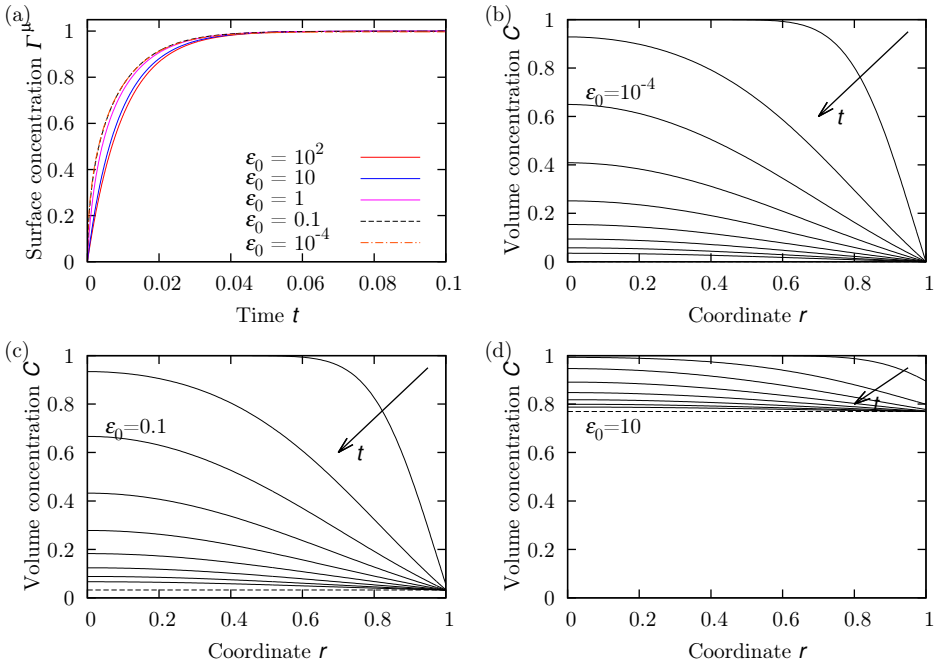

Fig. 20.11.: Discussion of the non-dimensional number ε_0. (a) Γ^{μ}-t-curves for different values of $\varepsilon_0 = 10^{-4} \ldots 100$. (b), (c) and (d) show different bulk concentration behaviors for $\varepsilon_0 = 10^{-4}$, 0.1 and 10, respectively (—). The behaviors tend to a regime of Ward-Tordai-type (panel (d)). The time step between two adjacent curves in a same graph is $t = 0.005$. The dashed line (– –) represents the bulk concentration value for $t \to \infty$. Time is measured in units of τ_{ads}, the other non-dimensional numbers are $\gg 1$.

$\Gamma_e = 2.7 \times 10^{-10}\,\text{mol/cm}^2$. This means that a µL-sized drop in a standard digital lab-on-a-chip can be considered as a semi-infinite system as long as the drop is larger than 100 µm. Whereas for the water/hexane interface ($k_d = 60\,/\text{s}$, $\Gamma_e = 1.63 \times 10^{-10}\,\text{mol/cm}^2$, the critical drop radius is $R_c^{\text{TX100,w/h}} = 11\,\mu\text{m}$. Hence, water/hexane mini- or nano-emulsions must be considered as finite systems to which the present theory is relevant.

Triton X-100 is only one example of many, and each surfactant specie (lipids, bio-molecules, nano-particles, etc.) needs to be evaluated independently considering its diffusion and adsorption properties for the respective volume and ambient phases.

20.6. Extension to sessile drops of arbitrary contact angle with instantaneous diffusion

The present model is extended to the case of a sessile drop with an arbitrary contact angle, but only a regime with (quasi) instantaneous diffusion can be considered.[5] The geometry of a (small enough) sessile drop corresponds to a spherical cap of radius R, with a contact angle $0 < \theta \leq \pi$. The diffusion kinetics is considered much faster than the adsorption and evaporation kinetics

[5]For an arbitrary value of contact angle, the diffusion equation (20.12a) on page 127 can not be analytically solved, especially when it is coupled with surface ageing.

($\tau_{\mathrm{diff}} \ll \tau_{\mathrm{ads}}, \tau_{\mathrm{evap}}$), such that the transport equation (20.12a) on page 127 does not need to be considered. Instead, the relation between surface and volume concentration, Γ and C, respectively, may be expressed by the non-dimensional equation for mass balance:

$$C = \frac{1}{R^3} - \frac{3\hat{F}}{\varepsilon_0 R}\Gamma, \tag{20.28}$$

where the form factor, $\hat{F} = 2/(1-\cos\theta)(2+\cos\theta)$, is introduced, translating the dependencies of the drop volume to surface ratio on the contact angle, θ. Hence, the Henry law (20.5) may be non-dimensionalized reformulated to express the surfactant transport at the surface:

$$j_{\mathrm{ads}} = \eta_{\mathrm{ea}} \left(C_1 - \Gamma\right),$$

and equation (20.28) may be substituted to find an expression of the adsorption flux without direct dependence on the volume concentration:

$$j_{\mathrm{ads}} = \eta_{\mathrm{ea}} \left[\frac{1}{R^3} - \left(\frac{3\hat{F}}{\varepsilon_0 R} + 1\right)\Gamma\right]. \tag{20.29}$$

Furthermore, to express the impact of the variable radius on surface concentration, the mass conservation for a spherical cap needs to be reconsidered:

$$0 = \frac{\mathrm{d}}{\mathrm{d}t}\left(\oint_{V(t)} C \,\mathrm{d}V\right) + \frac{3\hat{F}}{\varepsilon_0}\left(2R\Gamma\frac{\mathrm{d}R}{\mathrm{d}t} + R^2\frac{\mathrm{d}\Gamma}{\mathrm{d}t}\right).$$

With the Leibniz integral rule for differentiation under the integral sign for time-dependent limits, and subsequent substitution of Fick's second law (equivalent to the calculation of equation (20.3) on page 122), it is found:

$$0 = R^2 C\frac{\mathrm{d}R}{\mathrm{d}t} + \frac{3\hat{F}}{\varepsilon_0}\left(2R\Gamma\frac{\mathrm{d}R}{\mathrm{d}t} + R^2\frac{\mathrm{d}\Gamma}{\mathrm{d}t}\right),$$

using $\eta_{\mathrm{ed}} \to \infty$ ($\tau_{\mathrm{diff}} \to 0$). By substituting equation (20.28) into the latter equation and rearranging, an expression for the evaporation flux is found:

$$j_{\mathrm{evap}} = -\frac{\mathrm{d}R}{\mathrm{d}t}\left(\frac{\varepsilon_0}{3\hat{F}R^3} + \frac{\Gamma}{R}\right). \tag{20.30}$$

Combining equations (20.29)-(20.30) and writing,

$$\frac{\mathrm{d}\Gamma}{\mathrm{d}t} = j_{\mathrm{ads}} + j_{\mathrm{evap}},$$

an ordinary differential equation for the surface concentration can be derived as:

$$\frac{\mathrm{d}\Gamma}{\mathrm{d}t} = P(t) + Q(t)\Gamma, \tag{20.31}$$

with the time-dependent coefficients,

$$P(t) = \frac{1}{R^3}\left(\eta_{\mathrm{ea}} - \frac{\varepsilon_0}{3\hat{F}}\frac{\mathrm{d}R}{\mathrm{d}t}\right),$$

and

$$Q(t) = -\left(\frac{1}{R}\frac{\mathrm{d}R}{\mathrm{d}t} + \eta_{\mathrm{ea}}\left(\frac{3\hat{F}}{\varepsilon_0 R} + 1\right)\right).$$

The evaporation law (20.12g) also has to be modified for arbitrary contact angles:

$$R(t)^2 = 1 - 4\,t/F(\theta),$$

with $F = 2 - 3\cos\theta + \cos^3\theta$ (equation (15.1) on page 96). From this last expression for the time-dependent radius of the spherical cap, the differential equation (20.31) can be solved by making use of the Lagrange integral factor, $\exp(\int P(t)\,\mathrm{d}t)$.

Also, the surface concentration equilibrium value for microscopic systems, $\Gamma_{\mathrm{e}}^{\mu}$, depends on the contact angle. It may be calculated in diffusion-adsorption equilibrium ($\mathrm{d}\Gamma/\mathrm{d}t = 0$) without evaporation:

$$\Gamma_{\mathrm{e}}^{\mu} = \frac{\Gamma_{\mathrm{e}}}{1 + \frac{3\hat{F}}{\varepsilon_0}}.$$

Figure 20.12 represents the dimensionless curves for different contact angles ranging from $\pi/6$ to π, for the non-dimensional numbers, $\varepsilon_0 = 0.1$ and $\eta_{\mathrm{ea}} = 1$. It is remarkable that in the hydrophobic range, $\pi/2 \leq \theta \leq \pi$, surface ageing is hardly affected by a change in the contact angle, whereas in the hydrophilic range, $\pi/6 \leq \theta \leq \pi/2$, the impact of the contact angle becomes significant.

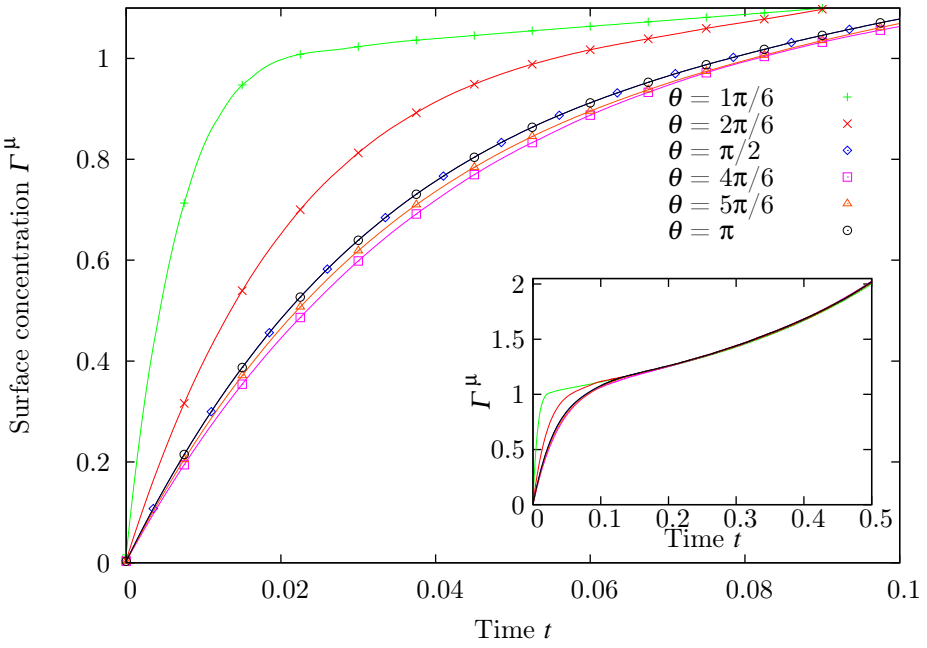

Fig. 20.12.: Impact of the contact angle, θ, upon surface ageing ($\varepsilon_0 = 0.1$, $\eta_{ea} = 1$). Hydrophilic, hydrophobic and superhydrophobic contact angles are considered. The curves for $\theta = \pi/2$ and $\theta = \pi$ yield consistently the same result as the one issued from the generalized formulation based on a spherical geometry (see Fig. 20.8 for comparison). Time is measured in units of τ_{evap}. The insert shows the same curves during a longer time (up to $0.5\,\tau_{evap}$).

21. Conclusion

In this part, a mathematic model for an (isotropic) spherical drop populated by soluble surfactants and subjected to diffusion and adsorption is developed in connection with evaporation-driven variation of the geometry. The known model used by Ward & Tordai, Filippov & Filippova and others is revisited via the outer boundary condition, which includes the time-dependent radius at the outer boundary of the liquid domain. Different cases are solved analytically in order to serve as benchmark for numerical simulations based on the finite element method and on the use of COMSOL software. In this way, several cases are analyzed: thermodynamic equilibrium and diffusion- and adsorption-limited regimes with and without evaporation. The results are compared to the actual state of the art.

The role of different non-dimensional numbers is evaluated later on: η_{ea}, characterizing the transition between evaporation- and diffusion-limited regimes; η_{ed}, characterizing the transition between evaporation- and diffusion-limited regimes. The transition between adsorption- and diffusion-limited regimes is characterized by η_{ad}. Regarding the finiteness of the liquid system, the non-dimensional number ε_0 is introduced in order to estimate how geometrical and physicochemical parameters influence adsorption in a finite system.

As a major result in this chapter, the surface concentration for microscopic systems, $\Gamma_{\mathrm{e}}^{\mu}$, is proposed as a new surface concentration scale. It is a very helpful parameter for design of microscopic systems and emulsions, for estimation of maximum solute concentrations. These values are smaller than for macroscopic systems, as the surface to volume ratio is diminished for microsystems. This is essential for expensive or time-consuming to produce molecules, as their use in a microsystem diminishes the necessary total quantity.

One first way to pursue this investigation is taking into account the Langmuir model for ad- and desorption phenomena (cf. Table 20.1):

$$\frac{\mathrm{d}\Gamma}{\mathrm{d}t} = k_{\mathrm{a}} C|_R \left(1 - \frac{\Gamma}{\Gamma_\infty}\right) - k_{\mathrm{d}} \frac{\Gamma}{\Gamma_\infty}$$

This model includes a parameter Γ_∞ which represents the maximum package concentration at the interface, when steric hindrance impedes further accumulation of surfactants along the surface. The adsorption rate tends to zero when $\Gamma \to \Gamma_\infty$, and the desorption rate tends to k_{d}, when $\Gamma \to \Gamma_\infty$. As a first improvement, a surface concentration $\Gamma > \Gamma_\infty$ can never be reached. Keeping this in mind, one may calculate an effective non-dimensional number $\varepsilon_0^{\mathrm{LM}}$ associated

to the Langmuir law:

$$\varepsilon_0^{\mathrm{LM}} = \frac{R_0 C_0}{\Gamma_{\mathrm{e}}^{\mathrm{LM}}} = \frac{R_0 C_0}{\Gamma_\infty}\left(1 - \frac{k_{\mathrm{d}} C_0}{k_{\mathrm{a}}}\right) \lesssim \frac{R_0 C_0}{\Gamma_\infty},$$

where $\Gamma_{\mathrm{e}}^{\mathrm{LM}}$ is the equilibrium surface concentration. Once Γ_∞ is reached, the surface is no longer able to adsorb any more molecules, the bulk concentration is no further affected by adsorption, meaning that a finite system is more difficult to realize for surfactants and concentrations yielding the use of the Langmuir law.

Conversely, the necessity to employ the Langmuir law is equally justified by the fact that the bulk concentration must be high enough in order for steric hindrance to become a limiting factor. This mainly depends on the surface-to-volume ratio of the considered system. As this ratio is low, enough molecules are present in the volume to densify the surface and experience steric effects. But as for finite systems, per definition, the surface-to-volume ratio exhibits a high value, the use of the Langmuir law will be necessary only for some special cases.

22. Streaming & surface diffusion

In contrast to the foregoing chapter 20 on diffusion, adsorption and evaporation processes creating isotropic volume concentration gradients in the applied conditions, steady streaming as a new physical process will now be introduced. It is induced by electrowetting-driven drop shape oscillations and contributes to a non-isotropic component to surfactant transport in the volume and along the drop surface. *Via* this convective mechanism, stirring or mixing enhancement of surface ageing kinetics is investigated.

The streaming current, which was theoretically introduced in chapter 6, displaces surfactant molecules and thus creates a non-isotropic distribution in the volume and at the surface of the drop. Several effects might ameliorate (or deteriorate) the efficiency of surfactant transport in the volume and at the surface, namely adsorption kinetics and the total amount of adsorbed molecules. First of all, the streaming current might accelerate the dispersion of molecules throughout the droplet, a kind of mixing, to outrun diffusion. Secondly, stirring might help to reinforce the surface concentration in one or several points (rings) along the surface, corresponding to the stagnation points of internal flows. The streaming current may thereby make the capillary wave pattern more sensible to the surfactant molecules. Molecular recognition might thereby increase sensitivity. As the cited effects might as well involve the opposite outcome (slower stirring time, lower sensitivity), the streaming current is included into the simulations. Since it engenders a non-uniform surface concentration, the effect of molecular diffusion within the surface may no longer be neglected.

22.1. Interfacial surfactant transport

The interfacial transport mechanism has until now been described by equation (20.3), $\mathrm{d}\Gamma/\mathrm{d}t = -D\,(\partial C/\partial r)|_{r=R} - (C + 2\Gamma/R)\,\mathrm{d}R/\mathrm{d}t$, which was nicely derived from mass balance. This equation does not reflect the whole truth. In order to complete it for streaming and surface diffusion, one may consider the equation for surfactant transport along an interface, also based on mass conservation. Considering a surfactant-laden interface, S (surface concentration Γ), without sorption processes, phase change and surfactant sources, the principle of mass conservation is used to introduce the missing terms for surface streaming current. The mass balance states that the quantity of surfactant molecules adsorbed to the surface, N, does not change with time. This quantity may be expressed by the integral over the whole surface, S:

$$\frac{\mathrm{d}}{\mathrm{d}t}N = \frac{\mathrm{d}}{\mathrm{d}t}\iint_S \Gamma\,\mathrm{d}S = \iint_S \frac{\mathrm{d}\Gamma}{\mathrm{d}t}\,\mathrm{d}S + \iint_S \Gamma\frac{\mathrm{d}}{\mathrm{d}t}\,\mathrm{d}S = 0.$$

Using elementary differential calculus, mainly the chain rule and partial integration, the terms of the above equation are transformed [112]. The first term on the right hand side becomes:

$$\iint_S \frac{\mathrm{d}\Gamma}{\mathrm{d}t}\,\mathrm{d}S = \iint_S \left(\frac{\partial \Gamma}{\partial t} + \boldsymbol{u}_\mathrm{s}\cdot(\nabla_s\Gamma)\right)\mathrm{d}S, \tag{22.1}$$

the second term becomes:

$$\iint_S \Gamma\frac{\mathrm{d}}{\mathrm{d}t}\mathrm{d}S = \iint_S \Gamma\ ((\nabla_\mathrm{s}\cdot\boldsymbol{u}_\mathrm{s}) + (\nabla\cdot\boldsymbol{n})(\boldsymbol{u}\cdot\boldsymbol{n}))\,\mathrm{d}S. \tag{22.2}$$

The first term (22.1) stands for transient surfactant concentration change, $\partial\Gamma/\partial t$, and a convection term, $\boldsymbol{u}_\mathrm{s}\cdot(\nabla_\mathrm{s}\Gamma)$. The velocity $\boldsymbol{u}_\mathrm{s}$ and the del operator ∇_s are the volume velocity of the flow along the drop surface and the del operator projected onto the tangent plane of the surface. This is done using a projection operator, $(\mathbb{1}-\boldsymbol{n}\otimes\boldsymbol{n})$ on the volume velocity, $\boldsymbol{u}$, and the del operator, ∇.

The first term on the right hand side of the second term (22.2) stands for surface stretching (retraction and elongation), $\Gamma\,(\nabla_\mathrm{s}\cdot\boldsymbol{u}_\mathrm{s})$. The second term, $\Gamma(\nabla\cdot\boldsymbol{n})(\boldsymbol{u}\cdot\boldsymbol{n})$, represents inflation and deflation of the surface due to, e.g. evaporation ($\boldsymbol{u}\cdot\boldsymbol{n}<0$), condensation ($\boldsymbol{u}\cdot\boldsymbol{n}>0$), or Ostwald ripening ($\boldsymbol{u}\cdot\boldsymbol{n}\neq 0$). The formulation needs to be completed with the already known contributions for sorption processes, j_ads, and a possible surfactant sources, σ, at the interface. Last but not least, a term for surface diffusion, $D_\mathrm{s}\nabla_\mathrm{s}\cdot\nabla_\mathrm{s}\Gamma$, is included, equivalent to Fick's second law of chemical species transport. It is obtained by projecting Fick's second law onto the surface. A gradient of surfactant concentration along the surface will engender a re-equilibration of surfactant density according to this surface diffusion term. The complete equation for interface surfactant transport reads:

$$\frac{\partial\Gamma}{\partial t} - \nabla_\mathrm{s}\cdot(D_\mathrm{s}\nabla_\mathrm{s}\Gamma) + (\nabla_\mathrm{s}\cdot\boldsymbol{u}_\mathrm{s})\Gamma + \boldsymbol{u}_\mathrm{s}\cdot(\nabla_\mathrm{s}\Gamma) + (\nabla\cdot\boldsymbol{n})(\boldsymbol{u}\cdot\boldsymbol{n})\Gamma = j_\mathrm{ads}+\sigma. \tag{22.3}$$

For the calculus, the notation will differ on whether del is used as a divergence, $\nabla_\mathrm{s}\cdot\boldsymbol{h}$, on a vector function, $\boldsymbol{h}$, or a gradient $\nabla_s h$, operator on a scalar function, h. The volume velocity, $\boldsymbol{u}$, may be transformed into the surface velocity, with $\boldsymbol{u}_\mathrm{s} = (\mathbb{1}-\boldsymbol{n}\otimes\boldsymbol{n})\,\boldsymbol{u}$, while here it is not mandatory in the case of steady streaming, since the streaming velocity, $\boldsymbol{U}_\mathrm{s} = U_\mathrm{s}\,\boldsymbol{t}$, already is tangent to the surface ($\boldsymbol{t} = (\mathbb{1}-\boldsymbol{n}\otimes\boldsymbol{n})\,\boldsymbol{t}$).

22.2. Adaptation of the surfactant transport equation to drop surface ageing in the presence of streaming

In order to implement the above equation of surface surfactant transport, it is necessary to know, which physical phenomena are interesting in the case of drop steady streaming. Therefore, the analysis of four values characterizing streaming may help (cf. chapter 6):

- $\xi = U_\infty/\omega R$, condition for streaming flow and application of the approximation done by Schlichting, $0 < \xi \ll 1$.
- $\delta_s = \sqrt{\eta/\rho\omega}$, Stokes layer thickness, $\delta_s \ll R$.
- $R_s = \rho U_\infty^2/\omega\eta$, condition for streaming flow extension beyond the Stokes layer, $R_s > 1$.
- $\delta_{Stu} = \sqrt{\eta/\rho\omega}/\xi$, penetration depth of streaming reflux, $\delta_{Stu} \approx R$.

For a 1 µL drop under oscillating electrowetting, the working conditions are typically the following: averaged radius $R = 1$ mm, oscillation mode $n = 2$ and pulsation $\omega_2 = 1500$ rad/s, oscillation amplitude $va_2^0 = 100$ µm. The following values are found: Schlichting parameter $\xi \approx 0.05$, the Stokes layer is about $\delta_s = 30$ µm thick, $R_s \approx 3.75$ and the Stuart depth is about $\delta_{Stu} = 0.6$ mm. These conditions suggest two important upshots:

- The Stokes layer is present with a thickness of several tens of µm.
- All conditions for steady streaming are fulfilled: Schlichting condition, condition for volume streaming, Stuart depth for streaming.

Conclusions may be made from these conditions: The Stokes layer is larger than the size of biological molecules, which are smaller than about 1 µm. The Stokes layer is the part of the flow pattern, which is governed by random vorticity and zero net flow. For this reason, the streaming does not contribute to surfactant convection at the surface, neither to surface retraction nor elongation. Thus, these two contributions may be disregarded when it comes to the formulation of interfacial surfactant transport.

Second, the conditions for steady streaming are present: Schlichting condition, condition for streaming flow beyond the Stokes layer (R_s) and a sufficiently large Stuart depth for penetration of the streaming flux into the volume. Streaming is thus to be taken into account for volumic surfactant convection. This is not in direct link to the interfacial transport equation, but nevertheless needs to be implemented into the numerical calculation. Volumic surfactant convection causes a gradient of surfactant concentration at the surface via the adsorption term in Henry's law, which is why it is necessary to consider surface diffusion. Evaporation and surfactant sources will not be treated in this part of the thesis, which is why the corresponding terms equal zero. Hence, the actual equation for interface surfactant transport is the following:

$$\frac{\partial \Gamma}{\partial t} - \nabla_s \cdot (D_s \nabla_s \Gamma) = j_{ads}. \tag{22.4}$$

This equation describing interface surfactant transport is now implemented for numerical analysis.

22.3. FEM implementation in 2D

As streaming is not an isotropic phenomenon – it depends on the polar angle φ –, the simplification of the three-dimensional system to a one-dimensional

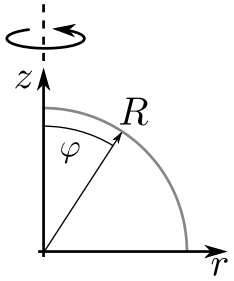

Fig. 22.1.: Geometry and coordinates used in COMSOL for the implementation of streaming. The symmetry axis is drawn with a dashed line.

mathematical problem, as in chapter 20 on diffusion, adsorption and evaporation only, is not possible anymore. The remaining symmetry is a rotational symmetry corresponding to the azimuthal angle. As of this, as far as the implementation in COMSOL is concerned, the geometry mode *2D axial symmetry* may be used to implement the equations. The symmetry axis is defined as the axis connecting the apex to the center of the droplet's base.

This geometry mode uses a cylindrical coordinate system based on two coordinates (r, z): r, the radial component and z, the vertical axis. In this coordinate system, a quadrant of a circle is used on the positive r- and z-axes, the symmetry axis being the z-axis ($r = 0$) and the base axis being the r-axis ($z = 0$), cf. Fig. 22.1. The polar angle, φ, is thus not taken into account for the calculations. For further technical details and for the calculation of the weak contributions used in this chapter, please refer to appendix G.

22.3.1. Implementation of the model without streaming and benchmarking

The purpose of this section is to use the one-dimensional model presented in the foregoing chapter as a benchmark for a two-dimensional model. In theory, the case for a free spherical drop (chapter 20) and a sessile drop of contact angle $\pi/2$ are equivalent, provided that adsorption on the solid substrate is neglected. For this case, which is treated in this section, diffusion and sorption phenomena will be taken into account using Fick's and Henry's laws for benchmarking. As of this, evaporation, surface diffusion and streaming processes will not be discussed for the moment.

Nevertheless, the numerical method and design of the domain need to be prepared to integrate these processes. Hence, a geometry is chosen, in which all of the processes can be progressively included. As already mentioned, the two-dimensional axial symmetry is preserved, whereas the polar rotational symmetry is broken by the streaming current configuration.

The strong form of the surfactant transport equation, which is used for benchmarking, is the following:

$$\frac{\partial \Gamma}{\partial t} = j_{\mathrm{ads}} = (k_{\mathrm{a}} C|_R - k_{\mathrm{d}} \Gamma).$$

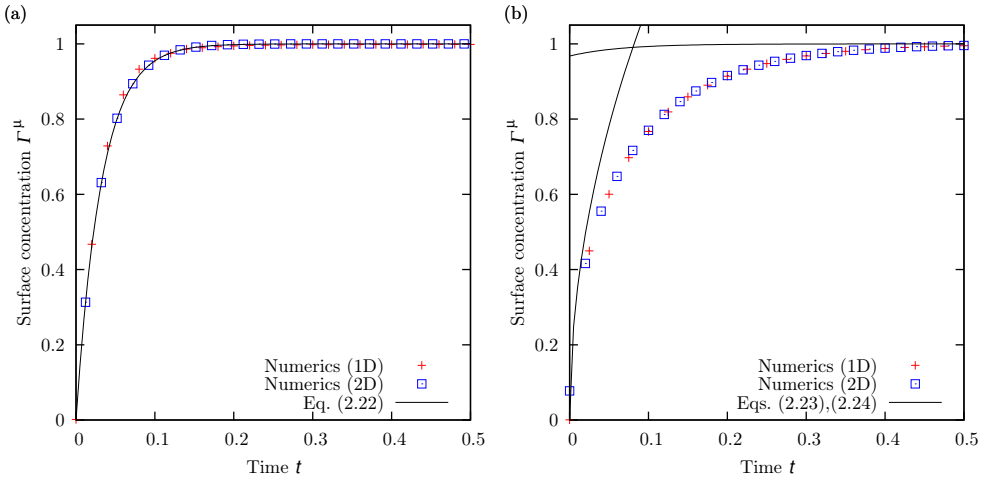

Fig. 22.2.: Comparison between the analytical solution, (–) and the numerical solutions of the 1D (+) and 2D (□) implementation.

The corresponding weak form is (please refer to appendix G):

$$\iint_S w(r,z)\left[\frac{\partial \Gamma}{\partial t} - (k_\mathrm{a} C|_R - k_\mathrm{d}\Gamma)\right] \mathrm{d}S = 0, \tag{22.5}$$

which is simple compared to the full coupling involving streaming and surface diffusion contributions. The results of the simulation using this weak form permit though a comparison to the analytical and numerical solutions of the one-dimensional model. This comparison is done in figure 22.2: Panel (a) shows the comparison for an adsorption-limited regime with quasi-homogeous bulk concentration, the equivalent of case 2 in section 20.3.1 (cf. page 135). The three curves for analytical and numerical solutions coincide. Panel (b) shows the comparison for a diffusion-limited regime with quasi-instantaneous adsorption/desorption equilibrium, corresponding to case 3 (cf. page 136). The analytical long- and short-time approximations perfectly matched by the numerical solutions. The two latter solutions coincide and suggest a correct implementation of the model in one- and two-dimensional geometries. The mass balance calculated via $(N - N_0)/N_0$, using the total amount of molecules, $N(t) = \oint_V C \, \mathrm{d}V + \oint_S \Gamma \, \mathrm{d}S$, and the initial amount of molecules, N_0, is constantly found to be smaller than 1 %. These results suggest, that the implementation of the diffusion-adsorption model using the weak formulation (22.5) in cylindrical coordinates is correct. It may now be considered to implement the last two physical mechanisms, surface diffusion and streaming, into the simulation.

22.3.2. Implementation of surface diffusion

Surface diffusion is an important ingredient before implementing the effects of streaming current. The reason for this lies in the fact that streaming is expected to generate a concentration gradient along the drop surface, which may complicate the numerical solution. By integrating surface diffusion, all concentration gradients are smoothed, such that the convergence of the calculation is favored.

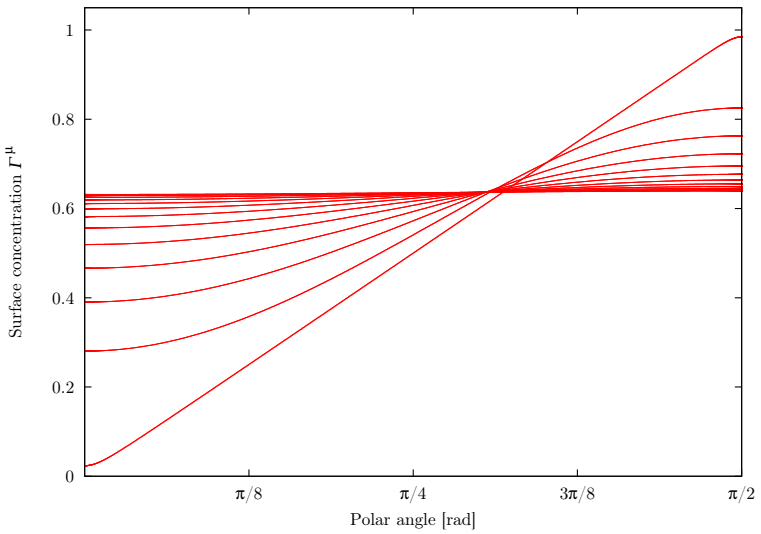

Fig. 22.3.: Test of surface diffusion: A linear distribution is homogenized with time. Due to the curvilinear nature of the surface, the equilibrium value is $\Gamma^\mu = 0.64$.

This means a rougher time stepping and thus less calculation time.

The demonstration of the weak form for surface diffusion is described in appendix G. In order to implement and test surface diffusion, adsorption from the volume to the surface is cut off by suppressing the term representing j_{ads}. The initial condition of surface concentration is set to $\Gamma^\mu(\varphi, t = 0) = 2\varphi/\pi$, which corresponds to $\Gamma^\mu(0) = 0$ and $\Gamma^\mu(1) = 1$, respectively a linear surface concentration gradient as a function of the polar angle, φ. The result of the simulation is shown in Fig. 22.3: the concentration gradient is nicely smoothed and the final value is $\Gamma^\mu(\varphi, t \to \infty) = 0.64$. Intuitively, a theoretical value of $\Gamma^\mu(\varphi, t \to \infty) = 0.5$ might be expected, which is evidently not true due to surface curvature of the domain. The equilibrium value, $\Gamma^\mu(\varphi, t \to \infty)$, as calculated numerically, is to be compared to the theoretical value found by calculating the total amount of surfactant molecules at the surface, N_s:

$$N_s = \int_0^{\pi R/2} 2\pi r(l)\Gamma^\mu(l)\, \mathrm{d}l = \int_0^{\pi/2} 4R^2\varphi \sin\varphi \, \mathrm{d}\varphi = 4R^2,$$

where l is the arc length of the surface. The equilibrium value of surface concentration as analytically calculated, is found to be:

$$\Gamma^\mu(\varphi, t \to \infty) = N_s/2\pi R^2 = 2/\pi = 0.637.$$

The relative error between the numerical and theoretical values is lower than 1×10^{-5} , which suggests a successful implementation of surface diffusion.

22.3.3. Calculation of steady streaming flow in the drop

The calculation of streaming in the volume is done using the *spf* module for Navier-Stokes fluid mechanics in a laminar flow regime. The chosen material

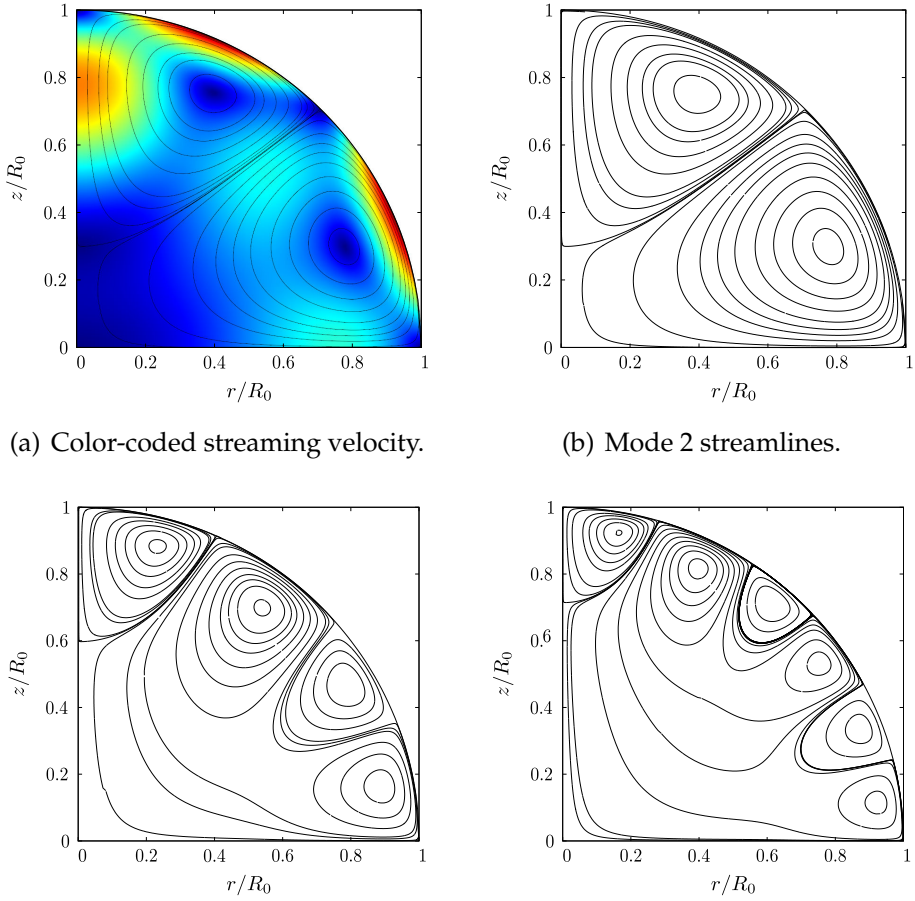

(a) Color-coded streaming velocity.

(b) Mode 2 streamlines.

(c) Mode 4 streamlines.

(d) Mode 6 streamlines.

Fig. 22.4.: Numerical calculation for the volume flow. Velocity color coding: red (15.8 mm/s), blue (0 mm/s), black lines represent streamlines. The flow direction for the upper toroidal flow (drop apex) is counter-clockwise: from the top to the center of the drop, then back to the surface. Following toroids alternate between clockwise and counter-clockwise flow direction.

type is water at room temperature, which fixes the material constants of viscosity, $\eta = 1\,\mathrm{mPa\,s}$, and density, $\rho = 1000\,\mathrm{kg/m^3}$. The geometry under consideration is the averaged shape of the oscillating drop. The boundary conditions for the volume flow are a symmetry condition on the symmetry axis, $r = 0$, a slip condition on the base axis, $z = 0$, and a sliding wall condition on a curved drop surface, $R = \sqrt{r^2 + z^2}$. The last condition serves to impose the streaming velocity, $U_{s,2}\cos(4\phi) \approx 16\,\mathrm{mm/s}\cos(4\phi)$. This surface flow will be transmitted by viscosity into the inner of the drop and create the toroidal flow pattern, which is presented in Fig. 22.4(a) (compare with Fig. 6.1 on page 60 for oscillation mode $n = 2$). In this figure, the velocity scale is color-coded and the streamlines are displayed in black. The direction of the flow is from the base center to the center of the surface. The recirculation passes by the contact line and the drop apex, respectively for the lower and upper toroid, back to the base center. In order for the method to work, a reference pressure needs to be chosen, which is arbitrary

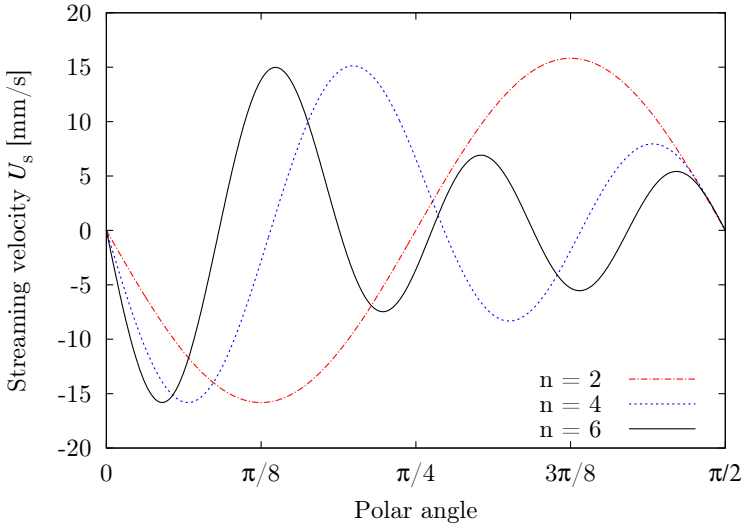

Fig. 22.5.: Representation of the three surface velocities, $U_s(\varphi)$, for modes $n = 2$, 4 and 6. For negative values, the streaming velocity is directed to the apex.

in this case, and set to $P = 0\,\mathrm{Pa}$ at the triple contact line.

It is easy to switch from the mode 2 driven flow pattern to a flow pattern driven by a higher mode by changing the sliding wall boundary condition at the drop surface and calculating the corresponding streaming velocity, which is displayed for the first three resonant modes in Fig. 22.5. The streamlines for the first three resonance modes $n = 2$, 4 and 6 are displayed in Fig. 22.4. In all cases, the flow direction of the upper toroidal vortex is counter-clockwise, the following vortices change flow direction alternatively.

22.4. Coupling of all physical mechanisms and non-dimensional analysis

The remaining physical phenomena to be coupled are volume streaming, governed by the outer boundary condition for the streaming velocity, and volume diffusion governed by Fick's law of diffusive mass transport. Furthermore, volume and surface are coupled by the law of ad- and desorption, Henry's law. The adsorbed surfactant molecules are transported under surface diffusion from high to low concentrations. These four phenomena, streaming, volume diffusion, sorption and surface diffusion, imply different time scales, which may be related to each other by means of non-dimensional numbers. Four non-dimensional numbers are relevant here:

- The Thiele number, $\mathrm{Th}^2 = \tau_{\mathrm{diff}}/\tau_{\mathrm{ads}} = R^2 k_d/D$
- The volume Peclet number, $\mathrm{Pe} := \tau_{\mathrm{diff}}/\tau_{\mathrm{stream}} = RU_s/D$.
- The Damköhler number, $\mathrm{Da} := \tau_{\mathrm{stream}}/\tau_{\mathrm{ads}} = Rk_d/U_s$.
- The surface Peclet number, $\mathrm{Pe}_s := \tau_{\mathrm{diff,s}}/\tau_{\mathrm{stream}} = RU_s/D_s$.

The associated time scales and non-dimensional numbers are recapitulated in table 22.1. The analysis of streaming efficiency is only relevant for diffusion-

$\tau_{\mathrm{ads}} = \frac{1}{k_{\mathrm{d}}}$	$\mathrm{Th}^2 := \frac{\tau_{\mathrm{diff}}}{\tau_{\mathrm{ads}}} = \frac{R_0^2\, k_{\mathrm{d}}}{D}$
$\tau_{\mathrm{diff}} = \frac{R_0^2}{D}$	$\mathrm{Pe} := \frac{\tau_{\mathrm{diff}}}{\tau_{\mathrm{stream}}} = \frac{R U_{\mathrm{s}}}{D}$
$\tau_{\mathrm{diff,s}} = \frac{R_0^2}{D_{\mathrm{s}}}$	$\mathrm{Da} := \frac{\tau_{\mathrm{stream}}}{\tau_{\mathrm{ads}}} = \frac{R k_{\mathrm{d}}}{U_{\mathrm{s}}} = \frac{\mathrm{Th}^2}{\mathrm{Pe}}$
$\tau_{\mathrm{stream}} = \frac{R}{U_{\mathrm{s}}}$	$\mathrm{Pe_s} := \frac{\tau_{\mathrm{diff,s}}}{\tau_{\mathrm{stream}}} = \frac{R U_{\mathrm{s}}}{D_{\mathrm{s}}}$

Table 22.1.: Recapitulation of the different time scales and associated non-dimensional numbers.

limited systems, because otherwise the concentration gradient at the direct vicinity of the drop surface would be too weak for streaming-induced convection to have an effect on surface ageing, cf. chapter 20. Hence, the Thiele number is generally assumed to exhibit a high enough value, $\mathrm{Th} \gg 1$. The initial conditions for volume and surface are, respectively:

$$C(r, 0) = C_0 \quad \text{and} \quad \Gamma(0) = 0.$$

22.4.1. Volume Peclet number

The volume Peclet number, $\mathrm{Pe} = \tau_{\mathrm{diff}}/\tau_{\mathrm{stream}}$, characterizes a system regarding the efficiency of (streaming-induced) convection versus the efficiency of diffusional transport. Systems with a high Peclet number are generally governed by convection, whereas a low Peclet number is preponderant in systems in which diffusion acts on a smaller time scale than convection. In this analysis, the Thiele number is set to $\mathrm{Th} = 10^3$, which means a diffusion-limited system as far as surface ageing is concerned. This is convenient, as the analysis of streaming will concentrate on mixing and ageing efficiency in diffusion-limited systems. Fig. 22.6 displays the variance, σ_C^2, of volume concentration in function of t/τ_{diff} (The surface Peclet number exhibits a high value, $\mathrm{Pe_s} \to \infty$, surface diffusion is thus neglected). The variance bears information on the mixing of solute molecules within the volume, and is defined as follows:

$$\sigma_C^2 := \frac{1}{N_{\mathrm{vol}}^2} \oint_V \left(C(r, z, t) - \bar{C}(t)\right)^2 \, \mathrm{d}V,$$

where $N_{\mathrm{vol}}(t) := \oint_V C(r, z, t) \, \mathrm{d}V$ corresponds to the amount of solute molecules in the volume[1], and where $\bar{C}(t) := N_{\mathrm{vol}}(t)/V$ is the mean concentration. The graph states that for a high Peclet number, the streaming generates a high variance of volume concentration, which falls quickly to zero at times about 0.01 to 0.05 τ_{diff}. Intermediate systems with a Peclet number close to $\mathrm{Pe} \gtrsim 1$ are hardly distinguishable from purely diffusional regime, $\mathrm{Pe} \leq 1$, for which σ_C^2 does not depend on the Peclet number. It is entirely governed by diffusion, and convection does not play a significant role for diffuso-convective kinetics. The relaxation time of σ_C^2 is near to the diffusion time scale, τ_{diff}.

[1] The amount of solute molecules in the volume is time-dependent, since adsorption of surfactants to the drop surface acts on this variable.

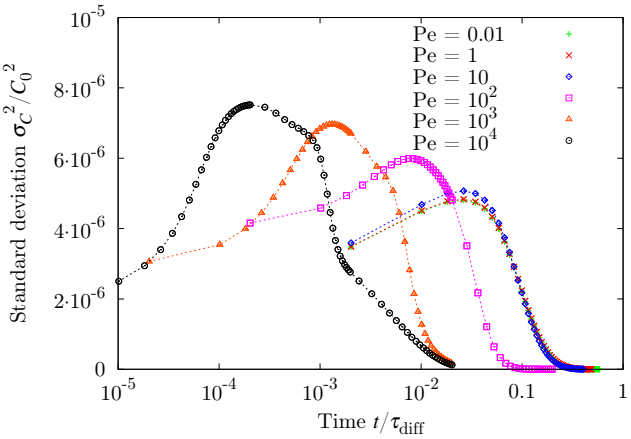

Fig. 22.6.: Behavior of the variance of volume concentration, σ_C^2, with Peclet number. For high Peclet numbers, the system tends to quickly homogenize the molecule distribution. For low Peclet numbers, the system seems to be governed by diffusion, as the kinetics do not depend on Pe and last for the diffusion time scale. The system is characterized by a high Thiele number (diffusion kinetics), $\mathrm{Th}^2 = 10^3$, and a high surface Peclet number (no surface diffusion), $\mathrm{Pe_s} \to \infty$. Time is non-dimensionalized by τ_{diff}.

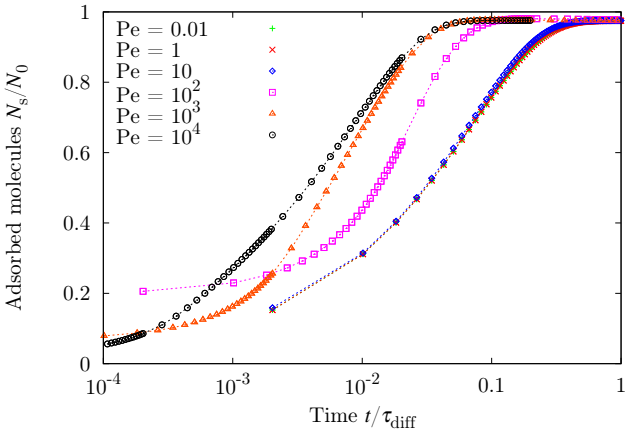

Fig. 22.7.: The adsorption of molecules and the reaching of a saturated surface is more rapid for high Peclet numbers. This is a first indication that streaming is likely to speed up surface ageing. The system is characterized by $\mathrm{Th}^2 = 10^2$ and $\mathrm{Pe_s} \to \infty$. Time is non-dimensionalized by τ_{diff}.

Practically speaking, the convection and diffusion act as follows in the two regimes:

- For high Peclet numbers, adsorption of surfactants to the drop surface will create a depleted boundary layer next to the surface. This boundary layer will be convected by the streaming current to the apex and the triple contact line, respectively. The diffusion boundary layer is pretty small, as diffusion will be outrun by convection. Please refer to Fig. 22.8 for an illustration of the convected boundary layer.

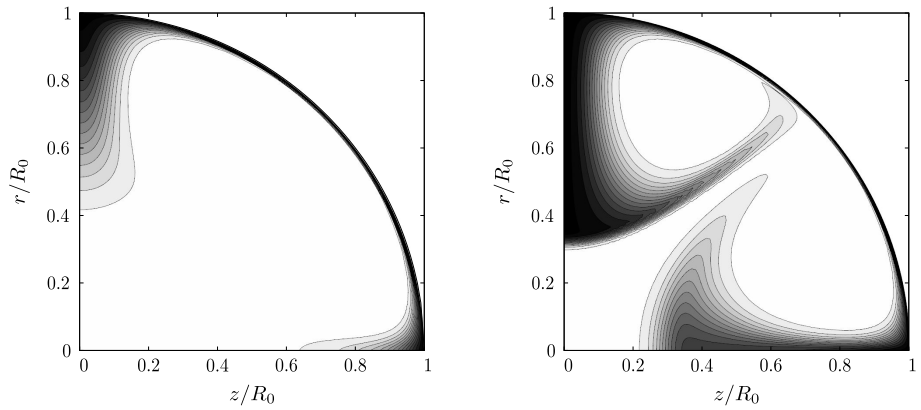

(a) Pe = 10^4, time $t = 0.5\,\tau_{\text{stream}}$.

(b) Pe = 10^4, time $t = 1.5\,\tau_{\text{stream}}$.

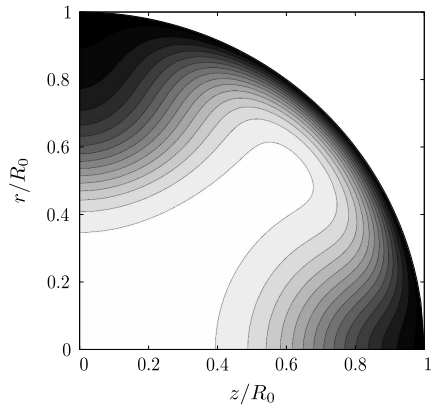

(c) Pe = 10^2, time $t = 0.5\,\tau_{\text{stream}}$.

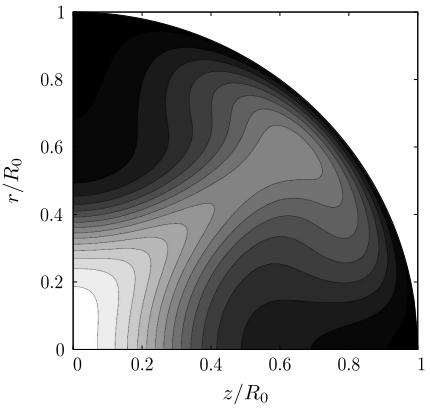

(d) Pe = 10^2, time $t = 1.5\,\tau_{\text{stream}}$.

Fig. 22.8.: Concentration plots for mode $n = 2$ and different Peclet numbers: For a high Peclet number, Pe = 10^4, the boundary layer is convected right away and has little time to develop. For an intermediate Peclet number, Pe = 10^2, the boundary layer develops further. For small Peclet numbers, Pe < 1, diffusion kinetics is too fast for streaming to convect the boundary layer, and streaming may be neglected. The concentration is coded in gray scale: white stands for $C = C_0$, black stands for $C = 0$, separated by fifteen equidistant levels on the gray scale.

- For low Peclet numbers, adsorption also takes place, but this time the boundary layer is not convected. The so created concentration gradient generates diffusive flux from the drop center to the surface, and thus sustains the adsorption flux. This extends the boundary layer more and more, until the droplet volume is emptied from solute molecules.

- For intermediate Peclet numbers, convection and diffusion exhibit approximately the same time scales and the boundary layer expands to the center of the droplet, while being convected slowly at the same time.

Regarding the curves for high Peclet numbers, especially the curve for Pe = 10^4, a shoulder is visible right after the local maximum. This shoulder is due to the recirculation of the boundary layer near the surface, which is emptied, or

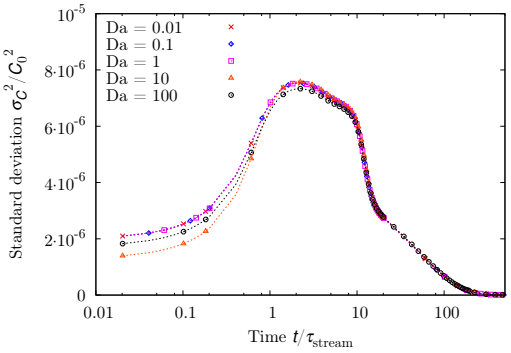

(a) Non-dimensionalization of time by τ_{stream}: the peak of variance is situated at $t/\tau_{stream} \approx 1$, indicating that mixing is due to streaming. Since the system is qualified by Pe = 10^4, essentially the same mixing behavior as in Fig. 22.6 can be observed.

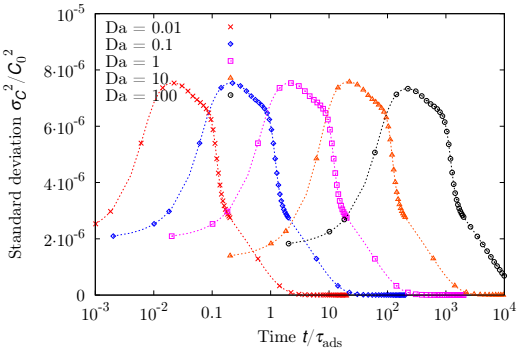

(b) Non-dimensionalization of time by τ_{ads}: the peak of variance is shifted to small times while decreasing Da. The fact that the system is diffusion-limited (Th $\gg$ 1) means that streaming-induced convection is able to mix the volume sufficiently for fast adsorption of surfactant molecules to the surface. With inefficient streaming, Da $\gg$ 1, adsorption requires more time to reach equilibrium.

Fig. 22.9.: Analysis of the volume concentration variation, σ_C^2. The system is characterized by a high Thiele number (diffusion kinetics), Th^2 $\gg$ 1, a Peclet number of Pe = 10^4 (streaming more efficient than streaming in the volume), and a high surface Peclet number (no surface diffusion), Pe$_s$ $\to \infty$.

nearly, by adsorption. This boundary layer is then convected to the base of the droplet via the apex and via the triple contact line.

Fig. 22.7 gives a first overview of the adsorption process in function of the Peclet number. This needs to be taken with care, as the Damköhler number, Da, is not yet taken into account. Nevertheless, the graph gives indications, that the time to reach an equilibrium is sped up in systems with a high Peclet number. Further analysis needs to be made in order to confirm these preliminary results.

22.4.2. Damköhler number

The Damköhler number, Da = τ_{stream}/τ_{ads}, characterizes a system regarding the efficiency of streaming-induced convection compared to adsorption. In order to introduce the analysis, the curves of the previous section on the Peclet number are redrawn for Pe = 10^4 in a diffusion-limited system, Th $\gg$ 1. The surface Peclet number exhibits a high value, Pe$_s$ $\to \infty$, surface diffusion is thus neglected. In Fig. 22.9(a), the variance of volume concentration, σ_C^2, is displayed for several values of the Damköhler number, from Da = 0.01 to Da = 100. Recall that for a high Damköhler number, surface ageing is controlled by a streaming-limited regime. The peak of variance can be observed and is approximately situated at $t/\tau_{stream} \approx 1$, when choosing a non-dimensionalization of time by τ_{stream}, indicating that mixing is essentially dictated by streaming. Since the system is qualified by Pe = 10^4, essentially the same mixing behavior as in Fig. 22.6 can be observed.

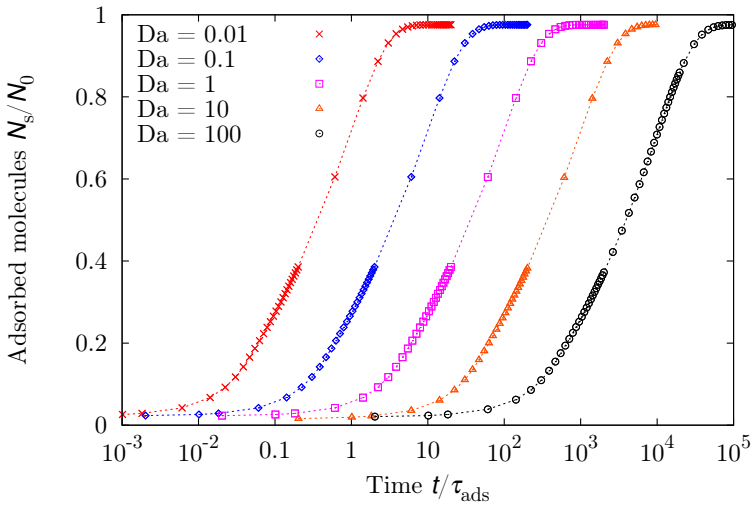

Fig. 22.10.: The time for adsorption of the major amount of surfactant molecules is shortened with decreasing Da. Streaming speeds up the adsorption process by "replacing" diffusional transport. The system is characterized by a high Thiele number (diffusion-limited system), $\mathrm{Th}^2 \gg 1$, a Peclet number of $\mathrm{Pe} = 10^4$ (streaming more efficient than diffusion in the volume), and a high surface Peclet number (no surface diffusion), $\mathrm{Pe_s} \to \infty$. Time is non-dimensionalized by τ_{ads}.

When choosing a non-dimensionalization of time by τ_{ads} (cf. Fig. 22.9(b)), the peak of variance is shifted to small times while decreasing Da. The fact that the system is diffusion-limited (Th $\gg$ 1, adsorption is quasi-instantaneous) means that streaming-induced convection is able to mix the volume sufficiently for a faster surface ageing. With inefficient streaming, Da $>$ 1, adsorption requires more time to reach thermodynamic equilibrium, and surface ageing passes off slowly. From a practical point of view it may be stated that streaming speeds up surface ageing by "replacing" efficiently diffusional transport (Pe $\gg$ 1), provided Da is small enough. This is also found when representing the total adsorbed surfactant amount as a function of time with a non-dimensionalization of time using τ_{ads} (cf. Fig. 22.10). The time for adsorption of the major amount of surfactant molecules is shortened with diminishing Da.

22.4.3. Surface Peclet number

The last dimensionless number to be considered in this analysis is called surface Peclet number, $\mathrm{Pe_s} = \tau_{\mathrm{diff,s}}/\tau_{\mathrm{stream}} = RU_s/D_s$, characterizing the relation between volume convection and surface diffusion. For a high surface Peclet number, surface diffusion is slow compared to streaming-induced effects, hence the distribution of adsorbed surfactant molecules is strongly influenced by the properties of steady streaming flow. A low surface Peclet number means fast surface diffusion kinetics, such that the surface gradient of surface concentration, $\nabla_s \Gamma$, due to streaming should vanish. The results of this analysis are shown in Figs. 22.11 and 22.12. The system is characterized by a high Thiele number (diffusion-limited system), $\mathrm{Th}^2 = 10^3$, a Peclet number of $\mathrm{Pe} = 10^4$, and a Damköhler number of Da = 0.1.

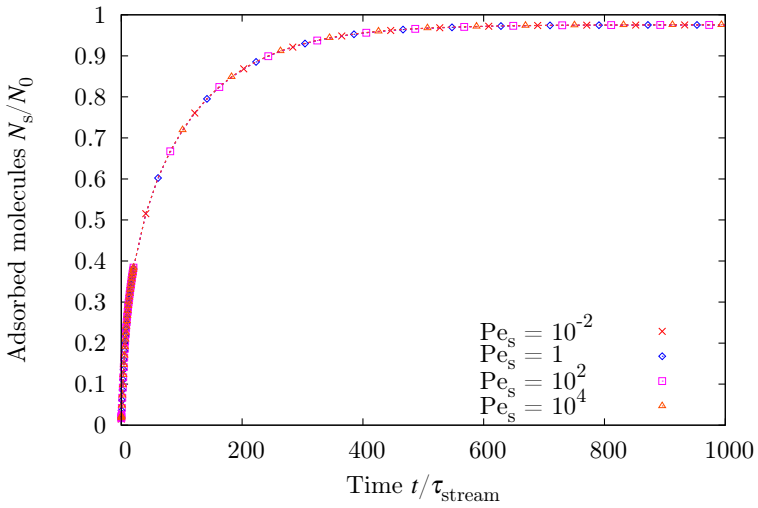

Fig. 22.11.: The time scale required to achieve thermodynamical equilibrium is independent of Pe_s. The time scale depends on the other dimensionless numbers, Th, Pe and Da. The system is characterized by a high Thiele number (diffusion-limited system), $Th^2 = 10^3$, a Peclet number of $Pe = 10^4$, and a Damköhler number of $Da = 0.1$. Time is non-dimensionalized by τ_{stream}.

Fig. 22.11 shows the total amount of adsorbed surfactant molecules at the surface. Whichever the value of Pe_s, the time scale for achieving thermodynamical equilibrium is independent of Pe_s, a fact which is due to the application of Henry's law. Since the kinetics of adsorption is only limited by the amount of molecules available in the vicinity of the surface and by the value of the Thiele number, the volume is nearly emptied in a constant time span, which is not affected by the redistribution of already adsorbed molecules at the surface. For an adsorption law implying steric effects, e.g. the Langmuir law with the concept of maximum packing concentration, Γ_∞, the same behavior may only be found for small surface concentrations. Nevertheless, the time scale for achieving thermodynamical equilibrium depends on the other dimensionless numbers, Th, Pe and Da.

In order to observe a dependence on Pe_s, the focus must be consistently placed on the spatial distribution of surfactant molecules, which is represented in Fig. 22.12 for different surface Peclet numbers, $Pe_s = 10^{-2}$ to $Pe_s = 10^5$, as a function of the polar angle, φ. The surface concentration is displayed at time intervals of $20\,\tau_{stream}$. Surprisingly, three regimes are made evident:

- For a low surface Peclet number, or efficient surface diffusion, the distribution of molecules is nearly horizontal. The effects of steady streaming on the surface distribution are quickly compensated by surface diffusion, such that Γ^μ is homogenized rapidly.
- For a surface Peclet number of the order $Pe_s \approx 10^2$ to $Pe_s \approx 10^3$, an initial non-homogeneity is found, which is dissipated with time. The system

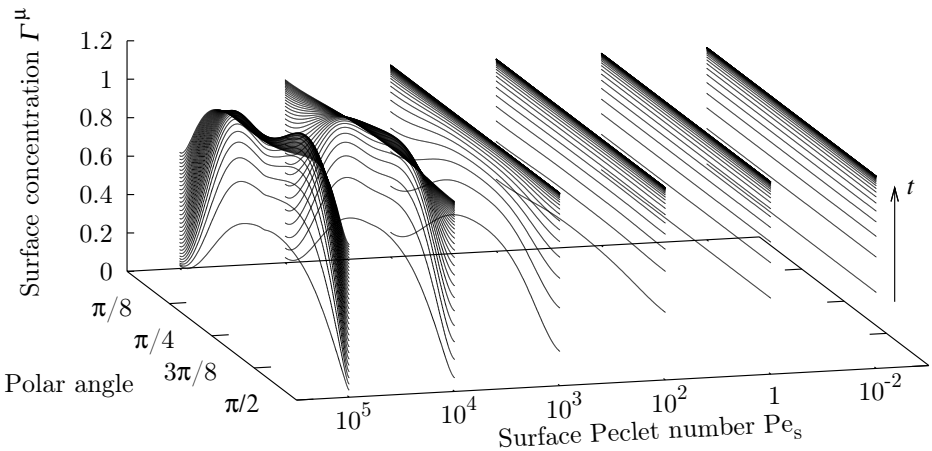

Fig. 22.12.: Representation of surface concentration, Γ^{μ}, as a function of the polar angle and for different surface Peclet numbers, $Pe_s = 10^{-2}$ to $Pe_s = 10^5$. The surface concentration distribution is displayed at time intervals of $20\,\tau_{stream}$. The system is characterized by a high Thiele number (diffusion-limited system), $Th^2 = 10^3$, a Peclet number of $Pe = 10^4$, and a Damköhler number of $Da = 0.1$.

tends again to the uniform distribution as obtained with a low surface Peclet number.

· For a high Peclet number of the order $Pe_s \gtrsim 10^4$, surface diffusion is not efficient enough to dissipate the initial non-homogeneity. The non-homogeneity grows to high surface concentration spots, before being dissipated by slow surface diffusion after the reach of thermodynamical equilibrium, $dN_s/dt = 0$. This is an interesting finding which strengthens the conclusion of the beginning of the analysis, that thermodynamical equilibrium is independent of surface diffusion effects. This is true not only as far as time scale is concerned, but hence also involves spatial molecule distribution. Again, this is not 100 % adaptable for adsorption laws introducing steric effects.

A last point is the nature of the origin of the non-homogeneity of surfactant distribution along the drop surface. This is a question of interest, since it strongly depends on the characteristics of steady streaming flow. In the analysis based on the volume Peclet number, Pe, it is shown how adsorption and streaming act together and cause convection of a volume concentration gradient along the streamlines. For a high volume Peclet number, Pe, the adsorption flux is mainly supplied by the recirculating flow, and not by the diffusive flux. This means that the recirculating flow is loaded with surfactant molecules while on the way to the drop center. On its way back to the surface, at a polar angle of about $\pi/4$, the recirculation will "discharge" and be emptied on its way from the surface center to the apex, and to the triple contact line, respectively, leaving behind a high surface concentration of surfactants at $\varphi \approx \pi/4$ at the surface.

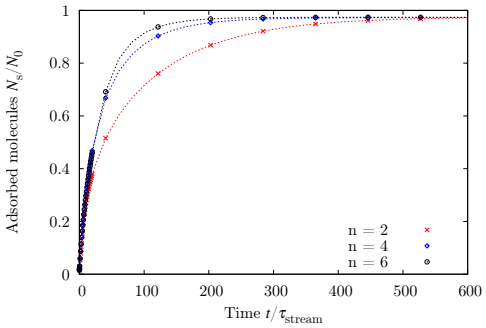

(a) Amount of adsorbed molecules as a function of time.

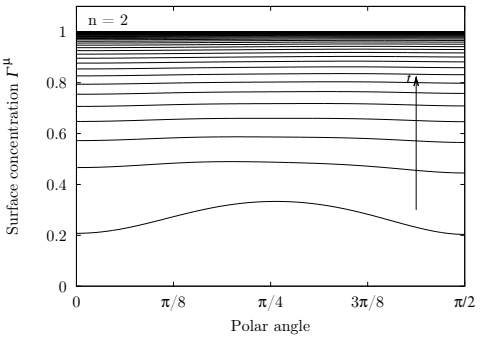

(b) Surface distribution of surfactant molecules for mode number 2.

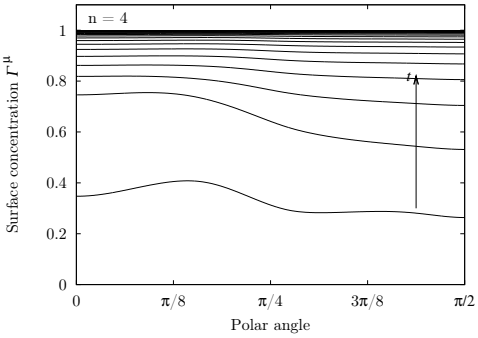

(c) Surface distribution of surfactant molecules for mode number 4.

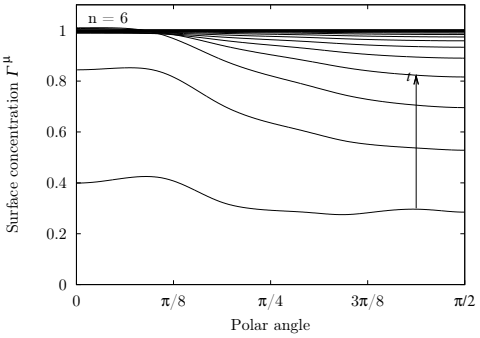

(d) Surface distribution of surfactant molecules for mode number 6.

Fig. 22.13.: Total amount and spatial distribution of surfactant molecules depend on mode number: mode $n = 6$ exhibits the fastest kinetics. Spatial distribution is affected by steady streaming for all oscillation modes. The system is characterized by the following dimensionless numbers: $Th^2 = 10^3$, $Pe = 10^4$, $Da = 0.1$ and $Pe_s = 10^2$. The time scale of panel (a) is non-dimensionalized by τ_{stream}, and time steps between the curves of panels (b), (c) and (d) are $20\,\tau_{stream}$ apart.

This mechanism is made possible due to the presence of a Stokes layer, which separates the bulk convection from the liquid surface, hence not introducing any streaming-induced convection in the surface. In contrast, would the thickness of the Stokes layer, δ_S, be of the size of the surfactants, steady streaming would have to be taken into account in the transport equation (22.3) (page 154), as stated in sections 22.1 and 22.2. Here, the thickness of the Stokes layer, δ_S, is much larger than several molecular lengths (adsorption barrier) while being much smaller than any other boundary layer thickness (diffusive or convective layers).

22.5. Beyond two vortices: higher order modes.

Higher order modes are consistently associated with a higher number of toroidal vortices. As far as stirring is concerned, the mode $n = 2$ with two vortices might be not as efficient as an oscillation with higher mode number. In this section,

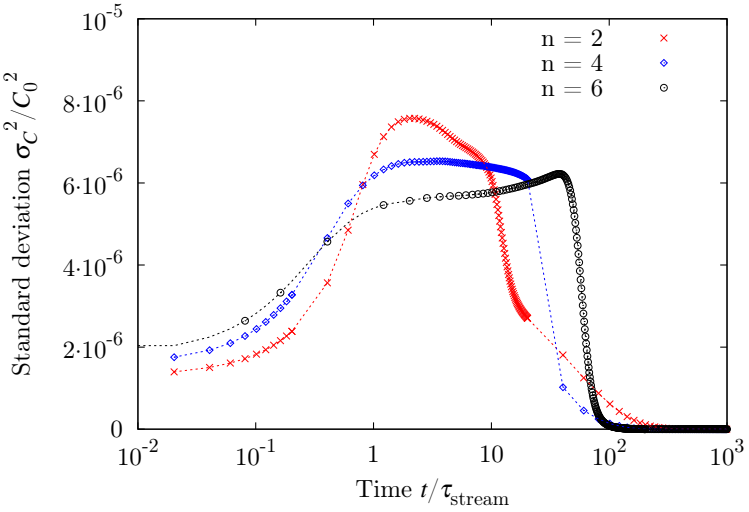

Fig. 22.14.: Variance of volume concentration: the difference of the curves in Fig. 22.13(a) can be characterized by σ_C^2, a measure for the mixing efficiency of streaming. The curve for mode $n = 6$, the most efficient mixing, starts at a higher value and exhibits the largest plateau. The system is characterized by the following dimensionless numbers: $\mathrm{Th}^2 = 10^3$, $\mathrm{Pe} = 10^4$, $\mathrm{Da} = 0.1$ and $\mathrm{Pe_s} = 10^2$. Time is non-dimensionalized by τ_{stream}.

the successive modes, $n = 2$, 4 and 6, are considered, each one with an equal maximum streaming velocity, $U_s = 15.8\,\mathrm{mm/s}$. As suggested by experiments [62], modes of even higher order, $n \geqslant 8$, do not seem to follow the theory of steady streaming presented in chapter 6. The system under consideration here is characterized by the following dimensionless numbers: $\mathrm{Th}^2 = 10^3$, $\mathrm{Pe} = 10^4$, $\mathrm{Da} = 0.1$ and $\mathrm{Pe_s} = 10^2$.

It is found that the time to reach a thermodynamical equilibrium is reduced with higher order modes, confer Fig. 22.13(a), the sixth mode being the mode with the fastest kinetics. The spatial distribution of surfactant molecules adsorbed to the surface is also altered in comparison with mode $n = 2$ (cf. Fig. 22.13(b)-(d)).

An indication how kinetics are modified may be found by considering the curves for variance of volume concentration (cf. Fig. 22.14): The curve for mode $n = 6$ with the most efficient mixing, starts at a higher value of σ_C^2 and exhibits the largest plateau. This apparently leads to the faster kinetics for reaching thermodynamical equilibrium.

22.6. What about adsorption to the bottom? “Real life” hybridization assays.

Many biochips and bioarrays for molecular recognition (e.g. SPR, QCM, cantilevers) rely on adsorption of ligand molecules to a biochemical receptor grafted to the solid substrate. Stirring is particularly useful to enhance biochemical transfers and gain a quicker response of the transduction mechanism. By stir-

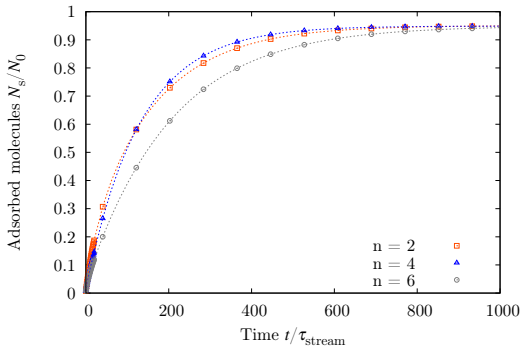

(a) Comparison of the three first resonant modes concerning adsorption at the solid substrate. Modes 2 and 4 exhibit a higher mixing efficiency than mode 6.

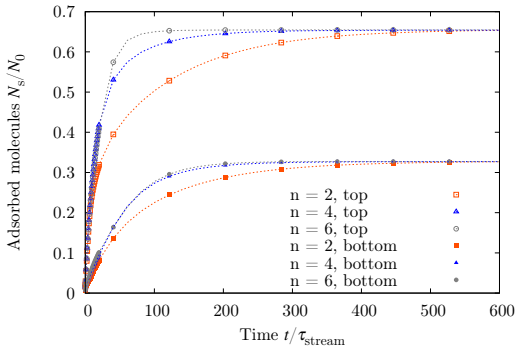

(b) Adsorption is enabled on both interfaces, the drop surface (top) and the liquid/solid interface (bottom). Streaming does not favor one or the other interface for adsorption: the equilibrium time scale for a specific resonant mode is equal in both cases.

Fig. 22.15.: Adsorption curves for different modes and adsorption conditions are compared. Please refer to the text for further details. The system is characterized by the following dimensionless numbers: $\mathrm{Th}^2 = 10^3$, $\mathrm{Pe} = 10^4$, $\mathrm{Da} = 0.1$ and $\mathrm{Pe_s} = 10^2$.

ring, faster ligand-receptor binding may be achieved.

In this section, streaming-induced stirring is investigated for the three first oscillation modes, and adsorption is set possible at the solid substrate, but no more at the drop surface. The system is again characterized by the following dimensionless numbers: $\mathrm{Th}^2 = 10^3$, $\mathrm{Pe} = 10^4$, $\mathrm{Da} = 0.1$ and $\mathrm{Pe_s} = 10^2$.

In Fig. 22.15(a), the curves for the adsorbed molecule quantity are shown for the first three resonant modes, $n = 2, 4$ and 6. The stirring efficiency of the different resonant modes is inversed in comparison with the situation of adsorption at the liquid surface. In the case of a solid substrate, modes 2 and 4 exhibit the fastest kinetics, and surface ageing in the case of mode 6 takes more time to reach thermodynamical equilibrium. The reason for this lies in the configuration of streaming, as is suggested by the analysis of the streamlines (cf. Fig. 22.4 on page 159). Hence for mode 6 and adsorption at the substrate, primarily the outer bottom vortex contributes to mixing, before the concentration gradient is propagated to the rest of the vortices. Whereas for mode 2, the concentration gradient is convected up to the middle of the drop, as the outer vortex is of greater extent. For adsorption at the drop surface, all vortices contribute equally to surfactant convection, as the concentration gradient is generated along the whole drop surface.

Furthermore, it is interesting to know whether steady streaming can have an effect on the repartition of surfactant, when adsorption is permitted to drop surface *and* solid substrate. The results of this analysis are shown in Fig. 22.15(b) for equal ad- and desorption coefficients, k_a and k_d, on both interfaces. The equilibrium value of adsorbed surfactant on the respective interfaces is different, since the total available surface for the drop surface (top) is greater

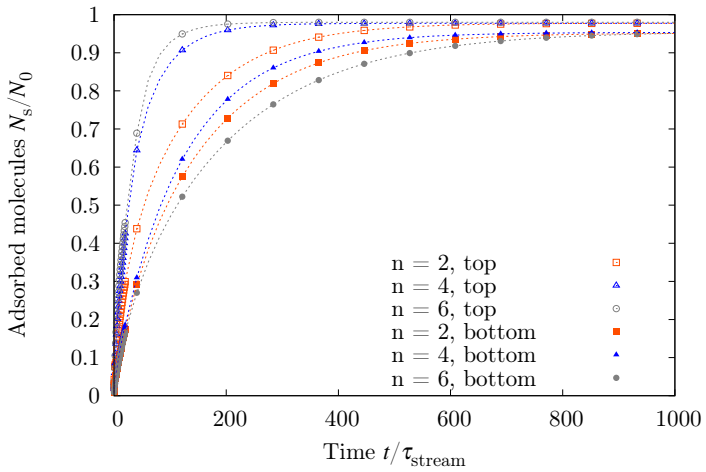

Fig. 22.16.: Comparison of the three first resonant modes for adsorption at the drop surface (top, open symbols) and at the solid substrate (bottom, opaque symbols), respectively. Here, the initial volume concentration is non-uniform (see text for further details).

than for the liquid/solid interface (bottom). A fact, which is not completely intuitive, is that the adsorption time scale for the respective interfaces is not altered by streaming for a specific resonant mode: surface ageing exhibits the same time scale for reach of equilibrium. Nevertheless, the initial kinetics is slightly more rapid for the adsorption at the drop surface, due to the reasons evoked earlier: the fact that the streaming vortices are situated in the vicinity of the drop surface is advantageous for mixing and surface ageing enhancement, especially for modes $n = 4$ and 6.

A last study is proposed, the results in Fig. 22.16 show the amount of adsorbed molecules for different resonant modes when surface ageing arises at the drop surface (top), or at the solid substrate (bottom). These calculations take into account a non-uniform initial concentration, $C(r, t = 0)/C_0 = \Theta(r/R_0 - 0.5)$, Θ being the Heaviside distribution[2]. This means that the drop is divided into two domains, the inner domain for $r/R_0 < 0.5$ is initially surfactant free, the outer domain, $r/R_0 \geqslant 0.5$ is at concentration $C/C_0 = 1$. A similar initial non-uniformity may be created by merging two drops as is often the case in standard lab-on-chips, where mixing of two reagents or samples is involved. The results of Fig. 22.16 suggest that adsorption at the drop surface is generally quicker than at the solid substrate. This may have two reasons:

- First, the area of the drop surface is larger than the contact area of the drop with the substrate, providing more active surface for molecule adsorption.
- Second, the mixing, especially for higher resonant modes, is more intense at the drop surface than at the substrate, as already pointed out in the last paragraph.

To conclude, as far as mixing is concerned, low order resonant modes should be preferred for adsorption at the solid substrate, while high order resonant modes are more efficient for adsorption at the drop surface.

[2]The Heaviside distribution is defined as follows: $\Theta(x) = 0 : (x < 0)$ and $\Theta(x) = 1 : (x \geqslant 0)$.

23. Conclusion

In this chapter, the foregoing analysis was enlarged to steady streaming, which necessitated a 2D implementation for numerical calculus. The weak form method was continued in a two-dimensional approach, making it possible to integrate the effects of steady streaming into the calculation for surface ageing. The results of the 2D implementation were successfully compared to the analytical and numerical results of chapter 20. By integrating streaming in the volume and along the surface, four dimensionless numbers were made evident and analyzed using a numerical approach.

These analyses led to several conclusions: In many conditions, characterized by the Peclet and Damköhler numbers, streaming actually can be of great interest for volume mixing and enhancement of drop surface ageing. The variance of volume concentration, σ_C^2, gives a hint on the mixing efficiency. Higher mode numbers privilege stirring in the vicinity of the drop surface and seem to be more efficient for homogenization of the volume concentration. On the contrary, for adsorption of molecules solely on the solid substrate, small mode numbers seem to be preferential.

As for outlooks, as a way to include steric effects, it is worthwhile to implement the Langmuir law as a source term into the equation for surface surfactant transport. A further aspect for future investigation is the implementation of more complex streaming currents: It might be worthwhile to implement a stirring protocol at fixed dimensionless numbers, providing more efficient stirring by exploiting the use of a sequence of different resonant modes. Also, the introduction of mechanical and electrical rugosities [62,63,116] to generate modified flow patterns with different symmetry is an interesting road to investigate. Furthermore, the dependence of surface ageing kinetics on the finiteness of the system, ε_0, might be interesting to investigate via the implementation of evaporation, for example. The same methodology as for the one-dimensional model may be applied.

In order to put into practice the gained knowledge on surfactant transport and streaming-enhanced surface ageing, the last part of this work is experimental and focuses on biological ageing of drops actuated at different electrowetting frequencies.

Part VI.

Electrowetting-Induced Enhancement of Surface Ageing: Towards Label-Free Biosensing.

The usefulness of a microscopic digital bio-assay is now more apprehensible. As the size of a liquid system is reduced[1]*, once a finite system is reached, the diffusion and adsorption will act on the whole scale of the system, which means that the impact of adsorption on volume concentration extends to the entire drop size. This dramatically reduces the time for adsorption of the major part of solute molecules to sensitive surfaces. Not only is the reagent amount reduced, also the time to execute such an assay. As far as stirring is concerned, electrowetting-induced streaming seems to offer an interesting means of speeding up diffusion-limited physicochemical processes, as demonstrated in the previous part. This last part is dedicated to the experimental combination of these two mechanisms: streaming-enhanced adsorption of biomolecules at drop scale.*

A simple system of a bovine serum albumin laden sessile microdrop is chosen. Adsorption of the albumin proteins to the lubricated solid substrate is observed by imaging, as adsorption of biomolecules diminish the solid-liquid surface tension, γ_{SL}. Via this mechanism, the drop spreads on the substrate in the course of time, which is an indicator for surface ageing, providing information on surface tension variation and the time scale for thermodynamical equilibrium. The influence of steady streaming on surface ageing is measured and discussed.

[1] A priori the physicochemical properties of the molecular components in use will not be altered.

24. Materials & methods

24.1. Cleaning protocol and receptacles

The need for extremely clean receptacles, flasks and laboratory material is obvious for work with physicochemically active components. A simple cleaning protocol was found to be very effective against biological and chemical contaminations. Metal, glass and plastic parts were first cleaned with soap and sponge under warm water, and then thoroughly rinsed. The second step is to clean with isopropanol. Then, 80 °C hot tap water (available in the laboratory) is used to remove any resting biological content and isopropanol.

For storing prepared solutions, glass receptacles are used and stored in a refrigerator at 4 °C, sealed with Teflon tape and Parafilm. Solutions are transfered to the experiment in low protein-binding Eppendorf reagent tubes (Protein LoBind Tube, volume 1.5 mL, PCR-clean).

24.2. Measurement of pH

The pH values were measured using a IQ240 pH meter, fabricated by IQ Scientific/Hach (Loveland, CO, United States). It is calibrated using three appropriate buffer solutions at fixed pH of 4.01, 7.01 and 10.01, respectively, purchased from Fisher Scientific (Illkirch, France). The pH meter automatically corrects the temperature dependence of pH. See also appendix E.2 on page 203.

24.3. Bovine serum albumin

Albumin from bovine serum (BSA) belongs to the group of albumin proteins, which are some of the most studied proteins and very abundant in blood plasma with a concentration of about 50 g/L. Hence, albumins are the most present proteins in the circulatory system and contribute, amongst others, to osmotic blood pressure [117] and the maintenance of pH [118].

In scientific developments, BSA is used in numerous biochemical applications, e.g. in enzyme-linked immunosorbent assays (ELISA) or as a nutrient in cell culture. It is also used as an anti-biofouling agent for the prevention of biomolecule adhesion to reaction tubes, pipette tips, as well as to microfluidic channel walls. Last but not least, it is low cost, since large quantities of it can be easily obtained from bovine blood.

Albumin from bovine serum (BSA) is produced in the liver and extracted from bovine blood serum. It is a protein with a molecular mass of 66.5 kDa and has the form of a prolate ellipsoid of dimensions $140\,\text{Å} \times 40\,\text{Å} \times 40\,\text{Å}$ in its natural conformation [119]. The structure of BSA is characterized by three main homologous domains, divided into two subdomains each. Depending

Conformation and transition pH:
Expanded $\underset{2.7}{\longleftrightarrow}$ Fast $\underset{4.3}{\longleftrightarrow}$ Normal $\underset{8}{\longleftrightarrow}$ Basic $\underset{10}{\longleftrightarrow}$ Aged

Table 24.1.: BSA conformations in function of pH value, pH transitions are given underneath the arrows [120]. Each conformation corresponds to a different protein conformation and behavior concerning physico-chemical properties.

on pH, these domains will adapt different conformations, cf. table 24.1 and reference [120], with different physicochemical properties, which is important for this study. Its isoelectric point in water is pI = 4.7 at room temperature. At more acid pH values, its charge is positive, whereas in more alkaline solutions, it bears a negative charge.

As far as physicochemical parameters are concerned, the following values can be obtained in current scientific literature for a Langmuir adsorption law [121, 122]:

- Volume diffusion coefficient, $D = 3.3 \times 10^{-7}\,\mathrm{cm^2/s}$,
- Adsorption coefficient, $k_\mathrm{a}^\mathrm{LM} = 2.2\,\mathrm{m^3/mol\,s}$,
- Desorption coefficient, $k_\mathrm{d} = 10^{-3}/\mathrm{s}$,
- Maximum surface concentration, $\Gamma_\infty = 4.5 \times 10^{-8}\,\mathrm{mol/m^2}$,
- Reconverted adsorption coefficient, $k_\mathrm{a} = k_\mathrm{a}^\mathrm{LM}\,\Gamma_\infty = 9.9 \times 10^{-8}\,\mathrm{m/s}$.

The reconverted adsorption coefficient from the Langmuir law, k_a, is valid for surface concentrations that are small compared to the maximum surface packing concentration, Γ_∞. The following dimensionless numbers can be obtained for a sessile drop of volume 1 µL:

- Finiteness of the system, $\varepsilon_0 = 8$,
- Thiele number, $\mathrm{Th}^2 = 18$,
- Peclet number, $\mathrm{Pe} = 4 \times 10^5$,
- Damköhler number, $\mathrm{Da} = 5 \times 10^{-5}$.

The values given in the literature are not exactly for the same conditions (pH value, salinity of the buffer) as used in this work, nevertheless they may give a fair idea on how the surfactant reacts. As far as the Peclet and Damköhler numbers are concerned, with BSA, convection acts on clearly shorter time scales than diffusion and adsorption. Concerning finiteness and Thiele number, BSA seems to be located at an intermediary regime, such that no conclusion can be drawn from the literature values.

For the experiments, the drops are applied to a lubricated electrowetting chip substrate using a standard 6 mPa s silicone oil.

24.4. BSA solutions & isotherms

A mother solution of BSA at a concentration of 2 mg/mL was prepared with BSA purchased from Sigma-Aldrich in form of lyophilized powder at ⩾ 98 % purity. The solution was prepared in reagent grade phosphate buffered saline (PBS, pH 7.4), purchased from Fisher Scientific in ten-fold concentrated form, PBS 10x. An amount of BSA powder was weighed with a microgramme balance and mixed with 1 % PBS in a glass receptacle, agitated by a heating magnetic stirrer until complete dissolution. The mother solution was then used to prepare solutions from 0.1 µg/mL to 200 µg/mL in 1 % and 100 % PBS[1]. The final solutions were adjusted to pH 4 and pH 7 using hydrochloric acid (HCl), purchased from Sigma-Aldrich (purity ⩾ 99 %).

The dependence of physicochemical properties on conformation and net charge mentioned in the foregoing section may be used for tuning the adsorption properties. For this study, an efficient adsorption is primordial. The transition from 'normal' to 'fast' conformation is known for a lowered solubility [123]. To test the difference between these two conformations, adsorption isotherms are recorded at pH 4 and pH 7, for two different concentrations of the used buffer, phosphate buffered saline (PBS). The isotherms for BSA are shown in Fig. 24.1. They were obtained by the Wilhelmy plate method described in chapter E.2 (page 203). The measurement is done in a Teflon receptacle of 15 mL capacity. For each solution, the Wilhelmy plate and Teflon receptacle were cleaned as explained in the cleaning protocol.

As far as pH value and PBS concentration are concerned, the solution at pH 4 and 100 % PBS is found to exhibit the most efficient adsorption characteristics. This composition is chosen for the following experimental investigations.

24.5. Drop geometry measurements – *EasyEWOD*

Throughout this part of the work, the electrowetting chip and drop are covered by the lid without confinement disks, as described in section 17.1 (page 105). To further limit evaporation, six 20 µL drops are placed alongside the perimeter of the drop, and the water channel is filled. The laser hole in the lid is sealed by clear adhesive tape, which does not complicate interferometry measurements. Drop evaporation is sufficiently slowed down and does not have a considerable impact on the radius for the duration of the measurements.

It is important to analyze the drop geometry precisely, but first of all rapidly and with the less user interaction possible, since a large number of images need to be parsed. An appropriate tool, named *EasyEWOD*, was developed during the thesis of Rachid Malk [62]. This program based on an algorithm implemented in MATLAB allows to extract the base radius, R_B, the radius of curvature, R_{curv}, and the contact angle, θ, from images. The algorithm is based on edge detection of the drop surface. For a horizontal image of the drop, the vertical drop base position is given by the user for one reference image. Then,

[1] The biological terminology would be 1x PBS for the 100 % solution, and 0.01x PBS for the 1 % solution of PBS.

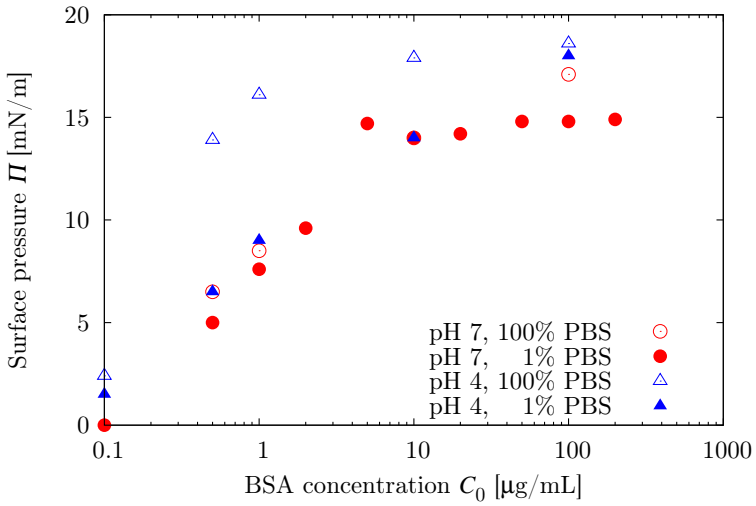

Fig. 24.1.: Bovine serum albumin isotherms for different pH values corresponding to the normal and fast conformations, for pH 4 and pH 7, respectively. Two concentrations of PBS are measured using the Wilhelmy plate technique. The solution at pH 4 – fast form – and 100 % PBS is the most surface active, and was therefore chosen in the experiments.

the algorithm applies the edge detection on all images, identifying the top point of the drop as the apex, and the two intersections of the drop base with the drop surface as the contact line, on the left and the right hand sides. More precise information on the algorithm and implementation in MATLAB is given in [62].

25. Experimental results

This chapter explains the measurements on dynamic surface tension of sessile drops contaminated with bovine serum albumin. Special attention is paid to the impact of electrowetting-driven drop shape oscillations on surface ageing kinetics. Also the impact of a voltage in the high-frequency electrowetting regime is measured.

25.1. Measurement of the liquid-gas surface tension

The initial goal of this thesis was to measure the dynamic liquid-gas surface tension, γ_{LG}, and thus the progressive functionalization of the drop surface, making use of the interferometry technique. To this end, a drop of BSA solution at an initial volume concentration of $C_0 = 30\,\mu g/mL$, in 100 % PBS buffer at pH value 4, is deposited on the solid surface above the electrodes. The electrodes are actuated with a dual-frequency voltage of high frequency, $\nu = 20\,kHz$, and with amplitude, $U_{rms} = 43\,V$. The low frequency of low amplitude is used to measure the amplitude response of the drop to the excitation frequency, f. The obtained spectra in the course of time reveal the first resonance frequency, f_2, which may be used to calculate the absolute value of γ_{LG}, using the resonance spectrum (5.9):

$$\gamma_{LG} = 2\pi^2 f_2^2 \rho R_{curv}^3 / \lambda_2(\theta).$$

Since in this part of the work, the contact angle is not regulated via U_1, imaging information on the contact angle, θ, as well as on the radius of curvature, R_{curv}, need to be obtained.[1] Using these information, the data of Fig. 25.1 are analyzed and show only a slight modification of surface tension, γ_{LG}, in the course of time. There are two remarkable facts for this curve. The first is that the value of the liquid-gas surface tension is excessively overestimated three- to four-fold by interferometry. Possible sources of error are the measurement of the radius of curvature, R_{curv}, and the theoretical prediction of the correction factor, $\lambda_2(\theta)$ (cf. Strani and Sabetta [42]). The second remark concerns the value of the contact angle, θ, measured by imaging which drops significantly: despite this obvious variation of the contact angle, indication for a modification of one of the surface tensions, γ_{LG}, γ_{SL} or γ_{SG}, the liquid-gas surface tension does not drop. As already examined by the BSA isotherms in Fig. 24.1 of the foregoing section, the liquid-gas surface tension should drop significantly about 15 to 20 mN/m at the given concentration.

Nevertheless, the surface tension equilibrium is affected by the adsorption of BSA, and the hypothesis is thus made that the modified surface tension is

[1] It would not be necessary to extract the radius from imaging data, if the drop did not evaporate. Since this is not the case, these data need to be obtained as well.

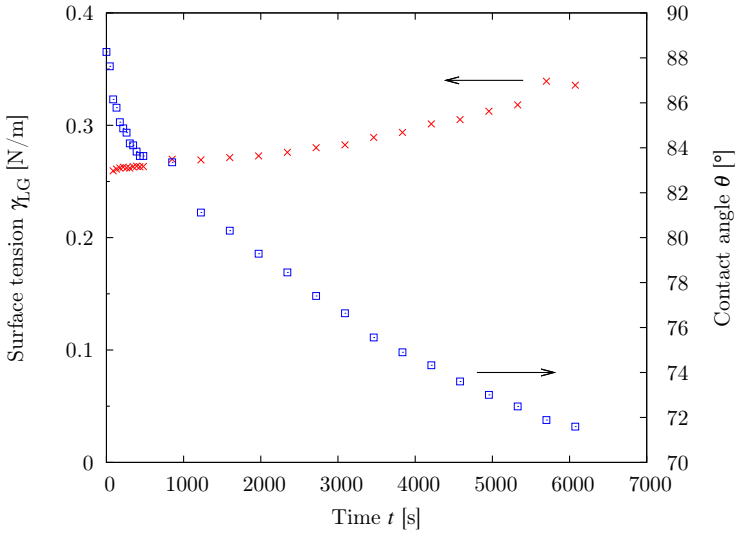

Fig. 25.1.: Evolution of γ_{LG} (left axis) and θ (right axis) as measured by interferometry and imaging, respectively, for a solution of BSA at $C_0 = 30\,\mu g/mL$ (buffer 100 % PBS, pH 4). Despite the obvious variation of the contact angle, indication for a modification of one of the surface tensions, γ_{LG}, γ_{SL} or γ_{SG}, the liquid-gas surface tension does not drop. Drop volume 1 µL.

γ_{SL}, which is the second drop interface in contact with BSA molecules. This possibility is investigated in the next section.

25.2. Surface tension measurements in the low-frequency regime

Surface tension measurements of γ_{SL} are carried out using imaging of the measured drop in the course of time and extracting its contact angle. Using the contact angle and the applied voltage, the variation of the solid-liquid surface tension, γ_{SL}, may be calculated from the Young equation evaluated in two situations; first for a drop with an uncontaminated surface:

$$\gamma_{LG} \cos\theta_0 = \gamma_{SG} - \gamma_{SL},$$

then for a drop of volume concentration C_0, RMS voltage U and dynamic surface tension, $\gamma_{SL}(t)$:

$$\gamma_{LG} \cos\theta(U,t) = \gamma_{SG} - \gamma_{SL}(U, C_0, t).$$

As for γ_{LG}, it is consistently supposed that the solid-gas surface tension, γ_{SG}, is not significantly affected by surfactant adsorption and that it remains constant. The subtraction of the two foregoing equations writes:

$$\gamma_{LG} (\cos\theta_0 - \cos\theta(U,t)) = \gamma_{SL}(U, C_0, t) - \gamma_{SL}.$$

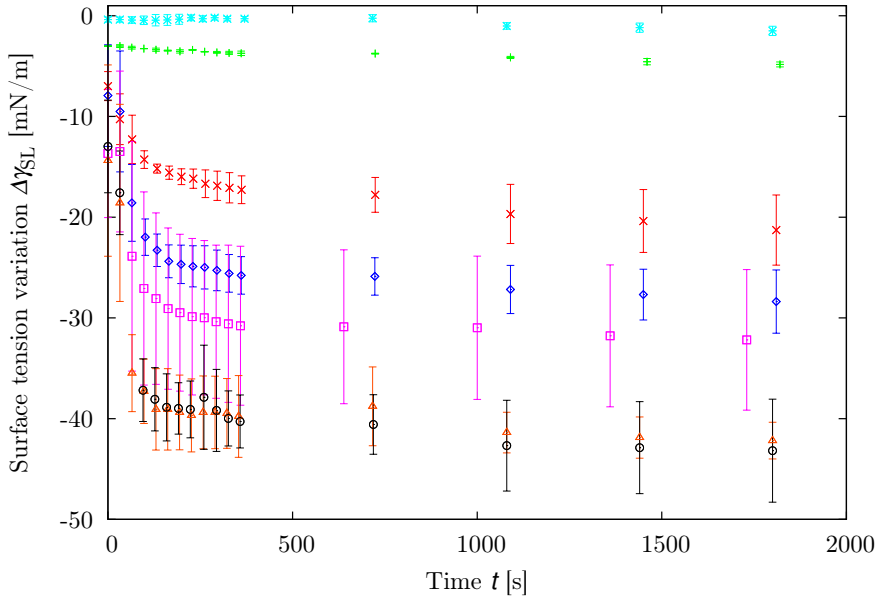

Fig. 25.2.: Incidence of low-frequency electrowetting on adsorption dynamics for different shape modes, $n = 2$, 4 and 6. Also, the dependence on amplitude for mode 2 is investigated. The PBS curve provides the reference value for surface tension. The BSA solution is of concentration $C_0 = 30\,\mu g/mL$ in 100 % PBS buffer at pH 4. The high-frequency electrowetting voltage is switched off. Drop volume 1 µL.
Legend: (+) pure water without actuation, without BSA, (∗) 100 % PBS buffer without actuation, without BSA, (×) PBS buffer without actuation, with BSA, (⋄) $n = 2$, $a_0 = 0.15\,H$, (□) $n = 2$, $a_0 = 0.3\,H$, (△) $n = 4$, $a_0 = 0.15\,H$, (○) $n = 6$, $a_0 = 0.15\,H$.

Last, the dependence of γ_{SL} on U and t needs to be dissociated by making use of the Lippmann-Young equation of electrowetting:

$$\gamma_{SL}(U, C_0, t) = \gamma_{SL}(0, C_0, t) - \frac{c}{8}U^2.$$

By supposing γ_{SG} and γ_{LG} to be constant, the variation of γ_{SL} may be expressed by the following equation:

$$\Delta\gamma_{SL} := \gamma_{SL}(C_0, t) - \gamma_{SL} = \gamma_{LG}\,(\cos\theta_0 - \cos\theta(U, t)) + \frac{c}{8}U^2, \tag{25.1}$$

where $\gamma_{SL}(0, C_0, t)$ is now denoted $\gamma_{SL}(C_0, t)$ for sake of readability. This equation was used to evaluate a number of experimental measurements. The following liquids were evaluated concerning their dynamic surface tension:

- Pure MilliQ water without electrowetting actuation
- Pure PBS buffer without electrowetting actuation

These liquids are measured in order to check that the value of surface tension remains at a constant level. Fig. 25.2 shows the experimental curves for these two liquids. It is seen that pure water exhibits a lower surface tension level than PBS buffer. This fact is correct and in par with theory, since salts tend to increase surface tension. PBS buffer has a concentration of about 150 mmol/L of different

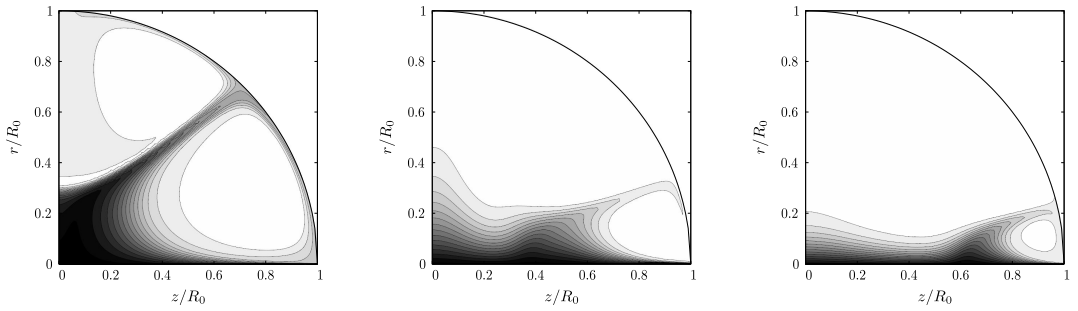

(a) Concentration for $n = 2$. (b) Concentration for $n = 4$. (c) Concentration for $n = 6$.

Fig. 25.3.: Plots of volume concentration, C, issued from the simulations of section 22.6: different shape modes are considered to investigate on the convection dynamics near the contact line. The concentration is coded in gray scale: white stands for $C = C_0$, black stands for $C = 0$, separated by fifteen equidistant levels on the gray scale.

salts, which is the physiological concentration in biological cells, and therefore a higher surface tension than pure water. The surface tension level of PBS buffer, $\gamma_{LG}^{PBS} = 70\,\mathrm{mN/m}$ is chosen as reference value in equation 25.1. The fact that this value is smaller than expected in theory is due to traces of contamination, which can never be totally avoided in practical conditions. The choice of PBS buffer as reference is obvious, since the sample of $C_0 = 30\,\mu\mathrm{g/mL}$ BSA solution is solubilized in undiluted PBS buffer.

Two series of experiments are conducted for a solution of BSA at volume concentration $C_0 = 30\,\mu\mathrm{g/mL}$: The first series focuses on the aspect of low-frequency electrowetting and its impact on albumin adsorption on the lubricated solid substrate. The high-frequency component of the EWOD actuation is switched off. In comparison to the experimental curve for adsorption without actuation, four cases are examined and displayed in Fig. 25.2:

- EW excitation of mode $n = 2$, oscillation amplitude $a_2^0/H = 15\,\%$
- EW excitation of mode $n = 2$, oscillation amplitude $a_2^0/H = 30\,\%$
- EW excitation of mode $n = 4$, oscillation amplitude $a_4^0/H = 15\,\%$
- EW excitation of mode $n = 6$, oscillation amplitude $a_6^0/H = 15\,\%$

The variable H is the drop height, as the radius length scales, neither for the base nor for curvature, do not characterize correctly the vertical length scale of the drop. The information on drop height and oscillation amplitude are extracted from images taken during oscillations.[2] Each data point, d, is the mean value for several measurements in the same conditions and at the same time. In order to show the reproducibility, the standard deviation for each data point is calculated and displayed as an error bar, $d \pm \sigma_d$. For certain data, the measured standard deviation is pretty high, which results in great error bars.

Several conclusions can be drawn from the data in Fig. 25.2: The curve without actuation (×) exhibits the least efficient adsorption in the sens that the steady

[2]The images to observe the contact angle are taken without low-frequency electrowetting actuation.

value of $\Delta\gamma_{SL}$ remains close to the initial value. Then, by increasing the mode number at constant drop oscillation amplitude, surface ageing increases dramatically, the mode $n = 6$ being the most efficient stirring regime. This means that electrowetting-induced stirring due to steady streaming reveals to be a means to enhance surfactant transport to an interface, i.e. the solid substrate.

Secondly, a comparison of simulation with experiments may be appropriate. It is worthwhile to consider Fig. 22.15(a) on page 170 and the correspondent text stating that, for adsorption at the lubricated substrate, mode number $n = 6$ would exhibit less significant adsorption characteristics than modes 2 and 4. At first sight, this seems to disagree with the experimental findings here, but there is an essential difference between numerical simulations and experiment: in the experiment, the contact angle varies during the adsorption process. BSA adsorbs progressively to the clean substrate near the contact line of the drop, which in the course of time spreads due to decreasing surface tension, γ_{SL}. At the "newly wetted" non-contaminated solid surface, BSA molecules are free to adsorb. According to the streamlines in Fig. 22.4 on page 159, the higher mode number vortices act locally in the vicinity of the contact line, in contrast to mode 2. This means that the efficiency of stirring-enhanced surface ageing might be higher for modes 4 and 6 with the hypothesis that the major part of the substrate, excluding the contact line, is already covered by BSA molecules, a point which is a fair assumption for the presented measurements. To underline the hypothesis of efficient stirring at the contact line for high mode numbers, isoconcentration contour plots are extracted from the simulation of section 22.6 (page 169) and displayed in Fig. 25.3. In these simulations, adsorption acts on the solid substrate only, and the highest gradient for concentration is visible for modes 4 and 6 at the contact line, whereas the gradient for mode 2 seems to be located a little further to the center of the drop. Please refer to Fig. 25.4 for a sketch of the process for modes $n = 2$ and $n = 6$.

To summarize, for the higher order modes, vortex structures are responsible for a more efficient molecular renewal in the vicinity of the contact line. In addition, the diffusive flux normal to the lubricated substrate, and near the contact line in general, is found to be intensified by convection in the vicinity of the contact line. Serially coupled with the energy barrier due to adsorption, surface ageing is therefore significantly enhanced.

25.3. Surface tension measurements in the high-frequency regime

In addition to the foregoing analysis, measurements of dynamic liquid-solid surface tension, γ_{SL}, are analyzed for the high-frequency electrowetting regime. As suggested by a recent study [124], internal flows are also created in the high-frequency electrowetting regime. In this regime, drop shape oscillations do not play the preponderant role, but other electrohydrodynamic effects of electrowetting come into play. In their work, the authors state that that the internal electric field is not homogeneous any more at high frequencies. The critical frequency depends on the solution conductivity. Above this critical

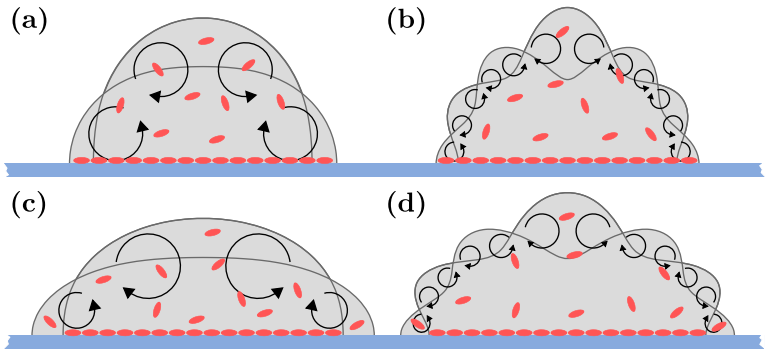

Fig. 25.4.: Sketch illustrating the stirring of different shape modes: (a) shape mode $n = 2$, (b) shape mode $n = 6$, (c) and (d) represent the configurations after spreading of the droplet, recirculations are indicated by arrows. The recirculations are localized more precisely at the contact line for mode 6, which may be a reason for adsorption enhancement of BSA molecules (red shapes).

frequency, a electrohydrodynamic (EHD) flow is created, depending on the electrowetting geometry. Ko et al. use a wire-in-drop geometry, and the EHD flow is strongly dependent on the position of the wire. In a coplanar geometry, the flow is supposed to be dependent on the position and size of the electrode gap, where a high electric field gradient should be generated at high frequencies.

Fig. 25.5 recapitulates the experimental observations for a BSA solution of 30 µg/L in comparison to pure water and PBS buffer. Three clear observations can be made:

- A higher amplitude of the EW actuation voltage acts in favor of surface ageing.
- The 20 kHz curves exhibit slightly stronger surface ageing kinetics than the 3 kHz curves, compared at constant actuation voltage.
- The overall efficiency of high-frequency EW for surface ageing enhancement is lower than achieved by low-frequency electrowetting.

Since the nature of the high-frequency electrowetting-induced flow is not further investigated, neither by Ko et al. [124] nor in this work, only assumptions could be issued concerning the reasons for these observations. Nevertheless, this methodology is interesting for practical reasons, since the possibility to implement it in confined spaces is straightforward. This is not especially true for drop oscillation-induced streaming, since the creation of a capillary wave network on a surface might be inhibited in strongly confined spaces.

25.4. Equilibrium value of surface tension

A general remark on the measured adsorption isotherms concerns the equilibrium value of surface tension, which is different for all recorded curves. Intuitively, the same equilibrium value should be reached after some time, but this does not seem to be the case. A possible reason for this may be the size of the system, which leads to a dimensionless number $\varepsilon_0 = k_d R_0/k_a \approx 10$, which is not far from unity, for a 1 µL sessile drop. Hence, it is not completely assured that the

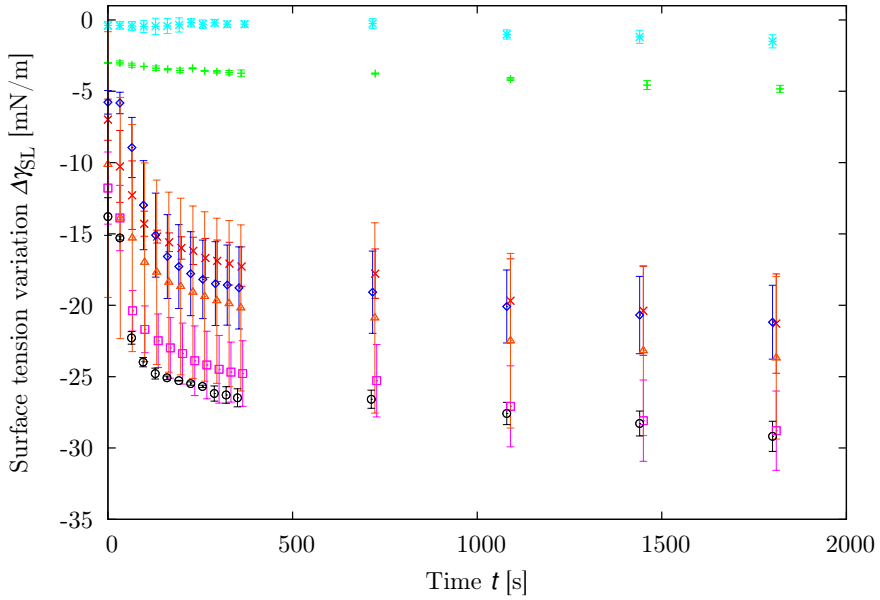

Fig. 25.5.: Incidence of high-frequency electrowetting on adsorption dynamics for different frequencies, $\nu = 3\,\mathrm{kHz}$ and $\nu = 20\,\mathrm{kHz}$, using two amplitudes of $43\,V_{rms}$ and $84\,V_{rms}$. The PBS curve provides the reference value for surface tension. The BSA solution is of concentration $C_0 = 30\,\mu g/mL$ in 100 % PBS buffer at pH 4. The low-frequency electrowetting voltage is switched off. Drop volume 1 µL.
Legend: (+) pure water without actuation, without BSA, (∗) 100 % PBS buffer without actuation, without BSA, (×) PBS buffer without actuation, with BSA, (⋄) $\nu = 3\,\mathrm{kHz}$, $U = 43\,V_{rms}$, (□) $\nu = 3\,\mathrm{kHz}$, $U = 84\,V_{rms}$, (△) $\nu = 20\,\mathrm{kHz}$, $U = 43\,V_{rms}$, (○) $\nu = 20\,\mathrm{kHz}$, $U = 84\,V_{rms}$.

studied system can be really considered as a semi-infinite geometry concerning the molecule amount in the volume. If this is not the case, the assumption of a saturated substrate surface made earlier can be challenged. How can the situation of adsorption then be interpreted? The newly wetted substrate interface, which is free of surfactant, competes with the formerly wetted substrate for molecule adsorption. In a semi-infinite system (high ε_0), this is not a real competition, since molecules are abundant. For a system with low ε_0, not enough molecules are present to "satisfy" both areas, formerly wetted and newly wetted. At this point, it is extremely interesting to consider the implication of the adsorption flux, $j_{ads} = k_a C|_s - k_d \Gamma$: Since the surface concentration is lower on the newly wetted surface, $\Gamma \approx 0$, the adsorption flux, is higher on this part of the substrate. It also depends on the volume concentration near the interface, $C|_s$. With the newly acquainted insights on how streaming interferes with the volume concentration (Fig. 25.2 and 25.3), it may be that the more efficiently streaming acts near the contact line, the higher the volume concentration will be at this point, which is in fact favoring drop spreading. It has to be kept in mind that the solid-liquid surface tension, as well as all other surface tensions, depends only on the surface concentration in direct vicinity of the contact line, and not on the concentration of surfactant molecules far from it. Following these considerations, the farther spreading of the drop can be explained, including the fact that streaming enhances adsorption for a drop of variable contact angle.

26. Conclusion and outlook – The next step: How to functionalize the free drop surface?

In this part, the dynamic solid-liquid surface tension of a lubricated surface wetted by an albumin-laden drop was investigated. It is seen in section 25.1, that it is not straightforward to functionalize a liquid-gas interface with partly soluble molecules: BSA molecules seems to exhibit a specific affinity for the solid-liquid interface, i.e. the lubricated solid substrate underneath the drop.

A means to circumvent this bottleneck could be to work with a non-miscible liquid ambient phase, e.g. silicone oil or alkanes. These tests were addressed before the end of the thesis and several recommendations can be given:

- Silicone oil as ambient phase is too viscous for drop oscillations to be created efficiently for interferometry measurements (dynamic viscosity of silicone oil used for the test, $\mu = 5\,\mathrm{mPa\,s}$).
- The liquids of the alkane class exist in a variety of different viscosities, depending on the size of the alkane molecules.
- Tests have been performed with hexadecane, $\mu = 3.3\,\mathrm{mPa\,s}$, which is too viscous, just as silicone oil.
- Tests have been performed with decane, with a viscosity approximately equal to water, $\mu = 920\,\mu\mathrm{Pa\,s}$: an interferometry spectrum can be measured at certain contact angles, but the quality factor is very poor compared to measurements in air.
- The least viscous liquid alkane is hexane with a viscosity of $\mu = 290\,\mu\mathrm{Pa\,s}$, tests have not been performed yet. This liquid is very volatile, which makes it necessary to cover the experiment. Furthermore, hexane is harmful to nature, which requires special attention for waste treatment.

When working in an ambient liquid medium, attention needs to be paid to the viscous dissipation, which not only acts in the inner of the drop, but also in the ambient phase. This means that damping of drop shape oscillations is greater than with a gas ambient phase. The oscillation amplitude will lower at the apex, which is a great disadvantage for the interferometry measurement. This effect remains though worthwhile to be used for tunable particle or cell focusing at certain locations in the vicinity of the liquid-liquid interface [62].

General conclusion

To conclude this work, a summary of the major achievements and results is appropriate. An experimental setup was realized, allowing end-users of digital microsystems to characterize by interferometry drop shape oscillations, including data acquisition and processing. The interferometry technique of Michelson type can be used to detect micrometric displacements of a liquid-gas interface using a 532 nm wavelength laser and an adapted avalanche photo diode.

The experimental technique was used to characterize the evaporation of a single isolated drop, as well as of a single drop within a complex drop array regarding several geometric parameters. The methodology is found to accurately translate the relative time-dependence of the evaporation process, and to measure fairly well the radius of the drop. Due to the usage of dual-frequency electrowetting, the contact angle can be controlled and its hysteresis reduced, which facilitates the analysis.

The theoretical part of this work concerns adsorption and diffusion phenomena in a drop. A mathematical model was established describing physicochemical processes in a free spherical (or half-spherical) drop, and for a finite amount of molecules. Furthermore, the geometry of the drop is variable, an application is given for evaporative mass transfer acting on the position of the outer drop boundary, i.e. a variable radius. A new dimensionless number, ε_0, was introduced by considering the amount of surfactant molecules on the surface, compared to the amount of molecules in the volume. Using Henry's law for ad- and desorption of surfactants, this dimensionless number can be expressed by the ad- and desorption constants of surfactant, and the size of the drop, bearing the possibility to compare different systems concerning their physicochemical behavior.

An interesting result is the introduction of a new equilibrium constant for finite systems, Γ_e^{μ}, which is calculated in function of the dimensionless number, ε_0. Depending on the geometry and the surfactant used, this number may differ by several orders of magnitude from the equilibrium surface concentration of macroscopic systems, Γ_e.

With this model, a non-dimensional analysis using the finite element method was conducted, giving insights in the influence of four dimensionless numbers, namely η_{ea}, η_{ed}, η_{ad} and ε_0. Furthermore, for adsorption-limited systems, the analytical model for finite-sized systems was enhanced to sessile droplets of arbitrary contact angle. It was found that the adsorption dynamics strongly depends on contact angle for geometries of low contact angle (hydrophilic), whereas for geometries of high contact angle (hydrophobic), the dependence on θ is nearly negligible.

The finite element method was then extended in order to take into account steady streaming, induced by oscillating electrowetting, and coupled to diffuso-

convective transport and sorption phenomena. The time scale for surface ageing was analyzed for diffusion-limited systems regarding three dimensionless numbers implying, amongst others, the amplitude of the streaming current. The influence of the oscillation mode number, imposing different convective regimes, was analyzed. In addition, a distinction was made between adsorption to the free drop surface and adsorption to the liquid-solid interface, hereby insights were gained on the local action of the streaming vortices on volume concentration gradients, which was helpful for the analysis of data in the last part of the work.

The last part of this work was experimental and dedicated to surface functionalization of the solid-liquid interface by bovine serum albumin. Giving up the regulation of contact angle to 90°, the dynamic liquid-solid surface tension was calculated in the course of time, and the effect of oscillation-induced streaming on adsorption dynamics was measured. The observations could be interpreted using the results of the finite element method. Furthermore, the influence of a high-frequency electrowetting voltage on stirring was measured in order to examine any effect on dynamic surface tension. Indeed, surface ageing enhancement due to stirring effect could be stated.

As far as future work is concerned, several proposals can be cited. Concerning instrumentation, it would be beneficial to use a four quadrant electrode design consisting of four congruent circle quadrants. This does not change anything regarding instrumentation, but exhibits an advantage for improved stabilization of the drop position. When actuating the electrodes alternatively (cf. Fig. 26.1(a)), the droplet is perfectly centered above the center of the electrode design. This means less user interaction and eventually even more precise measurements. Up to now, the drop sometimes sticks to the electrode borders due to a biased movement on the lubricated electrodes. Future electrode conception should fix this point.

Furthermore, the creation of a measurement spot in the centre of the electrode design is a valuable modification of the actual designs. This circumvents the problem of modulated intererometry signals due to the lubricating film. To push it even further, the centre of the design might be covered by a surface film with special reflectivity so as to maximize the intensity of the interferometry signal. This enhances light intensity of the superposition of the two laser beam reflexions and thus permits to work at even lower laser power.

Just as an electric actuation of the electrodes modifies drop mechanics, an interface motion of the drop will have an impact on the electronic circuit. This phenomenon is known as reverse electrowetting, or "REWOD" [125]. Also, capacitive sensing of the total capacity composed of the dielectric substrate and the drop, could be used to sense the mechanical and chemical properties of the drop [80,91]. These two phenomena could be interesting means to serve as a new measurement methodology, instead of the laser approach. The great advantage of this is that no optical detection would be required, combining actuation and acquisition using an electric approach, without altering data sampling and

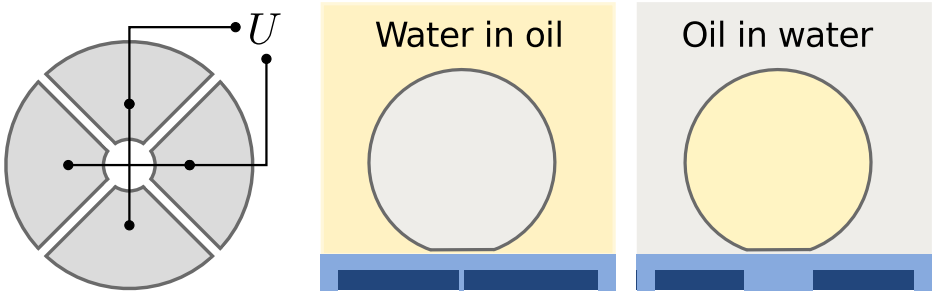

(a) Electrowetting geometry and actuation scheme using four congruent electrodes for symmetric wetting and perfect centering of the drop.

(b) Switching oil and aqueous phase is an interesting idea for developing environmental sensing in liquids and for having a more subtle control on the contact angle during adsorption due to the new electrode geometry.

Fig. 26.1.: Two new approaches: position control and a liquid/liquid methodology.

processing!

Finally, it is worthwhile to think about implementing transient analysis as already cited in parts II and III, and appendix D of this work. It could serve as a light weight methodology for excitation and analysis, compared to the stationary spectrum.

The theoretical part V on physicochemical phenomena and steady streaming could be extended to variable contact angles. Furthermore, the use of the Langmuir law for characterizing time-dependent adsorption would be an appropriate evolution of the up to now developed model. Another interesting point is the implementation of a surfactant concentration, $\Gamma_{\text{ext}} \neq 0$, in the up to now not existing ambient phase of the drop, bearing the possibility to consider ambient media for hybridization tests, environmental monitoring or emulsions, designed for adsorption of surfactant from the ambient phase.

The experimental part VI on biological applications may be continued in several directions. One of them would be to find an appropriate means of exploiting the liquid-gas surface tension for correct functionalization of the drop surface and pursuing the approach of label-free hybridization tests. First tests in this direction are already pursued to a small extent in this work (cf. chapter 26). One problem of pursuing this approach is the strong contact angle diminution with a lowered surface tension. Normally, with oil or an alkane as ambient phase, the drop will adopt a very high contact angle, which could solve this problem. Another issue is the rapid viscous dissipation of oscillations with a viscous ambient phase, which reduces the choice of ambient phase liquids to a very restrained panoply.

Now, if the aim is to keep air as ambient phase, then BSA, pluronics [74,126], or any other molecule with a strong affinity for the lubricated solid substrate, could be used with benefit to allow other biomolecules to adsorb at the (functionalized) drop surface. Such a detection at a fluid interface permits a streaming-induced flow-focusing along the interface with a greater detection sensitivity as a result.

An interesting configuration could also be to switch ambient and drop phase, i.e. use an oil or alkane drop in an aqueous ambient phase (cf. Fig. 26.1(b)). In this case, under electrowetting actuation, the contact line reduces in diameter. Electrowetting-induced oscillations are hence created not by spreading the drop with an AC voltage, but by retraction. Also, the contact line shrinks with adsorption of biomolecules in its vicinity. By correctly chosing the inner diameter of the electrowetting electrodes, an EW actuation might be sufficient to keep the contact line electrically pinned to the inner electrode border. Thus, the problem of extreme drop spreading as experienced in the last part of this work might be circumvented. This would allow using functionalized drops in an aqueous environment like a microchannel for detection of water-soluble ligand molecules.

Appendices

A. Coplanar electrowetting: influence of the gap potential

This appendix is based on the work of Yi and Kim [31], who give an introduction on how to adapt the electrowetting law (4.3) to coplanar electrode designs. For a plunging wire geometry, in contrast to coplanar electrowetting, the electrowetting tension U is equal to the tension applied across the solid/liquid interface, U_{SL}. This is not the case for coplanar electrowetting, where the potential difference is applied between different electrodes underneath the substrate, called driving and reference electrodes. The drop will not experience the same potential as in a plunging wire geometry. Hence, for a coplanar design, a correction factor needs to be included, cf. section 4.3. Yi and Kim [31] suggest a correction, which is based on the approximation of a zero gap potential. According to experimental observations made during this work [33], a doubt came up, as the observations were not in par with theory. In order to know, whether the hypothesis of a zero gap potential, $U_{\mathrm{g}} = 0$, made by Yi and Kim is too strong, or whether an experimental element was not completely understood, an effort was made to calculate the real gap potential between the electrodes. Using an exact expression for the gap potential, the correction factor established by Kim may be refined. The study was divided into three parts, modeling, simulation and experiments. In the modeling part, a theoretical expression for U_{g} was found and then validated by simulation. The experimental part finally served to compare the theoretical results to experimental observations.

For the modeling, a two-dimensional domain is considered (cf. Fig. A.1). The mathematic domain corresponds to the 2D plane as indicated in the figure, starting from the center of the electrode geometry ($x = 0$), ending at a distance $x = R_{\mathrm{B}}$ perpendicular to the gap axis, corresponding to the triple contact line of the drop. The symmetry axis divides the physical domain in the center of the gap area, the electrodes are at potential $U = \pm U_0/2$, respectively. The drop and the symmetry axis are considered isopotential, $U = 0\,\mathrm{V}$ at these boundaries, hypothesis which is verified by the simulation. The gap area is modeled using an insulation condition, $\partial U/\partial n = 0$. The dielectric is considered uniform as it is more convenient for modeling. Also, for a uniform dielectric, the potential of the gap and inside the dielectric does not depend on the dielectric constant. For calculation of the electric potential throughout the domain (dielectric material), the Laplace equation is considered:

$$\Delta U(x, y) = 0.$$

The solution of this equation with the corresponding boundary conditions is possible with conformal transformations [39]. In order to find a solution to the problem, three conformal transformations need to be applied. The starting point

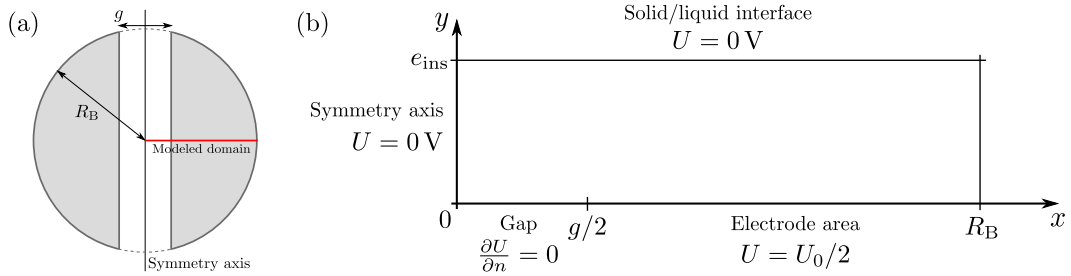

Fig. A.1.: Sketch of the two-dimensional domain with boundary conditions: (a) Part of the electrode geometry which is in contact with the drop of base radius R_B; gap width g, (b) boundary conditions; dielectric thickness e_{ins}.

is the complex representation of x and y, using the variable Z_1:

$$Z_1 := x + iy.$$

The following transformations are:

$$Z_2 := \cosh\left(\frac{\pi Z_1}{e}\right) = x_2 + iy_2,$$

$$Z_3 := \frac{2Z_2 - x_D + 1}{x_D + 1} = x_3 + iy_3,$$

$$Z_4 := \arcsin(Z_3)/\pi = x_4 + iy_4,$$

where $x_D := \cosh(\pi g/2e_{ins})$. The geometry in the Z_4 plane corresponds to a simple geometry. During conformal transformations, boundary conditions are conserved, and the solution for the potential takes a simple linear form:

$$U(Z_4) = U_0\,(2x_4 + 1)/4.$$

The potential can be retransformed to the Z_3 plane:

$$U_g(Z_3) = \frac{U_0}{4\pi}\left(2\arctan\left(\frac{x_3}{\sqrt{1 - x_3^2} - y_3}\right) + \pi\right).$$

By retransforming $Z_3 \rightarrow Z_2 \rightarrow Z_1$, the gap potential can be calculated using x- and y-coordinates, which is not shown here. Nevertheless, the retransformation of the last equation to the coordinates (x, y) is possible in an analytical manner. The implementation of the simulation is realized under COMSOL 4.2a and includes the same geometry and boundary conditions as for the modeling. The results of modeling and numerical method are compared and yield the same values with a maximum error of $< 1\,\%$ due to meshing and numerical discrepancies.

Depending on dielectric thickness and gap width, the gap potential adopts different shapes. Different non-dimensionalized curves of $U_g(x/g)/U_0$ are displayed in figure A.2. For large gaps, it is found that the gap potential undergoes

a transition of thickness $\approx 5\,\mu m$ from $U_g = \pm U_0/2$ at $x = \pm g/2$, to $U_g = 0$. For small gaps, this transition to $U_g = 0$ is perturbed by the proximity of the electrode, and a quasi-linear evolution of the potential is found (cf. Fig. A.2, $3\,\mu m$). In either case, the gap potential contributes to electrowetting, and the modified Lippmann-Young equation (4.5) may take into account this contribution via an integral, representing the intra-gap voltage distribution:

$$\gamma_{SL}(U) - \gamma_{SL}(0) = -\frac{c}{2}\left(\frac{S_d}{S_t}U_d^2 + \frac{S_r}{S_t}U_r^2 + 2R_B\int_{-g/2}^{g/2} U_g(x)^2\,dx\right).$$

The comparison between this expression for surface energy and the modified Lippmann-Young equation (4.5) will give the information to which extent the hypothesis of a zero gap-potential is acceptable. The considered equation is the following:

$$\delta_{Kim} = 1 - \frac{2R_B\int_{-g/2}^{g/2} U_g(x)^2\,dx}{A_d U_d^2 + A_r U_r^2} < 1\,\%.$$

This data is shown in Fig. A.3 in function of gap width. The conclusion is that the assumption of a zero gap potential, $U_g = 0\ \forall_x$, is perfectly adequate. The reason for the incongruence between experimental results and theoretical results pointed out in [33] is found to be due to the applied oil film.

The oil film thickness depends on the chronology of the applied voltage, U, and drainage of the film due to the electrostatic and Hamaker pressure [71]. The oil film thickness may be evaluated by measurement of electrowetting curves and subsequent evaluation of the capacitance, which depends on the oil film thickness. However, this approach bears several experimental difficulties, which is why it was not pursued. Nevertheless, by diminishing the amount of oil, a more stable oil film may be reached. For many applications, an lubricating oil film is not necessary, since dual-frequency electrowetting provides a high-frequency electrowetting tension, which diminishes contact angle hysteresis and stick-slip motion.

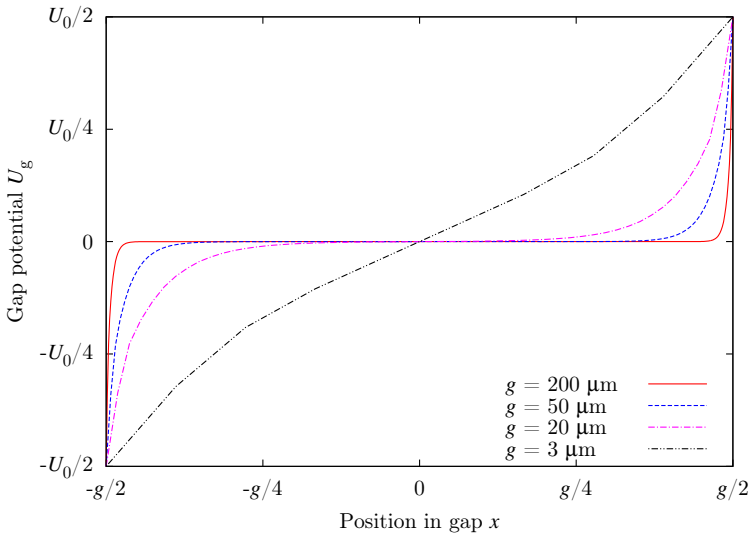

Fig. A.2.: Non-dimensionalized presentation of the intra-gap potential for different gap widths $g = 3, 20, 50, 200\,\mu m$. The dielectric thickness $e_{ins} = 1.6\,\mu m$, the curves are independent of the relative permittivity, ϵ_{ins}.

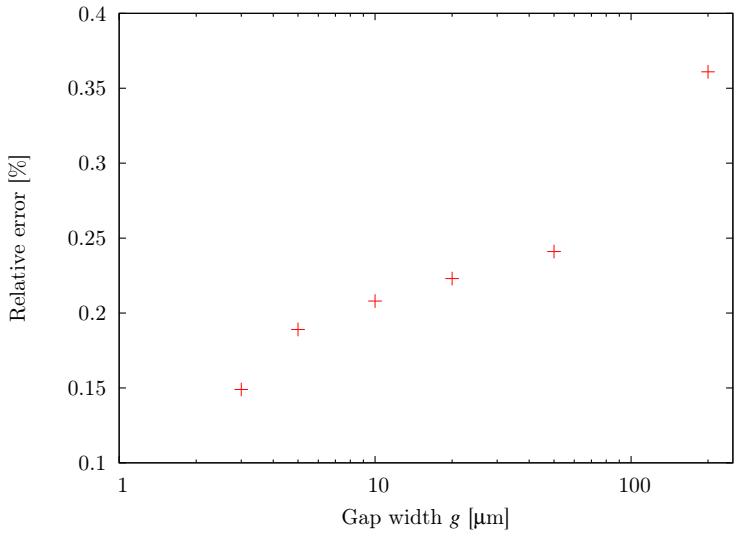

Fig. A.3.: Comparison between the exact formulation of U_g, and the approximation made by Yi and Kim, $U_g = 0$. The relative error, δ_{Kim}, between the exact and approximated expression is less than 1 % for common gap widths, $g \in [3\,\mu m, 200\,\mu m]$. The dielectric is $e_{ins} = 1.6\,\mu m$ thick.

B. Legendre polynomials

The first even Legendre polynomials are:

$$P_2(x) = \frac{1}{2}\left(3x^2 - 1\right),$$

$$P_4(x) = \frac{1}{8}\left(35x^4 - 30x^2 + 3\right),$$

$$P_6(x) = \frac{1}{16}\left(231x^6 - 315x^4 + 105x^2 - 5\right).$$

In the theory of drop shape oscillations, the polynomials are used to describe the shape of a drop, cf. equation (5.1) on page 46. In this case, $x = \cos\varphi$, $\varphi \in [0, \pi/2]$, which is equivalent to $x \in [0, 1]$, the apex being situated at $x = 0$, and the triple contact line at $x = 1$.

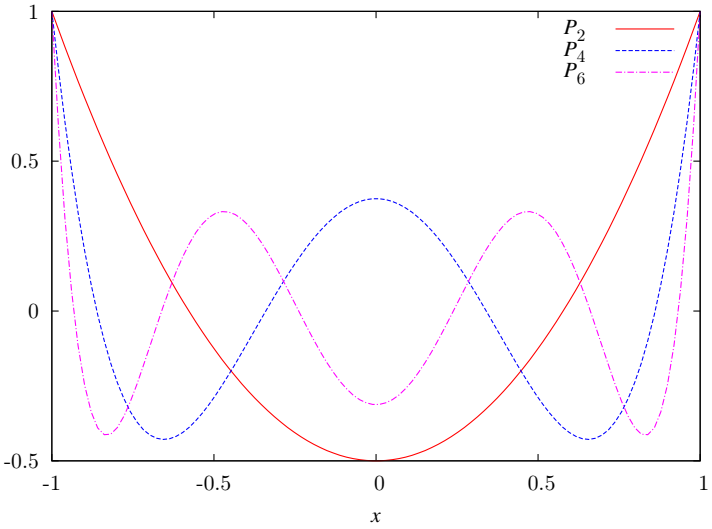

Fig. B.1.: The first even Legendre polynomials.

C. Calculation of the correction factors for sessile drop oscillations

The eigenvalues $\lambda_{\mathrm{n}}(\theta)$ defining the resonance spectrum, equation (5.9), were calculated by Strani and Sabetta in 1984 [42]. The calculation depends on the value of the contact angle θ, since the Green function of the solution diverges for $\theta = \pi/2$ and $\theta = \pi$. For the second case (flat liquid film), no solution is possible. The two solutions for $\theta \neq \pi/2$ and $\theta = \pi/2$ result in an eigenvector κ, which is correlated to the correction factors $\lambda_n(\theta)$:

$$\lambda_n(\theta) = 1/n(n-1)(n+2)\kappa_n.$$

The two calculations are implemented in a MATLAB routine for facile evaluation of imaging data in combination with measured resonance frequencies. In the case of a droplet with a fixed contact angle, no imaging is needed, and the correction factor may be evaluated prior to the data processing.

Contact angles $\theta \neq \pi/2$

Ignoring the influence of the ambient phase on drop shape oscillations ($\rho^{\mathrm{e}} \ll \rho^{\mathrm{i}}$), these eigenvalues are obtained by calculating the determinant of the matrix A_{ij}, following the methodology used by Smithwick and Boulet [127]:

$$\det(A_{ij} - \kappa_i \delta_{ij}) = 0,$$

where $i = 1, 2, \ldots$ and $j = 1, 2, \ldots$ and δ_{ij} is the Kronecker symbol. The elements of the matrix A_{ij} are defined by:

$$A_{ij} = A_{ji} = 2\left(\frac{G_{i0}\, G_{0j}}{G_{00}} - G_{ij}\right)\sqrt{\frac{1}{i(2i+1)j(2j+1)}},$$

using:

$$G_{ij} = \frac{(2i+1)(2j+1)}{4[j(j+1)-2]} \sum_{r=0}^{\lfloor j/2 \rfloor} \sum_{s=0}^{\lfloor i/2 \rfloor} C_{rs} D_{rs}.$$

Here, the coefficients C_{rs} and D_{rs} are given by:

$$C_{rs} = \frac{(-1)^{r+s}(2j-2r)!(2i-2s)!}{2^{i+j} r!s!(j-r)!(i-s)!(j-2r)!(i-2s)!},$$

$$D_{rs} = \frac{a^{j-2r-1} - a^w}{i-2s+2} + \frac{a^w - 1}{w}.$$

with $a = \cos\theta$, $w = j - 2r + i - 2s + 1$ and $\lfloor f \rfloor$, which represents the floor function. For all $i = j = 1$, the coefficient G_{11} needs to be calculated separately [42]:

$$G_{11} = (6\ln(1+a) - 3/a + 7 - 6\ln 2 - a^3 - 3a)/12.$$

The correction factors of mode $n = 2$ can also be fitted by the following polynomial:

$$\begin{aligned} K_2(\theta) =& 9.7951 \times 10^{-15}\theta^8 - 8.1938 \times 10^{-12}\theta^7 + 2.9528 \times 10^{-9}\theta^6 - 5.9956 \times 10^{-7}\theta^5 \\ &+ 7.5257 \times 10^{-5}\theta^4 - 6.0195 \times 10^{-3}\theta^3 + 0.303\,79\theta^2 - 9.1237\theta + 135.64, \end{aligned}$$

for the range of contact angles $\theta \in [31, 159]$, with a variance of $\sigma^2 < 10^{-3}$, or the range of contact angles $\theta \in [50, 155]$, with a variance of $\sigma^2 < 10^{-4}$.

Contact angle $\theta = \pi/2$

The matrix A_{ij} is singular for the case of $\theta = \pi/2$, a different calculation is done for this contact angle [42]:

$$\det(B_{ij} - \kappa_i \delta_{ij}) = 0,$$

where $i = 1, 2, \ldots$ and $j = 1, 2, \ldots$ and δ_{ij} is the Kronecker symbol. The elements of the matrix B_{ij} are defined by:

$$B_{ij} = B_{ji} = \frac{\sqrt{(2i+1)(2j+1)}}{2\sqrt{ij}\,(j(j+1) - 2)} H_{ij},$$

$$\begin{aligned} H_{ij} = H_{ji} = \Big(P_j(0)\Big(2\int_0^1 P_1(\tau)P_i(\tau)\,\mathrm{d}\tau - \int_0^1 P_i(\tau)\,\mathrm{d}\tau\Big) \\ - 2\int_0^1 P_1(\tau)P_i(\tau)\,\mathrm{d}\tau \int_0^1 P_j(\tau)\,\mathrm{d}\tau + \int_0^1 P_i(\tau)P_j(\tau)\,\mathrm{d}\tau\Big) \qquad \text{for } k \neq 1, \end{aligned}$$

$$H_{11} = -\frac{1}{3} + \frac{1}{2}\ln 2,$$

where $P_k(\tau)$ is the Legendre polynomial of kth order. This calculation is based on the assumption that the contact angle is equal to $\pi/2$. The same results are obtained by calculating the limit $\lim_{\theta\to\pi/2}$ of the calculation for $\theta \neq \pi/2$. The correction factors $\lambda_n(\pi/2)$ for the first resonant modes and a contact angle $\theta = \pi/2$ can be found in table C.1.

Mode n	Factor $\lambda_n(\pi/2)$
2	3.7766456
4	3.1539997
6	3.0236338
8	2.9756766

Table C.1.: Table recapitulating the correction factors, $\lambda_n(\theta)$, calculated by Strani and Sabetta for the first resonant modes $n = \{2, 4, 6, 8\}$ and a contact angle of 90°. The resonance frequencies of a sessile drop are weighted with $f_n^2 \propto \lambda_n(\theta)$.

D. Gauging contact line friction of droplets: in-situ measurement by interferometry.

This appendix is based on section 5.3 on transient droplet oscillations and on the scientific publication Theisen and Davoust (2012) [128]. Here is presented an interferometry technique to quantify damping of electrowetting-induced shape oscillations of a sessile micro-drop. This characterization method and its devoted chip can be inserted into a microsystem to quantify contact line friction and hence surface ageing in digital electrowetting applications (lab-on-chips, microfluidic lenses and displays). Here, the contact line friction is proposed as a criteria to distinguish sensor surfaces contaminated by adsorbed bio-molecules.

Microsystems using droplet microfluidics are subject to a major challenge: how to circumvent contact line friction, which opposes itself to drop motion, and, obviously, how to characterize it? The aim of this work is to deliver a surface degradation analysis based on wetting abilities, which can be inserted into micro-systems such as lab-on-a-chips [16], microfluidic optical lenses [68] or display technologies [85]. The characterization of dynamical wetting is of prior importance for quantifying the response time and stabilization of droplet motions involved in these systems. Here, the contact line friction is proposed as a sensitive criteria to distinguish between degraded and non-degraded surfaces.

The transduction mechanism used for quantifying the contact line friction is the transient regime of decaying, sessile droplet shape oscillations, initially induced by electrowetting on dielectrics (EWOD). EWOD is now a technology commonly used in digital lab-on-a-chips, for drops motion, mixing enhancement, break-up/coalescence of drops, aliquoting and other basic manipulations. EWOD is used as well in meniscus-based lenses to modify a focal length and in display technologies to create a luminosity contrast, for instance. The capillary wave damping results mainly from the contact line friction on the substrate, especially when the size of the drop is smaller than 1 mm, typically. The friction is composed of a linear friction term, proportional to the velocity of the contact line, and a non-linear term accounting for stick-slip motion due to surface roughness. Viscous damping in the drop volume can be neglected for water, as the corresponding time scale is much greater than the time scale for contact line

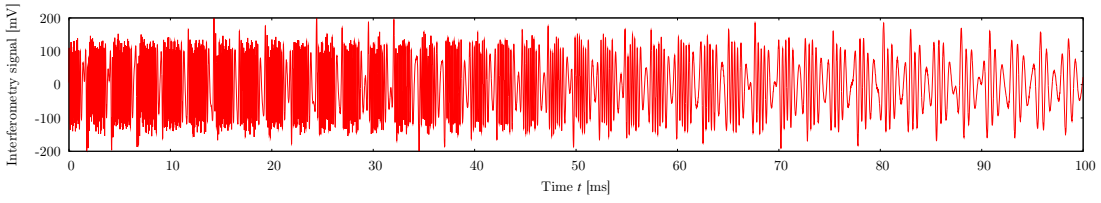

Fig. D.1.: Interferometry signal of a decaying droplet shape oscillation. With diminishing oscillation amplitude, the burst contains less extrema.

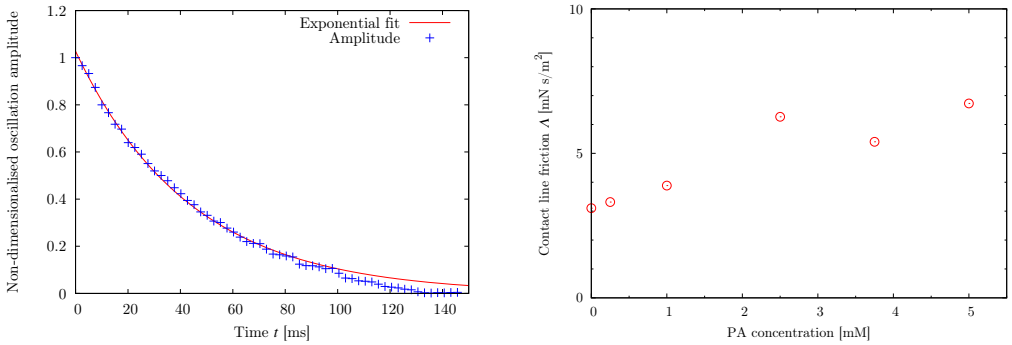

(a) Amplitude attenuation measured by interferometry. The red line corresponds to a fit with a time constant of attenuation of 43.71 ms.

(b) Contact line friction coefficient Λ for different concentrations of palmitic acid in the silicone oil film.

Fig. D.2.: Amplitude attenuation and deduced contact line friction coefficient.

friction [44] [129].

The interferometry technique presented here consists in measuring the interface displacement of the drop apex relative to the substrate by interferometry. The interferometry signal, which is frequency-modulated by the velocity of the interface, is related to the amplitude of the drop oscillation. This point is of prior importance: even small amplitudes, down to the order of several times the laser wavelength of 532 nm, may be detected with a nice precision. One full period of the interferometry signal corresponds to the displacement of the interface over an optical path of one wavelength. Figure D.1 shows an interferometry signal of a decaying drop oscillation.

The novelty of this approach is the combination of a facile in-situ analysis of droplet shape oscillations, with a fast and highly accurate measurement by laser interferometry, even for small amplitudes $< 10\,\mu$m, which is not possible with standard imaging techniques. The easy integration of this technology in microsystems based on electrowetting in a coplanar, non-intrusive electrode configuration is an inherent feature of the developments presented in this work.

Materials The drops with an initial volume of 1.5 µL consist of ultra-pure water (resistivity 18.2 MΩ). The surface tension is measured to be 57 mN/m with the Wilhelmy technique using a NIMA tensiometer. Due to residual traces of contamination, the surface tension is always lower than expected from theory. The drops are deposited on the electrodes, which are covered by a very thin film of silicone oil (viscosity 6 mPas) to avoid stick-slip motion and a too large value of the contact angle hysteresis as well. The silicone oil is used in six different solutions of 0 mM, 0.25 mM, 1 mM, 2.5 mM, 3.75 mM and 5 mM palmitic acid (PA). The PA is added to the silicone oil from a 1 mM solution of chloroform and PA.

Results For in-depth knowledge of the theory on which are based the results, please refer to section 5.3. The amplitude attenuation for a 1.5 µL water droplet

with an EWOD-induced contact angle, $\pi/2$, on a SiOC substrate covered by a thin drained silicone oil film (viscosity 6 mPa s, 0 mM palmitic acid) is shown in figure D.2(a). The exponential fit gives a damping factor of $22.88\,s^{-1}$, or respectively an attenuation time constant of 43.71 ms, corresponding to a contact line friction of $0.013\,N\,s/m^2$. In comparison with the experimental data of Kang [43] and Garimella [44], who find $0.4\,N\,s/m^2$ and $0.18\,N\,s/m^2$, respectively for non-lubricated Teflon substrates, this value seems reasonable. Figure D.2(b) shows the results for the different concentrations of palmitic acid in the silicone oil film. With increasing concentration of PA, the contact line friction coefficient increases.

Final remarks In this work, interferometry is demonstrated to be a very convenient detection method to measure the under-damped decay of surface capillary waves on sessile drops, induced by electrowetting. The time-dependent amplitude of the moving drop apex is shown to precisely translate the exponential attenuation of the oscillations, as illustrated here for a lubricated SiOC substrate. By contaminating the lubricating silicone oil with fatty acids, surface degradation is translated in an increase of the friction coefficient. As a means of drop shape oscillation detection, interferometry performed at the drop apex exhibits several advantages. The measurement of apex motion in the order of one laser wavelength is much more precise as image analysis and permits the analysis of small amplitude interface motions. In addition, the technique is adapted to situations, in which imaging could not be conveniently performed, as is the case for most microfluidic applications in micro-systems. For instance, the proposed methodology can be performed in confined geometries such as digital lab-on-a-chips and liquid lenses, thus providing design guidelines as well as a criteria to characterize the surface degradation of EWOD chips.

E. Tensiometry techniques

E.1. Pendant drop tensiometry technique

Several tensiometry techniques exist to monitor dynamic surface tension. The technique of the pendant drop will be presented shortly, as it is a standard technique and very similar to the goal pursued with this work. The technique of the pendant drop allows to measure dynamic interfacial tension by analyzing the shape of a drop, respectively a bubble. It is a very common technique which is industrialized and employed in many laboratories and in the industry. There exist four variants of the method, all based on the same principle:

- Pendant drop in a gaseous phase
- Pendant drop in a lighter immiscible liquid phase
- Floating drop in a heavier immiscible liquid phase
- Floating bubble in a liquid phase

For the sake of simplicity, the first variant of a liquid in a gaseous phase will be considered to explain the technique, but the principle applies more or less to all four of them. A drop is produced at the tip of a needle. The image of the drop is recorded by a camera as the drop interface ages due to surfactant diffusion and adsorption to the interface. The drop shape is defined by the balance between the gravitational force and the surface tension. When the surface tension γ diminishes with surfactant adsorption, the drop will adopt a more prolate form due to the counterweight of gravity.

The two major drop radii of the surface in a specific point R_1 and R_2 are described by the Young-Laplace equation which links surface curvature to surface tension and gravitational effects:

$$\Delta p = \gamma\Big(\frac{1}{R_1} + \frac{1}{R_2}\Big)$$

where Δp is the pressure difference between the outer and the inner phase, depending on the gravitational force and the surface tension. The pressure inside small drops can take values of several atmospheres due to the contribution of surface tension. It is possible to calculate the surface tension γ by means of geometric parameters characterizing Δp, R_1 and R_2.

In fact, the drop is required to be distorted by gravity in order for this technique to work. In physical terms, the drop needs to have a Bond number $\mathrm{Bo} = \rho g R^2/\gamma > 1$, where $g = 9.81\,\mathrm{m\,s^{-2}}$ is the gravitational acceleration, ρ is the density of the liquid and R the average radius of the droplet. The Bond number expresses the effect of gravity on the shape of a droplet. Conversely, a high Bond number signifies that the drop will not be sphere-shaped because of its large

volume. This has two main drawbacks when considering to measure dynamic surface tension for micro-drops, i.e. for emulsions:

- The spherical symmetry is not obeyed, which is necessary to describe micro- and mini-emulsions.
- The volume of the drop might not be in par with the claimed value of the ratio $VC/S\Gamma < 1$, signifying a non-constant bulk concentration (finite-sized system: adsorption affects bulk concentration).

This means that the pendant drop method is not quite adapted to measuring dynamic surface tension in spherical finite-sized systems.

The advantages of this technique are its precision and fast measurement. Each video frame gives precise information on surface tension with straightforward calibration. Furthermore, the low interaction between the apparatus and the drop due to the low contact surface means little impact on the results. Thus, the cleanliness of the tip apparatus does not affect the result as much as i.e. the cleanliness of surfaces in other techniques for surface tension measurement like the Wilhelmy or de Nouy techniques.

E.2. Wilhelmy plate technique

The Wilhelmy plate technique for surface tension measurements is based on the rupture force of an immersed thin plate in a liquid bath. During withdrawal of the plate out of the liquid, a meniscus will form around the perimeter, p, of the thin plate, which is held by the capillary force $P\gamma_{\mathrm{LG}}$. When further withdrawing the plate, at a critical point the meniscus will rupture. At this critical point the capillary force is at its maximum and equal to the exerted force by the tensiometer, F:

$$F = P\,\gamma_{\mathrm{LG}}\,\cos\theta.$$

The dependence on the contact angle is either neglected due to surface treatment, or the theoretical value for the material used is assumed. In this work, the Wilhelmy plate is cut out of a chromatography paper Whatman type 3001-614 1Chr (Whatman/GE Healthcare, Little Chalfont, United Kingdom), which, since it will soak with water, exhibits naturally a contact angle of $\theta = 0°$. Prior to and in between the measurements, the filter paper is thoroughly rinsed with isopropanol, hot water and Milli-Q water to remove traces of contamination and dust. The tensiometer used is a PS4 fabricated by NIMA (Espoo, Finland). A Teflon receptacle is used to test different solutions (cf. Fig. E.1). A computer program is used for calibration of the pressure sensor with a 100 µg calibration mass, for reading out the pressure sensor and calculating surface tension.

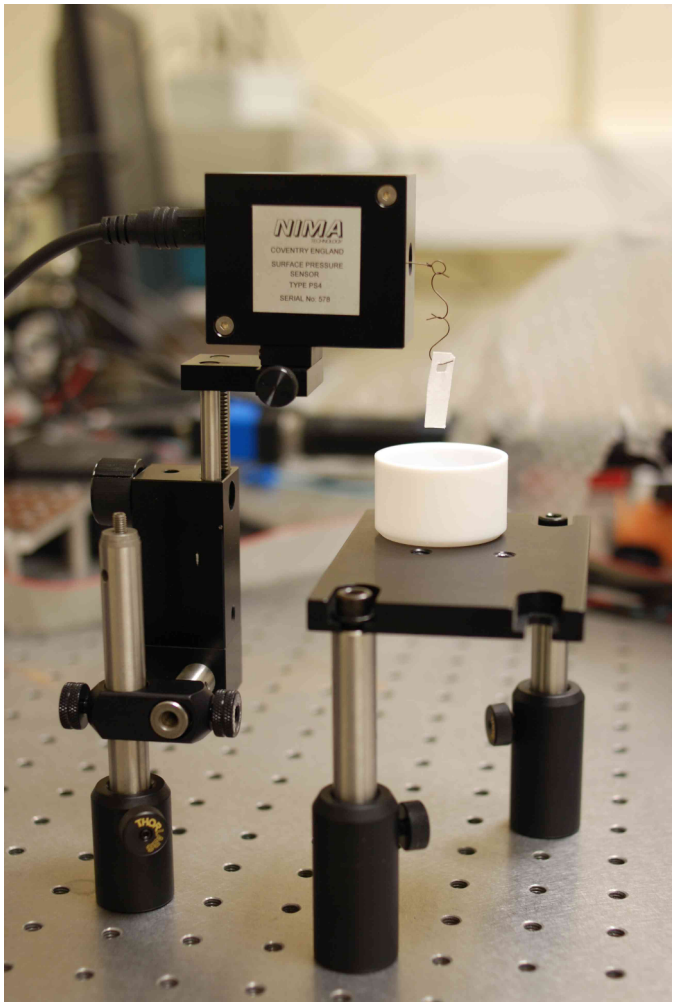

Fig. E.1.: Photo of the NIMA tensiometer PS4 with Wilhelmy plate and Teflon receptacle for liquid-air surface tension measurement. The plate is immersed into the liquid and withdrawn slowly. A computer program reads out the pressure sensor and calculates surface tension.

F. COMSOL Model Parameters (1D)

This appendix gives a detailed description on how to implement the diffusion-adsorption-model in COMSOL 3.5a, the version used for the 1D implementation of the surface ageing model in a spheric isotropic system. The partial differential equation (PDE) mode is used to numerically evaluate a partial differential equation in COMSOL. The weak form of the partial differential equation and its boundary conditions need to be calculated. The ALE method is implemented to describe time-variant mesh geometries using a ordinary differential equation. The given values constitute only an example and must be adapted to the values for each specific case.

F.1. Multiphysics

For the simulation, a 1D domain is chosen. The modules are chosen as follows:

Deformed mesh - Moving mesh (ALE):

- Transient analysis
- Dependent variable: `x lm3`
- Default element type: Lagrange - Quadratic
- Smoothing method: Laplace
- Allow remeshing: Off
- Defines frame: Frame(ale)
- Motion relative to: Frame(ref)
- Weak constraints: On
- Constraint type: Non-ideal

As default element type, a quadratic element should be chosen, as linear elements do often lead to rather high errors for the ALE method. As long as inverted elements are not encountered, remeshing can be turned off. Note that the ale frame is attached to the reference frame, in which the geometry (usually Geom1 in the Multiphysics model navigator) is defined. Make sure that the PDE module is linked to the ale-frame.

PDE mode - Weak form, subdomain:

- Time-dependent analysis
- Dependent variable: `c`
- Default element type: Lagrange - Quadratic
- Wave extension: Off
- Frame: ale
- Weak constraints: Off

F.2. Geometry and Constants

In order to create the geometry, select the line tool and draw a line from `0` to `1`. This is sufficient, as the spheric geometry can be reduced to a one-dimensional mathematic problem. In the options menu, choose constants and enter the following values:

Constants:

Name	Expression	Description
`ka`	`1`	Adsorption constant
`kd`	`1`	Desorption constant
`g0`	`0`	Initial surface concentration
`c0`	`1`	Initial bulk concentration
`D`	`100`	Bulk diffusivity
`R0`	`1`	Initial radius
`Tevap`	`200`	Evaporation time scale
`N0`	`4/3*pi*R0^3*c0`	Total amount of molecules

F.3. Weak Form Module

The weak form is entered in the physics menu. Chose this menu in the principal menu and enter the weak forms for the subdomain and the boundaries:

Subdomain:

Weak tab	
`weak`	`D*(2*test(c)/x-test(cx))*cx`
`dweak`	`ct*test(c)`
Init tab	
`c(t0)`	`c0`
`ct(t0)`	`0`

Boundary 2:

Weak tab	
`weak`	`-test(c)*xTIME*(c+2*Gamma/x)`
`dweak`	`test(c)*Gammat`

Here, `test(c)` and `test(cx)` correspond to the test function $w(r)$ and its derivative with respect to r, $\frac{\partial w1}{\partial r}$. `cx` and `ct` are the space and time derivatives of c. The variable `xTIME` corresponds to the time derivative of the x-coordinate in the ale-frame. At boundary 2, this is equal to the velocity of the radius due to evaporation, $\mathrm{d}R/\mathrm{d}t$. The variable `Gamma` corresponds to the surface concentration of molecules with its time derivative, `Gammat`. The governing differential equation for `Gamma` will be defined as a global equation in the physics menu:

Name (u)	Equation f(u,ut,utt,t)	Init (u)	Init (ut)
Gamma	Gammat - (ka*cR-kd*Gamma)	g0	ka*c0

The variable cR corresponds to the bulk concentration at the liquid/air interface and is defined as a boundary integration variable on boundary 2 in the options menu:

Name	Expression	Frame	Global destination
cR	c	Frame(ale)	✓

F.4. Moving Mesh (ALE) Module

Here, the evaporation dynamics will be defined. To do this, open the subdomain settings out of the physics menu and choose "Free displacement" as mesh displacement. The boundary settings should be edited as follows:

Boundary 1		
Mesh displacement	vx	Value/Expression
Mesh velocity	✓	0
Boundary 2		
Mesh displacement	vx	Value/Expression
Mesh velocity	✓	-R0^2/(Tevap*2*x)

Be sure to impose a zero velocity of the mesh at the center defined by boundary 1, otherwise it will move similar to the surface defined by boundary 2.

F.5. Diverse Expressions

Under the options menu, choose again integration coupling variables and define N_volume as a subdomain variable and N_surface as a boundary variable on boundary 2:

Name	Expression	Frame	Global destination
N_volume	4*pi*x^2*c	Frame(ale)	✓
N_surface	4*pi*x^2*Gamma	Frame(ale)	✓

Finally, under the options menu, enter N as a global expression:

Name	Expression	Description
N	N_volume+N_surface	Total amount of molecules

This will calculate the total molecular content at each time step.

F.6. Meshing and Solving

In the options menu select free mesh parameters and set the maximum element size to `0.01` on the subdomain tab, and to `0.001` on the boundary tab for boundary 2. Click on "`Remesh`" and leave the menu with "`OK`".
In the solver parameters, adjust the time stepping settings as follows, and solve the problem:

`Times`	`Relative tolerance`	`Absolute tolerance`
`range(0,0.01,100)`	`0.0001`	`0.00001`

F.7. Postprocessing

In the postprocessing menu, choose "`Global Variables Plot...`" and select "`Gamma`" out of the variable list. Choose "`Apply`" to plot the data.

In order to represent the evolution of `c`, select "`Plot Parameters...`", choose the animate tab, modify the "`Times`"-field to `range(0,1,100)` and choose "`Start Animation`". For a representation of the mass conservation, choose "`Domain Plot Parameters...`". Switch to the point tab, select any boundary and type "`(N-N0)/N0`" in the expression field. Click on "`Apply`" to plot the data. To export any kind of data into a text file, choose "`Export Postprocessing Data`" in the file menu.

G. Weak formulation for the 2D implementation in COMSOL 4.2a

G.1. Implementation of the involved phenomena

Different modules are available to implement the physical and physicochemical phenomena:

- Volume diffusion and convection: Chemical species transport → Transport of diluted species (*chds*).
- Streaming: Fluid flow → Single phase flow → Laminar flow (*spf*), coupled to the convection component of the *chds* module.
- Surfactant transport along the drop surface: Mathematics → PDE interfaces → Weak form boundary PDE (*wb*).
- Evaporation: Mathematics → Deformed mesh → Moving mesh (*ale*). Evaporation is though neglected in this chapter.

The chemical species transport module is a predefined module for diffusion and convection of diluted species, which implements the action of the corresponding differential equations. Hence, the implementation of a weak form for these processes in the volume is not necessary. It is sufficient to enter the volume diffusivity D and the flow velocities of the streaming current as input parameters. Furthermore, initial and boundary conditions need to be defined according to the mathematical model. Finally, the surface flux may be included to take into account sorption phenomena via equation (22.3) on page 154 for interface surfactant transport. This way, all the physical phenomena are linked to the chds module, which is valid throughout the entire domain.

The laminar flow module, representing the Navier-Stokes equations, serves to calculate the streaming current using a sliding wall boundary condition on the drop surface, imposing the streaming velocity as boundary condition. A symmetry condition is applied to the symmetry axis, and the base axis exhibits a slip condition. The emerging volume flow is coupled to the convection part of the *chds* module and to the weak formulation of the weak form module for adsorption. In practice, the streaming current is calculated seperately for a stationary analysis as a steady process. This permits to save calculation time for the transient analysis of surface ageing.

The weak form boundary module is a bit more sophisticated. With this module, a differential equation of any kind may be imposed by entering its weak formulation, just as the weak form module used in the prior chapter 20 for the one-dimensional problem. This differential equation needs to take into account all the necessary terms of the equation for interfacial surfactant transport, equation (22.3), to be correctly coupled to the diffusion and streaming physics. This way, all the couplings between the four modules are taken care of.

The calculation of the different weak form contributions for the *wb* module, are explained in the following sections.

The differential equations for the interface surfactant transport mechanisms need to be transformed into their weak formulations. As COMSOL uses a cylindrical coordinate system (r, z), as described in chapter 22, the weak formulations need to be calculated for these coordinates. Equation (22.3) for interface surfactant transport reads:

$$\frac{\mathrm{d}\Gamma}{\mathrm{d}t} - \nabla_\mathrm{s} \cdot (D_\mathrm{s} \nabla_\mathrm{s} \Gamma) + (\nabla_\mathrm{s} \cdot \boldsymbol{U}_\mathrm{s})\Gamma + (\nabla \cdot \boldsymbol{n})(\boldsymbol{u} \cdot \boldsymbol{n})\Gamma = j_\mathrm{ads} + \sigma.$$

This equation constitutes the basis for the calculation of the weak contributions. As explained in chapter 22, only three of the above terms need to be transformed into their respective weak contributions in order to constitute the weak formulation of the differential equation:

$$\frac{\mathrm{d}\Gamma}{\mathrm{d}t} - \nabla_\mathrm{s} \cdot (D_\mathrm{s} \nabla_\mathrm{s} \Gamma) - j_\mathrm{ads} = 0.$$

This strong form may be integrated over the domain, V, multiplied by the test functions, following the methodology described in section 20.4

$$\iint_V w(r,z) \left(\frac{\mathrm{d}\Gamma}{\mathrm{d}t} - \nabla_\mathrm{s} \cdot (D_\mathrm{s} \nabla_\mathrm{s} \Gamma) - j_\mathrm{ads} \right) \mathrm{d}V = 0.$$

In the following, the different strong formulations will be transformed into their weak form, which will be used in COMSOL.

G.2. Weak contribution of surface diffusion

The strong form for surface diffusion may be integrated by parts to diminish the order of derivatives. This greatly simplifies the calculations:

$$\begin{aligned} \iint_V w(r,z) \nabla_\mathrm{s} \cdot (D_\mathrm{s} \nabla_\mathrm{s} \Gamma) \, \mathrm{d}V &= \underbrace{[w(r,z) D_\mathrm{s} \nabla_\mathrm{s} \Gamma] \Big|_{r=0}^{R} \Big|_{z=0}^{R}}_{=0} - \iint_V (\nabla_\mathrm{s} w(r,z)) \cdot (D_\mathrm{s} \nabla_\mathrm{s} \Gamma) \, \mathrm{d}V \\ &= -D_\mathrm{s} \iint_V \left(\frac{\partial w}{\partial r} \frac{\partial \Gamma}{\partial r} + \frac{\partial w}{\partial z} \frac{\partial \Gamma}{\partial z} \right) \mathrm{d}V. \end{aligned}$$

This expression does only contain first order derivatives and no further partial integration is needed. The weak contribution to be included into COMSOL for surface diffusion is accordingly:

$$\mathcal{F}_\mathrm{D} := -D_\mathrm{s} \left(\frac{\partial w}{\partial r} \frac{\partial \Gamma}{\partial r} + \frac{\partial w}{\partial z} \frac{\partial \Gamma}{\partial z} \right).$$

G.3. Weak contribution of ad- & desorption flux

The strong form for ad- and desorption is expressed by the adsorption flux:

$$j_{\text{ads}} = k_{\text{a}} C|_R - k_{\text{d}} \Gamma.$$

Since the expression does not contain any derivatives, the associated weak contribution is easy and straightforward to write:

$$\mathcal{F}_{\text{ads}} := w(r,z)\,(k_{\text{a}} C|_R - k_{\text{d}} \Gamma).$$

G.4. Complete weak formulation

The complete formulation to be inserted into COMSOL reads:

$$w(r,z)\,\frac{\mathrm{d}\Gamma}{\mathrm{d}t} - \mathcal{F}_{\text{D}} - \mathcal{F}_{\text{ads}} = 0.$$

Since evaporation is disregarded, the weak contribution for evaporation is not included.

H. Scientific publications and conference contributions

H.1. Publications in scientific journals

Johannes Theisen, Laurent Davoust. *Surface ageing at drop scale.* Microfluidics and Nanofluidics 12 (2012) 607–614.

Abstract: Surface ageing of a micro-drop populated by surfactants below the critical micellar concentration and subject to evaporation is considered, motivated by our interest in the transport of biomolecules in digital microfluidics. The classical approach based on diffusion-sorption processes is reviewed in order to address a finite-sized system of digital microfluidics. Short-time and long-time asymptotic approximations for a diffusion-limited regime, as well as full analytical expressions for adsorption- and evaporation-limited regimes, are constructed, which help to validate numerical calculations of full coupling between all these kinetics. The impact of the small drop size and the continuous lack of equilibrium induced by evaporation are described by introducing specific dimensionless numbers. By taking into account evaporative mass transfer in the mass balance, the boundary condition for surfactant transport to and from the interface is modified. Furthermore, the small size of the geometry suggests allowing a novel non-dimensionalisation for surface concentration, following from the mass balance of surfactant molecules in thermo-dynamic equilibrium. This order of magnitude quantifies the equilibrium surface concentration for small-sized geometries.

Johannes Theisen, Laurent Davoust. *Dual-Frequency Electrowetting: Application to Drop Evaporation Gauging within a Digital Microsystem.* Langmuir 28 (2012) 1041–1048.

Abstract: This paper addresses a method to estimate the size of a sessile drop and to measure its evaporation kinetics by making use of both Michelson interferometry and coplanar electrowetting. From a high-frequency electrowetting voltage, the contact angle of the sessile droplet is monitored to permanently obtain a half-liquid sphere, thus complying perfectly with the drop evaporation theory based on a constant contact angle (Bexon, R.; Picknett, R. J. Colloid Interface Sci. 1977, 61, 336–350). Low-frequency modulation of the electrowetting actuation is also applied to cause droplet shape oscillations and capillary resonance. Interferometry allows us to measure a time-dependent capillary

spectrum and, in particular, the shift in natural frequencies induced by drop evaporation. Consequently, diffusive kinetics of drop evaporation can be properly estimated, as demonstrated. Because of coplanar electrode configuration, our methodology can be integrated in open and covered microsystems, such as digital lab-on-a-chip devices.

Johannes Theisen, Laurent Davoust. *Gauging contact line friction of droplets: In-situ measurement within a digital microsystem.* Microelectronic Engineering 98 (2012) 680–683.

Abstract: Here is presented an interferometry technique to quantify damping of electrowetting induced shape oscillations of a sessile microdrop. This characterization method and its devoted chip can be inserted into a microsystem to quantify contact line friction and hence surface ageing in digital electrowetting appli cations (lab-on-chips, microfluidic lenses and displays). Here, the contact line friction is proposed as a criteria to distinguish sensor surfaces contaminated by adsorbed bio-molecules.

Rachid Malk, Johannes Theisen, Yves Fouillet, Laurent Davoust. *EWOD-driven stirring in lab-on-a-chips: Dependence on the electrodes' geometry.* Microelectronic Engineering 97 (2012) 306–310.

Abstract: Electrowetting on dielectrics (EWOD) with coplanar electrodes is increasingly used in microsystems. This paper enlightens the physical mechanisms of stirring flows in sessile droplets actuated by oscillating EWOD with potential applications to biochemical reaction enhancement or cells handling. Depending on electrodes design (circular vs. square electrodes), EWOD-induced convective flow can be observed to switch from toroidal to quadripolar flows. Due to the coplanar geometry of the electrodes, a model can be proposed which helps to interpret EWOD-induced flow as a result of capillary streaming. Numerical calculations are compared with imaging of drops and demonstrate clearly the essential role of oscillating EWOD as a flow actuator.

Laurent Davoust, Johannes Theisen. *Evaporation rate of drop arrays within a digital microfluidic system.* Sensors and Actuators B: Chemical, 189 (2013) 157–164.

Abstract: One essential advantage of digital microfluidic systems such as, for instance, drop-based lab-on-a-chips, is a massive parallelization of biochemical functions achieved by moving drops under surface acoustic waves or electrowetting on dielectrics (EWOD). This paper aims at characterizing the evaporation rate of a population of drops in a microsystem. Up to now, and despite its importance for end-users, the evaporation rate of one target drop selected among a population of drops has not been measured. This is essentially due to the difficulty of developing imaging in confined microfluidic drop arrays. In this paper, interferometry together with coplanar electrowetting are proposed as a new (non-imaging) evaporation rate measurement method fully compatible with digital microfluidic systems, and easy to be integrated into closed or open geometries. We investigate the impact on drop evaporation of different arrangements of drops and for different degrees of confinement. Use is made of dual-frequency electrowetting [33]: a classical actuation at a high-frequency (15 kHz) allows to set the contact angle equal to 90Â° while the low-frequency actuation (100-500 Hz) is responsible for the excitation of a perfectly spherical standing capillary wave along the drop surface. By considering natural frequencies of the oscillating drop and its capillary spectrum, it is possible to measure a spectral shift under evaporation. The evaporation law by Picknett and Bexon [81] is found valid even for a matrix of drops.

Laurent Davoust, Yves Fouillet, Rachid Malk, Johannes Theisen. *Coplanar electrowetting-induced stirring as a tool to manipulate biological samples in lubricated digital microfluidics. Impact of ambient phase on drop internal flow pattern.* Biomicrofluidics, 7 (2013) 044104.

Abstract: Oscillating electrowetting on dielectrics (EWOD) with coplanar electrodes is investigated in this paper as a way to provide efficient stirring within a drop with biological content. A supporting model inspired from Ko et al. [Appl. Phys. Lett. 94, 194102 (2009)] is proposed allowing to interpret oscillating EWOD-induced drop internal flow as the result of a current streaming along the drop surface deformed by capillary waves. Current streaming behaves essentially as a surface flow generator and the momentum it sustains within the (viscous) drop is even more significant as the surface to volume ratio is small. With the circular electrode pair considered in this paper, oscillating EWOD sustains toroidal vortical flows when the experiments are conducted with aqueous drops in air as ambient phase. But when oil is used as ambient phase, it is demonstrated that the presence of an electrode gap is responsible for a change in drop shape: a pinch-off at the electrode gap yields a peanut-shaped drop and a symmetry break-up of the EWOD-induced flow pattern. Viscosity of oil is also

responsible for promoting an efficient damping of the capillary waves which populate the surface of the actuated drop. As a result, the capillary network switches from one standing wave to two superimposed traveling waves of different mechanical energy, provided that actuation frequency is large enough, for instance, as large as the one commonly used in electrowetting applications ($f \sim 500$ Hz and beyond). Special emphasis is put on stirring of biological samples. As a typical application, it is demonstrated how beads or cell clusters can be focused under flow either at mid-height of the drop or near the wetting plane, depending on how the nature of the capillary waves is (standing or traveling), and therefore, depending on the actuation frequency (150 Hz – 1 KHz).

Johannes Theisen, Carolina Abs da Cruz, Laurent Davoust. *Electrowetting-induced enhancement of surface ageing: towards label-free biosensing in drop microfluidics.* Submitted manuscript.

Abstract: Lab-on-a-chip devices have been extensively explored for label-free and real-time analyses in biological systems at micro-scale. At this scale, surface effects are dominant and can be put to good use for enhancing physico-chemical mechanisms, which are bottle-necks at macro-scale. With this goal, we have studied the streaming-enhanced surface ageing of biomolecules at drop scale. A simple system of a bovine serum albumin laden sessile microdrop is chosen. Electrowetting-on-dielectrics, which is more and more used in lab-on-chip systems for biotechnological applications, is implemented for driving capillary drop oscillations, inducing a steady streaming flow. This surface-driven convection mechanism speeds up surface ageing of albumin molecules. This influence of steady streaming is measured and discussed concerning different aspects. Concrete trends in solid-liquid and liquid-gas surface tension and time dependence are measured. Adsorption of the albumin proteins to the lubricated solid substrate is observed by imaging and reduction in the solid-liquid surface tension values for different capillary resonance frequency modes. We argue that for higher resonant modes, vortex structures are responsible for a more efficient molecular renewal in the vicinity of the contact line, leading to streaming-enhanced surface ageing.

Johannes Theisen, Laurent Davoust. *Adsorption and stirring enhancement at drop scale under electrowetting: the smaller, the better.* Submitted Manuscript.

Abstract: This work introduces a numerical study on stirring effects in small-scale systems, based on drop-shape oscillations induced by coplanar dual-frequency electrowetting. The calculations are based on a previous work of the

authors, which is now enhanced to a more complex symmetry of the involved physical and physico-chemical mechanisms, i.e. adsorption, volume and surface diffusion and stirring. The novelty of the approach is that the stirring effect is generated by a surface motor, which is extremely interesting for small-scale applications like e.g. lab-on-a-chips, where tiny amounts of liquids are used ($< 1\,\mu$L). A numerical study using the finite element method is proposed to analyze the effect of several non-dimensional numbers in order to investigate their implication in surface ageing kinetics.

H.2. Conference contributions

- Journée scientifique de la Fédération 3G (2011) Grenoble, France – Oral presentation.
- International conference on micro and nano engineering (2012) Berlin, Germany – One oral presentation, one poster presentation.
- International conference on microreaction technology (2012) Lyon, France – One oral presentation, one poster presentation.
- International symposium on applications of laser techniques to fluid mechanics (2012) Lisbon, Portugal – Oral presentation.
- "Eurosensors" International conference (2012) Kraków, Poland – Poster presentation.
- Microfluidics European conference (2012) Heidelberg, Germany – Two oral presentations.

I. Résumé en langue française

Première partie – Introduction

Inventés à la fin du 20ème siècle, les laboratoires-sur-puce représentent une innovation majeure pour les biotechnologies, en particulier l'analyse médicale ou environnementale, agro-alimentaire. Les premiers microsystèmes nommés "micro total analysis systems" (μTAS) ont été développés dans les années 90 pour les analyses chimiques. Le congrès scientifique annuel international "MicroTAS" a d'abord eu lieu en 1994, témoignant d'une vitalité toujours plus croissante des recherches dans le domaine des microsystèmes. Le développement des μTAS pour des applications biotechnologiques et médicales a été entraîné dans la même période et s'accompagne de la création de la revue scientifique internationale "Lab on a chip", qui est encore aujourd'hui un point de repère pour la publication de recherches dans ce domaine.

Etroitement associé au développement des laboratoires-sur-puce est le développement d'une discipline hydrodynamique appelée microfluidique. La microfluidique est la science des systèmes fluidiques, dont au moins une dimension présente une échelle de longueur micrométrique. En raison d'un rapport surface/volume élevé, de nouveaux phénomènes émergent fruit d'une combinaison fructueuse entre l'hydrodynamique et l'électrodynamique, le magnétisme, l'acoustique ou la physicochimie, par exemple.

D'un point de vue microfluidique, les laboratoires-sur-puce peuvent être divisés en deux groupes.

Un premier groupe est basé sur l'écoulement d'échantillons biologiques en phase fluide (liquide, gaz ou liquide/gaz) dans des microcanaux (taille caractéristique : 10 à 100 μm) fabriqués dans un substrat constitué le plus souvent de PDMS, verre ou silicium, et recouverts par un couvercle (cf. Fig. 1.1). Des entrées existent pour la fourniture de réactifs et d'échantillons liquides, déplacés dans les canaux par des systèmes de pompage externes. Dans certains cas, des microcanaux servent à transporter des entités de liquides, créées par un cisaillement entre deux liquides non miscibles au niveau de jonctions T ou X. Cette technologie est utilisée pour le tri ou l'analyse, par exemple, afin de créer des gouttes constituées de cellules individuelles encapsulées au sein de polymère ou de membranes.

Un second groupe concerne la microfluidique digitale définie comme le pilotage d'inclusions liquides par des forces (motrices) d'action à distance. Parmi celles-ci, on trouve typiquement des forces électriques responsables, par exemple, du phénomène d'électromouillage, des forces magnétiques, s'appliquant sur les entitès liquides ou bien sur des particules solubilisèes en leurs seins, ou bien des forces de pression engendrées par des ondes acoustiques de surface.

Pour ce qui concerne la microfluidique digitale, l'électromouillage sur diélectrique, développé dans ce travail, est un phénomène particulièrement adapté à la manipulation individuelle d'un ensemble de gouttes au sein de microsystèmes comme des laboratoires-sur-puce. Une matrice d'électrodes est déposée sur un substrat recouvert de deux couches minces, la couche inférieure, de nature diélectrique, recouvre les électrodes ; la couche supérieure, de nature hydrophobe, est en contact direct avec les gouttes de sorte que sans activation électrique des électrodes, celles-ci sont non mouillantes. Par activation des électrodes, les gouttes adoptent une configuration mouillante. En activant différentiellement les électrodes, il est donc possible d'engendrer un gradient de mouillabilité. En conséquence, des opérations fluidiques essentielles comme le déplacement, la coalescence ou la fragmentation, ou la dispense de gouttes sont ainsi mises en œuvre. Afin d'accentuer la valorisation industrielle des laboratoires-sur-puce "digitaux", un certain nombre de nouvelles fonctionnalités supplémentaires méritent d'être développées, en allant au-delà de la manipulation des entités liquides qui est bien maîtrisée. Parmi celles-ci, on trouve la purification des échantillons liquides en gouttes, la réaction en chaîne par polymérase (PCR, amplification d'acides nucléiques) en gouttes, les tests de détection / hybridation, entre autres.

Pour rappel, la plupart des essais biologiques sont basés sur l'interaction (affinité chimique) entre un récepteur biochimique et des molécules ligand, éventuellement présentes dans un échantillon biologique (plasma ou sérum sanguins, salive, urine, etc.). Afin de signaler la présence d'un ligand, différents mécanismes de transduction peuvent servir à transformer les interactions récepteur/ligand en une grandeur mesurable physiquement. En comparaison avec les méthodes d'analyse biochimiques classiques, les laboratoires-sur-puce impliquent des gains de temps et de miniaturisation significatifs, avec à la clef des économies de réactifs ainsi que la possibilité d'une analyse biochimique rapide voire embarquable. Contrairement à la technologie à microcanaux, les laboratoires-sur-puce digitaux offrent un ratio surface liquide / surface solide mouillée réduit, limitant ainsi certains risques de contamination croisée ou faux positifs.

Avec l'objectif à long terme de développer la détection sans marquage en gouttes, cette thèse apporte une contribution à l'électromouillage et au vieillissement biochimique en gouttes. Une attention toute particulière est donnée à l'électromouillage en conditions oscillatoires, en particulier aux potentialités qu'il offre par l'usage conjoint de haute (1 kHz) et basse (100 Hz) fréquences en termes de mélange induit par courant de dérive ou bien de détection optomécanique sans marquage par résonance capillaire.

Ce manuscrit est divisé en six parties. L'introduction récapitule l'état de l'art sur les laboratoires-sur-puce et la microfluidique ; l'accent est mis sur la manière dont ils sont utilisés pour manipuler les réactifs et solutions dans les applications biotechnologiques. Les caractéristiques et différences entre microfluidique continue (micro-canaux) et microfluidique digitale (gouttes) sont soulignées.

Le domaine de la reconnaissance moléculaire est ensuite présenté : les principes

physiques de transduction pour la détection avec et sans marquage sont brièvement présentés. Enfin, le contexte local du travail actuel est expliqué, avec une mise au point sur les travaux antérieurs et les objectifs réels.

Dans la deuxième partie, la théorie de l'électromouillage est introduite. Les concepts de base comme la tension de surface et l'angle de contact sont expliqués. La différence entre les régimes d'électromouillage haute et basse fréquences est explicitée. En combinant ces deux régimes, l'électromouillage bi-fréquence est présenté comme une méthodologie pertinente et innovante. Enfin, la théorie du courant de dérive à l'échelle d'une goutte oscillante sous l'effet de l'électromouillage est présentée rapidement, faisant écho aux travaux réalisés dans la thèse de R. Malk [62].

Les développements techniques et instrumentaux sont présentés dans la troisième partie. La technologie d'électromouillage et le montage expérimental sont détaillés, y compris le développement de l'interférométrie à l'échelle d'une goutte. Des précisions portant sur l'automatisation de l'expérience et le traitement du signal sont données.

L'évaporation d'une goutte posée est tout d'abord étudiée dans la quatrième partie. Il s'agit là d'une problématique importante de la microfluidique digitale lorsque la phase ambiante autour des gouttes est gazeuse. Le modèle d'évaporation diffusive d'une goutte posée de Picknett & Bexon [81] est tout d'abord sélectionné.

L'interférométrie utilisée conjointement avec la résonance capillaire d'une goutte posée, induite par électromouillage double-fréquence, est ensuite présentée comme une nouvelle méthode de mesure de l'évaporation de gouttes. La modification fréquencielle de la résonance capillaire avec le temps joue le rôle de mécanisme de transduction pour le transfert de masse induit par évaporation. Dans les faits, la diminution du rayon de goutte induit un décalage des fréquences de résonance.

En outre, des mesures de cinétiques d'évaporation dans un environnement composé de plusieurs gouttes sont effectuées, fournissant ainsi des informations sur l'influence du confinement, de la distance inter-gouttes et du nombre de gouttes dans un microsystème digital. Pour toute cette partie, en utilisant la composante haute-fréquence de l'électromouillage bi-fréquences, introduit dans la deuxième partie, on montre comment l'angle de contact est utilement maintenu à une valeur constante ($\pi/2$) tout au long des expériences.

Afin de mieux comprendre les mécanismes physico-chimiques à l'échelle d'une goutte, et leur impact sur l'électromouillage, la partie suivante propose une brève introduction sur les molécules tensioactives et leur transport de molécules. Un modèle est développé pour le transport chimique dans un système liquide sphérique ou hémi-sphérique, de taille finie ; sont pris en compte la diffusion, l'adsorption de molécules plus ou moins tensioactives dans une géométrie dépendante du temps (micro-goutte libre). Plusieurs nombres adi-

mensionnels sont mis en évidence à cette occasion. Sur la base de ce modèle, une simulation est développée, et l'influence des nombres adimensionnels est discutée. Le modèle est étendu au cas d'une goutte posée avec un angle de contact arbitraire dans un régime limité en adsorption. Par ailleurs, pour une goutte posée avec un angle de contact de $\pi/2$, les effets d'un courant de dérive à l'intérieur de la goutte sont examinés et l'intensification du vieillissement chimique à la surface de la goutte ou à l'interface liquide/solide sont discutés.

Les résultats de cette cinquième partie sont *in fine* utilisés dans la dernière partie (expérimentale) de la thèse, qui se consacre au vieillissement biochimique de surface induit par un courant de dérive en goutte oscillante. Un système modèle composé d'une goutte de PBS contaminée par une protéine tensioactive (BSA) est considéré. La BSA est présentée, la tension de surface dynamique est mesurée et des conclusions sur l'amélioration du vieillissement chimique induit par électromouillage oscillatoire sont établies, tout en s'appuyant sur les résultats de la simulation.

Microfluidique digitale et laboratoires-sur-puce

Contrairement à la microfluidique en micro-canaux, l'électromouillage sur diélectrique, utilisé dans ce travail, est un mécanisme particulièrement adapté pour la manipulation de gouttes dans l'environnement d'un laboratoire-sur-puce digital. Ce microsystème est conçu avec un substrat constitué d'un réseau d'électrodes coplanaires recouvert d'un film diélectrique et hydrophobe. En appliquant une différence de potentiel électrique entre deux électrodes sous la goutte, l'angle de contact peut être diminué par décroissance de l'énergie de surface solide/liquide. Avec l'application de la tension, la goutte subit une contrainte électrique focalisée à sa ligne de contact. Cette contrainte agit radialement vers l'extérieur, en élargissant la surface mouillée et réduisant ainsi l'angle de contact de la goutte avec le substrat. Par conséquent, l'application d'une tension électrique permet typiquement de passer d'un état non mouillant à un état mouillant. En appliquant une contrainte non-uniforme à la ligne de contact par activations successives des électrodes, un gradient de mouillabilité est engendré et la goutte est mise en mouvement (cf. Fig. 1.2). L'électromouillage permet ainsi la mise en œuvre de différentes opérations dont le déplacement de gouttes (jusqu'à 25 cm/s), la coalescence / la division des gouttes et donc l'aliquotage, le mélange et la création de gouttes à des volumes précis. Ces opérations de base réalisées au sein d'un laboratoire-sur-puce digital lui confère les avantages suivants :

- une parallélisation des opérations sur une matrice de gouttes (haut débit),
- une économie substantielle de réactifs par rapport aux dosages biologiques classiques à échelle macro,
- de faibles volumes d'échantillon et donc des prélèvements in vivo réduits,
- un environnement stérile,
- une intervention humaine très réduite par automatisation des opérations et donc une meilleure reproductibilité ainsi qu'un risque de contamination plus faible.

En utilisant différents réservoirs, plusieurs réactifs et échantillons peuvent être utilisés lors de l'analyse. Le même échantillon peut même être divisé en plusieurs entités liquides pour différents dosages biochimiques et différents essais.

Cela étant, afin de commercialiser les laboratoires-sur-puce digitaux, un certain nombre de fonctionnalités supplémentaires doivent encore être mises au point, tout en allant plus loin sur le niveau de préparation et manipulation des échantillons. Parmi les nouvelles fonctions à développer figurent la réaction en chaîne par polymérase (PCR, l'amplification d'acides nucléiques), la purification et la détection d'hybridation, entre autres.

Amélioration du mélange volumique

Avec un mouvement induit par électromouillage, deux gouttes différentes mais miscibles (par exemple un échantillon biologique et un réactif d'analyse) peuvent être mises en contact et coalescer pour engendrer une réaction chimique. Afin d'améliorer le brassage ou le mélange, différentes techniques ont déjà été développées. Outre l'approche du mélange basée sur un déplacement oscillatoire d'une inclusion liquide par électromouillage, une méthodologie différente consiste à tirer profit d'un grand rapport surface/volume, S/V, en développant un moteur à la surface de la goutte : des mécanismes physiques différents sont utilisés pour générer un écoulement de surface, qui se propage ensuite dans le volume sous l'effet de la viscosité, induisant ainsi un brassage dont l'efficacité augmente avec S/V.

En ce qui concerne les laboratoires-sur-puce à gouttes, plusieurs méthodes sont proposées dans la littérature scientifique afin de réaliser un brassage optimum pour accélérer les cinétiques de vieillissement chimique et d'hybridation. Toutes les méthodes ne sont pas destinées aux laboratoires-sur-puces digitaux, mais peuvent facilement être adaptées.

Gast et al. [9] utilisent des chaînes de billes paramagnétiques soumises à un champ magnétique tournant. Les chaînes adoptent un mouvement tourbillonnant et brassent ainsi le liquide qui héberge les chaînes.

Fair et al. [10] proposent une approche hydrodynamique : en utilisant l'électromouillage, une goutte va et vient le long de trois ou quatre électrodes dans un laboratoire-sur-puce digital. Le volume de la goutte est brassé par un écoulement de recirculation dû à la friction par cisaillement visqueux le long du substrat solide.

Bau et al. [11] utilisent la magnétohydrodynamique (MHD) afin d'induire une advection chaotique dans un volume de liquide.

Enfin, Ginot et al. [12] utilisent un gradient de température ménagé dans une goutte posée sur un substrat froid à l'apex de laquelle se trouve une pointe chaude. Par effet Marangoni à la surface de la goutte, de la quantité de mouvement est créée et se propage, *via* la viscosité, dans le volume ainsi brassé. Ces auteurs tiennent également compte de l'hybridation de molécules d'analytes sur le substrat froid avec des ligands solubilisés dans le volume, dont la cinétique

est mesurée. On constate que la cinétique d'hybridation avec un écoulement Marangoni est accélérée d'un facteur 2.3 par rapport à de la diffusion pure.

Plusieurs groupes de recherche ont récemment développé une technique prometteuse, consistant à générer un courant de dérive le long d'une surface liquide [13–15]. Le courant de dérive n'est autre qu'un écoulement net stationnaire, induit par d'oscillations capillaires de la goutte, engendrées par électromouillage oscillatoire (basse fréquence : 100Hz). Le courant de dérive ainsi créé le long de la surface se comporte comme un moteur surfacique dont la quantité de mouvement se propage jusqu'au centre de la goutte par diffusion visqueuse [13].

Reconnaissance moléculaire : l'aiguille dans une botte de foin.

Le domaine scientifique à l'interface biochimie - nanotechnologies a connu des développements importants au cours des dernières décennies. Les grands progrès dans la connaissance des processus biomoléculaires dans les systèmes vivants ont été facilités par le développement des nanotechnologies et de la physique pour la caractérisation. Citons par exemple les progrès accomplis dans l'imagerie par fluorescence, moléculaire et atomique, la microscopie, ainsi que l'analyse des matériaux par spectromètres de masse, HPLC ou spectrométrie à rayons X. Le rôle de l'ingénierie chimique pour l'analyse et la synthèse de nouvelles biomolécules a également été très important. Par conséquent, des protéines décisives et des structures moléculaires ont été identifiées et reliées à des processus biologiques, rendant possible la compréhension de nombreuses pathologies. Les origines de ces pathologies peuvent être liées à des biomolécules, comme les protéines, des virus ou à la modification ou la détérioration partielle de matériel génétique dans les cellules. Afin de détecter certaines pathologies, les médecins et les hôpitaux peuvent maintenant compter sur toute une panoplie de tests biochimiques et d'essais biologiques.

Les essais biologiques sont basés sur l'interaction entre un ligand et une molécule récepteur biochimique. La molécule ligand est représentative de la pathologie. Par exemple, une séquence d'ADN qui est liée à une certaine pathologie, peut être extraite à partir de l'échantillon d'un patient et amplifiée par une réaction en chaîne par polymérase. Un antigène ou un anticorps présent dans le sang des patients atteints d'une pathologie peuvent servir de ligand, par exemple. En outre, des échantillons de salive ou de frottis sont utilisés pour identifier certaines maladies. La molécule récepteur est une molécule souvent synthétisée, servant à tester l'échantillon d'un patient pour une pathologie éventuelle. La molécule récepteur présente une affinité chimique pour la molécule ligand, et celles-ci se lient par hybridation.

En dehors de la détection de pathologies, les progrès de la biotechnologie servent aux pharmacologues afin d'identifier de nouveaux composants actifs pour les produits pharmaceutiques. Dans les pathologies, les composants interviennent dans les processus biologiques complexes, comme différentes interactions biochimiques dans les cellules. La découverte de composants actifs nécessite de tester l'efficacité d'un grand nombre de molécules sur leurs effets par rapport aux molécules qui interagissent lors d'une pathologie. Cette recherche de com-

posants actifs est réalisée sur des substrats, appelé biopuces ou puces à ADN, afin de tester un grand nombre de composants différents pour un criblage rapide et fiable.

Ces deux approches in vitro, l'analyse de pathologies en médecine ou la recherche de composants actifs en pharmacologie, utilisent les mêmes principes biochimiques et la méthodologie s'appuie sur les cinq étapes suivantes à franchir :

- Trouver la molécule récepteur spécifique d'un certain ligand,
- Greffe de la molécule récepteur sur un support solide,
- Choix d'un mécanisme de transduction efficace, avec ou sans marquage (p.ex. transduction par fluorescence, par rayonnement nucléaire ou impédancemétrie électrique, . . .),
- La miniaturisation et le multiplexage de plusieurs récepteurs,
- La détection de plusieurs ligands.

Afin de qualitativement ou même quantitativement indiquer la présence d'un ligand, différents mécanismes de transduction peuvent servir comme moyen de transformation des interactions récepteur/ligand en un signal physiquement mesurable. Pour concevoir une biopuce ou puce à ADN, la molécule récepteur choisie pour un ligand spécifique est fixée au substrat. Ceci est fait en utilisant des approches classiques de la chimie de surface, souvent par une molécule de liaison, reliant récepteurs et substrats (p.ex. une liaison thiol avec l'or, une liaison silane avec du dioxyde de silicium). Certaines techniques reposent sur une interaction :

- électrostatique (récepteur électriquement chargées, p.ex. ADN/ amine)
- covalente (silane ou thiol à groupe fonctionnel d'amine, ce qui est possible pour les acides aminés et les protéines)
- hydrophobe (récepteur hydrophobe lié à octadecyltrichlorurerosilane (OTS) avec son groupe terminal CH_3, p.ex. anticorps)
- streptavidine/biotine (récepteurs biotinylés liés à une surface avec de la streptavidine greffée)

Dans le passé, différents mécanismes de détection ont été développés. Le choix du mécanisme dépend du récepteur et du ligand utilisés. Les mécanismes sont séparés en deux groupes, un groupe utilisant la détection avec marquage, et un second groupe utilisant une détection sans marquage.

La détection avec marquage, représente le choix standard pour des applications industrielles, avec par exemple la détection par fluorescence, le marquage radioactif, les nano-particules, entre autres.

Les techniques de détection sans marquage les plus connues sont par exemple : la résonance par plasmon de surface (SPR), les capteurs acoustiques (microbalance à quartz, les ondes acoustiques de surface et de volume), les micro -cantilever et -oscillateurs, les techniques d'interférométrie (Fabry-Pérot, Michelson).

Bref état de l'art sur la détection sans marquage en goutte

Nous proposons un bref résumé de techniques, délibérément développés pour les laboratoires-sur-puce à gouttes. Trois exemples sont donnés, empruntés à la littérature récente, publiée pendant cette thèse entre 2009 et 2012. Cette liste n'est donc pas exhaustive, et de nombreuses méthodologies, initialement non destinées à des dispositifs à base d'électromouillage, peuvent néanmoins être modifiées à fin d'adaptation.

Fonctionnalisation d'une biopuce utilisant l'électromouillage et l'imagerie SPR. Malic et al. présentent un laboratoire-sur-puce à électromouillage pour la détection de l'hybridation de l'ADN [19]. Le dispositif est équipé de quatre sites de détection dévolus à de l'imagerie par résonance de plasmons de surface (SPRi) pour des gouttes en dessous du microlitre. Les sites de détection (cf. Fig. I.1(a)) sont des trous ménagés dans un revêtement de téflon présent sur l'électrode en or dédiée aux mesures SPR. Par application d'un biais de tension continue, les cinétiques d'hybridation sont améliorées puisque l'ADN est chargée négativement, lorsque le pH est ajusté correctement. Les brins d'ADN récepteur sont greffés par un lien thiol sur les électrodes SPR en or.

Détection moléculaire par modification d'angle de contact. Bergese et al. [20] ont développé une méthodologie de reconnaissance moléculaire basée sur la variation de l'angle de contact en fonction de l'adsorption de biomolécules à la surface d'un substrat (cf. Fig. I.1(b)) : celui-ci est fonctionnalisé par des molécules récepteur d'un ADN simple brin. Un changement jusqu'à 25 % de l'angle de contact lors de l'hybridation de l'ADN complémentaire est détecté. Des brins d'ADN de 50 % de complémentarité engendre une variation moins significative, et de l'ADN non complémentaire n'a aucune incidence sur l'angle de contact. Il est également possible de mesurer une cinétique d'hybridation à partir de l'angle de mouillage sachant que le temps de réalisation d'un essai pour une goutte de 30 µL est d'environ 600 s.

Intégration d'un biocapteur à transistor à effet de champ au sein d'un dispositif de microfluidique digitale. Choi et al. présentent une technique [21] utilisant la dépendance d'un courant de drain sur l'hybridation d'un anticorps de la grippe aviaire, greffé à la surface de l'électrode du drain d'un transistor à effet de champ. La zone de détection du drain (cf. Fig. I.1(c).) est fonctionnalisée par un antigène de la grippe aviaire. Le transistor à effet de champ est intégré dans le substrat entre les électrodes d'électromouillage. Au-dessus du transistor à effet de champ, la couche de passivation diélectrique et la couche de CYTOP hydrophobe ne sont pas appliquées, laissant libre accès au transistor. Après dépôt de gouttes (volume 2.5 µL) au-dessus de la paire d'électrodes de détection, des molécules d'anticorps peuvent diffuser à la surface de détection. Le temps de réponse est inférieur à une minute ; ce qui est très rapide.

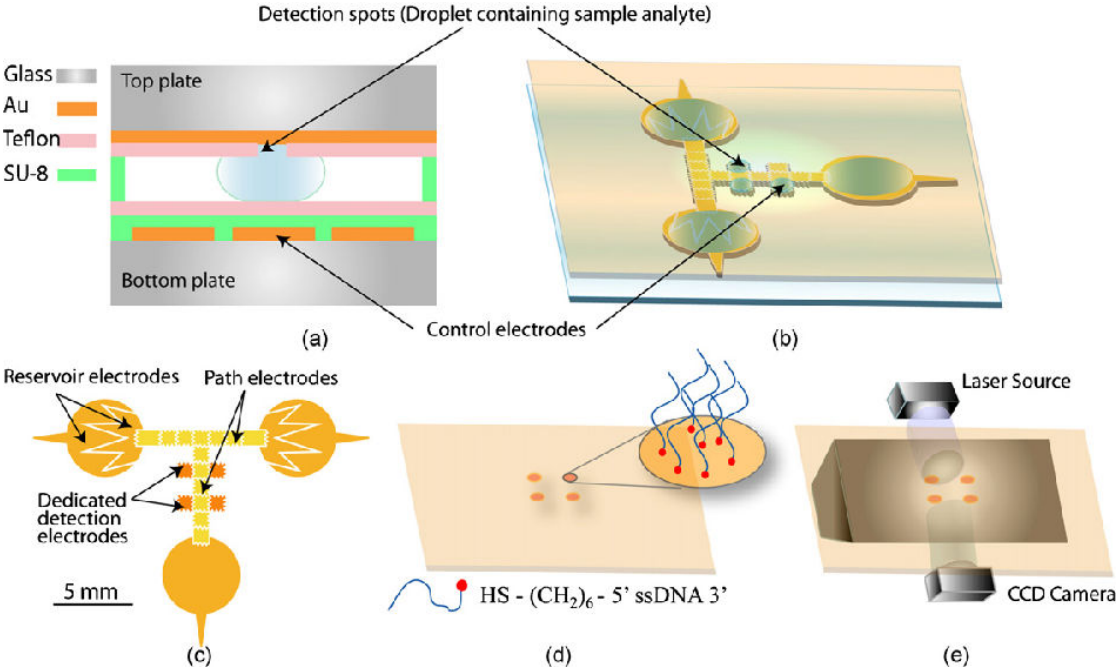

(a) Architecture d'électromouillage pour un laboratoire-sur-puce à capteur de plasmon de surface (architecture "sandwich" avec couvercle). Les sites de détection sont inclus dans des trous dans le revêtement de Teflon pour la réalisation des mesures de SPR. L'électrode de référence dans le couvercle est aussi utilisée pour l'excitation des plasmons de surface. Source : Malic et al. [19].

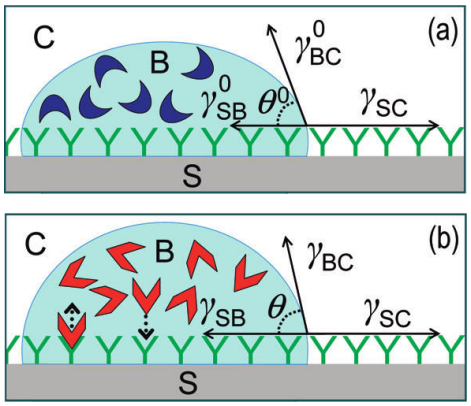

(b) Reconnaissance moléculaire à l'aide l'angle de contact : des molécules ligands complémentaires adsorbent à la surface fonctionnalisée du capteur et changent la tension de surface solide/liquide. Source : Bergese et al. [20].

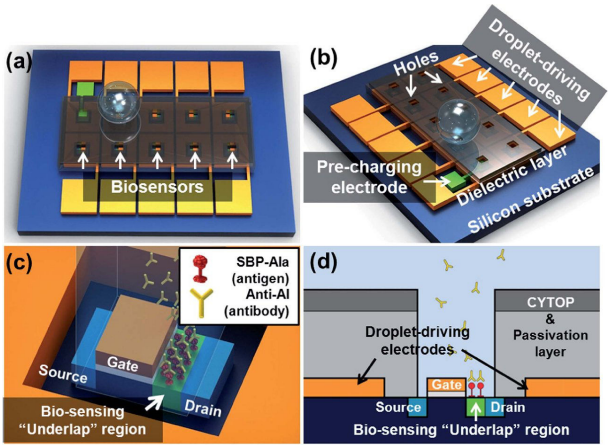

(c) L'adsorption d'anticorps d'influenza aviaire à une surface fonctionnalisée par des antigènes d'influenza aviaire modifie le courant drain d'un transistor à effet de champ. Source : Choi et al. [21].

Fig. I.1.: Exemples d'intégration de différents mécanismes de détection biomoléculaire dans des laboratoires-sur-puce à électromouillage.

Fonctionnalisation d'une surface fluide

Les mécanismes de transduction présentés jusqu'ici sont variés avec une large panoplie de mécanismes physiques et de chimie de surface, même si la liste n'est pas exhaustive.Il est donc possible d'adapter la conception d'un essai biologique à presque tous les systèmes récepteur/ligand. Bien que les mécanismes de transduction soient différents, les techniques de détection sont toutes basées sur des substrats solides nécessitant une fonctionnalisation de la surface solide par les molécules de liaison et le récepteur.

Avec la microfluidique digitale, il est possible de s'affranchir du support solide et de confier la détection des biomolécules à une interface liquide/liquide ou liquide/gaz, en développant une fonctionnalisation par des lipides par exemple. Cette méthode présente l'avantage d'être parfaitement biomimétique tout en permettant une réutilisation éventuelle de la puce après rinçage, ce qui n'est pas possible pour la plupart des techniques de fonctionnalisation reposant sur une chimie de surfaces solides, en particulier celles requérant une liaison covalente. En outre, en fonctionnalisant une interface fluide, les récepteurs restent mobiles, et une concentration locale de ces derniers est rendue possible. La concentration de molécules sur des sites spécifiques devient envisageable par des moyens hydrodynamiques, électrostatiques, acoustiques...etc, à l'apex d'une goutte fonctionnalisée typiquement. La sensibilité de détection peut donc être augmentée et la protection du substrat contre l'encrassement biologique peut être diminuée. Les lipides utilisés pour la mise en place d'une couche monomoléculaire à la surface fonctionnelle d'une goutte support peuvent être fonctionnalisés par des molécules de liaison, tels que la biotine, des groupes amines ou autres, en vue de fixer des molécules récepteur. Dans le cas de l'ADN, il peut être suffisant d'utiliser des lipides avec un groupe amine, qui présente une affinité pour l'ADN simple et double brin, en raison de la charge positive de l'amine.

Contexte de la thèse

La recherche développée dans cette thèse est une contribution amont au développement de laboratoires-sur-puce (LOC) pour les micro- et nano-biotechnologies, i.e. à la maturation des laboratoires-sur-puce à gouttes. Cette technologie émergente représente une alternative intéressante à la microfluidique continue, plus mature, basée sur les microcanaux. Des étapes d'innovation, cependant, sont encore nécessaires pour accélérer la valorisation industrielle des laboratoires-sur-puce à gouttes. Pendant la dernière décennie, les progrès ont essentiellement porté sur la manipulation des gouttes, généralement induite par électromouillage sur diélectrique (EWOD) ou ondes acoustiques de surface. A l'heure actuelle, les processus fondamentaux basés sur le déplacement de gouttes, à savoir la vectorisation d'espèces chimiques, la fusion ou l'aliquotage, peuvent être effectuées. Cependant, le but ultime d'un véritable microsystème industriel à base de gouttes ne sera atteint que si des opérations décisives, comme par exemple la séparation d'espèces ou la détection biomoléculaire sans marquage, sont mises en œuvre facilement et à faible coût. C'est dans ce contexte général que ce travail s'inscrit en proposant une nouvelle méthodologie de détection

sans marquage compatible avec les laboratoires sur puces à gouttes, actionnés par électromouillage. Les propriétés suivantes liées à l'électromouillage oscillatoire sont mises à profit :

- La quantité importante d'aire interfaciale liquide/liquide ou liquide/air par rapport à l'aire interfaciale liquide/solide,
- La présence d'électrodes qui peut être utilisée pour d'autres opérations que le seul déplacement de gouttes et ses propriétés dérivées (fusion, aliquotage),
- L'intensification du transport chimique par les courants de dérives induits par électromouillage oscillatoire.

La méthode de détection sans marquage proposée à l'échelle d'une microgoutte est basée sur une détection opto-mécanique de biomolécules capturées à une interface liquide/gaz. Comme mentionné auparavant, tous les microcapteurs biomoléculaires développés jusqu'à présent sont, sans exception, à notre connaisssance, basés sur l'immobilisation de biomolécules à des substrats solides. Dans ce contexte, la capture de biomolécules à une interface liquide au moyen de molécules récepteur amphiphiles adsorbées par exemple sous la forme d'un auto-assemblage type film de Langmuir, pourrait se révéler comme une innovation complète. D'une part, la capture à une interface liquide est particulièrement bien adaptée pour une intégration dans des laboratoires-sur-puce digitaux. D'autre part, le biomimétisme d'une telle capture à une monocouche fluide est préservé tout comme le sont à la fois la conformation et l'intégrité des bio-molécules. Grâce à la déformabilité de la surface liquide, la liaison de molécules ligands aux molécules récepteurs à la surface liquide peut être révélée optiquement par son effet sur la géométrie des ondes capillaires induites par électromouillage qui dépendent de la rhéologie de surface. Pour améliorer encore plus le seuil de détection, les biomolécules sont susceptibles d'être concentrés au sommet de la goutte par un mécanisme innovant basé sur le courant de dérive, induit par les ondes capillaires [130]. Par rapport aux capteurs à substrat solide, dans lesquels les biomolécules sont définitivement greffées sur la zone de détection du substrat, l'approche fondée sur une surface liquide permet potentiellement à l'utilisateur de facilement déplacer la goutte support et ses biomolécules à un autre endroit du laboratoire-sur-puce après l'étape de détection pour toute autre opération souhaitée (réaction ou séparation chimiques par exemple).

D'un ménisque...

Dans la thèse récente de C. Picard (2007) [22], une étude sur une surface liquide circulaire a été menée avec l'objectif sous-jacent de prouver la possibilité d'une approche fondée sur la détection optomécanique de l'hybridation de brins d'ADN à une interface liquide. La méthodologie retenue consiste en la génération d'un réseau d'onde capillaire, linéaire et stationnaire, sur un ménisque (diamètre 5 cm), créé par l'agitation électrodynamique d'une cellule cylindrique. L'amplitude de l'onde est de l'ordre de quelques micromètres, dans une gamme

de fréquences de 20 à 150 Hz. Deux techniques optiques sont mises en oeuvre, la réfractométrie pour la mesure de la géométrie du ménisque, et l'interférométrie pour l'évaluation de l'amplitude de l'onde au centre du ménisque (cf. Fig. 3.1). La contamination du ménisque par des molécules tensioactives conduit à une diminution drastique de l'amplitude de l'onde, et à un décalage des fréquences de résonance vers des valeurs plus faibles.

Afin de mettre en œuvre un test ADN dans cette approche, la surface liquide/air est fonctionnalisée par une monocouche de molécules de lipides (DOGS, nom commercial : Transfectam). Ces lipides exhibent un groupement polyamine chargée positivement et présentent donc une affinité à la fois à l'ADN simple brin et double brin. En injectant une solution de deux types de brins d'ADN dans la sous-phase aqueuse, le déplacement des fréquences de résonance est différent selon que les brins sont complémentaires ou non.

. . . vers une goutte.

L'objectif de la présente thèse est d'adapter la détection optomécanique ci-dessus, développée à l'échelle macro (taille caractéristique 1-10 cm), à l'échelle micro d'une goutte, de volume 1 μl environ ; ceci afin de développer la détection sans marquage dans un microsystème digital. L'actionnement électromécanique est par conséquent remplacé par l'électromouillage sur diélectrique dans cette thèse. Ce qui permet un contrôle facile de paramètres comme la fréquence d'excitation, l'amplitude d'oscillation et l'angle de contact, avec très peu d'énergie consommée. Le mécanisme de transduction est essentiellement le même, une onde capillaire stationnaire, non plus cylindrique mais sphérique, est entretenue le long de la surface de la goutte. Cependant, la physique sous-jacente est différente. L'onde présente plusieurs fréquences de résonance dans une plage de fréquences d'oscillation de 10 à 1000 Hz, dépendant essentiellement du volume de la goutte et de la tension superficielle. Les amplitudes d'oscillation sont de l'ordre de plusieurs micromètres au maximum. Grâce à la nouvelle géométrie sphérique de notre étude, l'interférométrie est développée à l'apex de la goutte. Notons que la taille de cette dernière est suffisamment petite pour négliger l'aplatissement gravitaire à l'apex.

Deuxième partie – Oscillations de gouttes induites par électromouillage

Cette partie introduit les bases physiques de l'électromouillage sur diélectrique. Les notions de tension de surface et d'angle de contact sont abordées. L'électromouillage est présenté en tant que moyen d'agir sur la tension de surface par l'énergie électrostatique, ce qui a pour conséquence de modifier l'angle de contact d'une interface fluide/fluide. L'électromouillage dans la configuration classique de l'électrode plongeante est discuté afin de justifier la pertinence de la configuration coplanaire : les électrodes sont positionnées côte à côte dans le même plan sous les films diélectrique et hydrophobe.

Le régime d'électromouillage basse fréquence est introduit car il est responsable des oscillations de goutte. L'origine des oscillations se trouve dans l'actionnement électrique et oscillatoire de la ligne de contact. A partir du mouvement oscillatoire de la ligne de contact, une onde capillaire à symétrie sphérique est excitée le long de la surface de la goutte. Ces oscillations sont caractérisées par des fréquences de résonance. Ces résonances varient selon le volume de la goutte, la tension superficielle et l'angle de contact de la goutte, entre autres facteurs. Afin de contourner la dépendance à l'angle de contact, une technique appelée "électromouillage bi-fréquence" a été développée durant cette thèse. Le principe est simple et repose sur la superposition de deux fréquences d'actionnement : l'amplitude d'une tension haute fréquence est ajustée afin de régler l'angle de contact à une certaine valeur (90° pour avoir une demi-sphère). Ensuite, cette tension est modulée par une basse fréquence qui génére les oscillations de forme de la goutte. Cette composante basse fréquence peut être ajustée en fréquence pour détecter, par exemple, un pic de résonance spécifique ou pour stimuler un certain mode de résonance. Elle peut également être ajustée de manière à modifier l'amplitude d'oscillation.

L'utilisation des oscillations de forme d'une goutte implique un phénomène fluidique, inattendu à une telle échelle microscopique, déjà connu sous le nom de "courant de dérive" ou "de Stokes", mais dans la littérature consacrée à l'hydraulique et en particulier à la houle. Le terme non-linéaire des équations de Navier-Stokes engendre le long d'une interface fluide oscillante sous l'effet d'une vague une source de débit net (contrairement à l'intuition et à la théorie des ondes purement linéaires). On démontre que ce phénomène reste encore valable pour les oscillations capillaires de gouttes, sous certaines conditions. Le courant de dérive se comporte ainsi comme une source de quantité de mouvement interfaciale qui se propage ensuite à l'intérieur de la goutte sous l'effet de la viscosité moléculaire. L'intensité et la géométrie du brassage en goutte ainsi généré dépendent également du spectre des fréquences d'oscillations de la goutte objet.

Dans un chapitre suivant, la théorie de l'électromouillage et des oscillations de gouttes induites par électromouillage est présentée. Le mouillage statique est expliqué, et différents facteurs de correction sont introduits afin de décrire correctement l'électromouillage coplanaire et les oscillations de gouttes posées. Il est rappelé que ces oscillations sont caractérisées par un mode propre n associé à des fréquences de résonance. Chaque fréquence de résonance entraîne un mode de déformation dominant, décrit par des polynômes de Legendre. Ce qui dans le cas d'une résonance donne lieu à un régime d'écoulement stationnaire organisé par le courant de dérive dans le volume de la goutte. Une vitesse de l'écoulement de plusieurs mm/s est atteinte pour des gouttes millimétriques. Les ondes capillaires stationnaires le long de la surface de la goutte se comportent donc comme un moteur surfacique d'autant plus efficace que le rapport surface/volume est important !

Troisième partie – Instrumentation et développements techniques

Cette partie présente les développements expérimentaux pour la caractérisation précise des oscillations de forme de goutte. Tous les éléments sont représentés, en commençant par l'actionnement d'une goutte d'eau par électromouillage dans une configuration coplanaire. Les étapes de microfabrication de la puce, le dispositif expérimental et la génération de tension bi-fréquence sont décrits. Sont ensuite présentés l'instrumentation, en particulier l'interféromètre de Michelson mis en œuvre à l'échelle de la goutte. Il est expliqué de quelle manière le signal d'interférométrie modulé en fréquence permet de remonter à l'amplitude d'oscillation. Deux approches différentes – stationnaire et transitoire – sont utilisées. Les deux approches nécessitent des automatisations et des algorithmes de traitement du signal distincts, qui sont expliqués dans les chapitres suivants. Enfin, l'influence du film lubrifiant d'huile silicone sur des mesures d'interférométrie est expliquée, ainsi que les solutions possibles pour éviter des franges interférométriques parasites.

Avec l'aide de nos collègues du CEA/LETI/DTBS, des puces à électromouillage de haute qualité fabriquées dans les salles blanches du LETI au CEA Grenoble ont pu être utilisées. Au début de la thèse, un support de puce adapté a été élaboré, comprenant un connecteur de tension sophistiqué et de l'imagerie. L'électromouillage bi-fréquence a été développé à l'aide d'une électronique pilotable, permettant à la fois le contrôle précis de l'angle de contact et la génération des oscillations de goutte.

Un interféromètre de Michelson adapté à l'échelle d'une goutte a également été conçu pour permettre une mesure locale de l'amplitude de déformation à l'apex de la goutte, ceci avec une résolution micrométrique (cf. Fig. I.2). Plusieurs problèmes d'instrumentation et de mesure (par exemple l'impact d'un film d'huile silicone en conditions lubrifiées sur les mesures d'interférométrie) ont été contournés. Avec un dispositif de mesure adapté comme la photodiode à avalanche, des signaux très stables et des résultats reproductibles ont été obtenus afin de caractériser le spectre capillaire des oscillations de goutte.

Enfin, une automatisation adaptée sous labview et la mise en place d'un traitement du signal ont permis la génération et l'acquisition précises des oscillations de gouttes en régimes stationnaire ou transitoire.

Quatrième partie – Evaporation de gouttes

La théorie et les développements techniques, présentées dans les parties II et III, sont mis à l'épreuve avec la caractérisation de l'évaporation d'une goutte posée : on tente de mettre en évidence la dépendance du spectre de résonance avec le rayon R d'une goutte posée. Au fur et à mesure que l'évaporation agit, ce rayon diminue et donc le spectre capillaire des fréquences de résonance est modifié. Ce faisant, la configuration expérimentale, l'automatisation, l'acquisition de données expérimentales et le traitement du signal sont utilisés. Pour se conformer à l'approche théorique de l'évaporation que nous proposons, fondée

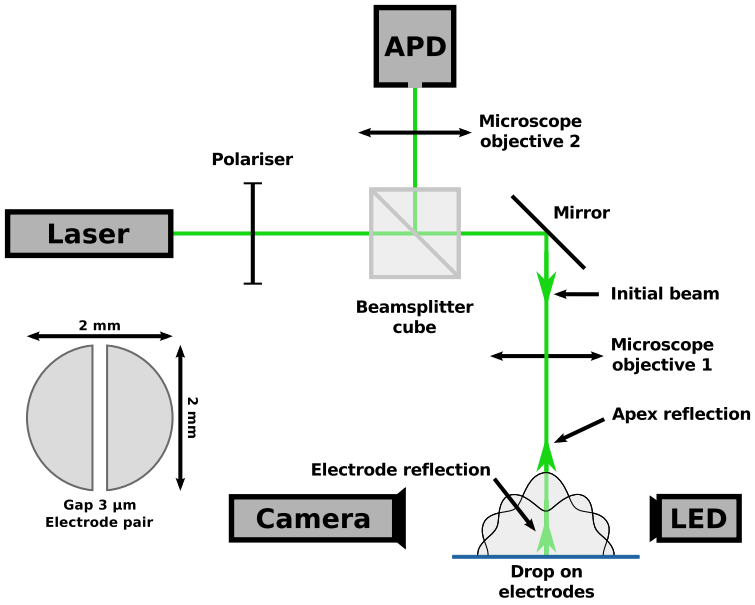

Fig. I.2.: L'interféromètre Michelson : Le faisceau laser traverse le cube séparateur et crée deux réflexions de premier ordre sur l'apex de la goutte et le substrat solide, qui sont détectées par la photodiode à avalanche. (Inset en bas à gauche) Le motif d'électrodes pour l'actuation par électromouillage.

sur l'hypothèse de demi-sphère, l'électromouillage bi-fréquence est utilisé pour ajuster en permanence l'angle de contact de la goutte à $\pi/2$.

Dans les microsystèmes qui impliquent de la microfluidique digitale, à base d'électromouillage ou non, il n'est pas facile de caractériser l'évaporation, tout spécialement dans les environnements comportant un réseau de gouttes, en configuration ouverte ou fermée (confinement variable). Et pourtant l'étude de ce phénomène est décisive dès lors qu'il s'agit de maîtriser les concentrations biochimiques dans des réactions chimiques ou des tests de reconnaissance antigène-anticorps par appariement voire coalescence de gouttes. On montre comment les mesures interférométriques en combinaison avec des oscillations de forme induites par électromouillage représentent un moyen non-intrusif - sans imagerie - pour qualifier l'évaporation dans les microsystèmes digitaux. Pour démontrer la faisabilité de cette approche, cette partie traitent la théorie de l'évaporation, et son application à l'évaporation d'une goutte (chapitre 16) ou d'un réseau de gouttes (chapitre 17) dans un microsystème. Dans le chapitre 17 l'accent est mis sur les impacts respectifs du confinement vertical, de la position relative d'une goutte individualisée dans un réseau de gouttes et de la distance de séparation entre gouttes.

Théorie de l'évaporation

L'évaporation d'une goutte posée est présentée à partir d'un point de vue théorique. On distingue deux régimes limites : l'évaporation limitée par la convection et l'évaporation limitée par la diffusion. L'évaporation convective prend en compte la convection thermique ou forcée dans la phase gazeuse ambiante.

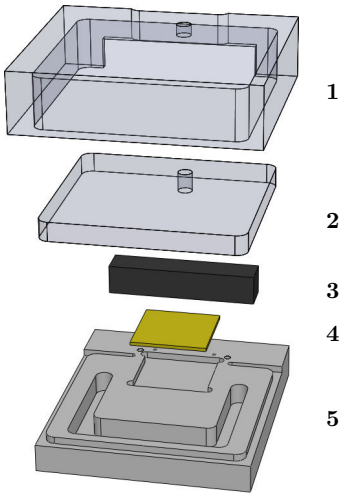

(a) 1, Couvercle en Plexiglas; 2, disque en Plexiglas pour le confinement variable; 3, partie connecteur pour l'alimentation de la tension; 4, puce EWOD; 5, support de puce avec réservoir d'eau en forme de U.

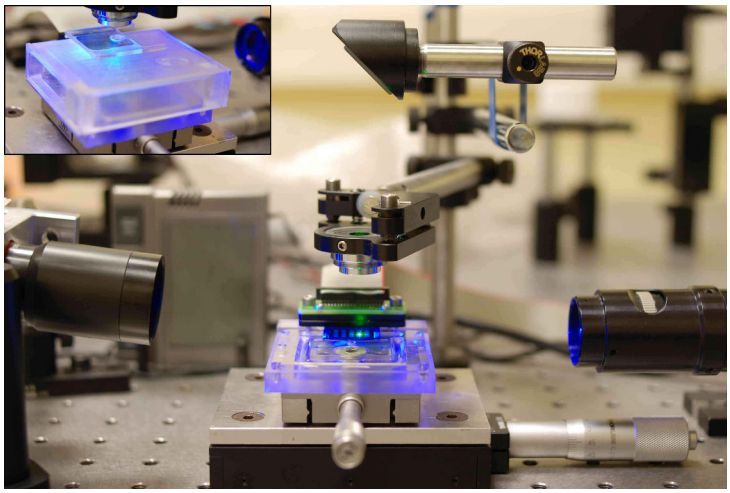

(b) Photo du système expérimental au sein du système optique (cf. chapitre 9) et du couvercle (insert) : diode à luminescence (gauche), caméra (droite) et plaques de translation x-y (bas).

Fig. I.3.: Dispositif expérimental : support de puce et confinement.

Ici, pour des raisons liées aux applications microsystèmes, l'accent est mis sur l'évaporation limitée par la diffusion, qui est basée sur le gradient de concentration et la diffusion de la vapeur d'eau dans la phase gazeuse ambiante. Il y a deux articles importants concernant l'évaporation de gouttes posées pilotée par la diffusion : le premier, par Picknett et Bexon [81], présente une analyse théorique et expérimentale, le second, par McHale et al. [82], présente une analyse expérimentale portant sur une goutte en configuration hydrophobe. Dans ces deux travaux, l'accent est mis sur la distinction entre les deux modes d'évaporation : 1) un mode à surface mouillée constante pour laquelle le rayon de contact n'évolue pas, et l'angle de contact diminue, 2) un mode à angle de contact constant pour lequel le rayon de la surface mouillée diminue. McHale et al. apportent une analyse complémentaire avec l'existence d'un mode d'évaporation mixte, qui est couramment observé à la fin du processus d'évaporation d'une goutte posée.

Evaporation d'une goutte unique

Ce chapitre traite d'une méthode pour estimer la taille d'une seule goutte posée et sa cinétique d'évaporation en utilisant l'interférométrie et l'électromouillage coplanaire bi-fréquence. Au-delà de l'objectif de stabiliser la position de la goutte posée, à l'aide de la tension d'électromouillage à haute fréquence, l'angle de contact de la goutte peut être ajusté afin d'obtenir en permanence une hémisphère liquide. De cette façon, les expériences se conforment parfaitement à la théorie

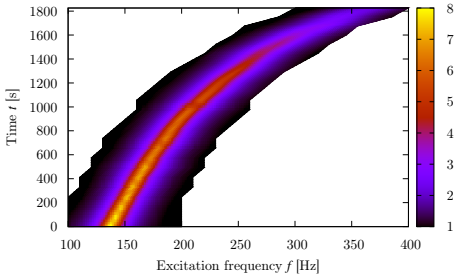

(a) Le codage couleur représente l'amplitude d'oscillation en µm à la fréquence de résonance f_2, mesurée par interférométrie. Le glissement spectral de f_2 est dû à la diminution du rayon, induite par l'évaporation.

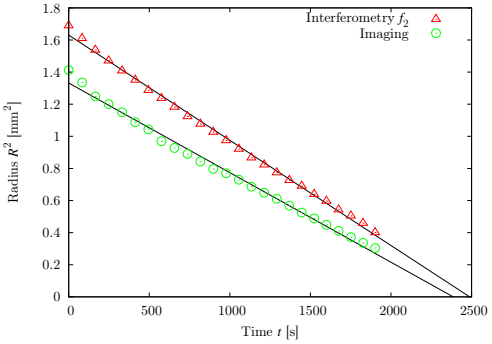

(b) Comparaison entre les résultats d'imagerie (○, τ_{evap} = 2488 s) et des résultats d'interférométrie (△, τ_{evap} = 2386 s).

Fig. I.4.: Evaporation d'une goutte de 4 µL pendant 47 minutes. La température ambiante est de 22.3 °C et l'humidité relative est de 44.5 %.

de l'évaporation des gouttes sur la base d'un angle de contact constant [81]. La modulation à basse fréquence de l'actionnement d'électromouillage est appliquée pour provoquer des oscillations de forme de la goutte et de la résonance capillaire. L'interférométrie permet de mesurer un spectre capillaire en fonction du temps, et en particulier le changement de fréquences résonantes induit par l'évaporation. Par conséquent, la cinétique de diffusion de l'évaporation des gouttes peut être correctement estimée. En raison de la configuration des électrodes coplanaires, notre méthode peut être intégré dans des microsystèmes ouverts et fermés tels que les appareils de laboratoire-sur-puce digitaux. Les mesures sont réalisées sur de l'eau pure et différents mélanges d'eau et de glycérol. Le système expérimental est présenté dans la Fig. I.3 avec (a), la cuve et le couvercle qui abritent la puce, et (b), une photo de l'insertion de cette cuve au sein du système optique. Les principaux résultats des expériences d'évaporation d'une goutte d'eau isolée sont présentés dans la Fig. I.4 : La Fig. I.4(a) montre la dépendance temporelle de la fréquence de résonance avec le temps. La Fig. I.4(b) compare le rayon calculé de cette dépendance avec les résultats issus de l'imagerie.

Evaporation d'une goutte au sein d'un réseau de gouttes. Application aux microsystèmes.

Ces dernières années, de plus en plus d'applications microfluidiques utilisant les transferts thermiques et l'électromouillage sur diélectrique [28, 65] ont émergé. Ainsi, outre les lentilles à focale variable [68], les écrans liquides [85], les laboratoires-sur-puce [84] ou la surveillance environnementale [86], de nouvelles applications de l'électromouillage pour la PCR [87,88] ont été développées (utilisation d'un cyclage thermique). Une application encore plus récente de l'électromouillage consiste en une méthode de refroidissement des circuits im-

primés (PCB) ou unités de processeur (PCU) [83]. L'EWOD est bien sûr couramment utilisé dans les laboratoires-sur-puce digitaux [16,69] : bien qu'une grande partie des applications bio-technologiques dans les laboratoires-sur-puce peuvent être effectuées avec de l'huile silicone comme phase ambiante, certaines applications telles que la lyophilisation ou les nez chimiques nécessitent encore une phase ambiante de gaz [84]. Pour toutes ces applications, l'évaporation est soit indésirable, car il y a la nécessité d'éviter la perte de masse, soit délibérée car il y a la nécessité de favoriser le changement de phase sans pour autant atteindre l'assèchement. Dans les deux cas, il est donc important de contrôler le transfert de masse par évaporation.

Les microsystèmes digitaux abritent normalement un réseau de gouttes afin d'exprimer pleinement leur potentiel de parallélisation, ce qui rend difficile l'évaluation correcte de l'évaporation à partir de méthodes conventionnelles basées sur l'imagerie ou la microscopie [89, 90]. L'impossibilité de développer l'imagerie est particulièrement importante lorsque le confinement est délibérément intense pour des raisons évidentes de miniaturisation et de portabilité. Typiquement, l'imagerie en fond clair est le seul moyen efficace d'observer la forme évolutive d'une goutte posée en fonction du temps. Mais cette technique est seulement possible pour une goutte suffisamment isolée et dans les dispositifs complètement transparents ; ce qui limite strictement le choix des matériaux utilisés dans les étapes de microfabrication (par exemple des électrodes en ITO en combinaison avec du PDMS ou du verre comme matériau pour les parois).En outre, l'angle de contact ne peut pas être contrôlé. Une autre méthode pour le contrôle sans imagerie de l'évaporation est la mesure capacitive du volume de goutte dans un microsystème fermé ou dans une configuration d'électromouillage en sandwich (électrodes superposées, voir par exemple [80, 91]). Dans le présent travail, la configuration en sandwich est délaissée, sans perte de généralité, au profit d'une configuration coplanaire plus adaptée à des méthodologies différentes. Avec l'électromouillage coplanaire, on sait que les oscillations de forme d'une goutte induites par actuation oscillatoire peuvent être facilement engendrées dans un microsystème fermé [31].

Dans ce chapitre, différents modèles sont proposés pour comparer le transfert de masse d'une goutte au centre puis au bord d'un réseau de gouttes (cf. Fig. I.5). En outre, différents confinements sont étudiés afin d'examiner les effets d'une réduction du volume de la phase ambiante autour du réseau de gouttes. Finalement, la distance inter-goutte est variée, fournissant des informations originales sur l'impact de la proximité d'autres gouttes sur l'évaporation d'une goutte.

La méthodologie présentée dans cette partie peut être insérée facilement dans les microsystèmes consacrés à la PCR en goutte sous cyclage thermique [92, 93]. Elle est également adaptée au contrôle du refroidissement de PCB ou PCU obtenu par changement de phase.

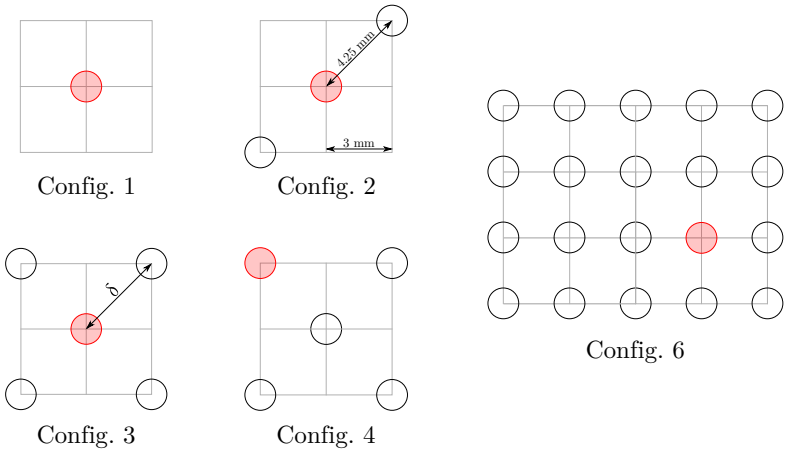

Fig. I.5.: Esquisse des différentes configurations : un cercle noir vide correspond à une goutte sacrificielle, un cercle rouge rempli correspond à la goutte mesurée.

Principales conclusions

L'évaporation des gouttes dans un microsystème ne peut jamais être totalement évitée. Comme dit auparavant, ce phénomène est déterminant pour les applications biologiques telles que la PCR basée sur des gouttes sous cyclage thermique, pour lesquelles il faut précisément connaître et contrôler la concentration des molécules solubilisées et sa dépendance à l'évaporation.

Dans ce travail, la dépendance temporelle d'une goutte hémisphérique au sein d'un réseau de gouttes a été examinée en ce qui concerne à la fois le nombre de gouttes voisines (sacrificielles) et leur proximité (distance inter-gouttes). L'efficacité de limiter l'évaporation par l'usage d'un bain d'eau ou de gouttes sacrificielles a été démontrée comme étant dépendante du confinement vertical, κ. L'influence encore plus forte de la distance entre les gouttes, δ, a été évaluée pour trois valeurs différentes du confinement. L'impact de δ sur la cinétique d'évaporation est le plus significatif.

Pour les faibles confinements, conformément à l'intuition, l'évaporation d'une goutte située au niveau du bord d'un motif de cinq gouttes est toujours trouvée plus rapide que la cinétique d'évaporation d'une goutte située au centre du motif. Inversement, pour un confinement assez fort, la position relative d'une goutte cible n'est plus significative : toutes les gouttes s'évaporent selon la même cinétique, dictée par la loi diffusive de Picknett et Bexon.

Enfin, si l'objectif est de ralentir le processus d'évaporation d'une goutte cible, nos données expérimentales suggèrent que la proximité de gouttes sacrificielles doit être préférée à l'utilisation d'un bain aqueux. Pour les utilisateurs de microsystèmes digitaux, il est intéressant de noter que pour des applications biologiques avec des gouttes **millimétriques**, le confinement doit être plus petit que 6 mm. Pour les applications impliquant un refroidissement par changement de phase au niveau de gouttes millimétriques, le confinement doit être au moins de 12 mm afin de ne pas perturber la cinétique d'évaporation et de garder un refroidissement efficace.

La validité du modèle diffusif développé à l'origine par Picknett et Bexon, pour une goutte unique et isolée avec un angle de contact constant, est étendue au cas d'une goutte cible, à angle de contact constant, choisie parmi une population de gouttes et quel que soit le confinement (cf. Fig. 17.4). Ceci constitue un nouvel élément, important pour les concepteurs ou utilisateurs finaux de microsystèmes digitaux. Il est connu que la mouillabilité de surface est un paramètre déterminant pour l'évaporation d'une goutte posée [95]. Dans ce chapitre, un seul angle de contact, $\theta = \pi/2$, a été étudié, mais il est facile de mettre en oeuvre d'autres valeurs de l'angle de contact en changeant la composante de tension haute fréquence de l'électromouillage bi-fréquence.

La mesure d'interférométrie des oscillations de gouttes induites par électromouillage est appliquée pour tenir compte de l'évaporation d'une goutte. En raison d'imperfections dans la théorie de Strani et Sabetta et des erreurs qui en découlent, la mesure absolue du rayon de la goutte par électromouillage et interférométrie n'est pas parfaite. Au contraire, une bonne précision est observée pour des mesures relatives de rayons et par conséquent pour l'estimation des cinétiques d'évaporation.

Dans la partie VI, la même méthodologie sera étendue à la mesure du vieillissement biochimique en goutte, caractérisé par une modification dynamique de la tension de surface [24, 96]. Par conséquent, la contribution de la cinétique d'évaporation dans l'équation (II.5.6) doit être correctement mesurée. En outre, les résultats devront être interprétés avec prudence car seules les variations relatives de tension superficielle dynamique sont mesurables.

Afin de mieux interpréter les mesures de tension de surface lors du vieillissement biochimique d'une goutte, une approche théorique du couplage entre transports chimiques volumique et surfacique est préalablement proposée dans le chapitre suivant.

Cinquième partie – Transport et vieillissement chimiques à l'échelle d'une goutte

Cette partie constitue la base théorique en complément du travail expérimental sur la fonctionnalisation de surface et les essais biologiques en goutte. Afin d'avoir une idée sur la manière dont les biomolécules sont distribuées localement à l'intérieur et à la surface d'une goutte, la diffusion ainsi que l'adsorption doivent être considérées, puisque les biomolécules présentent souvent des propriétés tensioactives. Contrairement à la plupart des études théoriques sur le vieillissement des interfaces liquides qui portent toutes sur des systèmes semi-infinis, ici, la géométrie est nécessairement considérée comme finie puisqu'il s'agit d'une goutte. De même la quantité de moles de l'espèce biochimique transportée doit impérativement être considérés comme limitée. Un effort spécifique est également produit afin de prendre en compte dans la modélisation une géométrie dépendante du temps sous l'effet de l'évaporation dans les expériences. Les équations de diffusion et d'adsorption sont résolues pour une géométrie sphérique. La loi d'évaporation (15.2) est prise en compte par une

condition aux limites cinématique. En raison de la symétrie sphérique, le problème mathématique peut être réduit à un cas unidimensionnel. Trois régimes chimiques asymptotiques sont abordés : i) le régime limité par l'adsorption, ii) le régime limité par la diffusion et iii) le régime limité par évaporation. La sensibilité aux différents nombres adimensionnels et au-delà, le cas des régimes mixtes, sont ensuite étudiés en utilisant une méthode de calcul numérique à base d'une formulation faible dans une approche fondée sur les éléments finis. Un résultat majeur obtenu à l'issue de ce travail est l'identification de la concentration d'un système physico-chimique de taille finie, qui se présente comme un paramètre important pour la conception d'un microsystème digital. On montre que par réduction du volume de goutte, la quantité totale de moles de soluté peut être considérablement diminuée jusqu'à atteindre une limite extrême telle que la quantité de moles en volume est commensurable avec celle en surface. Cela peut être particulièrement important pour les applications utilisant des solutés de synthèse, comme par exemple des poly-peptides. L'équilibre chimique en goutte est alors caractérisé par un nouveau nombre adimensionnel, ϵ_0, qui reflète le rapport entre les molécules de soluté dans le volume et celles adsorbées à la surface de la goutte. Le rôle de ce nouveau nombre adimensionnel est discuté ; il constitue un critère pour la distinction entre macro- et micro-systèmes chimiques. Enfin, pour le cas particulier des régimes limités en adsorption, le modèle est étendu à des angles de contact arbitraires, et donc à une symétrie qui n'est plus nécessairement sphérique ; on conserve cependant une symétrie cylindrique (2D-axisymétrique).

Dans le chapitre 22, le courant de dérive est pris en considération afin de compléter la théorie précédente par le transport convectif interne à la goutte. Le phénomène de courant de dérive n'étant pas isotrope, le calcul numérique est donc nécessaire pour résoudre un modèle 2D axisymétrique incluant : i) le transport diffuso-convectif en volume, les processus d'adsorption/désorption à la surface de la goutte, le transport diffusif le long de la surface. On montre que pour les réactions chimiques en gouttes limitées par la diffusion, le courant de dérive, de par sa capacité à engendrer du brassage, peut permettre d'intensifier le vieillissement chimique, résultat opportun repris dans la suite de ce travail.

Système fini

Ainsi dans les deux dernières décennies, la miniaturisation des dispositifs s'est intensifiée dans de nombreux domaines d'applications, dont les biotechnologies bien sûr. A cette tendance générale, on doit associer des techniques de caractérisation avancées comme la microscopie à force atomique, les techniques de spectroscopie locale, etc... Les modèles mathématiques doivent également être révisés pour prendre en compte des mécanismes physiques d'ordinaire négligés à échelle macroscopique.

Dans les problèmes de physique macroscopique, les frontières sont parfois repoussées à l'infini. Un exemple typique est l'étude thermique en conditions dynamiques d'un système froid positionné à l'instant initial dans un environ-

nement chaud (choc thermique) : l'environnement est alors censé être infini, ou de taille suffisamment grande pour ne pas changer sa température loin du système étudié pendant l'échange de chaleur.

Un second exemple est la surface active (fonctionnalisée) d'un biocapteur, qui peut réagir avec une espèce chimique (ou soluté). La réaction de capture avec les molécules de soluté à la surface active est supposée ne pas influencer la concentration volumique de soluté dans la phase ambiante, loin de la surface active. Le volume est donc considéré comme une source infinie d'espèces chimiques et fournit ainsi un flux diffusionnel sans changer sa concentration globale. Cette approximation n'est évidemment pas correcte du point de vue théorique, mais elle se révèle étonnamment précise pour des géométries macroscopiques.

Goutte sphérique isolée

Le vieillissement biochimique des surfaces en microfluidique monophasique ou diphasique est d'une importance remarquable pour une variété d'applications, dont les bio-puces ou les laboratoires-sur-puce, principales préoccupations de ce travail. Des molécules tensioactives sont utilisées pour la stabilisation des émulsions ou comme réactifs pour les essais immunologiques [70, 97, 98]. Ce travail concerne l'adsorption en transitoire, notamment induite par la dépendance temporelle de la taille des gouttes. Un modèle de vieillissement chimique à portée générique est développé dans cette section ; il peut tout autant être jugé pertinent pour la modélisation du mûrissement d'Ostwald (stabilité des émulsions eau/huile ou huile/eau) [99, 100] et des aérosols liquides [101] que pour modéliser les transferts biochimiques sous évaporation de gouttelettes fonctionnalisés, à micro-échelle [73, 74]. Typiquement, le système considéré ici est celui d'une goutte sphérique libre. On retrouve cette géométrie pour une goutte posée sur un substrat superhydrophobe (angle de contact : $\theta \approx \pi$), ainsi que pour une goutte posée dans la plupart des applications microfluidiques sous électromouillage (angle de contact proche de la valeur $\theta \approx \pi/2$). Dans le cas d'un régime limité en sorption (diffusion instantanée au sein d'une goutte posée), le modèle est étendu au cas d'un angle de contact arbitraire.

Le travail mené dans cette partie reprend l'état de l'art sur les modèles classiques de diffusion-sorption mais en considérant cette fois une goutte pour système liquide. On considère le rapport molaire, $CV/S\Gamma$, comme fini : C est la concentration volumique en espèce chimiques (éventuellement tensioactives) dans la goutte, Γ, la concentration surfacique, S et V sont la surface et le volume de goutte. Si ce ratio est supérieur à l'unité, la situation peut être considérée comme macroscopique, et la goutte est mathématiquement considéré comme un réservoir infini de molécules tensioactives : l'état de l'art est directement applicable. Dans le cas contraire, avec $CV/S\Gamma$ inférieur à (ou de l'ordre de) l'unité, le système est déclaré fini. Dans ce cas, l'adsorption des molécules à la surface liquide/gaz exerce un impact significatif sur la diffusion des espèces chimiques à l'intérieur de la goutte : typiquement, si la concentration de surface

augmente, la concentration volumique dans le centre de la goutte diminue dans le but d'alimenter le flux d'adsorption à l'interface.

On considère également que la surface sphérique ou hemisphérique de la goutte évolue en fonction du temps selon le rayon, $R(t)$. Avec l'évaporation, la surface se déplace radialement vers l'intérieur. Au-delà de la surface liquide ($r > R(t)$, r étant la coordonnée de l'espace pour un système sphérique isotrope), les tensioactifs sont considérés comme insoluble. Le système à l'instant initial est caractérisé par une surface libre du liquide avec une concentration initiale, $\Gamma(0) = 0$, une concentration volumique homogène dans tout le domaine, $C(r, 0) = C_0$, et un rayon initial, $R(0) = R_0$.

Depuis le modèle historique de Ward & Tordai sur les régimes limités en diffusion, des avancées théoriques ont été constamment axées sur l'amélioration de la modélisation du vieillissement chimique avec la prise en compte i) du couplage chimique par implémentation des lois d'adsorption et désorption, ii) du déséquilibre inital (régime transitoire) et, plus récemment, iii) les tentatives réussies pour prendre en compte la courbure de la surface sur la cinétique diffusionnelle [102–104]. Tous ces travaux sont basés sur l'hypothèse d'un demi-espace ($r > 0$) adjacent à une interface ($r = R$), à l'extérieur duquel les tensioactifs sont solubilisés. A notre connaissance, la seule étude qui n'invoque pas une condition de champ lointain pour la concentration, est celle développée par Filippov & Filippova [105] qui font appel à une symétrie au centre d'une goutte ($(\partial C/\partial r)|_{r=0} = 0$) afin de rendre compte du vieillissement chimique en régime limité diffusionnel.

Dans la littérature, deux aspects théoriques n'ont pas été étudiés analytiquement jusqu'alors, en dépit de leur importance pour la microfluidique diphasique ou digitale : le premier est l'impact d'une taille finie sur l'évolution des concentrations chimiques aussi bien volumique que surfacique, le second est le vieillissement d'une surface mobile (non-matérielle). Ces deux points sont traités dans ce chapitre.

La modélisation mise en place ici ayant vocation à être la plus générique possible, plusieurs cas asymptotiques sont analysés : l'équilibre thermodynamique ainsi que les régimes limités en diffusion, en sorption avec et sans évaporation. Les lois analytiques ainsi mises en évidence permettent de valider les calculs numériques et de se comparer également aux modèles historiques bien établis de Ward & Tordai, Filippov & Filippova et autres auteurs déjà référencés ci-dessus. Le caractère général de notre approche nous conduit à introduire différents nombres adimensionnels :

- dont η_{ea}, qui caractérise la transition entre régimes limités en évaporation et adsorption,
- η_{ed}, qui caractérise la transition entre régimes limités en évaporation et diffusion,
- η_{ad}, la transition entre régimes limités en adsorption et en diffusion se caractérise,

· enfin le nombre adimensionnel, $\varepsilon_0 = CV/S\Gamma$, est introduit afin d'estimer comment les paramètres géométriques et physico-chimiques influencent le vieillissement chimique dans un système fini.

L'un des résultats importants de ce chapitre est relatif à la concentration de surface à l'équilibre, Γ_e^{μ} qui est proposée comme une nouvelle échelle caractéristique de la concentration de surface dans la microfluidique en gouttes. Cette grandeur devient très utile pour la conception de systèmes microscopiques digitaux et pour les émulsions dès lors qu'il s'agit d'estimer au plus juste les concentrations réellement impliquées dans des réactions chimiques homogène ou hétérogène à l'échelle d'une goutte. Elle est également plus petite que dans les systèmes liquides macroscopiques, ce qui est essentiel pour des réactifs qui sont coûteux ou chronophages à produire.

Une première perspective de cette étude, qui repose sur la loi de Henri pour décrire les processus de sorption, consiste à adopter le modèle de Langmuir (cf. tableau 20.1) :

$$\frac{\mathrm{d}\Gamma}{\mathrm{d}t} = k_a C|_R \left(1 - \frac{\Gamma}{\Gamma_\infty}\right) - k_d \frac{\Gamma}{\Gamma_\infty}.$$

Ce modèle contient un paramètre Γ_∞ qui représente la concentration maximale à l'interface, et par conséquent l'encombrement stérique qui empêche une plus grande accumulation de biomolécules tensioactives à la surface.

Cela étant, la nécessité d'employer la loi de Langmuir se justifie par le fait que la concentration volumique doit être suffisamment élevée pour que l'encombrement stérique ne s'exprime de manière limitante. Si le rapport surface/volume reste faible, un nombre suffisant de molécules est présent dans le volume et autorise potentiellement la surface à se densifier jusqu'à subir l'encombrement stérique. Cependant, pour les systèmes finis, par définition, le rapport surface/volume présente une valeur plus élevée : la loi de Langmuir ne se révèle donc nécessaire que dans des cas particuliers.

Courant de dérive et diffusion de surface

Contrairement au chapitre 20 axé sur la diffusion, l'adsorption et l'évaporation, le courant de dérive est cette fois pris en compte et considéré comme capable d'engendrer des gradients de concentration volumique anisotropes. Induit par l'électromouillage oscillatoire basse-fréquence qui engendre des oscillations de gouttes, il contribue à installer une contribution non isotrope du transport convectif dans le volume ainsi que le long de la surface liquide. Ce mécanisme de transport est pris en considération dans cette étude tout autant que sa capacité de brassage et l'impact de celle-ci sur la cinétique de vieillissement. Dans la Fig. I.6 sont présentées les lignes de courant induites par courant de dérive dans la goutte pour les trois premiers modes d'oscillation.

Le courant de dérive, introduit dans le chapitre 6, déplace de manière stationnaire les biomolécules tensioactives. Parmi les avantages attendus du courant de dérive, on constate qu'il peut effectivement accélérer la dispersion des molécules

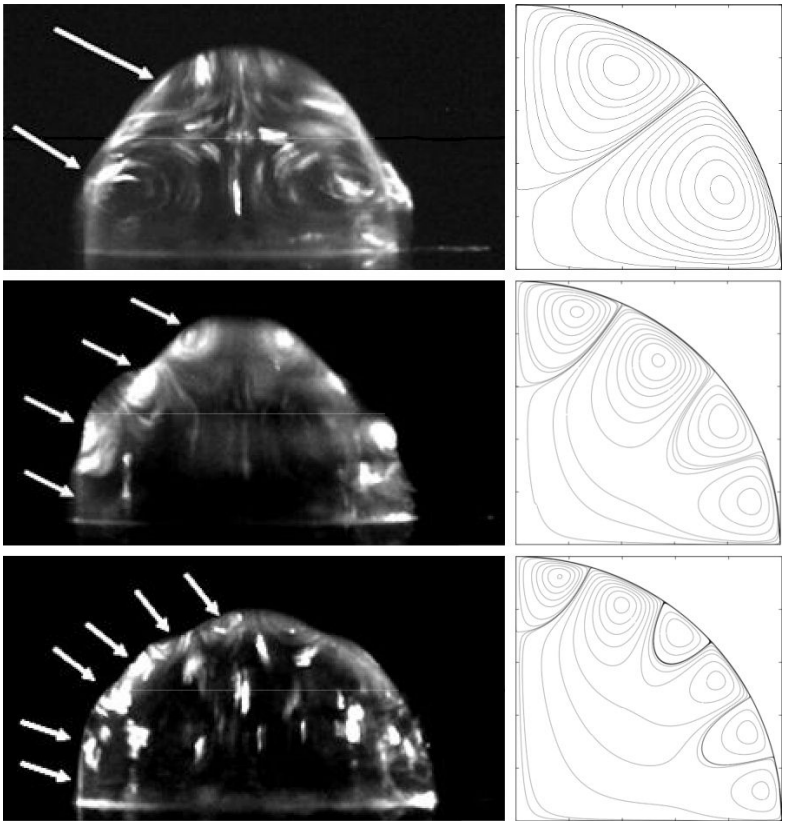

Fig. I.6.: Lignes de courant pour les trois premiers modes d'oscillation, de haut en bas : $n = \{2, 4, 6\}$. Comparaison de l'imagerie expérimentale à l'aide de particules traceurs (gauche) et des résultats de simulations (droite). Les flèches indiquent les structures de vortex également présentes dans la simulation. Les données expérimentales sont mises à disposition par Rachid Malk [62].

dans la goutte, favorisant le mélange et intensifiant le vieillissement biochimique en surfaces (substrat solide ou surface liquide enrobant la goutte). En outre, il contribue à renforcer la concentration de surface en une ou plusieurs régions (anneaux) localisées le long de la surface liquide sphérique à différentes latitudes, qui correspondent aux points de stagnation de l'onde stationnaire et des écoulements internes. Afin d'examiner le rôle des autres transports chimiques (diffusionnels, sorption) pour lesquels le brassage devient un élément supplémentaire contribuant à l'intensification du vieillissement chimique, le courant de dérive est pris en considération dans nos calculs. Puisqu'il engendre une concentration de surface non uniforme, l'effet de la diffusion moléculaire surfacique ne peut plus être négligé.

La contribution du courant de dérive au transport chimique en goutte nécessite une mise en œuvre 2D pour le calcul numérique. Afin de prendre en compte le transport chimique surfacique non homogène, une formulation faible a spécifiquement été dévelopée, qui permet d'intégrer les effets de diffusion de surface dans le calcul du vieillissement chimique. Les résultats de la mise en œuvre 2D ont été comparés avec succès aux résultats analytiques et numériques du chapitre 20 dans des cas asymptotiques. Dans une approche paramétrique,

quatre nombres adimensionnels ont été mis en évidence et analysés en utilisant le calcul numérique : les nombres de Péclet volumique et surfacique, le nombre de Damköhler et le nombre de Thiele.

Plusieurs conclusions sont ainsi émises : dans de nombreuses applications, gouvernées par les nombres de Peclet et de Damköhler, le courant de dérive peut effectivement être d'un grand intérêt pour le mélange volumique et les propriétés du vieillissement chimique de la goutte. La variance de la concentration volumique, σ_C^2, est le critère adopté pour quantifier l'efficacité du mélange. Des modes d'oscillations élevés privilégient le brassage au voisinage de la surface de la goutte et semblent être plus efficaces pour l'homogénéisation de la concentration volumique. Au contraire, pour l'adsorption des molécules uniquement sur le substrat solide, les petits nombres de mode sont préférables.

Du point de vue des perspectives, il est également intéressant en présence de brassage d'inclure les effets stériques aux surfaces, en mettant en œuvre une loi de Langmuir comme terme source dans l'équation de transport des tensioactifs. Un autre point intéressant à l'avenir est une mise en œuvre systématique de courants de dérive plus complexes : il pourrait être intéressant de mettre en place un protocole d'agitation à nombres adimensionnels fixes, fournissant une agitation plus efficace en exploitant l'utilisation d'une séquence de différents modes de résonance. En outre, l'introduction de rugosités mécaniques et électriques [62, 63, 116] pour générer des modèles d'écoulement modifiés avec des symétries différentes est une voie intéressante à explorer.

La dernière partie de la thèse est consacrée à une étude expérimentale mettant en oeuvre une protéine tensioactive du vivant (Bovine Serum Albumin). On se concentre sur le vieillissement surfacique de gouttes actionnées à différentes fréquences d'électromouillage. Les connaissances théoriques acquises ici sur le transport de surfactants et l'intensification du vieillissement chimique par courant de dérive nous aident à interpréter les résultats expérimentaux.

Sixième partie – Intensification du vieillissement chimique. Vers la biodétection sans marquage

A la lumière des chapitres précédents, l'utilité d'un essai biologique en microfluidique digitale est démontrée pour les raisons suivantes :

- avec une échelle de longueur réduite, celle d'une goutte (100 µm à 1 mm), et sous l'influence des processus de sorption, le flux diffusionnel ainsi engendré s'exerce sur l'ensemble du système fluidique, ce qui signifie que le gradient de concentration volumique s'étend à tout le volume liquide. Les temps d'adsorption ou de concentration sur des surfaces sensibles fonctionnalisées sont ainsi considérablement réduits pour la majeure partie des biomolécules cibles. Non seulement la quantité de réactif est réduite, mais également le temps d'exécution d'un bio-essai se trouve diminué.

· Par sa capacité de brassage, d'autant plus prononcée que l'échelle de longueur fluidique concernée est petite, le courant de dérive induit par électromouillage se révèle un outil pertinent pour l'intensification des processus physico-chimiques en régime limité par la diffusion, comme démontré dans la partie précédente.

Ce dernier chapitre est consacré à la combinaison expérimentale de ces deux avantages.
Une microgoutte chargée d'albumine de sérum bovin (BSA) est choisie comme système modèle. Le processus d'adsorption des protéines d'albumine au substrat solide lubrifié est observé par imagerie en observant la diminution de l'angle de contact. La loi de Young, combinée à la loi de Lippman et la prise en compte de l'isotherme d'adsorption de la BSA conduisent à expliquer cette évolution dynamique de l'angle de contact par le fait que l'adsorption de la BSA diminue la tension de surface solide/liquide, Γ_{SL}. Ainsi la goutte s'étale sur le substrat au cours du temps, ce qui indique le vieillissement chimique et fournit des informations sur l'échelle de temps nécessaire pour obtenir l'équilibre thermodynamique. L'impact du courant de dérive sur la cinétique de vieillissement de la surface solide est également quantifié.

A l'issue de la thèse, la tension de surface dynamique liquide/solide d'une surface lubrifiée et mouillée par une goutte chargée en albumine a donc été étudiée. On voit dans la section 25.1, qu'il n'est pas simple a priori de fonctionnaliser une interface liquide/gaz avec des molécules partiellement solubles : les molécules de BSA sont connues pour manifester une affinité chimique très forte pour les interfaces solide/liquide.

Un moyen de contourner cet obstacle pourrait être de travailler avec une phase ambiante liquide non miscible, p.ex. de l'huile silicone ou des alcanes. Quelques tests préliminaires ont été menés à la fin de la thèse et plusieurs recommandations peuvent être données :

· L'huile silicone comme phase ambiante est trop visqueuse pour maintenir des oscillations de goutte exploitables par interférométrie au niveau de l'apex de la goutte (viscosité dynamique de l'huile de silicone utilisée pour le test, $\mu = 5\,\mathrm{mPa\,s}$).

· Les liquides de la classe des alcanes existent dans une gamme de viscosité différente, en fonction de la taille des molécules d'alcanes.

  – Des essais ont été réalisés avec l'hexadécane comme phase ambiante ($\mu = 3.3\,\mathrm{mPa\,s}$). Il se révèle trop visqueux, comme l'huile de silicone.
  – D'autres essais ont été conduits avec du décane, dont la viscosité est approximativement égale à celle de l'eau, ($\mu = 920\,\mu\mathrm{Pa\,s}$) : un spectre de résonnance capillaire peut être mesuré par interférométrie pour certains angles de contact, mais le facteur de qualité reste très faible par rapport aux mesures effectuées dans l'air.

– Un alcane encore moins visqueux est l'hexane à une viscosité de $\mu = 290\,\mu$Pa s, mais les tests n'ont pas encore été réalisés. Ce liquide est très volatile, il est donc nécessaire de couvrir l'expérience. En outre, l'hexane est nocif pour l'environnement, ce qui nécessite une attention particulière pour le traitement des déchets.

Une autre piste mérite d'être tentée consistant à saturer l'interface solide/liquide sous la goutte avec la BSA particulièrement affine puis à solubiliser toute autre biomolécule d'intérêt (moins affine pour le substrat solide) capable de contribuer au vieillissement biochimique de l'interface liquide/gaz cette fois. Il s'agit là d'une stratégie utilisée dans les micro-canaux en microfluidique continue lorsque l'objectif est d'éviter les adsorptions non spécifiques.

Conclusion et perspectives

Pour conclure ce travail, un résumé des principales réalisations et résultats est approprié. Un dispositif expérimental a été réalisé, qui permet aux utilisateurs de microsystèmes digitaux la caractérisation par interférométrie d'oscillations de gouttes, engendrées par électromouillage double-fréquence. L'interférométrie de type Michelson peut être utilisée pour détecter les déplacements micrométriques d'interfaces liquide/gaz en utilisant un laser d'une longueur d'onde de 532 nm et une photodiode à avalanche adaptée.

Cette méthodologie expérimentale a été utilisée pour caractériser l'évaporation d'une goutte posée seule, ainsi que d'une goutte positionnée au sein d'une réseau de gouttes. L'influence respective de paramètres géométriques tels que le confinement du micro-système et l'espacement inter-gouttes a été étudiée. La méthodologie peut renseigner fidèlement sur la dépendance temporelle du processus d'évaporation, et donne une bonne estimation du rayon ou du volume de goutte. Avec l'électromouillage bi-fréquence, l'angle de contact peut être contrôlé et son hystérésis réduit, ce qui facilite l'analyse.

Des développements théoriques ont également été menés dans ce travail de thèse, portant sur les phénomènes de diffusion et de sorption au sein d'une goutte. Un modèle mathématique a été établi décrivant les processus physico-chimiques dans une goutte sphérique libre (ou hémi-sphérique posée), et pour une quantité finie de molécules. De plus, une géométrie de goutte variable a été prise en compte afin de rendre compte de l'évaporation agissant sur la surface de la goutte (rayon variable). Un nouveau nombre adimensionnel, ε_0, a été introduit afin de comparer la quantité de molécules adsorbées à la surface à la quantité de molécules dans le volume. En utilisant la loi de Henry pour décrire l'adsorption et la désorption de molécule tensioactives, ce nombre adimensionnel s'exprime en fonction des constantes d'adsorption et de désorption, et de la taille de la goutte ; ce qui rend possible la comparaison entre différents systèmes physico-chimiques.

Avec ce modèle, une analyse adimensionnelle a été réalisée, donnant un

aperçu de l'influence de quatre nombres adimensionnels impliqués dans le transport biochimique en gouttes, à savoir η_{ea}, η_{ed}, η_{ad} et ε_0. En outre, pour les régimes limités en adsorption, le modèle analytique a été étendu à des gouttes posées d'angle de contact arbitraire. Il a été constaté que la dynamique du vieillissement chimique dépend fortement de l'angle de contact pour les géométries de faible angle de contact (configuration hydrophile), alors que pour les géométries d'angle de contact élevé (configuration hydrophobe), la dépendance à celui-ci est presque négligeable.

La méthode des éléments finis a ensuite été utilisée afin de prendre en compte l'impact du courant de dérive, induit par électromouillage oscillatoire. Le couplage de la quantité de mouvement avec le transport diffuso-convectif en volume, les phénomènes de sorption à la surface d'une goutte et la diffusion surfacique le long de la dite surface sont résolus par introduction d'une nouvelle formulation faible pour le transport surfacique. La cinétique de vieillissement chimique a été analysée pour des régimes limités en sorption puis en diffusion, le tout en présence du courant de dérive. L'influence du nombre de modes d'oscillation, en imposant différents régimes convectifs, a été analysée. En outre, une distinction a été faite entre l'adsorption à la surface libre de la goutte et l'adsorption à l'interface liquide-solide. Ainsi, des connaissances ont été acquises sur l'action locale des tourbillons en gouttes sur les gradients de concentration volumique, ce qui s'est révélé utile pour l'interprétation des résultats dans la dernière partie de ce travail.

La dernière partie de ce travail est expérimentale et dédiée à la fonctionnalisation biologique de l'interface solide/liquide par l'albumine de sérum bovin. La tension de surface liquide/solide cinétique a été mesurée au cours du temps, et l'effet du courant de dérive sur la dynamique du vieillissement chimique a été étudiée.

En ce qui concerne d'éventuels travaux futurs, plusieurs propositions peuvent être citées. Concernant l'instrumentation, il serait avantageux d'utiliser des motifs d'électrodes à quatre quadrants composés de quatre quarts d'un cercle. Cela présente l'avantage de mieux stabiliser la goutte au centre du motif d'électrodes.

Si, comme montré dans cette thèse, un signal électrique basse fréquence appliqué à deux électrodes coplanaires peut engendrer la déformation mécanique d'une goutte, à l'inverse, une modification du mouillage de la goutte peut engendrer une variation de tension dans un circuit électronique spécifiquement conçu à cette fin, connecté aux deux électrodes coplanaires. Ce phénomène est l'électromouillage réversible (*Reverse ElectroWetting On Dielectric* ou REWOD) [125]. En outre, le suivi de l'impédance équivalente de l'empilement [substrat diélectrique - film lubrifiant - goutte], pourrait dans l'avenir être utilisé afin de détecter des variations de propriétés mécaniques et chimiques de la goutte [80, 91]. L'une de ces 2 approches pourrait se révéler être une approche intéressante afin de développer une nouvelle méthodologie de mesure, en remplacement de l'approche interférométrique. L'avantage attendu serait une meilleure intégration système dès lors que l'actuation et la détection seraient

menées avec les mêmes électrodes en configuration coplanaire.

Enfin, il est utile de réfléchir à une mise en œuvre plus systématique de l'analyse des oscillations en régime transitoire, qui constitue une méthodologie alternative à l'approche fondée sur l'entretien d'une onde capillaire stationnaire (voir parties II et III, voir également les détails de cette approche innovante dans l'annexe D).

Les développements théoriques de la partie V sur les phénomènes physico-chimiques et le courant de dérive devront à court terme être étendus à des angles de contact différents de $\pi/2$. En outre, la mise en oeuvre de la loi de Langmuir afin de caractériser le vieillissement dynamique des surfaces au voisinage de l'encombrement stérique constitue une évolution naturelle de nos modèles.

Un autre point intéressant est la prise en compte par la modélisation d'une phase ambiante liquide (non miscible avec la phase liquide constituant la goutte), susceptible d'héberger des biomolécules éventuellement tensioactives. Cette nouvelle étape permettrait, par exemple, de rendre compte d'essais d'hybridation à une interface liquide/liquide.

La partie expérimentale VI consacrée aux essais biologiques peut être étendue selon plusieurs directions. L'une d'entre elles serait de trouver un moyen approprié d'exploiter la tension de surface liquide/gaz pour la fonctionnalisation correcte de la surface de la goutte et la poursuite de l'approche de tests d'hybridation sans marquage. De premiers essais dans ce sens sont actuellement menés.

Maintenant, si le but est de garder l'air en tant que phase ambiante (nez chimiques), puis de détecter des biomolécules affines pour des supports solides (comme la BSA), des pluronics [74, 126], ou toute autre molécule avec une plus forte affinité pour un substrat solide lubrifié, pourrait être utilisées afin de saturer la surface solide et ainsi permettre aux autres biomolécules (comme la BSA) de venir s'adsorber à la surface de la goutte. Une telle détection au niveau d'une interface liquide déformée par une onde doit aussi permettre (comme montré par nos simulations) la focalisation de biomolécules adsorbées, ce qui garantit *in fine* une plus grande sensibilité de détection aux points de focalisation.

Bibliography

[1] S.C. Terry, J.H. Jerman, and J.B. Angell. A Gas Chromatographic Air Analyzer Fabricated on a Silicon Wafer. *IEEE Trans. Electron Devices*, 26(12):1880–1886, 1979.

[2] A. Manz, N. Graber, and H.M. Widmer. Miniaturized Total Chemical Analysis Systems: a Novel Concept for Chemical Sensing. *Sensor. Actuator. B*, pages 244–248, 1990.

[3] European Commission. Life sciences and biotechnology: A strategy for Europe, 2002.

[4] McWilliams. Biotechnologies for Medical Applications: Global Markets, 2010.

[5] D.J. Beebe, G.A. Mensing, and G.M. Walker. Physics and applications of microfluidics in biology. *Annu. Rev. Biomed. Eng.*, 4:261–286, 2002.

[6] V. Hessel, H. Löwe, and F. Schönfeld. Micromixers – a review on passive and active mixing principles. *Chem. Eng. Sci.*, 60(8–9):2479–2501, 2005.

[7] N. Pamme. Magnetism and microfluidics. *Lab Chip*, 6:24–38, 2006.

[8] M. Wiklund, R. Green, and M. Ohlin. Acoustofluidics 14: Applications of acoustic streaming in microfluidic devices. *Lab Chip*, 12:2438–2451, 2012.

[9] S.L. Biswal and A.P. Gast. Micromixing with Linked Chains of Paramagnetic Particles. *Anal. Chem.*, 76:6448–6455, 2004.

[10] P. Paik, V.K. Pamula, M.G. Pollack, and R.B. Fair. Electrowetting-based droplet mixers for microfluidic systems. *Lab Chip*, 3:28–33, 2003.

[11] S. Qian and H.H. Bau. Magneto-hydrodynamic stirrer for stationary and moving fluids. *Sensor. Actuator. B*, 106:859–870, 2005.

[12] P. Pham, J.L. Achard, J. Berthier, and F. Ginot. Modeling of the kinetics of capture of pathogens enhanced by a Marangoni flow. *NSTI-Nanotech 2003*, 1:202–205, 2003.

[13] R. Malk, Y. Fouillet, and L. Davoust. Rotating flow within a droplet actuated with AC EWOD. *Sensor. Actuator. B*, 154:191–198, 2011.

[14] F. Mugele, A. Staicu, R. Bakker, and D. van den Ende. Capillary Stokes drift: a new driving mechanism for mixing in AC-electrowetting. *Lab Chip*, 11:2011–2016, 2011.

[15] R. Miraghaie, J.D. Sterling, and A. Nadim. Shape Oscillation and Internal Mixing in Sessile Liquid Drops Using Electrowetting-on-Dielectric (EWOD). *NSTI-Nanotech*, 2:610–613, 2006.

[16] M.G. Pollack, A.D. Shenderov, and R.B. Fair. Electrowetting-based actuation of droplets for integrated microfluidics. *Lab Chip*, 2:96–101, 2002.

[17] H. Ren, R.B. Fair, and M.G. Pollack. Automated on-chip droplet dispensing with volume control by electro-wetting actuation and capacitance metering. *Sensor. Actuator. B*, 98:319–327, 2004.

[18] S. Zeng, K.-T. Yong, I. Roy, X.-Q. Dinh, X. Yu, and F. Luan. A Review on Functionalized Gold Nanoparticles for Biosensing Applications. *Plasmonics*, 6:491–506, 2011.

[19] L. Malic, T. Veres, and M. Tabrizian. Biochip functionalization using electrowettin-on-dielectric digital microfluidics for surface plasmon resonance imaging detection of DNA hybridization. *Biosens. Bioelectron.*, 24:2218–2224, 2009.

[20] P. Bergese, G. Oliviero, I. Colombo, and L.E. Depero. Molecular Recognition by Contact Angle: Proof of Concept with DNA Hybridization. *Langmuir*, 25(8):4271–4273, 2009.

[21] K. Choi, J.-Y. Kim, J.-H. Ahn, J.-M. Choi, M. Im, and Y.-K. Choi. Integration of field effect transistor-based biosensors with a digital microfluidic device for a lab-on-a-chip application. *Lab Chip*, 12:1533, 2012.

[22] Cyril Picard. *Ondes capillaires à une interface fluide fonctionnalisée : détection micromécanique de brins d'ADN*. PhD thesis, Grenoble INP, Grenoble, France, 2007.

[23] R. Malk, A. Rival, Y. Fouillet, and L. Davoust. EWOD in Coplanar Electrode Configurations. *ASME Conference Proceedings*, 2010(54501):239–248, 2010.

[24] C. Picard and L. Davoust. A "fluid cantilever" to detect amphiphilic biomolecules. *Colloid. Surface. A*, 343:12–19, 2009.

[25] G. Lippmann. Relation entre les phénomènes électriques et capillaires. *Annales de Chimie et de Physique*, 5:494–549, 1875.

[26] P.-G. de Gennes. Wetting: statics and dynamics. *Rev. Mod. Phys.*, 57(3), 1985.

[27] B. Berge, M. Vallet, and M. Vallade. Limiting phenomena for the spreading of water on polymer films by electrowetting. *Eur. Phys. J. B*, 11:583–591, 1999.

[28] B. Berge and C. Quilliet. Electrowetting: a recent outbreak. *Curr. Opin. Colloid In.*, 6:34–39, 2001.

[29] K.H. Kang, J.M. Oh, and S.H. Ko. Shape Oscillation of a Drop in AC Electrowetting. *Langmuir*, 23(15):8379–8386, 2008.

[30] P. Dubois, G. Marchand, Y. Fouillet, J. Berthier, T. Douki, F. Hassine, S. Gmouh, and M. Vaultier. Ionic Liquid Droplet as e-Microreactor. *Anal. Chem.*, 78:4909–4917, 2006.

[31] U.-C. Yi and C.-J. Kim. Characterization of electrowetting actuation on addressable single-side coplanar electrodes. *J. Micromech. Microeng.*, 16(10):2053–2059, 2006.

[32] P. Sen and C.-J. Kim. Capillary Spreading Dynamics of Electrowetted Sessile Droplets in Air. *Langmuir*, 25(8):4302–4305, 2009.

[33] J. Theisen and L. Davoust. Dual-Frequency Electrowetting: Application to Drop Evaporation Gauging within a Digital Microsystem. *Langmuir*, 28(1):1041–1048, 2012.

[34] K.H. Kang. How Electrostatic Fields Change Contact Angle in Electrowetting. *Langmuir*, 18(26):10318–10322, 2002.

[35] J.W.S. Rayleigh. On the capillary phenomena of jets. *Proc. R. Soc. Lond.*, 29:71–97, 1879.

[36] W.T.B. Kelvin and J. Larmor. *Mathematical and Physical Papers*. Cambridge University Press, 1890.

[37] H. Lamb. *Hydrodynamics*. Cambridge University Press, 1932.

[38] J.B. Bostwick and P.H. Steen. Capillary oscillations of a constrained liquid drop. *Phys. Fluids*, 21(3):032108, 2009.

[39] G.B. Arfken, H.J. Weber, and F.E. Harris. *Mathematical Methods for Physicists*. Academic Press, 2005.

[40] M.S. Plesset. On the Stability of Fluid Flows with Spherical Symmetry. *J. Appl. Phys.*, 25:96–98, 1954.

[41] A. Prosperetti. *Viscous and nonlinear effects in the oscillations of drops and bubbles*. PhD thesis, California Institute of Technology, Pasadena (CA), USA, 1974.

[42] M. Strani and F. Sabetta. Free vibrations of a drop in partial contact with a solid support. *J. Fluid Mech.*, 141:233–247, 1984.

[43] K.H. Kang, J.M. Oh, and S.H. Ko. Analysis of electrowetting-driven spreading of a drop in air. *Phys. Fluids*, 22:032002, 2010.

[44] S.R. Annapragada, S. Dash, S.V. Garimella, and J.Y. Murthy. Dynamics of Droplet Motion under Electrowetting Actuation. *Langmuir*, 27(13):8198–8204, 2011.

[45] D.M. Henderson, K. Larson, and Y.K. Rao. A Study of Wheat Storage Protein Monolayers by Faraday Wave Damping. *Langmuir*, 7:2731–2736, 1991.

[46] N.E. Huang. Mass Transport Induced by Wave Motion. *J. Mar. Res.*, 28(1):35–50, 1970.

[47] J. Lighthill. Biomechanics of Hearing Sensitivity. *J. Vib. Acoust.*, 113(1):1–13, 1991.

[48] J. Lighthill. Acoustic streaming in the ear itself. *J. Fluid Mech.*, 239:551–606, 1992.

[49] G. Jayaraman and A. Sarkar. Nonlinear analysis of arterial blood flow–steady streaming effect. *Nonlinear Anal.-Theor.*, 63(5):880–890, 2005.

[50] S.S. Sadhal. Acoustofluidics 13: Analysis of acoustic streaming by perturbation methods. *Lab Chip*, 12:2292–2300, 2012.

[51] P. Marmottant and S. Hilgenfeld. A bubble-driven microfluidic transport element for bioengineering. *P. Natl. Acad. Sci.*, 101(26):9523–9527, 2004.

[52] B.R. Lutz and J. Chen. Microfluidics without microfabrication. *P. Natl. Acad. Sci.*, 100(8):4395–4398, 2003.

[53] R.H. Liu and J.N. Yang. Bubble-induced acoustic micromixing. *Lab Chip*, 2(3):151–157, 2002.

[54] S.H. Ko, S.J. Lee, and K.H. Kang. A synthetic jet produced by electrowetting-driven bubble oscillations in aqueous solution. *Appl. Phys. Lett.*, 94:194102, 2009.

[55] M. Faraday. On a Peculiar Class of Acoustical Figures; and on Certain Forms Assumed by Groups of Particles upon Vibrating Elastic Surfaces. *Philos. T. Roy. Soc. A*, 121, 1831.

[56] J.W.S. Rayleigh. On the Circulation of Air observed in Kundt's Tubes, and on some allied Acoustical Problems. *Philos. T. Roy. Soc. A*, 175:1–21, 1884.

[57] J.T. Stuart, E.J. Watson, and G.B. Whitham. *Laminar Boundary Layers*, page 477. Oxford University Press, 1963.

[58] J.T. Stuart. Double boundary layers in oscillatory viscous flow. *J. Fluid Mech.*, 24(4):673–687, 1966.

[59] N. Riley. Oscillating viscous flows. *Mathematika*, 12:161–175, 1965.

[60] H. Schlichting and K. Gersten. *Boundary-Layer Theory*. Springer, 1979.

[61] N. Riley. Oscillatory Viscous Flows. Review and Extension. *IMA J. Appl. Math.*, 3(4):419–434, 1967.

[62] R. Malk. *Ecoulements en gouttes activés par électromouillage*. PhD thesis, Université de Grenoble, Grenoble, France, 2011.

[63] R. Malk, J. Theisen, Y. Fouillet, and L. Davoust. EWOD-driven stirring in lab-on-a-chips: Dependence on the electrodes' geometry. *Microelectron. Eng.*, 97:306–310, 2012.

[64] A.F. Stalder, G. Kulik, D. Sage, L. Barbieri, and P. Hoffmann. A Snake-Based Approach to Accurate Determination of Both Contact Points and Contact Angles. *Colloid. Surface. A*, 286(1-3):92–103, 2006.

[65] F. Mugele and J.-C. Baret. Electrowetting: from basics to applications. *J. Phys.: Condens. Matter*, 17:R705–R774, 2005.

[66] F. Mugele, J.-C. Baret, and D. Steinhauser. Microfluidic mixing through electrowetting-induced droplet oscillations. *Appl. Phys. Lett.*, 88:204106, 2006.

[67] F. Mugele. Fundamental challenges in electrowetting: from equilibrium shapes to contact angle saturation and drop dynamics. *Soft Matter*, 5:3377–3384, 2009.

[68] B. Berge and J. Peseux. Variable focal lens controlled by an external voltage: An application of electrowetting. *Eur. Phys. J. E*, 3:159–163, 2000.

[69] R.B. Fair. Digital microfluidics: is a true lab-on-a-chip possible? *Microfluid. Nanofluid.*, 3:245–281, 2007.

[70] G. Maglia, A.J. Heron, W.L. Hwang, M.A. Holden, E. Mikhailova, Q. Li, S. Cheley, and H. Bayley. Droplet networks with incorporated protein diodes show collective properties. *Nature Nanotech.*, 4:437–440, 2009.

[71] A. Staicu and F. Mugele. Electrowetting-Induced Oil Film Entrapment and Instability. *Phys. Rev. Lett.*, 97:167801, 2006.

[72] S.W. Walker, B. Shapiro, and R.H. Nochetto. Electrowetting with contact line pinning: Computational modeling and comparisons with experiments. *Phys. Fluids*, 21:102103, 2009.

[73] R.L. Garrell and J.-Y. Yoon. Preventing Biomolecular Adsorption in Electrowetting-Based Biofluidic Chips. *Anal. Chem.*, 75(19):5097–5102, 2003.

[74] A.R. Wheeler, V.N. Luk, and G.C.H. Mo. Pluronic Additives: A Solution to Sticky Problems in Digital Microfluidics. *Langmuir*, 24:6382–6389, 2008.

[75] H. Hu and R.G. Larson. Evaporation of a Sessile Droplet on a Substrate. *J. Phys. Chem. B*, 106:1334–1342, 2002.

[76] M.J. Joyce, P. Todaro, R. Penfold, S.N. Port, J.A.W. May, C. Barnes, and A.J. Peyton. Evaporation of Sessile Drops: Application of the Quartz Crystal Microbalance. *Langmuir*, 16:4024–4033, 2000.

[77] N.T. Pham, G. McHale, M.I. Newton, B.J. Carroll, and S.M. Rowan. Application of the Quartz Crystal Microbalance to the Evaporation of Colloidal Suspension Droplets. *Langmuir*, 20:841–847, 2004.

[78] J. Arcamone, E. Dujardin, G. Rius, R. Pérez-Murano, and T. Ondarçuhu. Evaporation of Femtoliter Sessile Droplets Monitored with Nanomechanical Mass Sensors. *J. Phys. Chem. B*, 111:13020–13027, 2007.

[79] C. Liu and E. Bonaccurso. Microcantilever sensors for monitoring the evaporation of microdrops of pure liquids and mixtures. *Rev. Sci. Instrum.*, 81:013702, 2010.

[80] J. Gong and C.J. Kim. All-electronic droplet generation on-chip with real-time feedback control for EWOD digital microfluidics. *Lab Chip*, 8:898–906, 2008.

[81] R. Bexon and R.G. Picknett. The Evaporation of Sessile or Pendant Drops in Still Air. *J. Colloid Interf. Sci.*, 61(2):336–350, 1977.

[82] G. McHale, S.M. Rowan, M.I. Newton, and M.K. Banerjee. Evaporation and the Wetting of a Low-Energy Solid Surface. *J. Phys. Chem. B*, 102:1964–1967, 1998.

[83] J.-T. Cheng and C.-L. Chen. Active thermal management of on-chip hot spots using EWOD-driven droplet microfluidics. *Exp. Fluids*, 49:1349–1357, 2010.

[84] M.G. Pollack, V.K. Pamula, V. Srinivasan, and A.E. Eckhardt. Applications of electrowetting-based digital microfluidics in clinical diagnostics. *Expert Rev. Mol. Diagn.*, 11(4):393–407, 2011.

[85] R.A. Hayes and B.J. Feenstra. Video-speed electronic paper based on electrowetting. *Nature*, 425:383–385, 2003.

[86] C. Delattre, C. Allier, Y. Fouillet, D. Jary, F. Bottausci, D. Bouvier, G. Delapierre, M. Quinaud, A. Rival, L. Davoust, and C. Peponnet. Macro to microfluidics system for biological environmental monitoring. *Biosens. Bioelectron.*, 36(1):230–235, 2012.

[87] M.G. Pollack, P.Y. Paik, A.D. Shenderog, V.K. Pamula, F.S. Dietrich, and R.B. Fair. Investigation of electrowetting-based microfluidics for real-time PCR applications. In *Proceedings of the* 7^{th} *Int. µTAS Conf.*, volume 1, pages 619–622, 2003.

[88] T. Zhang, K. Chakrabarty, and R. B. Fair. Behavioral Modeling and Performance Evaluation of Microelectrofluidics-Based PCR Systems Using SystemC. *IEEE T. Comput. Aid. D.*, 23:843–858, 2004.

[89] N. Zhang and D. F. Chao. A New Approach to Measure Contact Angle and Evaporation Rate With Flow Visualization in a Sessile Drop. *NASA/TM-1999-209636*, 1999.

[90] O.D. Gazzola, B. Iafelice, E. Jung, E. Franchi, and R. Guerrieri. An Integrated Electronic Meniscus Sensor for Measurement of Evaporative Flow. In *Solid-State Sensors, Actuators and Microsystems Conference, 2007. TRANSDUCERS 2007. International*, pages 1805–1808, June 2007.

[91] S. Sadeghi, H. Ding, G.J. Shah, S. Chen, P.Y. Keng, C.J. Kim, and R.M. van Dam. On Chip Droplet Characterization: A Practical, High-Sensitivity Measurement of Droplet Impedance in Digital Microfluidics. *Anal. Chem.*, 84:1915–1923, 2012.

[92] F. Wanget and A. Burns. Performance of nanoliter-sized droplet-based microfluidic PCR. *Biomed. Microdevices*, 11:1071–1080, 2009.

[93] A. C. Hatch, J. S. Fisher, A. R. Tovar, A. T. Hsieh, R. Lin, S. L. Pentoney, D. L. Yang, and A. P. Lee. 1-Million droplet array with wide-field fluorescence imaging for digital PCR. *Lab Chip*, 11:3838–3845, 2011.

[94] D.J. Harris, J.C. Conrad, and J.A. Lewis. Evaporative lithographic patterning of binary colloidal films. *Philos. T. Roy. Soc. A*, 367:5157–5165, 2009.

[95] H. Song, Y. Lee, S. Jin, H.-Y. Kim, and J. Y. Yoo. Prediction of sessile drop evaporation considering surface wettability. *Microelectron. Eng.*, 88(11):3249–3255, 2011.

[96] C. Picard and L. Davoust. Resonance Frequencies of Meniscus Waves as a Physical Mechanism for a DNA Biosensor. *Langmuir*, 23:1394–1402, 2007.

[97] K. Landfester, A. Musyanovich, and V. Mailänder. Miniemulsion Droplets as Single Molecule Nanoreactors for Polymerase Chain Reaction. *Biomacromolecules*, 6:1824–1828, 2005.

[98] H. K. Kim, Y. S. Nam, J.-W. Kim, J. Shim, and S. H. Han. Silicone oil emulsions stabilized by semi-solid nanostructures entrapped at the interface. *J. Colloid Interf. Sci.*, 351:102–107, 2010.

[99] J.M. Gutiérrez, M. Porras, C. Solans, C. Gonzalez, A. Martínez, and A. Guinart. Studies of formation of W/O nano-emulsions. *Colloid. Surface. A*, 249:115–118, 2004.

[100] M. Laradji and J.H. Yao. Dynamics of Ostwald ripening in the presence of surfactants. *Phys. Rev. E*, 47(4):2695–2701, 1993.

[101] Riikka Sorjamaa and Ari Laaksonen. The influence of surfactant properties on critical supersaturations of cloud condensation nuclei. *J. Aerosol Sci.*, 37(12):1730–1736, 2006.

[102] K.J. Stebe, F. Jin, and R. Balasubramaniam. Surfactant Adsorption to Spherical Particles: The Intrinsic Length Scale Governing the Shift from Diffusion to Kinetic-controlled Mass Transfer. *J. Adhesion*, 80:773–796, 2004.

[103] C. Picard and L. Davoust. Dilational rheology of an air-water interface functionalized by biomolecules: the role of surface diffusion. *Rheol. Acta*, 45:497–504, 2006.

[104] N.J. Alvarez, L.M. Walker, and S.L. Anna. Diffusion-limited Adsorption to a Spherical Geometry: The Impact of Curvature and Competitive Time Scales. *Phys. Rev. E*, 82:011604, 2010.

[105] L.K. Filippov and N.L. Filippova. Dynamic Surface Tension and Adsorption Kinetics in Finite Systems. *J. Colloid Interf. Sci.*, 187:352–362, 1996.

[106] A.-M. Cazabat and G. Guéna. Evaporation of macrosocopic sessile droplets. *Soft Matter*, 6:2591–2612, 2010.

[107] J.J. Hegseth. Natural convection in droplet evaporation. *Phys. Rev. E*, 54:1640–1644, 1996.

[108] B. Fischer. Particle Convection in an Evaporating Colloidal Droplet. *Langmuir*, 18:60–67, 2002.

[109] H. Hu and R.G. Larson. Analysis of the Effects of Marangoni Stresses on the Microflow in an Evaporating Sessile Droplet. *Langmuir*, 21:3972–3980, 2005.

[110] H. Hu and R.G. Larson. Marangoni Effect Reverses Coffee-Ring Depositions. *J. Phys. Chem. B*, 110:7090–7094, 2006.

[111] X. Xu and J. Luo. Marangoni flow in an evaporating water droplet. *Appl. Phys. Lett.*, 91:124102, 2007.

[112] H.A. Stone. A simple derivation of the time-dependent convective-diffusion equation for surfactant transport along a deforming interface. *Phys. Fluids A*, 2(1):111–112, 1990.

[113] A.F.H. Ward and L. Tordai. Time-Dependence of Boundary Tensions of Solutions. *J. Chem. Phys.*, 14(7):453–461, 1946.

[114] G. Doetsch. *Introduction to the Theory and Application of the Laplace Transformation*. Springer, 1974.

[115] J. van Hunsel and P. Joos. Adsorption Kinetics at the Oil/Water Interface. *Colloid. Surface.*, 24:139–158, 1987.

[116] D. Mampallil, D. van den Ende, and F. Mugele. Controlling flow patterns in oscillating sessile drops by breaking azimuthal symmetry. *Appl. Phys. Lett.*, 99:154102, 2011.

[117] D.C. Carter and J.X. Ho. Structure of Serum Albumin. *Adv. Protein Chem.*, 45:153–203, 1994.

[118] J. Figge, T.H. Rossing, and V. Fencl. The Role of serum-proteins in Acid-Base Equilibria. *J. Lab. Clin. Med.*, 117:453–467, 1991.

[119] A.K. Wright and M.R. Thompson. Hydrodynamic structure of bovine serum albumin determined by transient electric birefringence. *Biophys. J.*, 15:137–141, 1975.

[120] J.F. Foster. *Albumin Structure, Function and Uses*. Rosenoer, Oratz and Rothschild, Pergamon, Oxford, 1977.

[121] K.M. Yeung, Z.J. Lu, and N.H. Cheung. Adsorption of bovine serum albumin on fused silica: Elucidation of protein–protein interactions by single-molecule fluorescence microscopy. *Colloid. Surface. B*, 69:246–250, 2009.

[122] L. Huang and Z. Guo. Biosensing in a microelectrofluidic system using optical whispering-gallery mode spectroscopy. *Biomicrofluidics*, 5(3):034114, 2011.

[123] J.F. Foster. *The Plasma Proteins*, volume 1. Academic Press, New York, 1960.

[124] S.H. Ko, H. Lee, and K.H. Kang. Hydrodynamic Flows in Electrowetting. *Langmuir*, 24(3):1094–1101, 2008.

[125] T. Krupenkin and J.A. Taylor. Reverse electrowetting as a new approach to high-power energy harvesting. *Nature Comm.*, 2:448, 2011.

[126] Z. Wu and K. Hjort. Surface Modification of PDMS by Gradient-Induced Migration of Embedded Pluronic. *Lab Chip*, 9:1500–1503, 2009.

[127] R.W. Smithwick and J.A.M. Boulet. Vibrations of Microscopic Mercury Droplets on Glass. *J. Colloid Interf. Sci.*, 130(2):588–596, 1989.

[128] J. Theisen and L. Davoust. Gauging contact line friction of droplets: in-situ measurement within a digital micro-system. *Microelectron. Eng.*, Article in press.

[129] T. Funada, D. Joseph, and J. Wang. *Potential Flows of Viscous and Viscoelastic Fluids*. Cambridge University Press (New York), 2008.

[130] L. Davoust, Y. Fouillet, R. Malk, and J. Theisen. Coplanar electrowetting-induced stirring as a tool to manipulate biological samples in lubricated digital microfluidics. Impact of ambient phase on drop internal flow pattern. *Biomicrofluidics*, 7:044104, 2013.

Joint use of dual-frequency electrowetting and interferometry in a digital microsystem: Application to evaporation and surface ageing at drop scale.

Abstract: This PhD research is thought of as a first step towards label free digital biosensing. A novel transduction mechanism is developed, based on the generation of capillary waves along a drop surface induced by dual-frequency electrowetting. A capillary resonance is measured by interferometry at the moving drop apex. A proof of concept of this electro-optical methodology for further integration in a digital microsystem is given with characterization of drop evaporation kinetics. A second part focuses on modeling and numerical calculations of the transport of surface active biomolecules in the drop. The model includes diffusion, ad-/desorption phenomena together with a kinematic condition of a variable drop radius (evaporation) as well as a finite molecular amount of surface active biomolecules. A dimensionless number is suggested to take into account finite size effects. Drop steady streaming due to oscillating electrowetting is finally taken into account. Low- and high-frequency electrowetting is applied to a drop laden with bovine serum albumin. By jointly using interferometry and imaging, enhancement of surface ageing is made evident under electrowetting.

Keywords: Digital microfluidics, Drops, Electrowetting, Interferometry, Diffusion, Convection, Physico-sorption, Evaporation, Biomolecules.

Electromouillage bi-fréquence et interférométrie: Evaporation et vieillissement biochimique à l'échelle d'une goutte.

Abstract : La recherche développée durant cette thèse constitue la première étape de développement d'une nouvelle méthodologie de détection sans marquage à l'échelle d'une goutte : un nouveau mécanisme de transduction est développé, basé sur l'actuation par électromouillage bi-fréquence d'un réseau d'ondes capillaires à la surface d'une goutte. La résonance capillaire de la goutte est étudiée par détection interférométrique de son apex en mouvement. La faisabilité de cette méthodologie est prouvée en caractérisant la cinétique d'évaporation de la goutte par glissement spectral des ondes capillaires. La deuxième partie de la thèse porte sur la modélisation du transport de biomolécules tensioactives dans une goutte : le transport diffusif, les processus d'ad/désorption aux surfaces, la condition cinématique d'un rayon variable (évaporation) ainsi qu'une quantité molaire finie de biomolécules sont pris en compte. Un nouveau nombre adimensionnel est proposé pour rendre compte de la taille finie d'une goutte. Puis le transport chimique associé au courant de dérive induit par les ondes capillaires (excitées par électromouillage oscillatoire) est pris en compte à l'aide de simulations numériques. Finalement, l'électromouillage haute et basse fréquence est appliqué au cas d'une goutte enrichie par des molécules d'albumine de sérum bovin. En utilisant conjointement l'interférométrie optique et l'imagerie, et en considérant la loi de Lippmann-Young, le vieillissement biochimique de la surface solide mouillée par la goutte est détecté.

Mots clés : Microfluidique digitale, Gouttes, Electromouillage, Interférométrie, Diffusion, Convection, Physico-sorption, Evaporation, Biomolécules.